OPTICAL METHODS FOR DEEP-TISSUE IMAGING, PRECISE MAPPING OF CELLULAR TOPOGRAPHY AND SINGLE-MOLECULE STOICHIOMETRY ANALYSIS

A Dissertation

Presented to the Faculty of the Graduate School

of Cornell University

In Partial Fulfillment of the Requirements for the Degree of

Doctor of Philosophy

by

Avtar Singh

August 2016

OPTICAL METHODS FOR DEEP-TISSUE IMAGING, PRECISE MAPPING OF CELLULAR TOPOGRAPHY AND SINGLE-MOLECULE STOICHIOMETRY ANALYSIS

Avtar Singh, Ph. D.

Cornell University 2016

Fluorescence microscopy and spectroscopy have proven crucial to biological investigations because of their superior contrast, molecular specificity, gentle nature and diverse information content. However, despite these key advantages, the technologies are continually evolving to address limitations in spatiotemporal resolution, imaging depth, quantification, multiplexing and other areas. This thesis describes wide-ranging efforts to understand the capabilities of fluorescence-based methods and to push the boundaries of biophysical measurement through new instrumentation and analysis strategies.

We begin with an investigation into the depth limit of two-photon microscopy and its dependence on tissue scattering. A customized sample cell and two-detector measurement chamber are used to study the influence of fundamental objective lens parameters on fluorescence excitation and emission in turbid media. The results advocate the use of large field-of-view objectives with low excitation numerical aperture (NA) and high collection NA, encouraging the development of novel detection geometries and objective lens designs that decouple these latter two parameters.

The advent of super-resolution imaging has inspired a surge of innovation aimed at combatting longstanding problems in the field of microscopy. One especially challenging goal has been to develop methods with molecular-scale precision in the axial dimension. While interferometric approaches such as scanning angle interference microscopy (SAIM) have yielded the necessary precision, their ability to capture live-cell dynamics has remained limited. A second project details an azimuthal scanning platform that boosts SAIM temporal resolution by an order of magnitude without compromising on spatial information. Furthermore, our scanning instrumentation serves as versatile platform for general-purpose quantitative biological imaging.

A major caveat of single molecule imaging is the *in vitro* nature of many experiments. A third set of experiments aims to bridge the gap between traditional single molecule work and a biological relevant setting. We develop a new strategy to assemble protein complexes at physiological concentrations and dilute them to single molecule levels without any exogenous chemical agents. Fluorescence correlation spectroscopy and stepwise photobleaching are then used to study the oligomeric character of individual complexes without removing them from their native environment. Although we demonstrate the utility of our approach through subunit stoichiometry measurements, it represents a generalizable strategy to extend single molecule imaging to the cellular mileu.

BIOGRAPHICAL SKETCH

Avtar Singh was born and raised in New York City, where he first became acquainted with the world of scientific research during his time at Stuyvesant High School. During his summers, he worked with Miriam Rafailovich at the Garcia Center for Materials Research at SUNY Stony Brook, learning about the electrophoretic properties of macromolecules on semiconductors and biomaterial-cell interactions. After high school, Avtar left the hustle and bustle of NYC for the calmer world of Ithaca, NY, where he completed a Bachelor of Arts in Physics at Cornell University. Through research projects with Warren Zipfel, he discovered his interests in fluorescence microscopy and in pushing the limits of biophysical measurement.

In the fall of 2008, Avtar continued in Warren's lab as a PhD student in the School of Applied and Engineering Physics and shifted his focus to developing new single molecule and super-resolution fluorescence imaging methods. Through a wide variety of projects, Avtar honed his skills in nonlinear optics, single molecule fluorescence and molecular biology while dreaming of new ways to tackle fundamental problems in microscopy. Upon graduation, Avtar will remain with Warren and Matt Paszek as a postdoctoral fellow before continuing his research elsewhere.

To my parents

ACKNOWLEDGMENTS

When I first left New York City nearly twelve years ago, I certainly never expected to spend so much time in Ithaca, but almost immediately, its quaint charm and diversity of intellect and culture drew me in. The chapters of my life spent at Cornell have been invaluable to my growth both as a person and as a scientist and I owe so much to the wonderful people that I have met here. Your kindness, generosity and awe-inspiring talents have left me with new perspectives on the world and I am forever grateful to have crossed paths with you.

First and foremost, I must thank my advisor Warren Zipfel, who I fortuitously met one May afternoon during my sophomore year after many failed attempts to seek out research opportunities with other faculty. Warren was instantly welcoming and has always been approachable, putting me at ease to pick his brain about the minutiae of experimental parameters or even the travails of daily life. Although his jack-of-all-trades exceptionalism is humbling, Warren only knows to treat you like an equal and has always been patient when I needed time to process scientific ideas or methodology. As a mentor, he has supported my widespread interests and wildest ideas while providing steady doses of realism to help refine my scientific acumen. I consider myself incredibly fortunate to have trained with him.

I would also like to thank my committee members: John Lis and Michelle Wang. John's shoot-for-the-stars attitude and relentless dreaming have been invaluable in shaping my own academic philosophy. Meanwhile, his biweekly meetings and yearly retreats have been a hotbed of ideas, launching many exciting projects and collaborative endeavors. Michelle's remarkable energy and enthusiasm

for all things biophysics have challenged me to think on a broader scale than individual projects while her sharp ability to ask the right questions has guided my scientific inquiries. I greatly appreciate all that you have done to aid me through my graduate studies.

None of this would have been possible without the enduring support of my parents. From the earliest of days, they have encouraged me to aim high academically while emphasizing the need to enrich the lives of others. My father's industrious work ethic, impeccable character and fondness for virtue have set the standard that I strive to match while my mother has always been there to lend a helping hand when I bite off more than I can chew. From helping glue science fair posters in elementary school to picking me up after nights in lab during later years, their efforts have been boundless and not always duly recognized. My aunt and grandparents have played an equally important role, providing unwavering affection and frequent reminders to enjoy every step along the journey. My brother Ekonkar and my sister Kirtan have also offered whole-hearted support while pursuing their own dreams with equal devotion. I also owe immense thanks to my aunt and uncle from Ithaca, who lured the city boy to the small town and looked after him as one of their own.

The Zipfel group, both in its current iteration and previous DRBIO form, has been a magnet for talented biophysicists and a melting pot for interdisciplinary science. The endless stream of colleagues and collaborators were a continual source of intellectual stimulation spanning numerous academic fields. I want to begin by thanking previous and venerable members of the lab, who were seminal to my development back when I was an undergraduate and fledgling PhD student. Watt

Webb, who co-led DRBIO efforts with Warren, served as an inspiration for myself and countless others with his multidisciplinary style and unlimited support for students' ambitions. Rebecca Williams acted as a second mentor in the lab, offering astute analysis on wide-ranging topics and a level-headed approach to dealing with numerous situations. Jesse McMullen took me under his wing during my first two years and dealt with an endless barrage of questions while providing vital guidance and training. Huimin Chen has been a longstanding teacher and friend, advising me on issues ranging from career advancement to cooking ever since my days as an undergraduate. Bethsabe Romero was always there for a dose of fun in the wee hours of night or a dash of perspective when I needed it. Alex Kwan, Val Anderson, Hyungsik Lim, Ina Pavlova, Chris Brown and Dimitre Ouzounov also provided much-needed wisdom. Paul Lee, Lisa Toth, and Tae Cooke were instrumental in software and hardware development (along with Warren, of course) while Pam Gordnier kept the lab running in its early days; I owe Paul an additional debt of gratitude for his comprehensive tutorials in C++ and programming in general.

Amongst the newer group members, Julian Palacios Goerger has helped troubleshoot a wide assortment of problems spanning from instrumentation to cell culture. Juan Wang puts up with my unsolicited advising and frantic personality on a daily basis while maintaining her cool and doing great work on several fronts. Alexander van Slyke bravely grapples with challenging projects in single-molecule biophysics and regularly brings fun and interesting questions to lab. Max Kushner's determination and attention to detail have been vital and will surely guide him to future success. I have also had the pleasure of working alongside outstanding

undergraduate students during my time as a PhD student, many of whom have reinforced the notion that mentorship is a two-way street. Stephen Perry was my courageous first undergrad and did great work studying fundamental properties of photoconvertible fluorescent proteins. Vinh Le showed a spirited enthusiasm for various projects and a dedication to lab management that exceeded the rest of our lab. Han Gao's proactive and innovative nature repeatedly inspired new strategies for instrumentation and data collection. Alex Song truly deserves to be listed amongst graduate students, combining a relentless determination to tackle fundamental problems in single-molecule imaging with a hacker mentality for getting answers quickly. Samantha Zambuto repeatedly demonstrated great passion for molecular biology and biomedical engineering while also maintaining a fun atmosphere through her duties as lab social chair. Maria Sirenko never questioned the disparity between her projects and normal undergrad responsibilities, exceeding expectations at every turn and wowing me with her initiative. Kristine Chin, our high school prodigy, left an endless supply of post-it notes and lab decorations to bring color to our previously nondescript walls. Eli Doris applied himself resolutely to modeling our various optical configurations, teaching himself CodeV and LightTools along the way. And many others: Anna Dadhania, Mona Yuan, Sangamithra Vardhan, Reinaldo Hernandez, Nitya Deshmukh, Andrew Dorion and Maria Carvajal. You have all helped to make time in lab enjoyable.

The Lis group, who initiated me into the world of molecular biology and the intricacies of gene regulation, have been wonderful collaborators for many years. Digbijat Mahat, who has been both a close friend and colleague, taught me to embrace

a big picture vision of science while also engaging me in many captivating discussions over tea and macaroons. Abdullah Ozer has been overwhelmingly generous with both his time and patience in teaching myself and other Zipfel lab members. Martin Buckley and Katie Zobeck posed exciting questions about the mechanisms of transcription that commanded new technology development. Janis Werner was instrumental in all the support she provided, from sample prep to general lab organization. Hojoong Kwak has been encouraging for my future plans, sharing his wealth of knowledge about single-cell sequencing and helping to brainstorm exciting new directions. Jacob Tome, Fabiana Duarte, John Pagano and Judhajeet Ray have also provided keen insights and pleasant company.

The Paszek group: Matt Paszek, who I met while he was a postdoctoral fellow, has brought a surge of innovation and energy to single-molecule and super-resolution research at Cornell. Matt's transition to professorship has also taught me invaluable lessons and he has served as an outstanding mentor when it comes to experimental vision and career advancement. Marshall Colville has been an ideal colleague with an incredible mind, admirable work ethic and relentless drive for progress. Carolyn Shurer has always brought exciting new questions to push the limits of our methodologies and has served as a great resource for cutting-edge molecular biology techniques.

The Sondermann group: It has been a pleasure to work with Holger Sondermann, whose brilliant ability to tease apart molecular mechanisms using a wide variety of experimental methods has broadened my ambitions beyond tool development. Laura Byrnes was a fantastic collaborator, bringing unabated cheer and

merriment to long hours of troubleshooting and data collection.

The Baird-Holowka group. Barbara Baird and Dave Holowka have been supremely kind and supportive through my years at Cornell, aiding my investigations into cell signaling and membrane receptors through numerous insightful discussions and generous reagent contribution. Sarah Shelby was a super-resolution dynamo, driving forward our initial TIRF setup and motivating it with interesting questions about immune cell signaling; Sarah's renowned parties and roaring bonfires were also a welcome addition to many summer nights. Devin Wakefield was a vital collaborator who greatly accelerated progress on our DNA curtains front and educated me about the mechanisms and implications of EGFR signaling.

Many other faculty have made a significant impact my graduate school experience. Lois Pollack and Bruce Kusse initiated me into the rigors of teaching physics and impressed me with their pedagogical approaches. Paul Kammermeier, our collaborator from the University of Rochester Medical Center, posed difficult questions about the stoichiometry of metabotropic glutamate receptors that motivated the development of our cell fusion method for single molecule imaging. Chris Schaffer, Nozomi Nishimura and Steven Adie have been delightful lab neighbors, bringing an endless supply of caffeine, baked goods and stimulating conversation to the basement of Weill Hall. Iwijn de Vlaminck has shown a superb willingness to act as a mentor, acting as a sounding board for ideas on single cell sequencing while also opening my eyes to new opportunities. Countless other members of the Cornell faculty have contributed to my education—far too many to list here—and it is a true testimony to the spirit of generosity that lives on this campus.

A special thanks to all my friends outside of lab with whom I share so many happy memories. Joshua Tokuda—whose can-do attitude, multi-faceted skills and infectious positivity have led to so many adventures—has been an impeccable housemate, coworker, travel buddy, teammate and EMT. Stella (Yunxing) Li has cheered me along through school, basketball and life while also being one of the passionate, talented and thoughtful people I know. David Ackerman's eagerness to explore and unpredictable antics infused days with wonder and excitement. Vinh Le—my adopted sister and trusted gorge-searcher—brought so much joy to life and kept me young with all her singing, laughing and playing (hearts heart). Pinshane Huang has been a trustworthy supporter since day one—through classes, outreach and toy car joyrides—and provided sage advice in so many arenas (excluding Halloween costumes). Her unrivaled vision, passion, selflessness and humility continually inspire me and, undoubtedly, many others. Srikant Iyer's authenticity and undying loyalty made him a trusted confidant, whose jovial charm can always light up a room. Arun Batra was the cool older brother I never had and my personified conscience, providing surefire guidance in crucial moments. SueYeon Chung mesmerized me with her musings on physics and philosophy during many evenings at Stella's café. Kylan Szeto awed me with his all-around talents and mastery of diverse scientific fields while leaving a collection of "Kylan quotes" that always bring a smile to my face. Rupa Laxmi Shah was my trusty supplier of "chill pills" when life became too hectic. Praveen Gowtham's activities may not be repeated here, but it suffices to say that much fun was had. Melina Blees was the best neighbor you could ever ask for, offering endless hospitality that resonates with the warmth of her personality.

To my remarkable classmates Arthur Barnard, Nikhil Fernandes, Robin Havener, Pinshane Huang, David Hutchison, Hui Liu, John Mergo, Julia Mundy, Junbo Park and Kylan Szeto: first-year was a mishmash of problem sets, intriguing personalities and many fond memories. At that time, we were all finding ourselves after college and I'm glad to have had you there at my side.

To all the friends I have made through basketball, including Xiao Wang, Darryl Ngai, Will Baumgardner, Joshua Tokuda, Josh Kevek, Kai Yuan Chen, Robert (Corky) Wharton, Luke McDermott, Kevin Schindler and Marquis Riley: it was a privilege to share the court with you and to fight through many competitive intramural seasons together (Let's go PSBallers!).

My friends outside of Ithaca. Kevin Rubenstein is still good for entertaining articles, witty puns, midnight pizza runs or aimless wandering even after all these years. Madelyn Ho's refusal to accept or even see any limitations in life are a constant reminder to keep dreaming. Brandy Ma is a real-life superhero with the uncanny ability to sway me into salsa dancing or jumping into the Pacific. Jennifer Chen is a breath of fresh air and someone I have relied upon since my first days at Cornell. William Mui's visits are a flashback to younger days, when knocking down pins to the tune of "Wannabe" was all that mattered on Saturday nights. Sylvia Qu is the genie that grants my wishes for Knights who say Ni and delightful hikes on rain-filled mountaintops.

And many others: Jeahoo Kwon, Srilakshmi Raj, Devin Underwood, Alex Mull-Osborn, Tuyen Dang, Mohan Gudipati, Chinmayee Subban, Henry Wen, Joan and Igor Baskin, Pamela Tieu, Jennifer Shum, Cathy Lii, Steve Meisberger, Julie

Sutton, Rob Dick, Yi Wen, Milka Doktorova, Phillip Isermann, Catalina Pereira, Tiit Lukk, Julia Kumpf, Beth LaLonde, Andrew Recknagel, Kira Novakovski, Daniel Joh, Senthil Mudaliar, Puifai Santisakultarm, Jason Jones, Poornima Gadamsetty, JC Cruz, Mitch Pender, Bailey Cooper and Mingchee Tan… you have made the past few years a blast.

All of my thesis work was made possible by generous support from our government. I would like to thank the National Science Foundation for the independence granted by their Graduate Research Fellowship, which allowed me to pursue my wide-ranging ideas for new biophysical methods. I am also grateful for extensive National Institute of Health funding, including a Molecular Biophysics Traineeship and grants for aptamer development (R33CA193043) and scanning angle interference microscopy (5R01DA030329). Their sponsorship was essential for cutting-edge instrumentation development, fundamental inquiries and numerous educational activities.

Lastly, I would like to thank the outstanding facilities and research support at Cornell. The Biotechnology Resource Center has continually provided access to state-of-the-art tools for imaging and sequencing along with key expertise and training; I would like to single out Rebecca Williams, Peter Schweitzer, Carol Bayles and Johanna Delacruz for all their amazing work. Cynthia Kinsland of the Protein Production Facility patiently taught me about protein expression and purification when I barely knew what a plasmid was and also let me tinker with her stopped-flow instrument to do some fun work. I also want to thank the outstanding administrative and building staff, both in Biomedical Engineering and Applied and Engineering

Physics: Jason Millspaugh, Todd Pfeiffer, Amy Layton, Pam Gillow, Steve Sparling, Brianne Rockefeller, Lynn Benedetto, Jinhee Roper, Ralph Personius, Dan Sheerer and Cynthia Reynolds. You have always been there to lend a helping hand and to provide crucial behind-the-scenes support.

TABLE OF CONTENTS

LIST OF FIGURES

LIST OF TABLES

LIST OF ABBREVIATIONS

PSF	Point Spread Function
OTF	Optical Transfer Function
NA	Numerical Aperture
FOV	Field of View
OBA	Objective Back Aperture
OFA	Objective Front Aperture
OTF	Optical Transfer Function
QE	Quantum Efficiency
AOI	Angle of Incidence
2PM	Two Photon Microscopy
3PM	Three Photon Microscopy
MPM	Multiphoton Microscopy
SHG	Second Harmonic Generation
THG	Third Harmonic Generation
SIM	Structured Illumination Microscopy
STED	Stimulated Emission Depletion
STORM	Stochastic Optical Reconstruction Microscopy
dSTORM	direct Stochastic Optical Reconstruction Microscopy
PALM	Photo-Activation Localization Microscopy
iPALM	interferometric Photo-Activation Localization Microscopy
STAR	Simultaneous Two-wavelength Axial Radiometry
SAIM	Scanning Angle Interference Microscopy
FCS	Fluorescence Correlation Spectroscopy
FCCS	Fluorescence Cross-Correlation Spectroscopy
TIRF	Total Internal Reflection Fluorescence
HILO	Highly Inclined Laminated Optical sheet
SPT	Single Particle Tracking
FRET	Forster Resonance Energy Transfer
smFRET	single molecule Forster Resonance Energy Transfer
EMCCD	Electron Multiplying Charge Coupled Device
PMT	Photo-Multiplier Tube
SiMPull	Single Molecule Pulldown
SPReAD	Single Protein Recovery After Dilution

CHAPTER 1

BEYOND THE DIFFRACTION LIMIT: ADVANCES IN SINGLE-MOLECULE AND SUPER-RESOLUTION IMAGING

Fluorescence imaging and spectroscopy have had a profound impact on investigations of biological structure and mechanisms across many length scales. As the frontier of microscopy advances—with new developments to push limits on depth, speed, resolution and phototoxicity combined with new image processing and analytical tools–we are increasingly able to watch complex biological processes unfold before our eyes and to understand their functional relevance. This thesis describes efforts to understand and evolve these boundaries on many fronts, including deep-tissue nonlinear imaging, super-resolution microscopy and single-molecule fluorescence imaging. In this chapter, I present a history of super-resolution and single-molecule imaging, reviewing technical developments as well as applications to cell biology. Over the past decade, these sub-fields have radically altered our perspective on the fundamental capabilities of microscopy and unearthed new modes of analysis by which imaging can contribute to biological inquiry.

INTRODUCTION

The ability to directly watch complex processes unfold and to understand their mechanisms with minimal reliance on biochemical interpretations is invaluable. Toward this end, fluorescence microscopy has played a central role due to its ease of use, molecular specificity, contrast, and the feasibility of multi-color and live-cell modalities. However, optical imaging has one key limitation: the blurring of light by diffraction greatly hinders our ability to resolve features much smaller than a

wavelength [1]. Since most biomolecules are two orders of magnitude smaller, conventional light microscopy fails to provide much information about conformational changes, macromolecular assemblies and organelle ultrastructure.

While the 20th century produced large advances in fluorescence microscopy and spectroscopy—including methods for optical sectioning [2], diffusion measurements [3], orientation mapping and lifetime imaging [4]—most measurements were averaged over large numbers of biomolecules. The past two decades have marked a swift change in approach, with an emphasis on single molecule technologies and efforts to image structures below the diffraction limit. Pioneering work by multiple groups to bring single molecule fluorescence to the forefront of bio-imaging was rewarded with the 2014 Nobel Prize in Chemistry.

Much of this progress has come on the heels of improvements in underlying technologies. The development of sensitive detectors, such as electron multiplying charge-couple devices (EMCCDs) and scientific complementary metal oxide semiconductor (sCMOS) cameras has made shot-noise limited imaging of single fluorophores a routine process. New probes and labeling strategies have made it easier to tag specific targets within cells with high contrast and specificity while expanding opportunities for multiplexing. Meanwhile, continual advances in computing power and data storage have facilitated computationally intensive analyses of large data sets and real-time reconstruction of meaningful images.

Here, I aim to review recent advances in super-resolution and single-molecule technologies in the context of cell biology. I highlight specific methods, with an emphasis on developments in the past decade, and applications demonstrating their

utility, giving particular attention to studies of nuclear and membrane proteins. As these and other biophysical tools are adopted more broadly, our understanding of biological mechanisms will benefit greatly from the ability to probe intermolecular forces, population distributions and single molecule kinetics quantitatively at high spatiotemporal resolution.

SINGLE-MOLECULE METHODS

Single particle tracking

Single particle tracking has long been used to track clusters of fluorescent molecules with sub-resolution accuracy [5,6], owing to the general principle that the position of a signal can be localized with much higher precision than the signal width [7] (Figure 1.1a). A longstanding goal to bring imaging to the molecular regime led to the first images of single chromophores via absorption spectroscopy in 1989 [8] and fluorescence in 1990 [9], using cryogenics to exploit the fact that absorption cross sections are much higher at low temperatures and to mitigate photobleaching. Advances in optics and detector technology permitted the first room temperature images of single molecules by Near-Field Optical Scanning Microscopy (NSOM) [10,11], followed by the first aqueous experiments using Total Internal Reflection Fluorescence (TIRF) microscopy. [12] The latter opened the door for true biological investigations and tracking of single molecules soon followed [13], as did tracking of fluorescent proteins in solution [14]. The first live-cell single-molecule experiments visualized labeled EGF ligands binding to EGFR and used FRET to

discern receptor dimerization [15]. Today, single particle tracking (SPT) is readily accomplished in either point-scanning or widefield geometries.

Because SPT offers insights into molecular diffusion, association/dissociation rates and target search kinetics, efforts have been made to improve precision, optimize multi-color applications and extend tracking to three dimensions. Yildiz and colleagues pushed the resolving power by combining bead labels with back-thinned frame-transfer CCDs to resolve single myosin steps with 1.5 nm precision [16]. Using STED microscopy, nitrogen vacancy centers have been localized with Angstrom precision [17]. Ultimately, the limits on spatiotemporal resolution are determined by photon fluxes and signal-to-noise ratio, with the boundaries being pushed continually by the development of faster, more sensitive detectors and brighter, more resilient probes.

Accurate co-registration across multiple spectral channels is needed for interfluorophore distances to be meaningful. For point-scanning microscopies with a single excitation wavelength, the channels are intrinsically aligned and distances measurements with sub-10 nm have been achieved with nanoparticle probes [22,23]; more recently, sub-nanometer errors were reported by suppressing quantum dot blinking and using confocal microscopy with a stage scanner [24]. For many applications, imaging detectors are preferred for their parallelized readout and higher frame rates over large fields of view. Today, EMCCDs and sCMOS cameras are the detectors of choice due to their sensitivity, speed and low noise characteristics. However, cameras introduce additional difficulties, as chromatic aberrations in the imaging pathway and pixel non-uniformities distort the relationship between

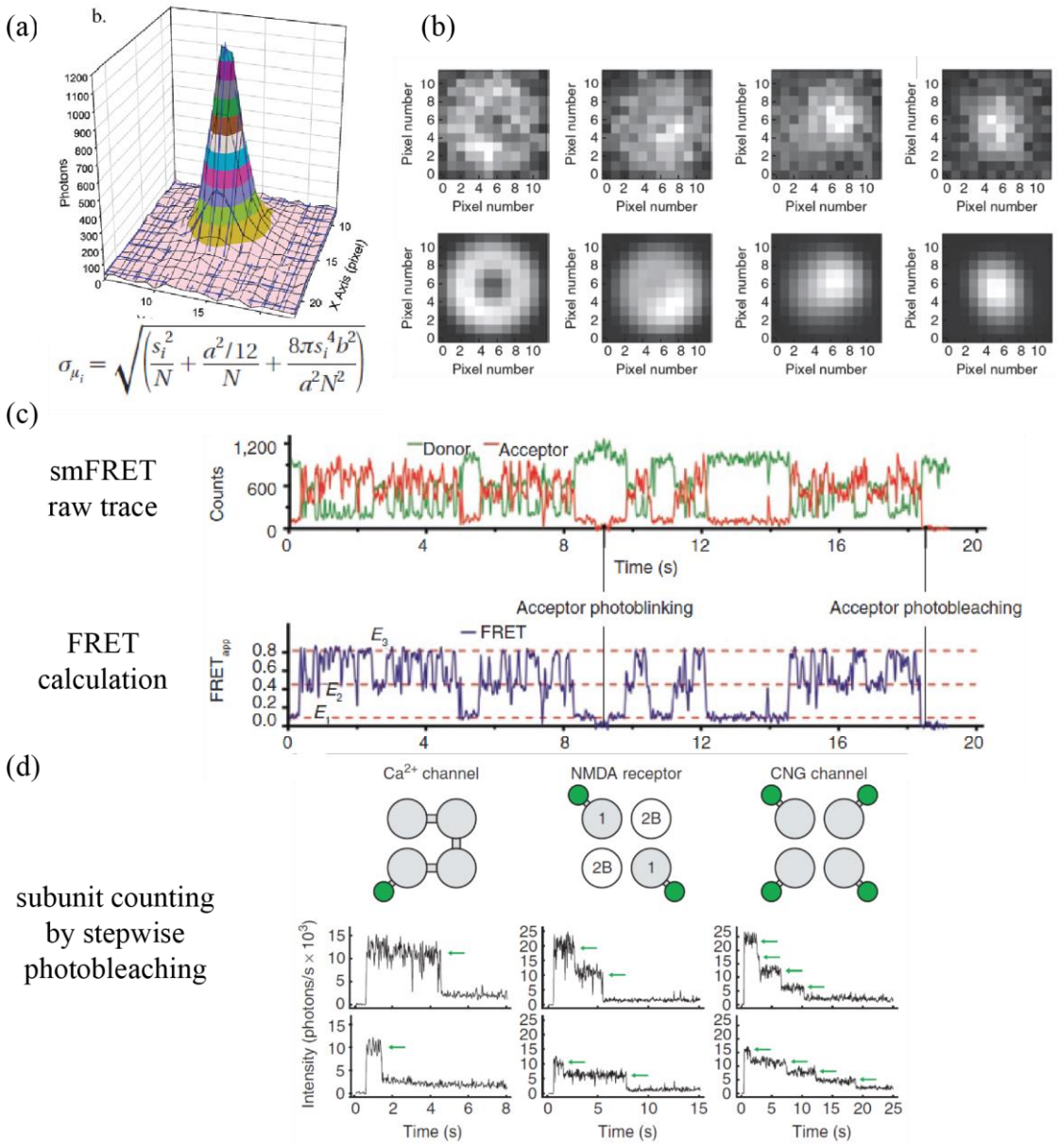

Figure 1.1 Single molecule fluorescence. (a) Image of a single Cy3 immobilized on glass. Fluorophore position can be estimated with significantly greater precision than the size of the emission point spread function. (b) Images of single rhodamine dyes immobilized on a substrate and their corresponding theoretical dipole emitter point spread functions. (c) Example single molecule FRET time traces and corresponding FRET calculation, showing discrete states. (d) Stepwise photobleaching of GFP-tagged membrane receptors. Figures adapted from [18–21].

different color channels. This co-registration error is independent from localization error associated with one-color SPT. Single-molecule high-resolution colocalization (SHREC) uses local mappings between color channels to achieve sub-5 nm co-registration across the field-of-view [25]. In a newer report, active feedback was used to position dye centroids onto a single pixel to minimize pixel non-uniformity effects, allowing Cy3-Cy5 molecules to be co-registered with subnanometer accuracy [26].

In order to track particles in three dimensions, z-scanning is simplest, but comes at the cost of temporal resolution. If particle movement is constrained to a few microns axially, there are a handful of methods that can map z-position instantly without sample movement. Biplane imaging collects two focal planes of data and uses PSF shape and intensity information in each image to determine z-location [27,28]. This idea was extended to more focal planes in multifocus microscopy (not to be confused with parallelized multifocal multiphoton or confocal microscopy) by using a diffractive grating and dispersion-compensating prism to image 9-25 planes onto a single camera [29,30]. Alternatively, weak cylindrical optics may be used in the detection path to introduce purposeful astigmatism [31,32]; in this case, the orientation of an oblong point spread function shape encodes molecular height information. Pavani et al. have used a spatial light modulator to create a double-helical point spread function (DH-PSF) for 3-D tracking with 10-20 nm precision [33–36]. Orbital tracking microscopy scans a focused laser spot around a moving particle. As the particle deviates from the orbit center, the fluorescence readout is modulated and the scan pattern may be adjusted on-the-fly to maintain orbit. 3D orbital tracking uses two pinholes to create image planes above and below the moving particle and a piezo stage

to clamp position [37,38]. With the advent of localization microscopy, many of these methods have found utility in extending super-resolution imaging to the third dimension.

Dye orientation can provide insight into molecular interactions and is also a key determinant of photophysical phenomena such as FRET. For molecules undergoing hindered or free diffusing in solution, single molecule anisotropy measurement can help determine rotational degrees of freedom and rotational timescales [39]. Although orientation can be inferred from ratiometric measurements of the same molecule with different excitation and emission polarization states [11,39,40], the angular distribution of fluorescence in a single molecule image also contains orientation information. The first NSOM images of single molecules also showed characteristic dipole emission patterns [11]. Early methods of imaging dipole orientation used slight defocus or introduced aberrations in the optical system to spread information over more pixels to better resolve different angles within the imaging plane [41–43]. More recently, Mortensen et al. have shown that complete orientation information can be retrieved from in-focus emitters [20] (Figure 1.1b).

Single-molecule FRET

Resonance energy transfer was one of the earliest optical methods for probing distances below the Rayleigh limit. Due to its $1/R^6$ dependence on intermolecular separation, energy transfer is negligible for distances over 10 nm. Since the first smFRET measurements of DNA hybrids dried on glass [44], the technique has

flourished as a method for measuring conformational changes and binding kinetics (Figure 1.1c).

smFRET measurements are typically performed on molecules freely diffusing in solution or immobilized on a substrate. Confocal or multiphoton geometries are used to minimize out-of-focus background in the former case while TIRF is advantageous for the latter. Bright, photostable dyes such as Cy3 and Cy5 are used to achieve long-term, high-SNR imaging. Furthermore, buffer properties may be tuned to reduce soluble oxygen and minimize time spent in the triplet state to improve photophysical characteristics [45,46]. Alternating laser schemes have been used to measure spectral bleedthrough and improve FRET quantification [47–49]. Multicolor FRET allows simultaneous measurement of multiple biomolecular distances, but comes with additional complications. The various dyes must be spectrally resolved, yet still have enough overlap for energy transfer to occur. Despite these challenges, three and four-color FRET have been realized and used to map complex multi-state dynamics [50–54].

For immobilization experiments, biomolecules may be tethered to a passivated surface or confined within nanocontainers. Surface passivation is the simpler approach, with polyethylene glycol being a popular choice due to its inertness. A newer dichlorodimethylsilane-Tween 20 surface has been reported to achieve even lower background binding [55]. For membrane proteins, lipid bilayers provide a biologically relevant passivation layer [56]. In certain cases, high concentrations of labelled molecules are needed to mirror the situation *in vivo*. To alleviate background fluorescence, nanocontainers may be used to maintain these concentrations locally

while the overall fluorophore density is kept low. Zero-mode waveguides are tiny apertures within an aluminum film deposited on a glass substrate that prevent any optical modes from propagating into the aqueous medium above. By using ZMWs and TIRF, background is substantially limited and excitation is confined to attoliter nanowells [57]. If long-term imaging of the same molecule is desirable, small unilamellar vesicles tethered to a supported lipid bilayer may be used as nanoscale reaction volumes. This approach has the added benefit of minimizing interactions with the substrate. Pores may be engineered into vesicles to allow small molecules exchange, either by exploiting leakiness near the lipid melting temperature or by incorporating pore proteins.

smFRET experiments are often used to probe transitions between various discrete states of molecular conformations or interactions. For relatively simple systems, such as those occupying two or three possible states, state transitions may be marked manually or automated by using thresholding algorithms [58]. For more complex systems, probabilistic algorithms such as those based on Hidden Markov Models [59] or Maximum Likelihood Estimation have been used [60]. A Markov chain is a random progression of a system between discrete states, with state-to-state transitions following exponential decay kinetics. smFRET trajectories are classified as hidden because noise clouds our observations of which state the system is in at any given time. HMMs use an emission probability function (the probably of measuring a particular FRET value given that the system is in a particular state) and a transition probability matrix (the probably of the system transitioning from one state to another) to calculate the relative probabilities of different possible trajectories [59]. Since the

transition probabilities and emission probabilities are also unknowns, multi-dimensional optimization routines are used to determine these functions simultaneously. Maximum likelihood approaches are appealing because they require no a priori knowledge about which states are accessible, but have been known to introduce errors due to overfitting.

Stoichiometry determination

Single molecule fluorescence traces contain information about molecular movements as well as photophysical transitions. In cases where photobleaching is the predominant cause for intensity changes, the number of discrete steps in the time trace provides a direct readout of labelled biomolecules present and may be used to extract stoichiometry information (Figure 1.1d). This method has previously been used to determine the subunit stoichiometry of membrane protein oligomers expressed in frog oocytes (*Xenopus laevis*) [21]. In this case, protein expression was limited by microinjecting small amounts of mRNA into individual cells. In some cases, artificially low expression can bias oligomerization states. To avoid potential artifacts, a single-molecule pulldown approach has been developed to allow physiological expression followed by cell lysate preparation and dilution for single molecule observation in a PEG-passivated flow cell [61,62]. Because detergents can significantly perturb interactions between proteins, I present an alternative method to dilute proteins *in situ* for stepwise photobleaching analysis in Chapter 4.

As with FRET traces, photobleaching steps may be coded manually or by a computer. Automation relies on filters to denoise the data trace and aid in step

detection. The Chung-Kennedy filter is a popular choice due to its edge-preserving characteristics [63,64], but other methods have also been applied and compared quantitatively [65,66]. Step detection becomes difficult as the time between steps gets shorter, but automated methods have been able to detect up to 20 steps in bleach traces [64,67].

SUPER-RESOLUTION METHODS

Traditional approaches

The earliest methods for optical super-resolution circumnavigated the diffraction limit by using near-field imaging. Near-field optical scanning microscopy achieved sub-100 nm resolution by scanning a tiny probe in close proximity to the sample [68]. However, near-field imaging is impractical for most biological applications. The potential for super-resolution with confocal microscopy has long been known, with 2x resolution enhancement if a small detection pinhole is used along with computational deconvolution [69]. However, such a geometry is highly photon-inefficient and generally not advantageous. More recently, Zeiss has introduced an AiryScan module based on the same principle but using virtual pinholes to achieve 1.7x super-resolution without sacrificing overall light-collection.

Another class of techniques relies on a second objective lens to extend microscope resolution. Standing wave microscopy uses opposing objectives or a single-objective and mirror to generate a standing wave in the illumination pattern, which can be swept across structures of interest [70,71]. By acquiring multiple images with different phases of the excitation pattern, sub-100 nm axial resolution can be

realized. When applied to thin samples and combined with localization, precision can exceed one nanometer [72]. Successive dual-objective methods came in either point-scanning (4Pi microscopy) or imaging (image interference microscopy, I^nM) flavors [73–75]. The simplest of each, 4Pi(B) confocal and I^2M, relies on interference of fluorescence captured by the two objectives to capture high-resolution axial information which was absent in the corresponding single-lens microscopies. 4Pi(A) and I^3M used opposed objectives to create an axially patterned excitation field, while 4Pi(C) and I^5M combined patterned excitation with image interference for the best resolution gains. While all of these methods pushed the diffraction limit, the resolution gains were fairly moderate and the increased complexity of dual-objective modalities often outweighed the benefits.

Structured illumination

Structured illumination was first used as means of optical sectioning [76]. Imaging with a striped illumination pattern has high contrast only in the vicinity of the objective focus. By acquiring three images at different phases of the pattern and applying a simple image processing formula, one can obtain optically sectioning images on par with confocal microscopy without any light loss.

The concept of resolution enhancement by structured illumination was put forth and demonstrated by Heintzmann and Cremer in 1998 [77] and fully developed by Gustaffson in 2000 [78]. The principle hinges on the fact that the microscope point spread function, a measure of resolution, maps to an optical transfer function (OTF) in Fourier space and can support a limited subset of k-space vectors (Figure 1.2a). The

Rayleigh limit is the outer edge of this disk in x-y. When a sample is illuminated with modulated excitation, the fluorescence generated is a product of the illumination pattern and the local concentration of fluorophores. This real-space product projects to a convolution in k-space of the analogous quantities. As a result, sample information is shifted in k-space by an amount determined by the frequencies in the patterned light, allowing previously inaccessible sample information to now fall under the support of the OTF. Moire fringes present a strong visual of the same phenomenon. When two fine striped patterns are superimposed, a new pattern with lower spatial frequencies appears. By choosing a diffraction-limited modulation frequency, the resolution of the microscope can be doubled in one direction by acquiring images at 3 different phases. For 2-D or 3-D resolution doubling, 9 or 15 images are required [78,79]. Harmonic Excitation Microscopy achieves similar results using a mesh excitation pattern [80].

SIM is usually implemented by rotating or translating a diffraction grating to acquire images at different phases and directions. Electro-optic components, such as spatial light modulators, may also be used for faster pattern switching. For 2-D SIM, light from the -1 and +1 orders is retained to generate laterally modulated excitation; all other orders are blocked by a mask. For 3-D SIM, the -1, 0 and +1 orders are used to produce a pattern modulated both laterally and axially (Figure 1.2b). Additional efforts have been made to introduce spatial incoherence to the beam to avoid stray interference due to dust particles, for example by introducing a rotating diffuser into the light path and coupling lasers through a multimode fiber. After acquisition of sufficient images (3 or 5 different phases for 2-D and 3-D, respectively, for each of 3 different pattern orientations), raw data is background subtracted and drift-corrected.

Figure 1.2 Structured Illumination Microscopy. (a) *Top:* Moire fringes seen in two superimposed line patterns, representing the product between a sinusoidal illumination pattern and arbitrary sample. Fringes shift high spatial frequency information to lower spatial frequencies *Bottom:* In Fourier space, the spatial frequencies resolved by the microscope fill a disk, called the microscope optical transfer function (OTF). Sequential imaging with a sinusoidal pattern at three phases and reconstruction can double the extent of the OTF in one direction. By acquiring sufficient images at different phases and orientations of the pattern, resolution can be doubled in all directions (b) Schematic of a typical SIM apparatus. Illumination is coupled through a fiber to eliminate spatial coherence, then collimated and projected onto a grating. Light from the -1, 0 and +1 orders is focused onto the objective back aperture to generate a 3-D sinusoidal intensity pattern in the sample; 2-D SIM uses only the -1 and +1 orders. The grating is shifted and rotated to acquire different phases and orientations. (c) Nonlinear SIM based on fluorescent protein photoswitching is capable of achieving higher resolution than traditional SIM by detecting higher harmonics in the SIM images and uses significantly lower illumination intensities than saturated SIM. The degree of nonlinearity, and the number of detectable harmonics, is determined by the saturation level of photoswitching. (d) SIM images of actin demonstrate the difference between conventional widefield, linear SIM and nonlinear SIM using Dronpa. Figures adapted from [78,79,81,82].

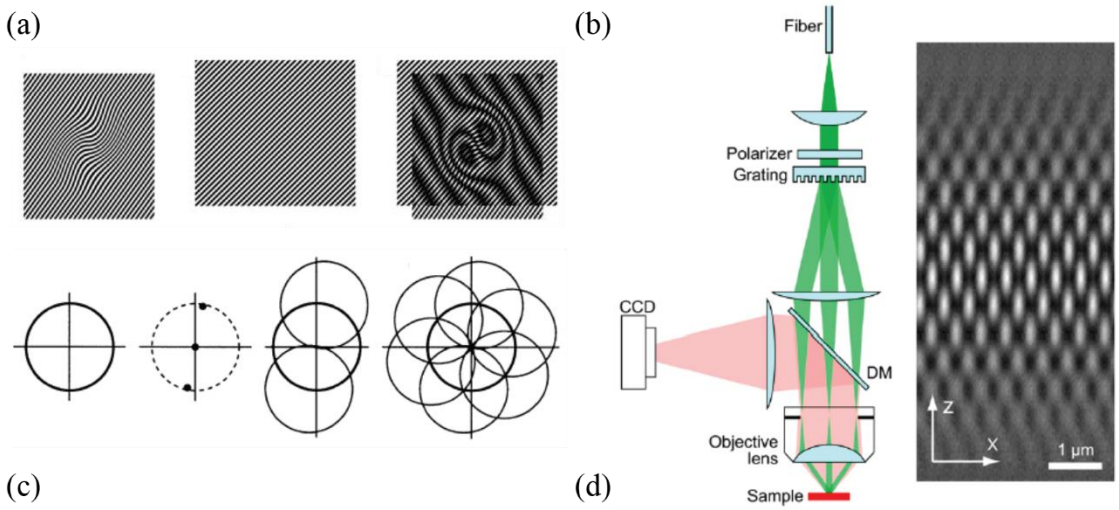
(a)
(b)
Fiber
Polarizer
Grating
CCD
DM
Objective lens
Sample
Z
X
1 µm
(c)
(d)
p
FWHM
Saturation level, η = 5
Saturation level, η = 30
Illumination intensity of the off light
Fraction of molecules remaining on
x
A
B
C
D
1 µm
5 µm
position (nm)

After Fourier transformation of each raw image, grating period, phase and orientation are estimated. Once these are known, Fourier components for the sample data are determined by cross-correlation and shifted back to their true positions in k-space. Here, they're combined using a weighted average (typically a specialized Weiner filter) and then shifted back to real-space. SIM images typically take a few seconds to record and minutes-hours to analyze, depending on how many z-slices were acquired.

Multicolor imaging is readily achieved by SIM due to its compatibility with all probes [83]; in contrast, STED and localization microscopy require careful selection of fluorophores. Video-rate 2D imaging was achieved by using spatial light modulator to generate and switch the illumination pattern. An SLM can achieve submillisecond switching of its pixels, compared to 1 second rotations and 10 ms translations of a diffraction grating [84]. 3-D imaging of live-cell dynamics was performed by using an SLM to generate 3-D excitation patterns, acquiring whole-cell stacks in 5 seconds [85].

While traditional SIM achieves ~100 nm resolution by shifting the information in k-space by one order, more significant resolution gains can be realized by exploiting nonlinear mechanisms and higher-order shifts (Figure 1.2c,d). Saturated structured illumination microscopy uses the nonlinearity associated with fluorescence saturation to generate higher-order frequencies in the excitation pattern [81,86,87]. These frequencies shift information further in k-space and bring even smaller features into the OTF support. One major drawback of this approach is that the high intensities needed may lead to substantial photodamage and photobleaching of the sample. A gentler nonlinear approach employs photoswitching as a nonlinearity mechanism [82].

Photoswitching between dark and bright states is also saturable and is accomplished at much lower light intensities than excitation saturation. Sub-50 nm resolution was achieved using the reversibly photoswitchable fluorescent protein Dronpa and 2 higher order peaks in the excitation pattern (63 raw images per 2D reconstruction). A recent publication combines saturable photoactivation with TIRF and an improved rsFP to achieve fast high-resolution imaging of cellular dynamics [88].

Structured illumination has been combined with other methods to increase functionality. TIRF-SIM confines excitation within 100 nm of the coverslip and uses similar instrumentation and analysis methodology to 2D-SIM [84,89–91]. SIM can be combined with image interference microscopy to achieve nearly isotropic resolution [92,93]. Sparse patterns of activation, such as scanned lines or spots, allow for rejection of out-of-focus light and are useful for thicker samples [94,95]; using the same principles, a spinning disk confocal may be modified for super-resolution imaging [96]. For the multifocal approach, an all-optical analog called instant SIM has recently been introduced to greatly speed up acquisition and process images on the fly [97]. Two photon excitation can be used to further extend the imaging depth of multifocal and instant SIM [98,99].

Although resolution gains from linear structured illumination are fairly modest, they are realized with minimal tradeoffs compared to widefield imaging. Aside from a roughly ten-fold reduction in frame rate, SIM performs much like a conventional fluorescence microscope, using much lower powers than other super-resolution methods and retaining compatibility with all probe types. Furthermore, imaging speed with multifocal and instant SIM can approach 100 fps which is hardly a limitation for

most applications. If reversibly switchable proteins are suitable, nonlinear SIM provides all the same advantages with higher resolution, although the currently available rsFPs limit utility to one spectral channel. As newer FPs are developed, nonlinear SIM remains a leading candidate for live-cell imaging of cellular ultrastructure with minimal light perturbations.

Stimulated emission depletion

Stimulated emission depletion microscopy is part of a class of methods that aim to shape the illumination point spread function by exploiting the nonlinearity associated with Reversible Saturable Optical Fluorescence Transitions (RESOLFT). Although microscope optics cannot create illumination structures with features smaller than the Rayleigh limit, nonlinear photophysical processes can generate responses with higher spatial resolution. Stimulated emission is one such nonlinear process. For a group of molecules in the excited state, incident photons with a wavelength matching the energy difference between that state and a ground state can cause stimulated emission—driving the molecules back to the ground state with the emission of a photon of the same energy and direction as the incident photon. In this case, fluorescence (spontaneous emission) is no longer possible. For low incident energies, the rate of stimulated emission is linear with power. However, as the incident power is increased, the dependence becomes nonlinear and eventually saturates; at very high powers, all molecules are driven back to the ground state. Stefan Hall proposed the idea of using stimulated emission as a means of achieving far field optical super resolution in 1994, theorizing that by offsetting the STED beams relative to the

excitation beam, sub-resolution features could be created in the spontaneous emission profile [100]. In 2000, the first STED microscope was reported and demonstrated two-fold improvement in lateral resolution with six-fold improvement in axial resolution [101] (Figure 1.3a).

Typically, STED uses pulsed lasers for excitation and stimulated emission because it is advantageous to temporally separate those processes [100]. Excitation pulses are generally very short (sub-picosecond) while stimulated emission pulses are stretched to more efficiently deplete the excited state. For one-photon excitation, the STED wavelength is redder than the illumination and stimulated emission may be spectrally isolated from fluorescence by appropriate choice of filters. Illumination is often provided by using ultrafast lasers along with nonlinear optical devices, such as optical parametric oscillators, optical parametric amplifiers and regenerative amplifiers to generate specific frequencies or redistribute energy in laser pulses. Excitation and STED beams may be provided by a single laser source and using nonlinear optics to tune the frequency of some fraction or by using multiple oscillators operated in a slave-master configuration.

Various phase patterns have been used to engineer the STED beam, but the most common choices are a vortex phase ramp that produces a STED donut in the focal plane [102] or an annular phase mask [101] to produce a 3D confined volume (Figure 1.3b). Recordings are usually achieved in laser-scanning mode, with much of the same instrumentation as a confocal microscope and super-resolution images may be acquired with little to no processing required. STED and related techniques have been successfully applied for imaging with antibodies [103], fluorescent proteins [104]

or nanoparticle probes [17,105] in samples ranging from live cells [106–108]at to cultured tissue [109] and live animals [110,111]. Multicolor imaging has also been realized, both with organic fluorophores and fluorescent proteins [112–116].

Early STED imaging achieved fairly modest resolution gains with very high powers, which led to excessive photobleaching and photodamage. Efforts were made to engineer better point spread functions and reduce light exposure by using smarter illumination strategies or different photophysical mechanisms to achieve smaller excitation spots (Figure 1.3c). A major breakthrough was the development of aberration-resistant donut modes for the depletion beam [117–119], which led to sub-30 nm lateral resolution [102]. Simultaneous xyz resolution improvements have been realized by using two STED beams, one for lateral and one for the axial gains [124,125]; this may be implemented in a dual-objective setup to achieve even better resolution due to coherent addition of the depletion beam wavefronts [124]. While early methods to create donut modes used spatial light modulators, the development of vortex phase plates led to better intensity minima at the focus [113].

Bleaching and phototoxicity were a significant concern in early STED implementations, due to the elevated powers needed for fluorescence depletion and the nonlinear dependence of bleaching on light intensity. In this way, photobleaching severely limited the resolutions attainable by STED. Since higher order triplet states have been theorized to produce accelerated bleaching, triplet-state relaxation (T-Rex) was proposed as a means of mitigating photobleaching [102]. T-Rex was implemented by using low rep-rate (0.25-1 MHz) pulsed lasers rather than the traditional 40-80 MHz lasers to allow the typical triplet state (lifetime τ_T ~1 μs) to relax back to

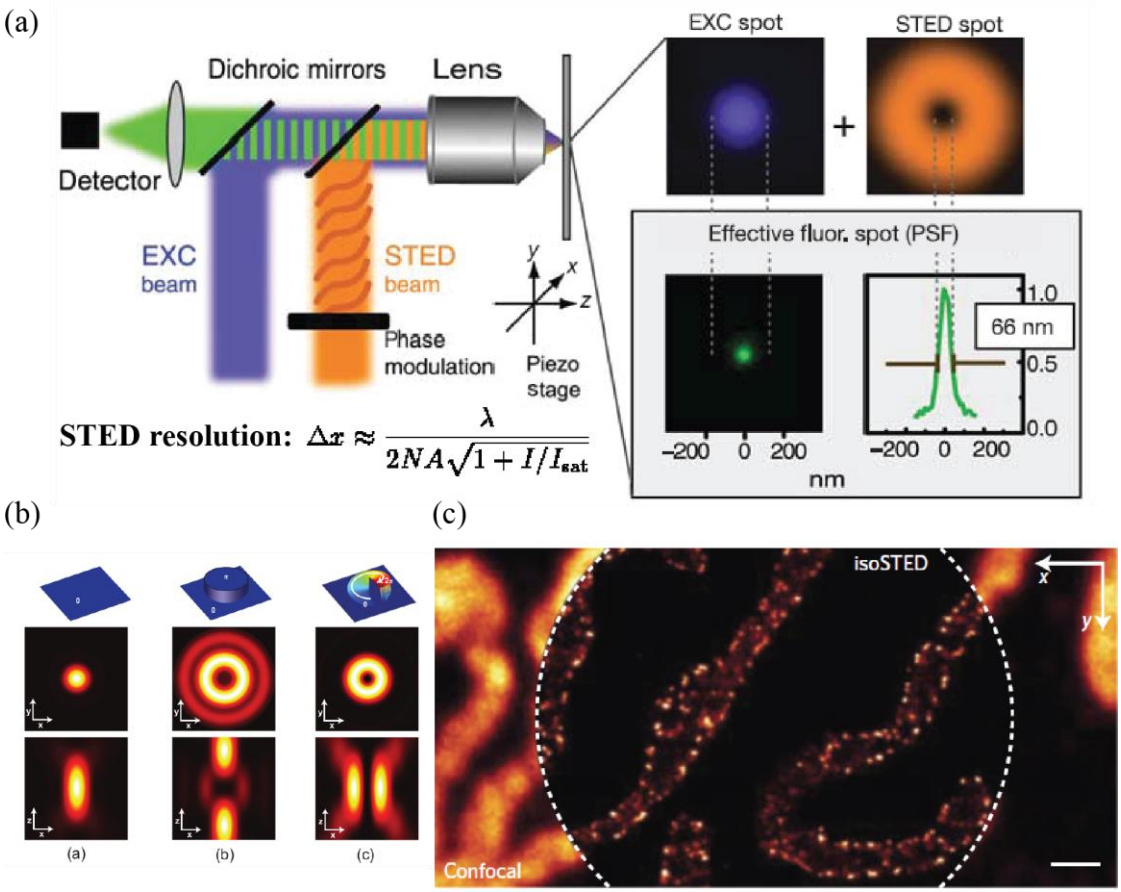

Figure 1.3 Stimulated Emission Depletion Microscopy. (a) Schematic of a typical STED microscope. Lasers for excitation and stimulated emission are combined while the latter is shaped by a phase modulator (phase plate or SLM) to generate an intensity minimum at the focal spot. STED resolution is determined by the intensity of the STED beam and follows a simple mathematical formula (inset). (b) Annular/Vortex phase plates are the most popular designs for point spread function engineering and generate 3D/2D super-resolved spots, respectively. (c) STED imaging of mitochondria clearly resolves the presence of Tom20 in the outer membrane, whereas confocal microscopy cannot discern any ultrastructural information. Figures adapted from [102,120–123].

the singlet ground state. Reduced bleaching by T-Rex was also shown to greatly improve fluorescence yields, boosting outputs 5-25 fold for both one-photon and two-photon excitation [126]. Cycling of molecules between the ground and excited states when no fluorescence feature is located at the focal spot was also deemed unnecessary. Based on an earlier method applied to confocal microscopy, REduction of State transition Cycles (RESCue)-STED blanks both the excitation and STED beams if insufficient fluorescence is recorded during a decision time less than the pixel dwell time [123]. Blanking may also be implemented if the fluorescence reaches an upper limit, with pixel values being scaled by the actual dwell time.

Photodamage may also be reduced by using a different RESOLFT mechanism to achieve subdiffractive focal spots. Ground state depletion microscopy shelves molecules in the triplet state and other long-lived dark states and was one of the earliest mechanisms proposed [127]. Compared to the GW/cm^2 intensities needed for STED, GSD requires a meager kW/cm^2. However, due to the involvement of triplet states in bleaching pathways, GSD microscopy was not realized until over a decade later, using photophysically favorable environmental conditions [128]. Reversible photoswitching of fluorescent proteins can also produce subdiffractive spots with kW/cm^2 intensities. In this case, molecules are switched to a dark state at the periphery of the focal spot via light-induced conformational changes in order to boost resolution. One drawback of the GSD and rsFP approaches is a significantly longer acquisition time due to the slow optical transitions being used, with pixel dwell times being on the order of ~50 ms and single frames taking an hour to record. The recent development

of a fast switching GFP variant has reduced pixel times over 100-fold and enabled fast RESOLFT imaging [129].

Another means of improving spatial resolution relies on the temporal aspects of STED. Fluorescence recorded before the STED beam has a chance to completely deplete excited states does not yield optimal resolution because the focal spot has not yet reached its minimum size [130,131]. Gated detection, accomplished by post-processing of time-correlated single photon counting data or by implementation of a fast electronic gate, can solve this problem. One drawback of this approach is that useful photons—originating from fluorophores within the final subdiffraction spot, but emitted early after the excitation pulse—are also discarded. This effect can be mitigated by using a short gate, which can still improve resolution without reducing signal too much (~50%).

Improvements in temporal resolution have also been critical. STED and RESOLFT imaging suffer from increased recording times compared to confocal due to the lower number of emitting fluorophores per focal volume and the increased number of pixels needed to satisfy the Nyquist sampling criterion. Video-rate imaging has been realized by using a resonant scanner over a small field-of-view, but compromises were made between spatial and temporal resolution [106]. More robust approaches involve parallelization of acquisition, either by scanning multiple spots [115,132,133] or lines [134]. Recently, a novel approach based on kilohertz accumulation of multiple frames using a fast electro-optic scanner has been reported [135]. Nanosecond dwell times cause each molecule to experience ~1 excitation cycle per pixel, resulting in stochastic emission. Consecutive frames may be binned either on-line or during post-

processing to balance spatial and temporal resolution but, compared to earlier STED approaches, fast scanning has the benefit of minimizing exposure to molecules while in the triplet state. This allows them to relax back to ground state, minimizing photobleaching and improving fluorescence yield.

As a point-scanning approach, STED benefits from many of the same extensions as confocal microscopy. It may be combined with correlation spectroscopy [107,136] or fluorescence recovery after photobleaching [137] for measurement of dynamic behavior. Two photon excitation [138,139] or adaptive optics [140] may be used to improve depth penetration in thick, scattering samples. Time-correlated single-photon counting may be used to discern between spectrally similar species with dissimilar kinetics [116].

Significant effort has gone into making STED and RESOLFT more accessible to the public and user-friendly. While early implementations required high-end equipment and expertise in ultrafast optics, the advent of cheap, turn-key pulsed supercontinuum sources has made STED cheaper and easier to set up [125,141]. STED imaging has also been performed with continuous wave lasers [142], eliminating the need for temporal alignment, and fast beam scanning may be used to reduce triplet build-up, as with pulsed T-Rex STED [143]. Further simplifications are afforded by novel phase masks, such as a dispersive dual-wedge phase plate that eliminates one beam path by focusing the excitation light to a small spot while creating a donut mode with the STED wavelengths [122]. Another means to the same end is to use a birefringent waveplate with chromatic dependence to achieve beam shaping, with the added benefit that it can be placed immediately next to the objective

lens [144]; this easySTED segmented waveplate can transform a scanning confocal microscope to a STED for approximately $5000.

Although STED is inherently an ensemble technique, single molecule sensitivity can be achieved with sufficiently high resolution or sparsely-labeled samples. As with conventional microscopy, reducing and oxidizing systems (ROXS) can substantially reduce photobleaching and improve photon yields for STED. ROXS buffers have been used to visualize single oligonucleotides immobilized on a substrate [145]. Another approach relies on the fact that a single molecule can emit only one photon at a time. By using pulsed lasers with a photon anti-bunching model, laser-scanning microscopy was used to estimate the number of emitters within the focal volume [146]. Single-molecule behavior such as stepwise photobleaching was observed and up to 20 emitters could be detected per diffraction-limited volume. Furthermore, it was argued that the method is more robust for molecular mapping than stepwise photobleaching, where multiple bleach steps close in time may not be resolved. Another application of STED to mapping single chromophores is the imaging of nitrogen vacancies in diamond [17]. Because these defects are invulnerable to photobleaching, STED can image their positions with nanometer resolution and localize their centers with Angstrom precision.

PSF-engineering approaches such as STED and RESOLFT have many of the benefits of a confocal microscope with higher resolution. From a user perspective, image acquisition is intuitive and super-resolution is achieved in real-time, without a requirement for post-processing. Additionally, like confocal, STED and RESOLFT may be combined with two-photon absorption, FRAP, FCS or TCSPC to improve the

imaging capabilities or access new forms of information. One of the primary drawbacks of STED—the extremely high powers needed for efficient depletion–is alleviated in RESOLFT, enhancing compatibility with live specimen. Furthermore, parallelization can eliminate speed limitations present in earlier iterations. For these reasons, STED has carved out a niche in the super-resolution arena, especially for visualizing thicker samples where point-scanning is better-suited than imaging-based approaches.

Localization microscopy

Of the existing super-resolution methods, localization microscopy is the only one which is intrinsically a single-molecule technique. Although the notion of fitting the image of an emitter to determine its location has been around for decades, this alone did not achieve super-resolution. In order to resolve multiple close emitters via localization, methods to keep emitters in dark states were needed. This was first accomplished using activator-emitter dye pairs, caged dyes and photoactivatable fluorescent proteins in Stochastitic Optical Reconstruction Microscopy (STORM) [147], Photo-Activated Localization Microscopy (PALM) [148] and Fluorescence Photo-Activated Localization Microscopy (FPALM) [149] (Figure 1.4a,d). Since then, the number of acronyms has grown uncontrollably, with photoswitching mechanisms based on ground-state depletion(dSTORM/GSDIM) [150–153], binding of fluorogenic probes [154], binding of diffusing probes [155,156] and fluorescence complementation [157,158], among

others [159]. Among these, dSTORM and PALM have risen to the forefront for ease-of-use and maximum compatibility with live cells, respectively.

Methods based on ground state depletion such as direct STORM (dSTORM) and ground state depletion followed by individual molecule return (GSDIM) rely on the finite probability of intersystem crossing as a means of keeping some fluorophores dark. However, triplet relaxation usually occurs within a few microseconds—slower than fluorescence emission but usually not slow enough to achieve the emitter densities needed for localization. Fortunately, the triplet is an intermediate in pathways to longer-lived dark states. To increase the rates of those transitions, high concentrations of thiols are often included in the imaging buffer. Thiols can react with the triplet to generate long-lived radical anions, with lifetimes on the order of milliseconds to seconds. Both the triplet and the radical states are efficiently quenched by molecular oxygen to replenish the ground state. In order to increase dark state lifetimes and facilitate transitions to the longer-lived states, soluble oxygen is depleted using enzymatic scavengers, nitrogen purging or polymer embedding. Compared to other photoswitching mechanisms, dSTORM is advantageous because it can be implemented with a single narrowband source. At low illumination intensities, triplet transitions are rare and imaging is diffraction-limited. However, as the excitation power is increased, molecules are driven to the triplet and associated dark states. Most chromophores are turned off and fluorescent spots appear as molecules stochastically return to the singlet system. In addition to optical simplicity, dSTORM is advantageous because it can be realized with conventional immunostaining. However, if live-cell experiments are being conducted, care must be taken to ensure that the high

powers needed for singlet depletion do not affect the biological processes being studied.

The realization that most fluorescent proteins have multiple absorption peaks quickly led to another means of photoconversion. Photocontrollable proteins come in three varieties. Photoactivatable fluorescent proteins (PAFPs) are irreversibly activated from a dark state, usually by UV illumination, to a bright state. Photoswitchable proteins (PSFPs) irreversibly shift from one spectral range to another e.g. green to red. Reversibly switchable fluorescent proteins (rsFPs) reversibly switch between two states, either bright-dark or different colors. By using low light intensities for activation/switching, molecules can be stochastically turned on for imaging and localization. These modalities require significantly lower powers than dSTORM and are compatible with physiological buffers, making FPs more suitable for live-cell experiments. Low light intensities can also be used to spread signal over multiple camera frames for particle tracking applications. Furthermore, because FPs are genetically encodable, labeling efficiency and specificity are less of a concern than with affinity or enzyme-based labeling methods. The main drawback of FPs, compared to organic fluorophores, is their reduced photon output; still, 20-40 nm lateral resolution is readily achieved.

Caged fluorophores are initially dark due to a photolabile caging group which prevents the chromophore from assuming its fluorescent state. Illumination with UV light releases the cage, shifting the absorbance peak to the visible regime. Because sparse activation is readily achieved at low powers and readout is decoupled from activation, low-intensity excitation of uncaged fluorophores can produce tremendously

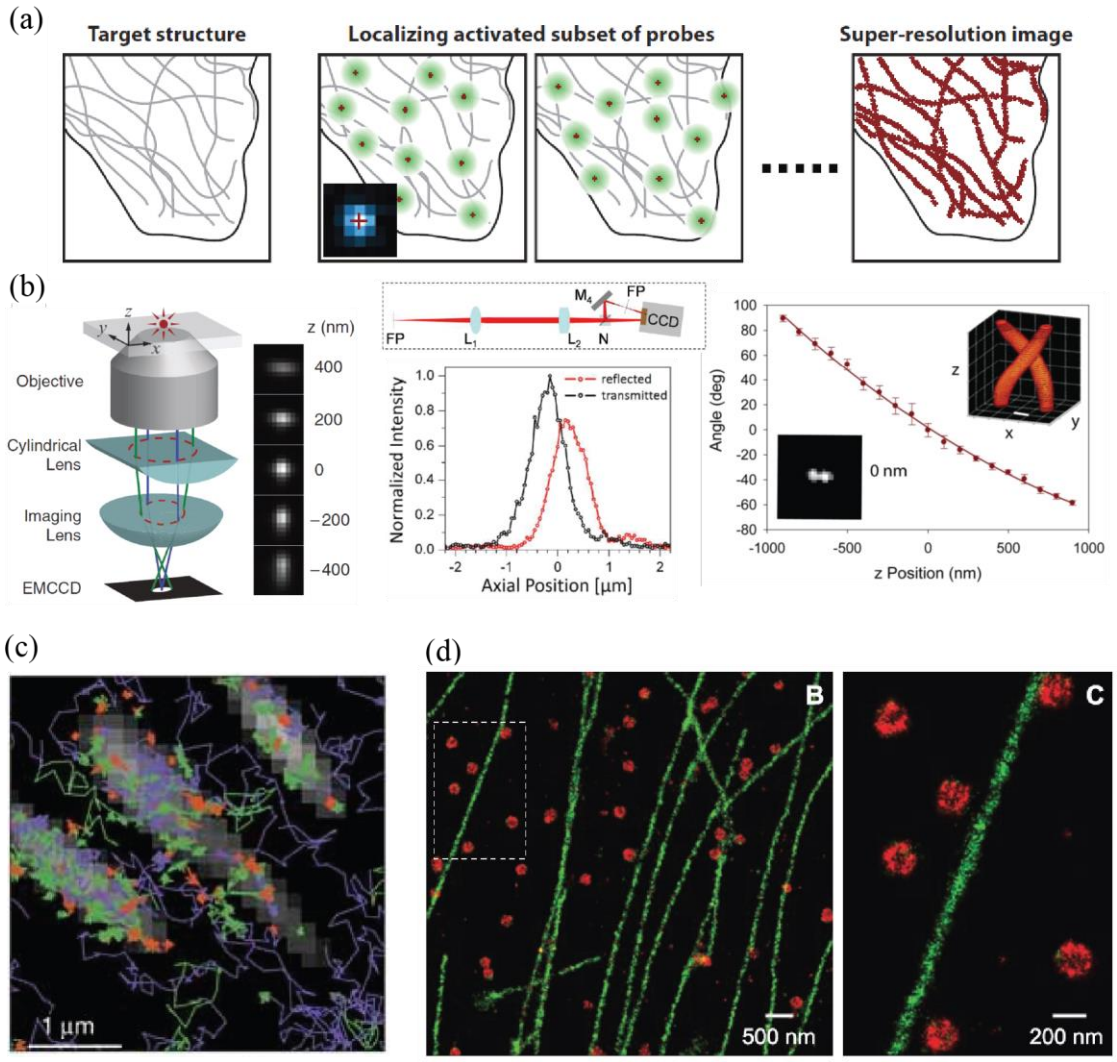

Figure 1.4 Localization microscopy. (a) Localization microscopy is predicated on the principle that single fluorescent molecules can be localized with significantly higher precision than the Rayleigh limit. By stochastically activating, imaging and turning off single emitters over many cycles and maintaining a sparse distribution of emitters in any given camera frame, a super-resolution image can be built up in a pointillistic fashion. (b) Popular methods for determining the axial position of an emitter by using astigmatism (left), biplane imaging (middle) or a double-helix point spread function (right) (c) Single-particle tracking PALM can map trajectories of labelled biomolecules at high density. (d) Two-color STORM image of microtubules and clathrin-coated pits, clearly resolving CCPs are hollow spheres. Of the various super-resolution methods, localization microscopy routinely achieves the best overall resolution in biological samples. Figures adapted from [36,160–166].

high photon yields [167]. Although the catalog of caged fluorophores is significantly smaller than conventional probes, there are commercially available options spanning the visible spectrum. Furthermore, a recent method for reductively uncaging conventional probes using sodium borohydride allows most conventional dyes to be caged [167].

Dual-labeling with activator and emitter dyes was the initial labeling strategy for STORM. Thiol in solution was found to mediate transitions of the emitter to a long-lived dark state, but the presence of a nearby activator dye (bluer in the spectrum and located < 1 nm) away was found to enhance rates of recovery by a non-FRET mechanism [168,169]. Dyes were paired by co-labeling oligonucleotides/antibodies or by chemical synthesis. This strategy has largely fallen out of favor because of the additional complexity (need for multiple dyes, multiple lasers and lack of commercial options) compared to dSTORM, but is still used occasionally for multiplexing applications.

Methods to extend localization microscopy to 3-D parallel the approaches used for particle tracking, with biplane imaging [170] and astigmatic detection [165,171] being adopted early on (Figure 1.4b). Another strategy places the sample on a tilted mirror and exploits the fact that axial structures in the real sample are converted to lateral structures in the virtual image [172]. More recently, a self-bending point spread function has been used to map z-coordinates of single molecules in STORM [173]. An SLM was used to convert the emission into an Airy beam, which undergoes a lateral displacement that depends on the distance of propagation, thus encoding z-position. Dual-objective collection with interferometric detection has also been used, yielding

the highest z-precision reported thus far, albeit with a complicated apparatus requiring two-objectives, three cameras and a custom three-way beamsplitter [174]. A simpler method using TIRF illumination and supercritical angle detection was able to achieve 20 nm z-resolution with two channels—one collecting the total signal from fluorophores and the other rejecting supercritical angles—and straightforward image processing [175].

Although localization microscopy achieves its best results near the substrate, where TIRF excitation may be used to reduce background, it has also been used to image structures further into cells [171]. Imaging depth may be increased by axially confining photoactivation. One strategy uses nonlinear photo-activation, implemented either via conventional two photon microscopy [176] or temporal focusing [177,178]; in this case, line-scanned temporally focusing has been shown to achieve the best combination of speed and axial confinement. Alternatively, selective plane illumination may be used for both photoactivation and readout and has imaged over 100 μm into multicellular structures [179].

One of the primary drawbacks of localization microscopy is the large number of frames needed for a single reconstruction, which can severely limit observation of dynamics. Furthermore, thiol-based imaging buffers can have deleterious effects on cell health. Although PALM was readily adapted for live-cell imaging without many alterations to the original protocol [180,181], STORM buffers have been modified to mitigate toxicity [182]. Fast localization imaging is possible by using high powers and small camera subframes to enhance switching and readout speeds. In these cases, 40-60 nm Nyquist-limited resolution has been achieved in sub-minute intervals with

PALM and 30 nm resolution has been realized with STORM in as little as 1-2 seconds.

Of the various super-resolution techniques, localization microscopy has been the most widely adopted because of its ease of implementation. Most TIRF setups with sufficiently high-powered lasers are capable of dSTORM or PALM and multiple software packages for localization are freely available [183,184]. Strategies for localization fall into three broad classes: fit-free methods, model-based fitting of single emitters and multi-emitter algorithms. Fit-free methods are capable of localizing single molecules without a model for the point spread function, relying instead on centroid measurement [185] [186], Fourier transformation and phase estimation [187], radial symmetry [188]or triangulation [189,190]. Fitting methods rely on a model for the point-spread function, often assuming a radially symmetric PSF such as Gaussian or a more complicated model for dipole emitters and determining optimal model parameters by least-squares fitting or maximum likelihood estimation. Among the two, iterative fitting yields better results in a wide range of scenarios. Single-pass fit-free methods may be used if computation time is a priority, with the knowledge that precision is sacrificed and localization bias may also be an issue. Often during acquisition, multiple emitters are activated within a single diffraction-limited region. Single-emitter algorithms reject these cases, on the basis of image ellipticity or brightness, in order to remain faithful to their *a priori* assumptions. Multi-emitter algorithms are capable of discerning these events and determining the positions of multiple fluorophores, facilitating faster imaging and more efficient data collection. Algorithms based on least-squares fitting [191], maximum likelihood estimation [192],

Bayesian information criterion [193,194], Richardson-Lucy deconvolution [195] or compressed sensing [196]. Compared to model-free methods, fitting retrieves parameters more accurately and is less prone to bias. Aside from precision and accuracy, computing time is an important parameter to consider. Analysis may be accelerated via implementation on a graphics processing unit [192,194] or field-programmable gate array [197] and achieve reconstruction in less than a minute. Rigorous comparisons of allow users to understand the various tradeoffs involved between resolution and computing time [183,184].

Because localization microscopy is inherently a single molecule technique, additional information can be extracted from the emission pattern, spectral signature or molecular trajectory. Localization microscopy combined with anisotropy imaging can map molecular orientations at high resolution [198]. By using a dual-objective setup and a dispersive element in one detection path, spectral information can be co-registered with high-resolution spatial information in the other channel [199]; this can be used to discern between spectrally overlapping probes to extend multiplexing capabilities. The use of low excitation intensities with photoactivable probes extends fluorophore emissions over multiple camera frames and permits the observation of molecular trajectories at much higher densities than traditional particle tracking [163] (Figure 1.4c). Probing at the single-molecule level, this approach is more sensitive to population heterogeneities than bulk methods such as correlation spectroscopy or photobleaching recovery.

The molecular nature of localization microscopy is its strongest selling point. Although it requires significantly longer acquisition times compared to other imaging

methods, perhaps a better comparison is to the many low-throughput single-molecule experiments it can potentially replace. sptPALM and pair-correlation PALM provide a direct look at heterogeneities in protein kinetics and spatial organization. With regard to imaging resolution, localization-based methods lead the pack and should only get better as brighter fluorescent proteins and dyes are introduced. One particular focus of future endeavors will surely be the development of improved dark-to-bright photoactivatable proteins in the green and red spectral classes. Currently, these proteins lag behind the photoconvertible proteins (mEos3.2, Dendra2, mMaple2) in photon output while the latter severely hinder multicolor imaging. Fortunately, the burgeoning interest in localization microscopy has greatly stimulated fluorescent protein research and these limitations should soon disappear.

Interference-based approaches for axial super-resolution

Because of its subwavength dependence on distance, interferometry can probe structures at super-resolution. Standing wave-fluorescence microscopy (SWFM) [70,72], 4Pi microscopy [75], image interference microscopy and interferometric PALM (iPALM) [174] have all used interference of laser illumination or detected photons to boost axial resolution. In particular, SWFM has achieved sub-nanometer localization when applied to thin single-layer samples. Another technique, fluorescence interference contrast (FLIC) microscopy, maps the height of dye molecules above a silicon substrate by using standing waves generated by laser light with nonzero incidence angle [200]. An improvement to this strategy is to use variable incidence angles (VIA-FLIC) to measure angle-intensity profiles for a dye layer and

determine height absolutely, without periodicity artifacts associated with a single-angle standing wave [201]. Scanning angle interference microscopy (SAIM) adapts this variable incidence angle approach for convenient implementation on a standard TIRF microscope [202] (Figure 1.5a-d). SAIM readily achieves multicolor imaging of live-cell dynamics at molecular axial resolution.

In collaboration with the Paszek lab, I have developed a next-generation SAIM microscope. One problem with traditional SAIM is that stray fringing, due to laser scatter from dust or other surfaces, can corrupt the data. To combat this, I combine SAIM with our galvanometer-based TIRF, which allows azimuthal rotation of the laser beam for spatial averaging of stray fringes. Chapter 3 discusses azimuthally-scanned TIRF and SAIM along with potential applications to single molecule imaging.

NEW TECHNOLOGIES

Detectors

Single-molecule imaging has been assisted by the development of sensitive detectors with low noise characteristics. Today, electron-multiplying CCDs and scientific CMOS cameras are the preferred detectors for imaging, while photomultiplier tubes and avalanche photodiodes are used for point-scanning applications. While all optical measurements must deal with the Poisson noise in photon arrival, detectors introduce additional noise stemming from thermal currents or electron readout. EMCCDs are popular because of their high quantum efficiency (QE > 90%) and negligible dark current if cooled. Furthermore, although their intrinsic

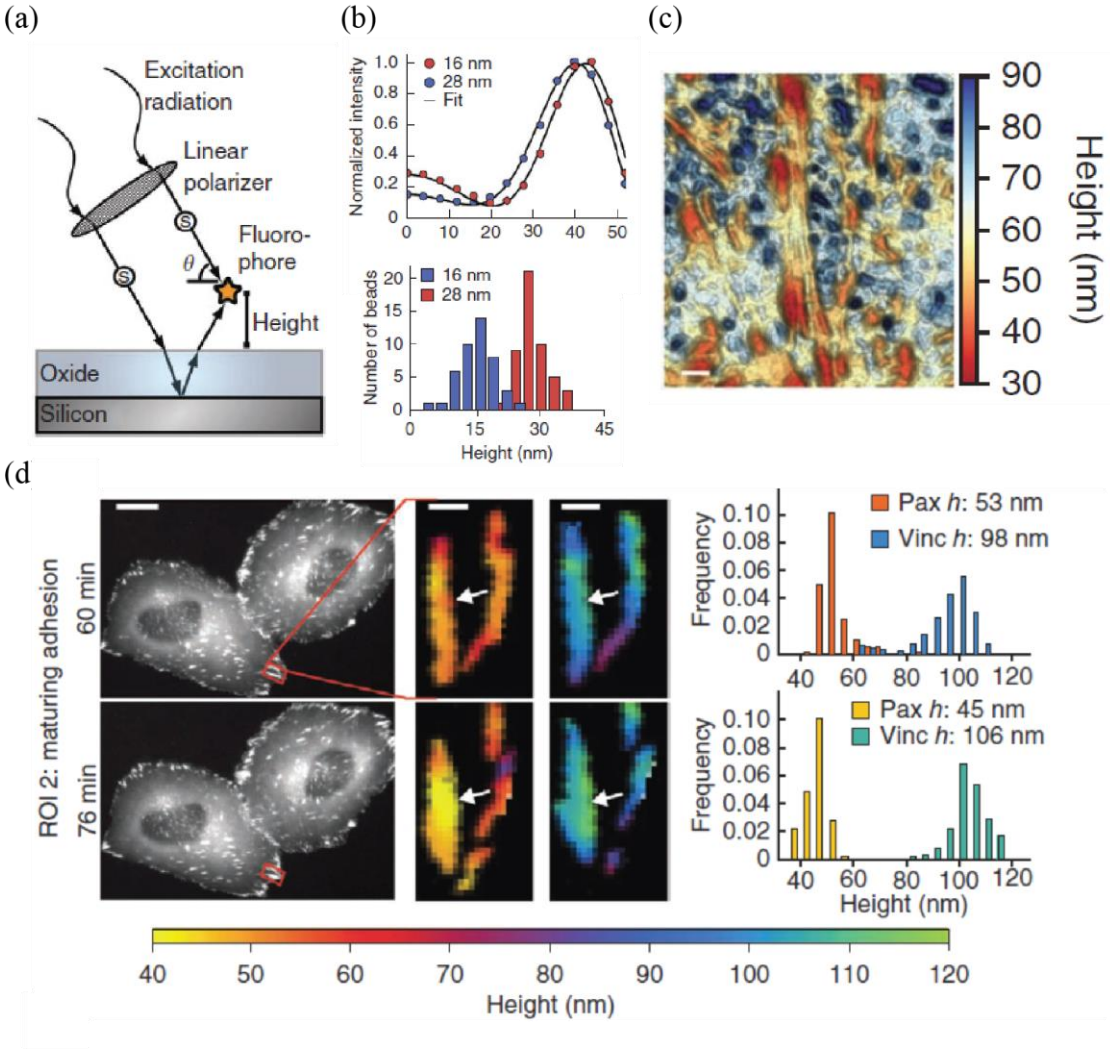

Figure 1.5 Scanning Angle Interference Microscopy. (a) Coherent excitation light reflected from a mirrored surface generates a standing wave pattern with fringe spacing determined by illumination wavelength and the angle of incidence. Fluorophore emission is modulated by the local field intensity and, for axially thin samples, can be used to determine height from the substrate with high precision. (b) Signal is measured as a function of the angle-of-illumination and compared to theoretical models to determine height. Fluorescent beads differing by only 12 nm in radius are clearly resolved. (c) SAIM of DiO-labeled cell membranes shows topographic features corresponding to sites of focal adhesions and variations in glycocalyx thickness. (d) SAIM clearly resolves protein strata in focal adhesions and can be used to measure dynamics as cells adhere to substrates and migrate. Figures adapted from [203,202].

read noise is fairly high (~10s of e- per pixel), electron multiplication amplifies the signal relative to this and the effective read noise may be much less than 1 electron.

However, electron multiplication does come with a cost as the impact ionization process also doubles the variance of the signal and diminishing the signal-to-noise ratio. This can be interpreted as an effective reduction of QE to ~40-50%. Scientific CMOS cameras are another attractive option, because they have low readout noise (<1-2 e- per pixel) and require no EM gain, thus achieving real QEs of 50-70%. sCMOS cameras are also capable of operating at high speeds (>100 fps at full frame) because there are multiple readout registers (two per column with dual-amplifiers to increase dynamic range). They also benefit from having smaller pixels (4-6 μm compared to 12-24 μm for EMCCDs), allowing for larger fields of view or oversampling if desired. One sometimes confusing aspect of sCMOS technology is the presence two types of exposure and readout modes: global and rolling shutter. In a global shutter exposure, the entire pixelated array is records charge at the same time and electrons are transferred from all pixels simultaneously for readout. In rolling shutter mode, rows are exposed and read out sequentially, with exposure and charge transfer for pixels in one row occurring ~10 μs earlier than the row below. This modality is known to generate motion artifacts, especially for large objects moving quickly transverse to the readout wave. However, it is also capable of operating at twice the frame rate of global shutter with lower read noise, due to the correlated double-sampling mechanism of sCMOS readout. For these reasons, rolling shutter is often preferable for most applications.

Both EMCCDs and sCMOS detectors are sufficiently sensitive for most single molecule imaging situations, but EMCCDs are generally preferred when light fluxes are particularly low. sCMOS cameras are used when sensitivity is not the utmost concern, since they can provide a larger field-of-view or spread the signal from single fluorophores over more pixels. In addition, they're generally the cheaper option, currently priced ~$20k while EMCCDs are in the $30-40k range. The SNR crossover point for EMCCD and sCMOS technologies has been estimated to be around 40-60 photons/pixel (Andor white papers), signifying the level where the drawbacks of EM multiplication noise begin to outweigh the benefits of read noise reduction. Single-molecule imaging and localization microscopy are typically the only scenarios where pixels experience light fluxes below this level. While EMCCDs are still generally preferred for these applications, sCMOS detectors have proven to be capable as well [204].

For quantitative imaging, the photoresponse and noise characteristics of the detector must be carefully considered. For example, localization microscopy requires conversion of signals to photon units in order for theoretical precision formulas to apply. Furthermore, photon units are system-independent and important for comparisons between different microscopes or researchers. Although various methods have been used for photon conversion, including manufacturer formulas and pixel histograms [21,205], I find a photon transfer method from astronomy to work best and have verified it by digital photon counting [206–208] (Appendix B).
details the noise characteristics for EMCCDs and a simple method for photon transfer measurements.

Probes

Rapid developments in probe technology, spanning fluorescent proteins, organic fluorophores and nanoparticles, have expanded the possibilities for single-molecule fluorescence experiments (Figure 1.6a). Mutagenesis of native FPs from *Aequorea victoria*, *Discosoma striata* and other species have yielded a palette of chromophores covering the visible spectrum [212,213]. FP brightness, maturation efficiency and kinetics, photostability and oligomerization state must be considered when choosing the optimal label. Furthermore, for single molecule applications, photon yields and dark state transitions must be characterized as a function of light intensity and buffer conditions [214]. I generally prefer mNeongreen and mCherry within the green and red spectral classes for their superior photophysical properties and monomeric behavior. Localization microscopy has spurred progress in the field of photocontrollable proteins. Building off the knowledge that wildtype GFP can reversibly access dark states [215], mutagenesis approaches have engineered a host of photoactivatable FPs which can be switched on from an initially dark state (Figure 1.6b). PAGFP and PAmCherry were early entrants into this class, based on mutagenesis of GFP and mCherry [216,217]. Photoconvertible proteins which irreversibly switch from one color to another have also found applications in localization microscopy and, owing to their superior photon yields, are generally the FPs of choice, with mEos3.2 being a current favorite [218]. Reversibly switchable proteins have gained a foothold in RESOLFT and nonlinear SIM microscopies and

Figure 1.6 Probes for single molecule imaging (a) While most fluorophores exist in two general states, active and bleached, photocontrollable fluorophores have additional states and enable new modes of imaging. Photoactivtable fluorophores are inactive by default, but activated by illumination at a certain wavelength (usually UV). Photoswitchable fluorophores have multiple spectrally distinct active states and can be switched from one form to another by specific wavelengths. Switching may be unidirectional or reversible, depending on the fluorophore and mechanism of photoconversion. (b) Representative chromophores of fluorescent proteins, showing photoactivation by decarboxylation (top), photoconversion by backbone cleavage (middle) and reversible photoswitching by cis-trans isomerization (bottom) (c) Jablonski diagram depicting the photophysics of dSTORM/GSDIM. Molecules undergoing single transitions can stochastically cross over from 1F1 into the triplet state 3F. Under normal conditions, they would eventually relax back to the ground state 1F0, often due to collisional quenching with molecular oxygen. dSTORM buffers include oxygen scavengers to inhibit this process as well as high concentrations of thiols to increase transitions to longer-lived dark states. (d) Triplet state quenchers limit fluorophore blinking and enhance photon yields by aiding molecules in their return to the singlet pathway. TSQs are often including in single-molecule imaging buffer, but have recently been conjugated directly to create "self-healing dyes" with improved photophysical properties. Figures adapted from [153,209–211].

(a)

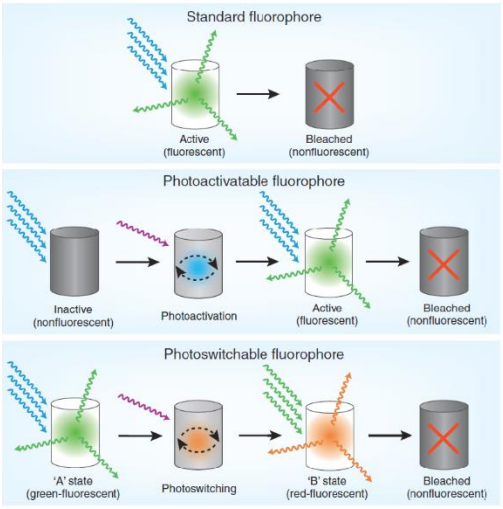
Standard fluorophore
Active
(fluorescent)
Bleached
(nonfluorescent)
Photoactivatable fluorophore
Inactive
(nonfluorescent)
Photoactivation
Active
(fluorescent)
Bleached
(nonfluorescent)
Photoswitchable fluorophore
'A' state
(green-fluorescent)
Photoswitching
'B' state
(red-fluorescent)
Bleached
(nonfluorescent)

(b)

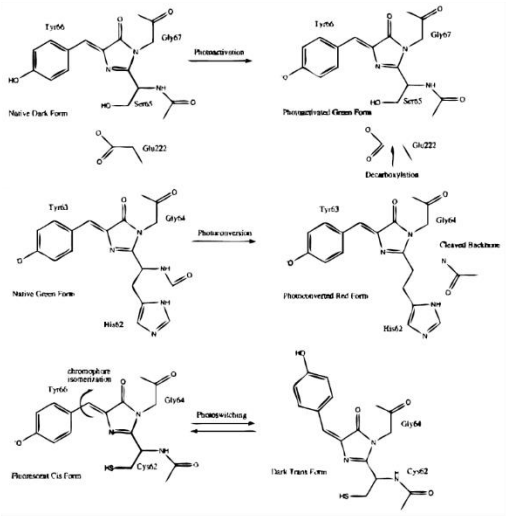

(c)

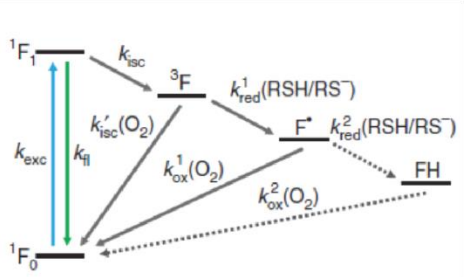
$^1F_1$
k_{isc}
^3F
$k^1_{red}(RSH/RS^-)$
$k'_{isc}(O_2)$
$F^\bullet$
$k^2_{red}(RSH/RS^-)$
k_{exc}
k_{fl}
$k^1_{ox}(O_2)$
FH
$k^2_{ox}(O_2)$
$^1F_0$

(d)

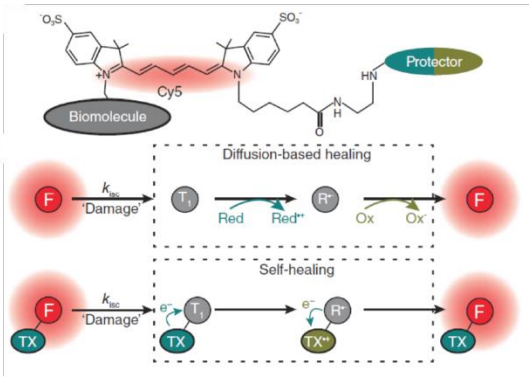
Protector
Cy5
Biomolecule
Diffusion-based healing
'Damage'
Red
Red•⁺
Ox
Ox⁻
Self-healing
'Damage'
TX
TX•⁺

progress has been made in improving their switching kinetics and increasing the number of switching cycles before permanent photobleaching. Dronpa was an early variant in this class and is still used today [219], while rsEGFP and Skylan-NS have shown improved characteristics [88,129,220].

The superior brightness of organic dyes has proven invaluable for single molecule imaging and localization microscopy, often generating photon yields 4-1000x more than those of FPs [167,214]. Cy3 and Cy5 have traditionally been go-to dyes in the red and far-red regimes, but there are countless others, primarily in the cyanine, rhodamine and oxazine classes with favorable properties [221]. Lavis and colleagues found that azetidinylation of many dyes improved brightness and photostability [222].The Zhuang lab at Harvard has performed a useful comparison of these fluorophores for dSTORM microscopy [223], delineating probes in the green, red, far-red and IR classes which provide acceptable blinking characteristics (Figure 1.6c). Aside from dye choice, buffer conditions can be modified to tune photophysical properties [214]. Oxygen scavengers such as the glucose oxidase/catalase or protocatechuic acid/protocatechuate-3,4-dioxygenase systems [224] are routinely added because oxygen can quickly quench the dye triplet state, generating harmful superoxide which may accelerate photobleaching. One problem with these systems is that they have been shown to acidify buffers over time. A recent system based on pyranose oxidase lacks this quality and is useful for long-term imaging applications [225]. In order to diminish blinking and improve photon yields, protective agents such as Trolox [45], Nitrobenzyl alcohol, cyclooctatetraene [226] are often added to buffers. These redox chemicals stabilize fluorophores in ways which are still

not completely understood, though triplet quenching is believed to be one mechanism [227,228]. Recently, covalent attachment of these small molecules to organic dyes has been shown to generate "self-healing dyes" with even better photophysical properties [229–231] (Figure 1.6d). In other cases, such as localization microscopy, blinking is actually the preferred outcome. Thiol additives such as beta-mercaptoethanol, mercaptoethanolamine and glutathione can increase transitions from the triplet state to longer-lived dark states to facilitate dSTORM [232]. Improvements in dye chemistry and understanding of photophysics should yield brighter probes with tunable properties for a wide array of applications.

Fluorescent nanoparticles are the brightest, most resilient probe family and are useful when tracking single particles for long time periods. The gold standard in this area are semiconductor nanocrystals or quantum dots, typically made from cadmium selenide or zinc sulfide [233]. These nanocrystals generate a bound electron-hole pair when excited by light and fluoresce by a process of radiative recombination. Absorption is broad-band, with higher cross-sections at shorter wavelengths, and emission follows a Gaussian spectral profile with color determined by QD size and composition. QDs are renowned for their excellent photostability and may be tracked for hours. However, millisecond-second blinking of quantum dots has been problematic. One hypothesis is that excitons get trapped surface defects where they cannot undergo radiative recombination. Shell layers have been shown to reduce the frequency of defects, reduce blinking and increase quantum efficiency overall. Thiols in solution can donate electrons to quench surface traps and nearly eliminate blinking [234]. Although quantum dots are not terrible large on their only, typically 2-

7 nm, they are often encapsulated with passivation layers such as polymer coats, dendrimers or micelles to improve biocompatibility. These additional layers can drive nanoparticle size above 20 nm, which can severely hinder the mobility of tagged biomolecules or sterically limit diffusion. The synthesis of small QDs with thinner passivation layers has been a longstanding goal, but stability has been a key hurdle. The recent development of small stable QDs promises to open doors for more applications [235,236]. Another concern with QD labeling is the multi-valency of attached molecules e.g. biotin, streptavidin, antibodies, etc. The use of steric exclusion to limit access to binding sites has been used to create monovalent quantum dots for stoichiometric labeling [237]. Silica or polymer encapsulated dyes are another class of nanoparticle probe. Encapsulation can improve quantum yield by reducing nonradiative energy dissipation and can protect fluorophores from photodegradation. Single-atom defects in carbon are another promising nanoparticle probe, particularly nitrogen-vacancy centers [238]. These defects absorb broadly in the 500-625 nm and have a large Stokes shift, with peak emission around 700 nm. Although single vacancies have fairly low absorption cross-sections (typically 10-100x lower than those of organic dyes or QDs), multiple vacancies may be present in a 10 nm nanodiamond. The most appealing quality of NV-centers is their resistance to photobleaching, making them a viable alternative to quantum dots for long-term imaging.

Labeling strategies

Affinity-based labeling is a good starting point for many experiments because it requires the least time investment and can be used to study endogenous proteins. However, once the optical resolution approaches the macromolecular regime, linkage error between the structure-of-interest and probe must be considered. For this reason, smaller probes such as antibody fragments, nanobodies [236,239] or aptamers [240] have found use. A recently developed strategy fuses multiple copies of a short peptide epitope to the protein of interest. This SunTag may be labeled with exogenous antibodies or FP-labelled Fab fragments to significantly boost single molecule signals within cells [241].

Fluorescent protein labeling is advantageous for its efficiency and specificity. Degree-of-labeling is mostly determined by the protein maturation efficiency and kinetics in its host. Since many FPs are known to multimerize, care must be taken to verify that observed protein-protein interactions are real and not an artifact of the labeling. There are also numerous enzymatic approaches for covalent attachment of organic probes to a target [242–248]. These are attractive due to the superior brightness and small size of organic dyes compared to FPs, but labeling efficiency is usually lower with higher background labeling. Most tags have commercially available dye counterparts, but specific analogs may be synthesized by fairly simple reactions and purification. Non-natural amino acids are another promising strategy for efficient site-specific labeling of proteins for in vitro studies [249].

Probe delivery is an important consideration for exogenous labels, particularly when working with living cells. Ideally, labels are cell permeable or modified to

facilitate passage across the cell membrane. If this is not the case, microinjection or electroporation can aid in delivery [182]. Newer approaches based on cell-penetrating peptides [250,251], silicon nanowires [252], carbon nanoparticles [253] and laser-induced cavitation [254] have also been used. For all of these strategies, labeling efficiency and specificity (especially when wash steps are not possible) and effects of the delivery method on cell viability must be weighed carefully.

APPLICATIONS

From a physical perspective, super resolution imaging is fascinating because it took new perspectives on what a microscope is and what it can be in order to topple the longstanding diffraction limit. However, practically speaking, these tools are only as good as the science they enable. Fortunately, single molecule and super resolution techniques have helped push our understanding of cell biology in a wide array of subfields and we can only expect this trend to accelerate as the broader community gains a better appreciation for the methods and their utility. Here, I highlight a few of the arenas where these methods have made an impact.

Plasma membrane

Membranes are a key interfacial material in biology, forming the barrier between cell interior and exterior while also compartmentalizing the cell into discrete organelles that perform specific functions. The composition and arrangement of lipids, proteins, sterols and other biomolecules in the plasma membrane has long been studied due to their roles in controlling transport, mediating cell attachment and initiation of

signaling, among other things. However, proposed units of spatial organization such as lipid rafts are small and highly dynamic, thus evading detection by conventional microscopy. While correlation spectroscopy has been used to study lipid diffusion for decades, the reduced spot size in STED has greatly enhanced the sensitivity of the technique. STED-FCS has clearly resolved mobility differences between phosphoethanolamine and sphingomyelin in the plasma membrane of living cells [107] (Figure 1.7a). While the former always makes quick transits (~1 ms) thru the STED focal volume (~30 nm laterally), the latter can spend anywhere between 1 and 50 ms, potentially due to transient interactions with cholesterol-enriched nanodomains. Cholesterol depletion was shown to eliminate slow transits and any mobility differences between PE and SM. A later study also found sphingolipid analogs to interact strongly with transient cholesterol nanodomains and actin-based assemblies [255].

The protein component of the plasma membrane has a direct role in its rich array of functions. Oligomerization and formation of larger spatial clusters is critical to the mechanisms of many membrane proteins. Stepwise photobleaching has been a key tool in elucidating the subunit stoichiometry of numerous membrane proteins [21,256], including the Hv1 voltage gated channel [262] and the calcium-release-activated calcium (CRAC) channel [263]. Localization microscopy has resolved higher-order clustering of membrane-bound proteins, with improved quantification tools enabling molecular counting. sptPALM of FcεRI rececters in mast cells showed receptor immobilization soon after antigen stimulation, followed by receptor clustering measured by pair correlation analysis [264,265]. These

Figure 1.7 Biological applications of super resolution microscopy. (a)STED-FCS of membrane lipids clearly resolves non-interacting lipids (polyethanolamine, PE) from lipids which interact with cholesterol-enriched nanodomains (sphingomyelin, SM). Cholesterol depletion by COase eliminates these interactions, causing SM to exhibit a PE-like transit through the focal spot. (b) Interferometric PALM distinguishes between protein strata in focal adhesions and yields a model of focal adhesion coupling to the extracellular matrix and actin meshwork. (c) Perioidic lattices of spectrin, actin and associated proteins were discovered by STORM in dissociated hippocampal neurons cultured *in vitro*. Lattice development starts proximal to the cell body and propagates distally over several days. (d) Particle tracking of Sox2 transcription factors measures their movements through the nucleus and can be used to determine kinetics of bound states and free diffusion. A Sox2M variant with mutations in the DNA-binding domain takes longer to find its final target and spends more time diffusing on average. (e) DNA curtains can be used to investigate DNA-protein interactions in a high-throughput manner. Imaging of Cas9 with a λ2 guide RNA reveals on-target and off-target interaction with λ-DNA. Histograms of Cas9 occupancy provide a measure of specificity. (f) Multiplexed error-robust fluorescence in situ hybridization (MERFISH) imaging of 1001 RNAs can be used to map transcriptional activity and probe regulatory circuits at the single-cell level. Figures adapted from [107,257–261].

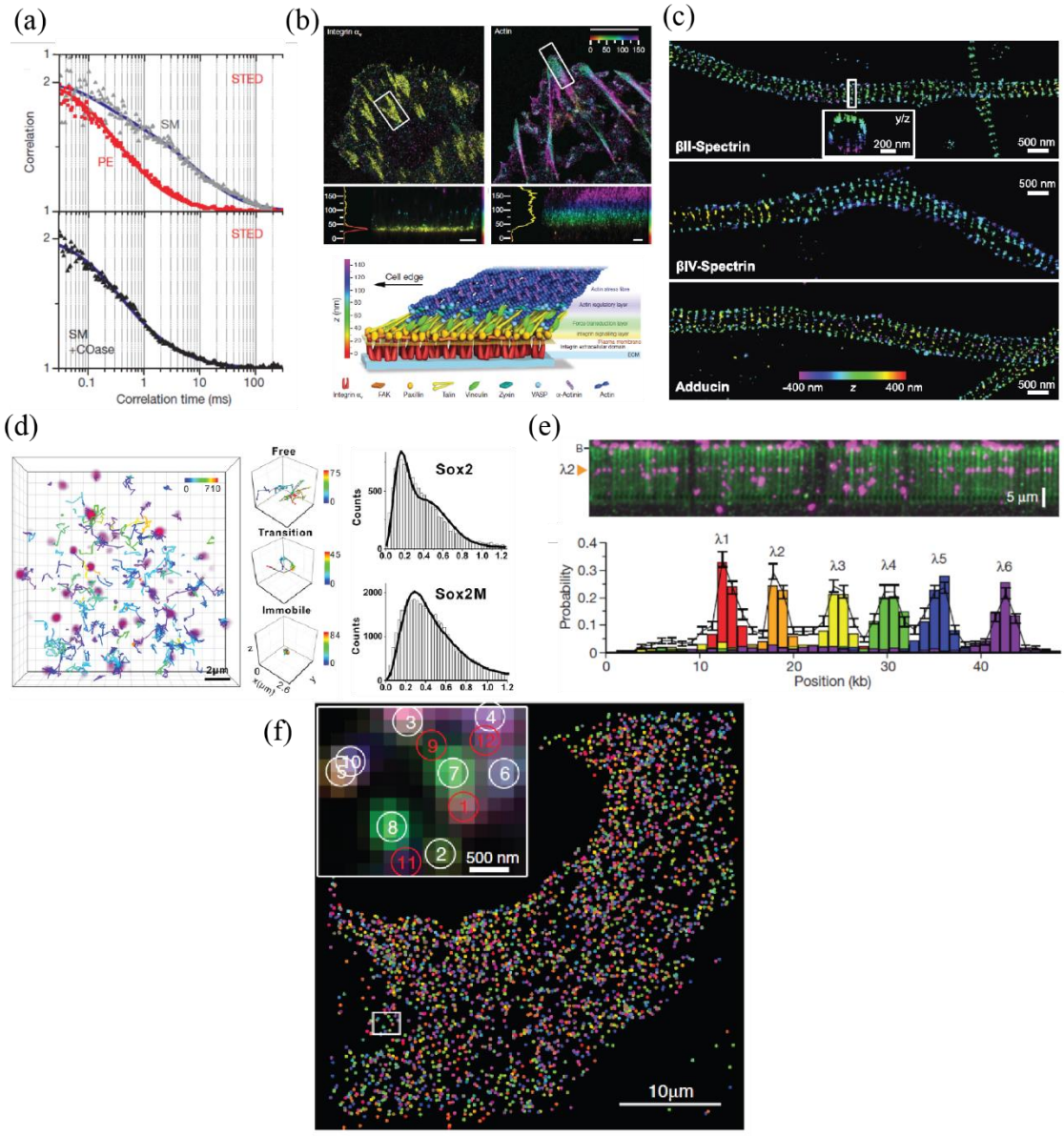
(a)
STED
SM
PE
STED
SM
+COase
Correlation
Correlation time (ms)
(b)
Integrin α_v
Actin
Cell edge
Integrin α_v
FAK
Paxillin
Talin
Vinculin
Zyxin
VASP
α-Actinin
Actin
(c)
βII-Spectrin
y/z
200 nm
500 nm
βIV-Spectrin
500 nm
Adducin
-400 nm
z
400 nm
500 nm
(d)
2μm
Free
Transition
Immobile
Sox2
Sox2M
Counts
(e)
λ2
5 μm
λ1
λ2
λ3
λ4
λ5
λ6
Probability
Position (kb)
(f)
500 nm
10μm

approaches will be essential for understanding the timecourse of signaling and how extracellular cues reshape the cell periphery.

Mechanobiology

Although forces are ubiquitous in biology, their roles in molecular mechanisms are still widely uncharacterized. At the cellular level, forces play a role in morphogenesis, cell migration and cell adhesion. Adhesion structures at the plasma membrane help cells sense their environment while the cytoskeleton provides integrity and may compartmentalize diffusion of membrane proteins. Meanwhile, the role of the glycocalyx in shaping protein organization at the cell surface is just starting to be understood.

Focal adhesions are large multiprotein assemblies that form a mechanical link between the actin cytoskeleton and the extracellular matrix, communicating forces and regulatory signals in both directions. Direct imaging of focal adhesion proteins by interferometric PALM revealed the discrete strata of their organization [258] (Figure 1.7b). The lowest layer is composed of integrins, paxillin and focal adhesion kinase, which together form an integrin signaling layer. Upon integrin binding to the ECM, FAK is activated and phosphorylates paxillin to stabilize its interactions with other proteins. The middle layer contains vinculin and talin, adapter proteins that mediate force transduction. The topmost layer of zyxin, VASP and α-actinin makes direct contact with actin and may regulate its remodeling. sptPALM of focal adhesion proteins demonstrated that integrins undergo multiple free-diffusion and immobilization cycles in the membrane, with integrin activation promoting

immobilization [266]. In contrast, talin is recruited directly from the cytosol and does not find its target sites by diffusion in the membrane. Furthermore, immobilized β1 integrin and talin showed rearward flow within FA structures, suggesting links with retrograde actin flow.

The role of the glycocalyx in sensing forces and signaling through contacts with the plasma membrane is largely unstudied. Scanning angle interference microscopy has shown that the bulky glycoprotein MUC1 spatially excludes integrins and is compressed or bent near focal adhesions [203]. Furthermore, sptPALM demonstrated that MUC1 overexpression significantly reduced immobilization of integrins, especially outside of FA structures. Unlike membrane proteins, cell surface glycans labeled by click chemistry show a homogeneous distribution and lack any clustering on the plasma membrane [267]. Improvements in glycan-specific labeling coupled with high-resolution imaging may begin to shed light on the complexity of the cell's outer coat and its role in communicating environmental messages.

Cytoskeletal structures give cells their shape and aid in force transduction, both inward and outward. Recent STORM experiments discovered a new lattice structure of actin, spectrin and adducin (an actin capping protein) in the axons of cultured hippocampal neurons [260,268] (Figure 1.7c). The βII spectrin lattice appears first, starting proximal to the cell body and propagating distally, followed by the other lattices several days later. sptPALM was used to show that these lattices are very stable, with little protein exchange. Discoveries like this highlight the remarkable architecture which has remained hidden due to decades of imaging through a blurry lens.

Nucleus

The compaction of DNA inside the nucleus is facilitated by numerous layers of organization, starting from nucleosomes to higher-order structures such as 30-nm fibers and eventually chromosomes. Chromatin structure is highly dynamic, with regulatory elements interacting over long distances, transcription factors relaying extracellular cues and chromatin decondensation accompanying gene activation. Imaging these events is difficult because the nucleus is such a dense structure in three dimensions, with no landmarks for orientation. Nonetheless, single molecule techniques have started to provide some insight into these complex processes. sptPALM of c-myc and PTEF-b showed that the former is a global explorer of the nucleus while PTEF-b diffusion is directed, likely due to interactions with nuclear structures [269]. Lattice light sheet particle tracking of enhanceosome members revealed that Sox2 undergoes multiple cycles of 3D diffusion and transient binding/1D search until it binds stably to its final target [270,271] (Figure 1.7d). Furthermore, Sox2 precedes Oct4 in enhanceosome assembly and is excluded from heterochromatin. Localization microscopy of Pol II inside the nucleus has produced contradictory results, with one study finding that most Pol II foci are single molecules, contradicting the notion of transcription factories [272], while a time-correlated analysis observed transient Pol II clusters that increased in size and frequency with serum stimulation [273]. While many of these studies were conducted as averages over the entire nucleus, new strategies to visualize specific endogenous loci via

CRISPR/TALE-guided fluorescent proteins should facilitate more targeted experiments [274–276].

The crowded nature of the nucleus impedes the observation of single fibers and mapping of adjacent loci. For this reason, methods of chromatin extraction and in vitro reconstitution of genomic interactions have played a major role in elucidating nuclear mechanisms. Localization microscopy of chromatin extracts from HeLa cells showed that Pol II was surrounded by gap structures in the YOYO stain, believed to represent decondensed chromatin [277]. Serum response factor was also enriched in these gaps and gap frequency was reduced when cells were serum-starved. Arrays of substrate immobilized DNA molecules have been used to reconstitute protein-DNA interactions in a high-throughput manner and observe molecular dynamics. One such approach, DNA curtains, attaches DNA to a supported lipid bilayer and uses a diffusion barrier to constrain its movement. Under hydrodynamic force, DNA molecules diffuse up the barrier and stretch out for observation, allowing base pair differences to be mapped onto physical distances. DNA curtains have been used to test *in silico* models of nucleosome occupancy and found that Scm3 aids CenH3-containing nucleosomes in binding A-T rich regions which they otherwise avoided [278]. Imaging of Cas9 on DNA curtains showed that binding and cleavage were PAM-dependent and that DNA-RNA duplex formation followed a Brownian ratchet mechanism [279] (Figure 1.7e). The combination of highly parallelized methods for DNA interrogation and high-resolution *in vivo* imaging serve as a valuable complement to sequencing-based approaches in unraveling the energy landscapes of DNA binding proteins and 3D architecture of chromatin.

RNA imaging

While transcriptome analysis has primarily fallen under the purview of microarray and sequencing approaches, imaging-based methods capture spatial and temporal information directly, both within cells and populations. Single-molecule fluorescence in situ hybridization (smFISH) labels native RNAs with multiple labeled oligos for detection in fixed samples and has been used to show that some genes display transcriptional bursting, the synthesis of multiple RNAs in a short period followed by long periods of inactivity [280]. GFP-labeled phage proteins that bind the short RNA hairpins MS2 and PP7 have been used to track mRNA synthesis in living cells, with two-color imaging permitting the measurement of Pol II elongation rates [281] and observation of the first round of translation [282]. While most MS2 experiments introduce an exogenous transgene, a recent study tagged all endogenous β-actin mRNAs in a mouse with hairpin repeats and observed activity-dependent production of mRNA-protein complexes in isolated neurons [283].

Traditional multicolor FISH typically permits visualization of up to four different RNAs simultaneously, limited by the number of spectrally discernable channels on the microscope. Newer methods, combining localization microscopy with spatial or spectral barcoding, have increased that number by an order of magnitude [284,285], permitting single-cell observations of gene regulatory circuits. A method combining sequential hybridization of oligonucleotide probes with error-robust encoding schemes can detect thousands of RNAs in single cells, further expanding the networks which may be studied [261] (Figure 1.7f). Spatially-resolved

transcriptomics will play an important role in understanding variations in gene expression, particularly in multicellular conglomerates such as tissue and biofilms.

CONCLUSION

As super-resolution technology has matured, we have come to understand the advantages and limitations of the various techniques. Importantly, there is no one "ultimate microscope" but rather a Swiss army knife of methods best suited for specific applications. When deciding a strategy, it is important to remember the fundamental tradeoffs between spatial resolution, temporal resolution and phototoxicity, even after excitation confinement is used to minimize exposure to non-imaged regions [286]. The development of brighter probes with specialized properties coupled with improved strategies for mitigating photobleaching and photodamage will push these boundaries further. As these tools continue to be commercialized and fall into the hands of researchers, we can expect rich new insights into molecular interactions and dynamics that underlie cell biology.

REFERENCES

1. E. Abbe, "Beiträge zur Theorie des Mikroskops und der mikroskopischen Wahrnehmung," Arch. für Mikroskopische Anat. **9**, 413–418 (1873).

2. W. Denk, J. Strickler, and W. Webb, "Two-photon laser scanning fluorescence microscopy," Science (80-.). **248**, 73–76 (1990).

3. D. Axelrod, D. E. Koppel, J. Schlessinger, E. Elson, and W. W. Webb, "Mobility measurement by analysis of fluorescence photobleaching recovery kinetics.," Biophys. J. **16**, 1055–69 (1976).

4. J. R. Lakowicz, *Principles of Fluorescence Spectroscopy*, 3rd ed. (Springer US, 2007).

5. D. Gross and W. W. Webb, "Molecular counting of low-density lipoprotein particles as individuals and small clusters on cell surfaces.," Biophys. J. **49**, 901–11 (1986).

6. R. N. Ghosh and W. W. Webb, "Automated detection and tracking of individual and clustered cell surface low density lipoprotein receptor molecules.," Biophys. J. **66**, 1301–18 (1994).

7. N. Bobroff, "Position measurement with a resolution and noise-limited instrument," Rev. Sci. Instrum. **57**, 1152 (1986).

8. W. E. Moerner and L. Kador, "Optical detection and spectroscopy of single molecules in a solid," Phys. Rev. Lett. **62**, 2535–2538 (1989).

9. M. Orrit and J. Bernard, "Single pentacene molecules detected by fluorescence excitation in a p -terphenyl crystal," Phys. Rev. Lett. **65**, 2716–2719 (1990).

10. T. Xia, N. Li, and X. Fang, "Single-molecule fluorescence imaging in living cells.," Annu. Rev. Phys. Chem. **64**, 459–80 (2013).

11. E. Betzig and R. J. Chichester, "Single Molecules Observed by Near-Field Scanning Optical Microscopy," Science (80-.). **262**, 1422–1425 (1993).

12. T. Funatsu, Y. Harada, M. Tokunaga, K. Saito, and T. Yanagida, "Imaging of

single fluorescent molecules and individual ATP turnovers by single myosin molecules in aqueous solution.," Nature **374**, 555–9 (1995).

13. T. Schmidt, G. J. Schutz, W. Baumgartner, H. J. Gruber, and H. Schindler, "Imaging of single molecule diffusion.," Proc. Natl. Acad. Sci. **93**, 2926–2929 (1996).

14. U. Kubitscheck, O. Kückmann, T. Kues, and R. Peters, "Imaging and tracking of single GFP molecules in solution.," Biophys. J. **78**, 2170–9 (2000).

15. Y. Sako, S. Minoghchi, and T. Yanagida, "Single-molecule imaging of EGFR signalling on the surface of living cells.," Nat. Cell Biol. **2**, 168–72 (2000).

16. A. Yildiz, J. N. Forkey, S. a McKinney, T. Ha, Y. E. Goldman, and P. R. Selvin, "Myosin V walks hand-over-hand: single fluorophore imaging with 1.5-nm localization.," Science **300**, 2061–5 (2003).

17. E. Rittweger, K. Y. Han, S. E. Irvine, C. Eggeling, and S. W. Hell, "STED microscopy reveals crystal colour centres with nanometric resolution," Nat. Photonics **3**, 144–147 (2009).

18. A. Yildiz and P. R. Selvin, "Fluorescence imaging with one nanometer accuracy: application to molecular motors.," Acc. Chem. Res. **38**, 574–82 (2005).

19. R. Roy, S. Hohng, and T. Ha, "A practical guide to single-molecule FRET.," Nat. Methods **5**, 507–16 (2008).

20. K. I. Mortensen, L. S. Churchman, J. a Spudich, and H. Flyvbjerg, "Optimized localization analysis for single-molecule tracking and super-resolution microscopy.," Nat. Methods **7**, 377–81 (2010).

21. M. H. Ulbrich and E. Y. Isacoff, "Subunit counting in membrane-bound proteins.," Nat. Methods **4**, 319–21 (2007).

22. T. D. Lacoste, X. Michalet, F. Pinaud, D. S. Chemla, A. P. Alivisatos, and S. Weiss, "Ultrahigh-resolution multicolor colocalization of single fluorescent probes.," Proc. Natl. Acad. Sci. U. S. A. **97**, 9461–6 (2000).

23. X. Michalet, T. D. Lacoste, and S. Weiss, "Ultrahigh-resolution colocalization of spectrally separable point-like fluorescent probes.," Methods **25**, 87–102 (2001).

24. J. Antelman, C. Wilking-Chang, S. Weiss, and X. Michalet, "Nanometer distance measurements between multicolor quantum dots.," Nano Lett. **9**, 2199–205 (2009).

25. L. S. Churchman, Z. Okten, R. S. Rock, J. F. Dawson, and J. a Spudich, "Single molecule high-resolution colocalization of Cy3 and Cy5 attached to macromolecules measures intramolecular distances through time.," Proc. Natl. Acad. Sci. U. S. A. **102**, 1419–23 (2005).

26. A. Pertsinidis, Y. Zhang, and S. Chu, "Subnanometre single-molecule localization, registration and distance measurements," Nature **466**, 647–651 (2010).

27. E. Toprak, H. Balci, B. H. Blehm, and P. R. Selvin, "Three-dimensional particle tracking via bifocal imaging.," Nano Lett. **7**, 2043–5 (2007).

28. P. Prabhat, Z. Gan, J. Chao, S. Ram, C. Vaccaro, S. Gibbons, R. J. Ober, and E. S. Ward, "Elucidation of intracellular recycling pathways leading to exocytosis of the Fc receptor, FcRn, by using multifocal plane microscopy.," Proc. Natl. Acad. Sci. U. S. A. **104**, 5889–94 (2007).

29. S. Abrahamsson, J. Chen, B. Hajj, S. Stallinga, A. Y. Katsov, J. Wisniewski, G. Mizuguchi, P. Soule, F. Mueller, C. Dugast Darzacq, X. Darzacq, C. Wu, C. I. Bargmann, D. A. Agard, M. Dahan, and M. G. L. Gustafsson, "Fast multicolor 3D imaging using aberration-corrected multifocus microscopy.," Nat. Methods **10**, 60–3 (2013).

30. S. Abrahamsson, M. McQuilken, S. B. Mehta, A. Verma, J. Larsch, R. Ilic, R. Heintzmann, C. I. Bargmann, A. S. Gladfelter, and R. Oldenbourg, "MultiFocus Polarization Microscope (MF-PolScope) for 3D polarization imaging of up to 25 focal planes simultaneously.," Opt. Express **23**, 7734–54 (2015).

31. H. P. Kao and A. S. Verkman, "Tracking of single fluorescent particles in three dimensions: use of cylindrical optics to encode particle position.," Biophys. J. **67**, 1291–300 (1994).

32. L. Holtzer, T. Meckel, and T. Schmidt, "Nanometric three-dimensional tracking of individual quantum dots in cells," Appl. Phys. Lett. **90**, 053902 (2007).

33. S. R. P. Pavani and R. Piestun, "High-efficiency rotating point spread functions," Opt. Express **16**, 3484 (2008).

34. S. R. P. Pavani and R. Piestun, "Three dimensional tracking of fluorescent microparticles using a photon-limited double-helix response system," Opt. Express **16**, 22048 (2008).

35. S. R. P. Pavani, A. Greengard, and R. Piestun, "Three-dimensional localization with nanometer accuracy using a detector-limited double-helix point spread function system," Appl. Phys. Lett. **95**, 021103 (2009).

36. S. Rama, P. Pavani, M. A. Thompson, J. S. Biteen, S. J. Lord, N. Liu, R. J. Twieg, R. Piestun, W. E. Moerner, S. R. P. Pavani, M. A. Thompson, J. S. Biteen, S. J. Lord, N. Liu, R. J. Twieg, R. Piestun, and W. E. Moerner, "Three-dimensional, single-molecule fluorescence imaging beyond the diffraction limit by using a double-helix point spread function.," Proc. Natl. Acad. Sci. U. S. A. **106**, 2995–9 (2009).

37. V. Levi, Q. Ruan, and E. Gratton, "3-D particle tracking in a two-photon microscope: application to the study of molecular dynamics in cells.," Biophys. J. **88**, 2919–28 (2005).

38. Y. Katayama, O. Burkacky, M. Meyer, C. Bräuchle, E. Gratton, and D. C. Lamb, "Real-time nanomicroscopy via three-dimensional single-particle tracking.," Chemphyschem **10**, 2458–64 (2009).

39. T. Ha, T. A. Laurence, D. S. Chemla, and S. Weiss, "Polarization Spectroscopy of Single Fluorescent Molecules," J. Phys. Chem. B **103**, 6839–6850 (1999).

40. J. N. Forkey, M. E. Quinlan, M. A. Shaw, J. E. T. Corrie, and Y. E. Goldman, "Three-dimensional structural dynamics of myosin V by single-molecule fluorescence polarization.," Nature **422**, 399–404 (2003).

41. A. P. Bartko and R. M. Dickson, "Imaging Three-Dimensional Single Molecule Orientations," J. Phys. Chem. B **103**, 11237–11241 (1999).

42. M. Böhmer and J. Enderlein, "Orientation imaging of single molecules by wide-field epifluorescence microscopy," J. Opt. Soc. Am. B **20**, 554 (2003).

43. E. Toprak, J. Enderlein, S. Syed, S. A. McKinney, R. G. Petschek, T. Ha, Y. E. Goldman, and P. R. Selvin, "Defocused orientation and position imaging (DOPI) of myosin V.," Proc. Natl. Acad. Sci. U. S. A. **103**, 6495–9 (2006).

44. T. Ha, T. Enderle, D. F. Ogletree, D. S. Chemla, P. R. Selvin, and S. Weiss,

"Probing the interaction between two single molecules: fluorescence resonance energy transfer between a single donor and a single acceptor.," Proc. Natl. Acad. Sci. **93**, 6264–6268 (1996).

45. I. Rasnik, S. A. McKinney, and T. Ha, "Nonblinking and long-lasting single-molecule fluorescence imaging.," Nat. Methods **3**, 891–3 (2006).

46. M. F. Juette, D. S. Terry, M. R. Wasserman, Z. Zhou, R. B. Altman, Q. Zheng, and S. C. Blanchard, "The bright future of single-molecule fluorescence imaging.," Curr. Opin. Chem. Biol. **20**, 103–11 (2014).

47. A. N. Kapanidis, N. K. Lee, T. A. Laurence, S. Doose, E. Margeat, and S. Weiss, "Fluorescence-aided molecule sorting: analysis of structure and interactions by alternating-laser excitation of single molecules.," Proc. Natl. Acad. Sci. U. S. A. **101**, 8936–41 (2004).

48. N. K. Lee, A. N. Kapanidis, Y. Wang, X. Michalet, J. Mukhopadhyay, R. H. Ebright, and S. Weiss, "Accurate FRET measurements within single diffusing biomolecules using alternating-laser excitation.," Biophys. J. **88**, 2939–53 (2005).

49. B. K. Müller, E. Zaychikov, C. Bräuchle, and D. C. Lamb, "Pulsed interleaved excitation.," Biophys. J. **89**, 3508–22 (2005).

50. S. Hohng, C. Joo, and T. Ha, "Single-molecule three-color FRET.," Biophys. J. **87**, 1328–37 (2004).

51. M. Heilemann, P. Tinnefeld, G. Sanchez Mosteiro, M. Garcia Parajo, N. F. Van Hulst, and M. Sauer, "Multistep energy transfer in single molecular photonic wires.," J. Am. Chem. Soc. **126**, 6514–5 (2004).

52. J.-P. Clamme and A. A. Deniz, "Three-color single-molecule fluorescence resonance energy transfer.," Chemphyschem **6**, 74–7 (2005).

53. N. K. Lee, A. N. Kapanidis, H. R. Koh, Y. Korlann, S. O. Ho, Y. Kim, N. Gassman, S. K. Kim, and S. Weiss, "Three-color alternating-laser excitation of single molecules: monitoring multiple interactions and distances.," Biophys. J. **92**, 303–12 (2007).

54. J. Lee, S. Lee, K. Ragunathan, C. Joo, T. Ha, S. Hohng, J. Lee , S. Lee , K. Ragunathan, C. Joo, T. Ha, and S. Hohng, "Single-molecule four-color FRET.," Angew. Chem. Int. Ed. Engl. **49**, 9922–5 (2010).

55. B. Hua, K. Y. Han, R. Zhou, H. Kim, X. Shi, S. C. Abeysirigunawardena, A. Jain, D. Singh, V. Aggarwal, S. A. Woodson, and T. Ha, "An improved surface passivation method for single-molecule studies," Nat. Methods **11**, 1233–1236 (2014).

56. U. B. Choi, P. Strop, M. Vrljic, S. Chu, A. T. Brunger, and K. R. Weninger, "Single-molecule FRET–derived model of the synaptotagmin 1–SNARE fusion complex," Nat. Struct. Mol. Biol. **17**, 318–324 (2010).

57. Y. Zhao, D. Chen, H. Yue, M. M. Spiering, C. Zhao, S. J. Benkovic, and T. J. Huang, "Dark-field illumination on zero-mode waveguide/microfluidic hybrid chip reveals T4 replisomal protein interactions.," Nano Lett. **14**, 1952–60 (2014).

58. S. A. McKinney, A.-C. Déclais, D. M. J. Lilley, and T. Ha, "Structural dynamics of individual Holliday junctions.," Nat. Struct. Biol. **10**, 93–7 (2003).

59. S. a McKinney, C. Joo, and T. Ha, "Analysis of single-molecule FRET trajectories using hidden Markov modeling.," Biophys. J. **91**, 1941–51 (2006).

60. L. P. Watkins and H. Yang, "Detection of intensity change points in time-resolved single-molecule measurements.," J. Phys. Chem. B **109**, 617–28 (2005).

61. A. Jain, R. Liu, B. Ramani, E. Arauz, Y. Ishitsuka, K. Ragunathan, J. Park, J. Chen, Y. K. Xiang, and T. Ha, "Probing cellular protein complexes using single-molecule pull-down.," Nature **473**, 484–8 (2011).

62. A. Jain, R. Liu, Y. K. Xiang, and T. Ha, "Single-molecule pull-down for studying protein interactions.," Nat. Protoc. **7**, 445–52 (2012).

63. S. H. Chung and R. A. Kennedy, "Forward-backward non-linear filtering technique for extracting small biological signals from noise.," J. Neurosci. Methods **40**, 71–86 (1991).

64. S. K. Das, M. Darshi, S. Cheley, M. I. Wallace, and H. Bayley, "Membrane protein stoichiometry determined from the step-wise photobleaching of dye-labelled subunits.," Chembiochem **8**, 994–9 (2007).

65. B. C. Carter, M. Vershinin, and S. P. Gross, "A comparison of step-detection

methods: how well can you do?," Biophys. J. **94**, 306–19 (2008).

66. M. A. Little, B. C. Steel, F. Bai, Y. Sowa, T. Bilyard, D. M. Mueller, R. M. Berry, and N. S. Jones, "Steps and bumps: precision extraction of discrete states of molecular machines.," Biophys. J. **101**, 477–85 (2011).

67. B. D. Engel, W. B. Ludington, and W. F. Marshall, "Intraflagellar transport particle size scales inversely with flagellar length: revisiting the balance-point length control model.," J. Cell Biol. **187**, 81–9 (2009).

68. A. Harootunian, E. Betzig, M. Isaacson, and A. Lewis, "Super-resolution fluorescence near-field scanning optical microscopy," Appl. Phys. Lett. **49**, 674 (1986).

69. T. Wilson, "The Role of the Pinhole in Confocal Imaging System," in *Handbook of Biological Confocal Microscopy SE - 11*, J. Pawley, ed. (Springer US, 1995), pp. 167–182.

70. B. Bailey, D. L. Farkas, D. L. Taylor, and F. Lanni, "Enhancement of axial resolution in fluorescence microscopy by standing-wave excitation.," Nature **366**, 44–8 (1993).

71. F. Lanni and B. Bailey, "Standing-wave excitation for fluorescence microscopy," Trends Cell Biol. **4**, 262–265 (1994).

72. F. Lanni, B. Bailey, D. L. Farkas, and D. L. Taylor, "Excitation field synthesis as a means for obtaining enhanced axial resolution in fluorescence microscopes," Bioimaging **1**, 187–196 (1993).

73. S. Hell and E. H. K. Stelzer, "Properties of a 4Pi confocal fluorescence microscope," J. Opt. Soc. Am. A **9**, 2159 (1992).

74. M. G. Gustafsson, D. A. Agard, and J. W. Sedat, "I5M: 3D widefield light microscopy with better than 100 nm axial resolution.," J. Microsc. **195**, 10–16 (1999).

75. M. G. Gustafsson, "Extended resolution fluorescence microscopy," Curr. Opin. Struct. Biol. **9**, 627–628 (1999).

76. M. A. A. Neil, R. Juskaitis, and T. Wilson, "Method of obtaining optical sectioning by using structured light in a conventional microscope.," Opt. Lett. **22**, 1905–7 (1997).

77. R. Heintzmann and C. G. Cremer, "Laterally modulated excitation microscopy: improvement of resolution by using a diffraction grating," in *Proc. SPIE*, I. J. Bigio, H. Schneckenburger, J. Slavik, K. Svanberg, and P. M. Viallet, eds. (International Society for Optics and Photonics, 1999), Vol. 3568, pp. 185–196.

78. M. G. L. Gustafsson, "Surpassing the lateral resolution limit by a factor of two using structured illumination microscopy.," J. Microsc. **198**, 82–7 (2000).

79. M. G. L. Gustafsson, L. Shao, P. M. Carlton, C. J. R. Wang, I. N. Golubovskaya, W. Z. Cande, D. a Agard, and J. W. Sedat, "Three-dimensional resolution doubling in wide-field fluorescence microscopy by structured illumination.," Biophys. J. **94**, 4957–70 (2008).

80. J. T. Frohn, H. F. Knapp, and a Stemmer, "True optical resolution beyond the Rayleigh limit achieved by standing wave illumination.," Proc. Natl. Acad. Sci. U. S. A. **97**, 7232–6 (2000).

81. M. G. L. Gustafsson, "Nonlinear structured-illumination microscopy: wide-field fluorescence imaging with theoretically unlimited resolution.," Proc. Natl. Acad. Sci. U. S. A. **102**, 13081–6 (2005).

82. E. H. Rego, L. Shao, J. J. Macklin, L. Winoto, G. A. Johansson, N. Kamps-Hughes, M. W. Davidson, and M. G. L. Gustafsson, "Nonlinear structured-illumination microscopy with a photoswitchable protein reveals cellular structures at 50-nm resolution.," Proc. Natl. Acad. Sci. U. S. A. **109**, E135–43 (2012).

83. L. Schermelleh, P. M. Carlton, S. Haase, L. Shao, L. Winoto, P. Kner, B. Burke, M. C. Cardoso, D. a Agard, M. G. L. Gustafsson, H. Leonhardt, and J. W. Sedat, "Subdiffraction multicolor imaging of the nuclear periphery with 3D structured illumination microscopy.," Science **320**, 1332–6 (2008).

84. P. Kner, B. B. Chhun, E. R. Griffis, L. Winoto, and M. G. L. Gustafsson, "Super-resolution video microscopy of live cells by structured illumination.," Nat. Methods **6**, 339–42 (2009).

85. L. Shao, P. Kner, E. H. Rego, and M. G. L. Gustafsson, "Super-resolution 3D microscopy of live whole cells using structured illumination," Nat. Methods **8**, 1044–1046 (2011).

86. R. Heintzmann, T. M. Jovin, and C. Cremer, "Saturated patterned excitation

microscopy—a concept for optical resolution improvement," J. Opt. Soc. Am. A **19**, 1599 (2002).

87. R. Heintzmann, "Saturated patterned excitation microscopy with two-dimensional excitation patterns.," Micron **34**, 283–91 (2003).

88. D. Li, L. Shao, B.-C. Chen, X. Zhang, M. Zhang, B. Moses, D. E. Milkie, J. R. Beach, J. A. Hammer, M. Pasham, T. Kirchhausen, M. A. Baird, M. W. Davidson, P. Xu, and E. Betzig, "Extended-resolution structured illumination imaging of endocytic and cytoskeletal dynamics," Science (80-.). **349**, aab3500–aab3500 (2015).

89. E. Chung, D. Kim, Y. Cui, Y.-H. Kim, and P. T. C. So, "Two-dimensional standing wave total internal reflection fluorescence microscopy: superresolution imaging of single molecular and biological specimens.," Biophys. J. **93**, 1747–57 (2007).

90. O. Gliko, G. D. Reddy, B. Anvari, W. E. Brownell, and P. Saggau, "Standing wave total internal reflection fluorescence microscopy to measure the size of nanostructures in living cells.," J. Biomed. Opt. **11**, 064013 (2006).

91. R. Fiolka, M. Beck, and A. Stemmer, "Structured illumination in total internal reflection fluorescence microscopy using a spatial light modulator," Opt. Lett. **33**, 1629 (2008).

92. L. Shao, B. Isaac, S. Uzawa, D. A. Agard, J. W. Sedat, and M. G. L. Gustafsson, "I5S: wide-field light microscopy with 100-nm-scale resolution in three dimensions.," Biophys. J. **94**, 4971–83 (2008).

93. L. Shao, L. Winoto, D. A. Agard, M. G. L. Gustafsson, and J. W. Sedat, "Interferometer-based structured-illumination microscopy utilizing complementary phase relationship through constructive and destructive image detection by two cameras.," J. Microsc. **246**, 229–36 (2012).

94. O. Mandula, M. Kielhorn, K. Wicker, G. Krampert, I. Kleppe, and R. Heintzmann, "Line scan--structured illumination microscopy super-resolution imaging in thick fluorescent samples.," Opt. Express **20**, 24167–74 (2012).

95. A. G. York, S. H. Parekh, D. Dalle Nogare, R. S. Fischer, K. Temprine, M. Mione, A. B. Chitnis, C. A. Combs, and H. Shroff, "Resolution doubling in live, multicellular organisms via multifocal structured illumination microscopy.," Nat. Methods **9**, 749–54 (2012).

96. S. Hayashi and Y. Okada, "Ultrafast superresolution fluorescence imaging with

spinning disk confocal microscope optics.," Mol. Biol. Cell **26**, 1743–51 (2015).

97. A. G. York, P. Chandris, D. D. Nogare, J. Head, P. Wawrzusin, R. S. Fischer, A. Chitnis, and H. Shroff, "Instant super-resolution imaging in live cells and embryos via analog image processing.," Nat. Methods **10**, 1122–6 (2013).

98. M. Ingaramo, A. G. York, P. Wawrzusin, O. Milberg, A. Hong, R. Weigert, H. Shroff, and G. H. Patterson, "Two-photon excitation improves multifocal structured illumination microscopy in thick scattering tissue.," Proc. Natl. Acad. Sci. U. S. A. **111**, 5254–9 (2014).

99. P. W. Winter, A. G. York, D. D. Nogare, M. Ingaramo, R. Christensen, A. Chitnis, G. H. Patterson, and H. Shroff, "Two-photon instant structured illumination microscopy improves the depth penetration of super-resolution imaging in thick scattering samples.," Optica **1**, 181–191 (2014).

100. S. W. Hell and J. Wichmann, "Breaking the diffraction resolution limit by stimulated emission: stimulated-emission-depletion fluorescence microscopy," Opt. Lett. **19**, 780 (1994).

101. T. A. Klar, S. Jakobs, M. Dyba, A. Egner, and S. W. Hell, "Fluorescence microscopy with diffraction resolution barrier broken by stimulated emission," Proc. Natl. Acad. Sci. **97**, 8206–8210 (2000).

102. G. Donnert, J. Keller, R. Medda, M. A. Andrei, S. O. Rizzoli, R. Lührmann, R. Jahn, C. Eggeling, and S. W. Hell, "Macromolecular-scale resolution in biological fluorescence microscopy.," Proc. Natl. Acad. Sci. U. S. A. **103**, 11440–5 (2006).

103. M. Dyba, S. Jakobs, and S. W. Hell, "Immunofluorescence stimulated emission depletion microscopy.," Nat. Biotechnol. **21**, 1303–4 (2003).

104. K. I. Willig, R. R. Kellner, R. Medda, B. Hein, S. Jakobs, and S. W. Hell, "Nanoscale resolution in GFP-based microscopy.," Nat. Methods **3**, 721–3 (2006).

105. J. Hanne, H. J. Falk, F. Görlitz, P. Hoyer, J. Engelhardt, S. J. Sahl, and S. W. Hell, "STED nanoscopy with fluorescent quantum dots," Nat. Commun. **6**, 7127 (2015).

106. V. Westphal, S. O. Rizzoli, M. A. Lauterbach, D. Kamin, R. Jahn, and S. W. Hell, "Video-rate far-field optical nanoscopy dissects synaptic vesicle movement.," Science **320**, 246–9 (2008).

107. C. Eggeling, C. Ringemann, R. Medda, G. Schwarzmann, K. Sandhoff, S. Polyakova, V. N. Belov, B. Hein, C. von Middendorff, A. Schönle, and S. W. Hell, "Direct observation of the nanoscale dynamics of membrane lipids in a living cell.," Nature **457**, 1159–62 (2009).

108. U. V. Nägerl, K. I. Willig, B. Hein, S. W. Hell, and T. Bonhoeffer, "Live-cell imaging of dendritic spines by STED microscopy.," Proc. Natl. Acad. Sci. U. S. A. **105**, 18982–7 (2008).

109. I. Testa, N. T. Urban, S. Jakobs, C. Eggeling, K. I. Willig, and S. W. Hell, "Nanoscopy of living brain slices with low light levels.," Neuron **75**, 992–1000 (2012).

110. B. R. Rankin, G. Moneron, C. A. Wurm, J. C. Nelson, A. Walter, D. Schwarzer, J. Schroeder, D. A. Colón-Ramos, and S. W. Hell, "Nanoscopy in a living multicellular organism expressing GFP.," Biophys. J. **100**, L63–5 (2011).

111. S. Berning, K. I. Willig, H. Steffens, P. Dibaj, and S. W. Hell, "Nanoscopy in a living mouse brain.," Science **335**, 551 (2012).

112. G. Donnert, J. Keller, C. A. Wurm, S. O. Rizzoli, V. Westphal, A. Schönle, R. Jahn, S. Jakobs, C. Eggeling, and S. W. Hell, "Two-color far-field fluorescence nanoscopy.," Biophys. J. **92**, L67–9 (2007).

113. L. Meyer, D. Wildanger, R. Medda, A. Punge, S. O. Rizzoli, G. Donnert, and S. W. Hell, "Dual-color STED microscopy at 30-nm focal-plane resolution.," Small **4**, 1095–100 (2008).

114. F. Lavoie-Cardinal, N. A. Jensen, V. Westphal, A. C. Stiel, A. Chmyrov, J. Bierwagen, I. Testa, S. Jakobs, and S. W. Hell, "Two-color RESOLFT nanoscopy with green and red fluorescent photochromic proteins.," Chemphyschem **15**, 655–63 (2014).

115. F. Bergermann, L. Alber, S. J. Sahl, J. Engelhardt, and S. W. Hell, "2000-fold parallelized dual-color STED fluorescence nanoscopy.," Opt. Express **23**, 211–23 (2015).

116. I. Testa, E. D'Este, N. T. Urban, F. Balzarotti, and S. W. Hell, "Dual channel RESOLFT nanoscopy by using fluorescent state kinetics.," Nano Lett. **15**, 103–6 (2015).

117. K. Youngworth and T. Brown, "Focusing of high numerical aperture cylindrical-vector beams," Opt. Express **7**, 77 (2000).

118. E. ENGEL, N. HUSE, T. A. KLAR, and S. W. HELL, "Creating λ/3 focal holes with a Mach-Zehnder interferometer," Appl. Phys. B. **77**, 11–17 (n.d.).

119. P. Török and P. R. T. Munro, "The use of Gauss-Laguerre vector beams in STED microscopy," Opt. Express **12**, 3605 (2004).

120. K. I. Willig, S. O. Rizzoli, V. Westphal, R. Jahn, and S. W. Hell, "STED microscopy reveals that synaptotagmin remains clustered after synaptic vesicle exocytosis.," Nature **440**, 935–9 (2006).

121. S. W. Hell, R. Schmidt, and A. Egner, "Diffraction-unlimited three-dimensional optical nanoscopy with opposing lenses," Nat. Photonics **3**, 381–387 (2009).

122. D. Wildanger, J. Bückers, V. Westphal, S. W. Hell, and L. Kastrup, "A STED microscope aligned by design.," Opt. Express **17**, 16100–10 (2009).

123. T. Staudt, A. Engler, E. Rittweger, B. Harke, J. Engelhardt, and S. W. Hell, "Far-field optical nanoscopy with reduced number of state transition cycles.," Opt. Express **19**, 5644–57 (2011).

124. R. Schmidt, C. A. Wurm, S. Jakobs, J. Engelhardt, A. Egner, and S. W. Hell, "Spherical nanosized focal spot unravels the interior of cells.," Nat. Methods **5**, 539–44 (2008).

125. D. Wildanger, R. Medda, L. Kastrup, and S. W. Hell, "A compact STED microscope providing 3D nanoscale resolution.," J. Microsc. **236**, 35–43 (2009).

126. G. Donnert, C. Eggeling, and S. W. Hell, "Major signal increase in fluorescence microscopy through dark-state relaxation.," Nat. Methods **4**, 81–6 (2007).

127. S. W. Hell and M. Kroug, "Ground-state-depletion fluorscence microscopy: A concept for breaking the diffraction resolution limit," Appl. Phys. B Lasers Opt. **60**, 495–497 (1995).

128. S. Bretschneider, C. Eggeling, and S. W. Hell, "Breaking the diffraction barrier in fluorescence microscopy by optical shelving.," Phys. Rev. Lett. **98**, 218103

(2007).

129. T. Grotjohann, I. Testa, M. Reuss, T. Brakemann, C. Eggeling, S. W. Hell, and S. Jakobs, "rsEGFP2 enables fast RESOLFT nanoscopy of living cells.," Elife **1**, e00248 (2012).

130. E. Auksorius, B. R. Boruah, C. Dunsby, P. M. P. Lanigan, G. Kennedy, M. A. A. Neil, and P. M. W. French, "Stimulated emission depletion microscopy with a supercontinuum source and fluorescence lifetime imaging," Opt. Lett. **33**, 113 (2008).

131. G. Vicidomini, G. Moneron, K. Y. Han, V. Westphal, H. Ta, M. Reuss, J. Engelhardt, C. Eggeling, and S. W. Hell, "Sharper low-power STED nanoscopy by time gating.," Nat. Methods **8**, 571–3 (2011).

132. P. Bingen, M. Reuss, J. Engelhardt, and S. W. Hell, "Parallelized STED fluorescence nanoscopy.," Opt. Express **19**, 23716–26 (2011).

133. A. Chmyrov, J. Keller, T. Grotjohann, M. Ratz, E. d'Este, S. Jakobs, C. Eggeling, and S. W. Hell, "Nanoscopy with more than 100,000 "doughnuts"." Nat. Methods **10**, 737–40 (2013).

134. M. A. Schwentker, H. Bock, M. Hofmann, S. Jakobs, J. Bewersdorf, C. Eggeling, and S. W. Hell, "Wide-field subdiffraction RESOLFT microscopy using fluorescent protein photoswitching.," Microsc. Res. Tech. **70**, 269–80 (2007).

135. J. Schneider, J. Zahn, M. Maglione, S. J. Sigrist, J. Marquard, J. Chojnacki, H.-G. Kräusslich, S. J. Sahl, J. Engelhardt, and S. W. Hell, "Ultrafast, temporally stochastic STED nanoscopy of millisecond dynamics.," Nat. Methods **12**, 827–830 (2015).

136. A. Honigmann, V. Mueller, H. Ta, A. Schoenle, E. Sezgin, S. W. Hell, and C. Eggeling, "Scanning STED-FCS reveals spatiotemporal heterogeneity of lipid interaction in the plasma membrane of living cells.," Nat. Commun. **5**, 5412 (2014).

137. J. J. Sieber, K. I. Willig, C. Kutzner, C. Gerding-Reimers, B. Harke, G. Donnert, B. Rammner, C. Eggeling, S. W. Hell, H. Grubmüller, and T. Lang, "Anatomy and dynamics of a supramolecular membrane protein cluster.," Science **317**, 1072–6 (2007).

138. G. Moneron and S. W. Hell, "Two-photon excitation STED microscopy.," Opt.

Express **17**, 14567–73 (2009).

139. K. T. Takasaki, J. B. Ding, and B. L. Sabatini, "Live-cell superresolution imaging by pulsed STED two-photon excitation microscopy.," Biophys. J. **104**, 770–7 (2013).

140. T. J. Gould, D. Burke, J. Bewersdorf, and M. J. Booth, "Adaptive optics enables 3D STED microscopy in aberrating specimens.," Opt. Express **20**, 20998–1009 (2012).

141. D. Wildanger, E. Rittweger, L. Kastrup, and S. W. Hell, "STED microscopy with a supercontinuum laser source.," Opt. Express **16**, 9614–21 (2008).

142. K. I. Willig, B. Harke, R. Medda, and S. W. Hell, "STED microscopy with continuous wave beams.," Nat. Methods **4**, 915–8 (2007).

143. G. Moneron, R. Medda, B. Hein, A. Giske, V. Westphal, and S. W. Hell, "Fast STED microscopy with continuous wave fiber lasers.," Opt. Express **18**, 1302–9 (2010).

144. M. Reuss, J. Engelhardt, and S. W. Hell, "Birefringent device converts a standard scanning microscope into a STED microscope that also maps molecular orientation.," Opt. Express **18**, 1049–58 (2010).

145. R. Kasper, B. Harke, C. Forthmann, P. Tinnefeld, S. W. Hell, and M. Sauer, "Single-molecule STED microscopy with photostable organic fluorophores.," Small **6**, 1379–84 (2010).

146. H. Ta, J. Keller, M. Haltmeier, S. K. Saka, J. Schmied, F. Opazo, P. Tinnefeld, A. Munk, and S. W. Hell, "Mapping molecules in scanning far-field fluorescence nanoscopy.," Nat. Commun. **6**, 7977 (2015).

147. M. J. Rust, M. Bates, and X. Zhuang, "Sub-diffraction-limit imaging by stochastic optical reconstruction microscopy (STORM).," Nat. Methods **3**, 793–5 (2006).

148. E. Betzig, G. H. Patterson, R. Sougrat, O. W. Lindwasser, S. Olenych, J. S. Bonifacino, M. W. Davidson, J. Lippincott-Schwartz, and H. F. Hess, "Imaging intracellular fluorescent proteins at nanometer resolution.," Science **313**, 1642–5 (2006).

149. S. T. Hess, T. P. K. Girirajan, and M. D. Mason, "Ultra-high resolution imaging

by fluorescence photoactivation localization microscopy.," Biophys. J. **91**, 4258–72 (2006).

150. J. Fölling, M. Bossi, H. Bock, R. Medda, C. A. Wurm, B. Hein, S. Jakobs, C. Eggeling, and S. W. Hell, "Fluorescence nanoscopy by ground-state depletion and single-molecule return.," Nat. Methods **5**, 943–5 (2008).

151. M. Heilemann, S. van de Linde, M. Schüttpelz, R. Kasper, B. Seefeldt, A. Mukherjee, P. Tinnefeld, and M. Sauer, "Subdiffraction-resolution fluorescence imaging with conventional fluorescent probes.," Angew. Chem. Int. Ed. Engl. **47**, 6172–6 (2008).

152. M. Heilemann, S. van de Linde, A. Mukherjee, and M. Sauer, "Super-resolution imaging with small organic fluorophores.," Angew. Chem. Int. Ed. Engl. **48**, 6903–8 (2009).

153. S. van de Linde, A. Löschberger, T. Klein, M. Heidbreder, S. Wolter, M. Heilemann, and M. Sauer, "Direct stochastic optical reconstruction microscopy with standard fluorescent probes.," Nat. Protoc. **6**, 991–1009 (2011).

154. I. Schoen, J. Ries, E. Klotzsch, H. Ewers, and V. Vogel, "Binding-activated localization microscopy of DNA structures.," Nano Lett. **11**, 4008–11 (2011).

155. A. Sharonov and R. M. Hochstrasser, "Wide-field subdiffraction imaging by accumulated binding of diffusing probes.," Proc. Natl. Acad. Sci. U. S. A. **103**, 18911–6 (2006).

156. G. Giannone, E. Hosy, F. Levet, A. Constals, K. Schulze, A. I. Sobolevsky, M. P. Rosconi, E. Gouaux, R. Tampé, D. Choquet, and L. Cognet, "Dynamic superresolution imaging of endogenous proteins on living cells at ultra-high density.," Biophys. J. **99**, 1303–10 (2010).

157. F. Pinaud and M. Dahan, "Targeting and imaging single biomolecules in living cells by complementation-activated light microscopy with split-fluorescent proteins.," Proc. Natl. Acad. Sci. U. S. A. **108**, E201–10 (2011).

158. A. Nickerson, T. Huang, L.-J. Lin, and X. Nan, "Photoactivated localization microscopy with bimolecular fluorescence complementation (BiFC-PALM) for nanoscale imaging of protein-protein interactions in cells.," PLoS One **9**, e100589 (2014).

159. A. Egner, C. Geisler, C. von Middendorff, H. Bock, D. Wenzel, R. Medda, M. Andresen, A. C. Stiel, S. Jakobs, C. Eggeling, A. Schönle, and S. W. Hell, "Fluorescence nanoscopy in whole cells by asynchronous localization of

photoswitching emitters.," Biophys. J. **93**, 3285–90 (2007).

160. G. Grover, S. Quirin, C. Fiedler, and R. Piestun, "Photon efficient double-helix PSF microscopy with application to 3D photo-activation localization imaging.," Biomed. Opt. Express **2**, 3010–20 (2011).

161. M. Bates, B. Huang, G. T. Dempsey, and X. Zhuang, "Multicolor super-resolution imaging with photo-switchable fluorescent probes.," Science **317**, 1749–53 (2007).

162. B. Hajj, M. El Beheiry, I. Izeddin, X. Darzacq, and M. Dahan, "Accessing the third dimension in localization-based super-resolution microscopy.," Phys. Chem. Chem. Phys. **16**, 16340–8 (2014).

163. S. Manley, J. M. Gillette, G. H. Patterson, H. Shroff, H. F. Hess, E. Betzig, and J. Lippincott-schwartz, "High-density mapping of single-molecule trajectories with photoactivated localization microscopy.," Nat. Methods **5**, 155–7 (2008).

164. M. J. Mlodzianoski, M. F. Juette, G. L. Beane, and J. Bewersdorf, "Experimental characterization of 3D localization techniques for particle-tracking and super-resolution microscopy," Opt. Express **17**, 8264 (2009).

165. B. Huang, W. Wang, M. Bates, and X. Zhuang, "Three-dimensional super-resolution imaging by stochastic optical reconstruction microscopy.," Science **319**, 810–3 (2008).

166. B. Huang, M. Bates, and X. Zhuang, "Super-resolution fluorescence microscopy.," Annu. Rev. Biochem. **78**, 993–1016 (2009).

167. J. C. Vaughan, S. Jia, and X. Zhuang, "Ultrabright photoactivatable fluorophores created by reductive caging.," Nat. Methods **9**, 1181–4 (2012).

168. M. Bates, T. Blosser, and X. Zhuang, "Short-Range Spectroscopic Ruler Based on a Single-Molecule Optical Switch," Phys. Rev. Lett. **94**, 108101 (2005).

169. G. T. Dempsey, M. Bates, W. E. Kowtoniuk, D. R. Liu, R. Y. Tsien, and X. Zhuang, "Photoswitching mechanism of cyanine dyes.," J. Am. Chem. Soc. **131**, 18192–3 (2009).

170. M. F. Juette, T. J. Gould, M. D. Lessard, M. J. Mlodzianoski, B. S. Nagpure, B. T. Bennett, S. T. Hess, and J. Bewersdorf, "Three-dimensional sub-100 nm resolution fluorescence microscopy of thick samples.," Nat. Methods **5**, 527–9

(2008).

171. B. Huang, S. A. Jones, B. Brandenburg, and X. Zhuang, "Whole-cell 3D STORM reveals interactions between cellular structures with nanometer-scale resolution.," Nat. Methods **5**, 1047–52 (2008).

172. J. Tang, J. Akerboom, A. Vaziri, L. L. Looger, and C. V Shank, "Near-isotropic 3D optical nanoscopy with photon-limited chromophores.," Proc. Natl. Acad. Sci. U. S. A. **107**, 10068–73 (2010).

173. S. Jia, J. C. Vaughan, and X. Zhuang, "Isotropic 3D Super-resolution Imaging with a Self-bending Point Spread Function.," Nat. Photonics **8**, 302–306 (2014).

174. G. Shtengel, J. a Galbraith, C. G. Galbraith, J. Lippincott-Schwartz, J. M. Gillette, S. Manley, R. Sougrat, C. M. Waterman, P. Kanchanawong, M. W. Davidson, R. D. Fetter, and H. F. Hess, "Interferometric fluorescent super-resolution microscopy resolves 3D cellular ultrastructure.," Proc. Natl. Acad. Sci. U. S. A. **106**, 3125–30 (2009).

175. N. Bourg, C. Mayet, G. Dupuis, T. Barroca, P. Bon, S. Lécart, E. Fort, and S. Lévêque-Fort, "Direct optical nanoscopy with axially localized detection," Nat. Photonics **9**, 587–593 (2015).

176. J. Fölling, V. Belov, R. Kunetsky, R. Medda, A. Schönle, A. Egner, C. Eggeling, M. Bossi, and S. W. Hell, "Photochromic rhodamines provide nanoscopy with optical sectioning.," Angew. Chem. Int. Ed. Engl. **46**, 6266–70 (2007).

177. A. Vaziri, J. Tang, H. Shroff, and C. V Shank, "Multilayer three-dimensional super resolution imaging of thick biological samples.," Proc. Natl. Acad. Sci. U. S. A. **105**, 20221–6 (2008).

178. A. G. York, A. Ghitani, A. Vaziri, M. W. Davidson, and H. Shroff, "Confined activation and subdiffractive localization enables whole-cell PALM with genetically expressed probes.," Nat. Methods **8**, 327–33 (2011).

179. F. Cella Zanacchi, Z. Lavagnino, M. Perrone Donnorso, A. Del Bue, L. Furia, M. Faretta, and A. Diaspro, "Live-cell 3D super-resolution imaging in thick biological samples.," Nat. Methods **8**, 1047–9 (2011).

180. H. Shroff, C. G. Galbraith, J. A. Galbraith, and E. Betzig, "Live-cell photoactivated localization microscopy of nanoscale adhesion dynamics.," Nat. Methods **5**, 417–23 (2008).

181. S. T. Hess, T. J. Gould, M. V Gudheti, S. A. Maas, K. D. Mills, and J. Zimmerberg, "Dynamic clustered distribution of hemagglutinin resolved at 40 nm in living cell membranes discriminates between raft theories.," Proc. Natl. Acad. Sci. U. S. A. **104**, 17370–5 (2007).

182. S. A. Jones, S.-H. Shim, J. He, and X. Zhuang, "Fast, three-dimensional super-resolution imaging of live cells.," Nat. Methods **8**, 499–508 (2011).

183. D. Sage, H. Kirshner, T. Pengo, N. Stuurman, J. Min, S. Manley, and M. Unser, "Quantitative evaluation of software packages for single-molecule localization microscopy.," Nat. Methods **12**, 717–724 (2015).

184. A. Small and S. Stahlheber, "Fluorophore localization algorithms for super-resolution microscopy," Nat. Methods **11**, 267–279 (2014).

185. R. Henriques, M. Lelek, E. F. Fornasiero, F. Valtorta, C. Zimmer, and M. M. Mhlanga, "QuickPALM: 3D real-time photoactivation nanoscopy image processing in ImageJ.," Nat. Methods **7**, 339–40 (2010).

186. A. J. Berglund, M. D. McMahon, J. J. McClelland, and J. A. Liddle, "Fast, bias-free algorithm for tracking single particles with variable size and shape.," Opt. Express **16**, 14064–75 (2008).

187. B. Yu, D. Chen, J. Qu, and H. Niu, "Fast Fourier domain localization algorithm of a single molecule with nanometer precision.," Opt. Lett. **36**, 4317–9 (2011).

188. H. Ma, F. Long, S. Zeng, and Z.-L. Huang, "Fast and precise algorithm based on maximum radial symmetry for single molecule localization.," Opt. Lett. **37**, 2481–3 (2012).

189. S. Andersson, "Localization of a fluorescent source without numerical fitting," Opt. Express **16**, 18714 (2008).

190. P. N. Hedde, J. Fuchs, F. Oswald, J. Wiedenmann, and G. U. Nienhaus, "Online image analysis software for photoactivation localization microscopy.," Nat. Methods **6**, 689–90 (2009).

191. S. J. Holden, S. Uphoff, and A. N. Kapanidis, "DAOSTORM: an algorithm for high- density super-resolution microscopy.," Nat. Methods **8**, 279–80 (2011).

192. F. Huang, S. L. Schwartz, J. M. Byars, and K. a Lidke, "Simultaneous multiple-emitter fitting for single molecule super-resolution imaging.," Biomed. Opt. Express **2**, 1377–93 (2011).

193. T. Quan, H. Zhu, X. Liu, Y. Liu, J. Ding, S. Zeng, and Z.-L. Huang, "High-density localization of active molecules using Structured Sparse Model and Bayesian Information Criterion.," Opt. Express **19**, 16963–74 (2011).

194. Y. Wang, T. Quan, S. Zeng, and Z.-L. Huang, "PALMER: a method capable of parallel localization of multiple emitters for high-density localization microscopy.," Opt. Express **20**, 16039–49 (2012).

195. E. A. Mukamel, H. Babcock, and X. Zhuang, "Statistical deconvolution for superresolution fluorescence microscopy.," Biophys. J. **102**, 2391–400 (2012).

196. L. Zhu, W. Zhang, D. Elnatan, and B. Huang, "Faster STORM using compressed sensing.," Nat. Methods **9**, 721–3 (2012).

197. F. Grull, M. Kirchgessner, R. Kaufmann, M. Hausmann, and U. Kebschull, "Accelerating Image Analysis for Localization Microscopy with FPGAs," in *2011 21st International Conference on Field Programmable Logic and Applications* (IEEE, 2011), pp. 1–5.

198. T. J. Gould, M. S. Gunewardene, M. V Gudheti, V. V Verkhusha, S. Yin, J. a Gosse, and S. T. Hess, "Nanoscale imaging of molecular positions and anisotropies.," Nat. Methods **5**, 1027–30 (2008).

199. Z. Zhang, S. J. Kenny, M. Hauser, W. Li, and K. Xu, "Ultrahigh-throughput single-molecule spectroscopy and spectrally resolved super-resolution microscopy," Nat. Methods **advance on**, (2015).

200. A. Lambacher and P. Fromherz, "Fluorescence interference-contrast microscopy on oxidized silicon using a monomolecular dye layer," Appl. Phys. A Mater. Sci. Process. **63**, 207–216 (1996).

201. C. M. Ajo-Franklin, P. V Ganesan, and S. G. Boxer, "Variable incidence angle fluorescence interference contrast microscopy for z-imaging single objects.," Biophys. J. **89**, 2759–69 (2005).

202. M. J. Paszek, C. C. DuFort, M. G. Rubashkin, M. W. Davidson, K. S. Thorn, J. T. Liphardt, and V. M. Weaver, "Scanning angle interference microscopy

reveals cell dynamics at the nanoscale.," Nat. Methods **9**, 825–7 (2012).

203. M. J. Paszek, C. C. DuFort, O. Rossier, R. Bainer, J. K. Mouw, K. Godula, J. E. Hudak, J. N. Lakins, A. C. Wijekoon, L. Cassereau, M. G. Rubashkin, M. J. Magbanua, K. S. Thorn, M. W. Davidson, H. S. Rugo, J. W. Park, D. A. Hammer, G. Giannone, C. R. Bertozzi, and V. M. Weaver, "The cancer glycocalyx mechanically primes integrin-mediated growth and survival," Nature **advance on**, (2014).

204. F. Huang, T. M. P. Hartwich, F. E. Rivera-Molina, Y. Lin, W. C. Duim, J. J. Long, P. D. Uchil, J. R. Myers, M. A. Baird, W. Mothes, M. W. Davidson, D. Toomre, and J. Bewersdorf, "Video-rate nanoscopy using sCMOS camera-specific single-molecule localization algorithms.," Nat. Methods **10**, 653–8 (2013).

205. T. Plakhotnik, A. Chennu, and A. V. Zvyagin, "Statistics of single-electron signals in electron-multiplying charge-coupled devices," IEEE Trans. Electron Devices **53**, 618–622 (2006).

206. J. R. Janesick, *Scientific Charge-Coupled Devices*, Press Monographs (Society of Photo Optical, 2001).

207. Z.-L. Huang, H. Zhu, F. Long, H. Ma, L. Qin, Y. Liu, J. Ding, Z. Zhang, Q. Luo, and S. Zeng, "Localization-based super-resolution microscopy with an sCMOS camera.," Opt. Express **19**, 19156–68 (2011).

208. F. Long, S. Zeng, and Z.-L. Huang, "Localization-based super-resolution microscopy with an sCMOS camera part II: experimental methodology for comparing sCMOS with EMCCD cameras.," Opt. Express **20**, 17741–59 (2012).

209. S. T. Hess, "Red lights, camera, photoactivation!," Nat. Methods **6**, 124–5 (2009).

210. M. Zimmer, "GFP: from jellyfish to the Nobel prize and beyond.," Chem. Soc. Rev. **38**, 2823–32 (2009).

211. P. Tinnefeld and T. Cordes, "“Self-healing” dyes: intramolecular stabilization of organic fluorophores.," Nat. Methods **9**, 426–7; author reply 427–8 (2012).

212. R. N. Day and M. W. Davidson, "The fluorescent protein palette: tools for cellular imaging.," Chem. Soc. Rev. **38**, 2887–921 (2009).

213. D. M. Chudakov, M. V Matz, S. Lukyanov, and K. A. Lukyanov, "Fluorescent proteins and their applications in imaging living cells and tissues.," Physiol. Rev. **90**, 1103–63 (2010).

214. T. Ha and P. Tinnefeld, "Photophysics of fluorescent probes for single-molecule biophysics and super-resolution imaging.," Annu. Rev. Phys. Chem. **63**, 595–617 (2012).

215. R. M. Dickson, A. B. Cubitt, R. Y. Tsien, and W. E. Moerner, "On/off blinking and switching behaviour of single molecules of green fluorescent protein.," Nature **388**, 355–8 (1997).

216. G. H. Patterson and J. Lippincott-Schwartz, "A photoactivatable GFP for selective photolabeling of proteins and cells.," Science **297**, 1873–7 (2002).

217. F. V Subach, G. H. Patterson, S. Manley, J. M. Gillette, J. Lippincott-schwartz, and V. V Verkhusha, "Photoactivatable mCherry for high-resolution two-color fluorescence microscopy.," Nat. Methods **6**, 153–9 (2009).

218. M. Zhang, H. Chang, Y. Zhang, J. Yu, L. Wu, W. Ji, J. Chen, B. Liu, J. Lu, Y. Liu, J. Zhang, P. Xu, and T. Xu, "Rational design of true monomeric and bright photoactivatable fluorescent proteins.," Nat. Methods **9**, 727–9 (2012).

219. S. Habuchi, R. Ando, P. Dedecker, W. Verheijen, H. Mizuno, A. Miyawaki, and J. Hofkens, "Reversible single-molecule photoswitching in the GFP-like fluorescent protein Dronpa.," Proc. Natl. Acad. Sci. U. S. A. **102**, 9511–6 (2005).

220. X. Zhang, X. Chen, Z. Zeng, M. Zhang, Y. Sun, P. Xi, J. Peng, and P. Xu, "Development of a reversibly switchable fluorescent protein for super-resolution optical fluctuation imaging (SOFI).," ACS Nano **9**, 2659–67 (2015).

221. L. D. Lavis and R. T. Raines, "Bright building blocks for chemical biology.," ACS Chem. Biol. **9**, 855–66 (2014).

222. J. B. Grimm, B. P. English, J. Chen, J. P. Slaughter, Z. Zhang, A. Revyakin, R. Patel, J. J. Macklin, D. Normanno, R. H. Singer, T. Lionnet, and L. D. Lavis, "A general method to improve fluorophores for live-cell and single-molecule microscopy.," Nat. Methods **12**, 244–50, 3 p following 250 (2015).

223. G. T. Dempsey, J. C. Vaughan, K. H. Chen, M. Bates, and X. Zhuang,

"Evaluation of fluorophores for optimal performance in localization-based super-resolution imaging.," Nat. Methods **8**, 1027–36 (2011).

224. C. E. Aitken, R. A. Marshall, and J. D. Puglisi, "An oxygen scavenging system for improvement of dye stability in single-molecule fluorescence experiments.," Biophys. J. **94**, 1826–35 (2008).

225. M. Swoboda, J. Henig, H.-M. Cheng, D. Brugger, D. Haltrich, N. Plumeré, and M. Schlierf, "Enzymatic oxygen scavenging for photostability without pH drop in single-molecule experiments.," ACS Nano **6**, 6364–9 (2012).

226. N. Olivier, D. Keller, P. Gönczy, and S. Manley, "Resolution doubling in 3D-STORM imaging through improved buffers.," PLoS One **8**, e69004 (2013).

227. R. Dave, D. S. Terry, J. B. Munro, and S. C. Blanchard, "Mitigating unwanted photophysical processes for improved single-molecule fluorescence imaging.," Biophys. J. **96**, 2371–81 (2009).

228. J. Enderlein, E. Toprak, and P. R. Selvin, "Polarization effect on position accuracy of fluorophore localization," Opt. Express **14**, 8111 (2006).

229. R. B. Altman, D. S. Terry, Z. Zhou, Q. Zheng, P. Geggier, R. A. Kolster, Y. Zhao, J. A. Javitch, J. D. Warren, and S. C. Blanchard, "Cyanine fluorophore derivatives with enhanced photostability.," Nat. Methods **9**, 68–71 (2012).

230. R. B. Altman, Q. Zheng, Z. Zhou, D. S. Terry, J. D. Warren, and S. C. Blanchard, "Enhanced photostability of cyanine fluorophores across the visible spectrum.," Nat. Methods **9**, 428–9 (2012).

231. Q. Zheng, S. Jockusch, Z. Zhou, R. B. Altman, J. D. Warren, N. J. Turro, and S. C. Blanchard, "On the Mechanisms of Cyanine Fluorophore Photostabilization.," J. Phys. Chem. Lett. **3**, 2200–2203 (2012).

232. S. van de Linde, M. Heilemann, and M. Sauer, "Live-cell super-resolution imaging with synthetic fluorophores.," Annu. Rev. Phys. Chem. **63**, 519–40 (2012).

233. X. Michalet, F. F. Pinaud, L. A. Bentolila, J. M. Tsay, S. Doose, J. J. Li, G. Sundaresan, A. M. Wu, S. S. Gambhir, and S. Weiss, "Quantum dots for live cells, in vivo imaging, and diagnostics.," Science **307**, 538–44 (2005).

234. S. Hohng and T. Ha, "Near-complete suppression of quantum dot blinking in ambient conditions.," J. Am. Chem. Soc. **126**, 1324–5 (2004).

235. E. Cai, P. Ge, S. H. Lee, O. Jeyifous, Y. Wang, Y. Liu, K. M. Wilson, S. J. Lim, M. A. Baird, J. E. Stone, K. Y. Lee, M. W. Davidson, H. J. Chung, K. Schulten, A. M. Smith, W. N. Green, and P. R. Selvin, "Stable small quantum dots for synaptic receptor tracking on live neurons.," Angew. Chem. Int. Ed. Engl. **53**, 12484–8 (2014).

236. Y. Wang, E. Cai, T. Rosenkranz, P. Ge, K. W. Teng, S. J. Lim, A. M. Smith, H. J. Chung, F. Sachs, W. N. Green, P. Gottlieb, and P. R. Selvin, "Small quantum dots conjugated to nanobodies as immunofluorescence probes for nanometric microscopy.," Bioconjug. Chem. **25**, 2205–11 (2014).

237. J. Farlow, D. Seo, K. E. Broaders, M. J. Taylor, Z. J. Gartner, and Y.-W. Jun, "Formation of targeted monovalent quantum dots by steric exclusion.," Nat. Methods **10**, 1203–5 (2013).

238. R. Schirhagl, K. Chang, M. Loretz, and C. L. Degen, "Nitrogen-vacancy centers in diamond: nanoscale sensors for physics and biology.," Annu. Rev. Phys. Chem. **65**, 83–105 (2014).

239. J. Ries, C. Kaplan, E. Platonova, H. Eghlidi, and H. Ewers, "A simple, versatile method for GFP-based super-resolution microscopy via nanobodies.," Nat. Methods **9**, 582–4 (2012).

240. F. Opazo, M. Levy, M. Byrom, C. Schäfer, C. Geisler, T. W. Groemer, A. D. Ellington, and S. O. Rizzoli, "Aptamers as potential tools for super-resolution microscopy.," Nat. Methods **9**, 938–9 (2012).

241. M. E. Tanenbaum, L. A. Gilbert, L. S. Qi, J. S. Weissman, and R. D. Vale, "A Protein-Tagging System for Signal Amplification in Gene Expression and Fluorescence Imaging," Cell **159**, 635–646 (2014).

242. A. Keppler, S. Gendreizig, T. Gronemeyer, H. Pick, H. Vogel, and K. Johnsson, "A general method for the covalent labeling of fusion proteins with small molecules in vivo.," Nat. Biotechnol. **21**, 86–9 (2003).

243. A. Gautier, A. Juillerat, C. Heinis, I. R. Corrêa, M. Kindermann, F. Beaufils, and K. Johnsson, "An Engineered Protein Tag for Multiprotein Labeling in Living Cells," Chem. Biol. **15**, 128–136 (2008).

244. G. V Los, L. P. Encell, M. G. McDougall, D. D. Hartzell, N. Karassina, C. Zimprich, M. G. Wood, R. Learish, R. F. Ohana, M. Urh, D. Simpson, J.

Mendez, K. Zimmerman, P. Otto, G. Vidugiris, J. Zhu, A. Darzins, D. H. Klaubert, R. F. Bulleit, and K. V Wood, "HaloTag: a novel protein labeling technology for cell imaging and protein analysis.," ACS Chem. Biol. **3**, 373–82 (2008).

245. J. Yin, P. D. Straight, S. M. McLoughlin, Z. Zhou, A. J. Lin, D. E. Golan, N. L. Kelleher, R. Kolter, and C. T. Walsh, "Genetically encoded short peptide tag for versatile protein labeling by Sfp phosphopantetheinyl transferase.," Proc. Natl. Acad. Sci. U. S. A. **102**, 15815–20 (2005).

246. Z. Zhou, P. Cironi, A. J. Lin, Y. Xu, S. Hrvatin, D. E. Golan, P. A. Silver, C. T. Walsh, and J. Yin, "Genetically encoded short peptide tags for orthogonal protein labeling by Sfp and AcpS phosphopantetheinyl transferases.," ACS Chem. Biol. **2**, 337–46 (2007).

247. B. Zakeri, J. O. Fierer, E. Celik, E. C. Chittock, U. Schwarz-Linek, V. T. Moy, and M. Howarth, "Peptide tag forming a rapid covalent bond to a protein, through engineering a bacterial adhesin.," Proc. Natl. Acad. Sci. U. S. A. **109**, E690–7 (2012).

248. X. Shi, Y. Jung, L.-J. Lin, C. Liu, C. Wu, I. K. O. Cann, and T. Ha, "Quantitative fluorescence labeling of aldehyde-tagged proteins for single-molecule imaging.," Nat. Methods **9**, 499–503 (2012).

249. K. Wang, A. Sachdeva, D. J. Cox, N. M. Wilf, N. W. Wilf, K. Lang, S. Wallace, R. A. Mehl, and J. W. Chin, "Optimized orthogonal translation of unnatural amino acids enables spontaneous protein double-labelling and FRET.," Nat. Chem. **6**, 393–403 (2014).

250. D. Pan, Z. Hu, F. Qiu, Z.-L. Huang, Y. Ma, Y. Wang, L. Qin, Z. Zhang, S. Zeng, and Y.-H. Zhang, "A general strategy for developing cell-permeable photo-modulatable organic fluorescent probes for live-cell super-resolution imaging.," Nat. Commun. **5**, 5573 (2014).

251. A. Erazo-Oliveras, K. Najjar, L. Dayani, T.-Y. Wang, G. A. Johnson, and J.-P. Pellois, "Protein delivery into live cells by incubation with an endosomolytic agent.," Nat. Methods **11**, 861–7 (2014).

252. A. K. Shalek, J. T. Robinson, E. S. Karp, J. S. Lee, D.-R. Ahn, M.-H. Yoon, A. Sutton, M. Jorgolli, R. S. Gertner, T. S. Gujral, G. MacBeath, E. G. Yang, and H. Park, "Vertical silicon nanowires as a universal platform for delivering biomolecules into living cells.," Proc. Natl. Acad. Sci. U. S. A. **107**, 1870–5 (2010).

253. P. Chakravarty, W. Qian, M. A. El-Sayed, and M. R. Prausnitz, "Delivery of molecules into cells using carbon nanoparticles activated by femtosecond laser pulses.," Nat. Nanotechnol. **5**, 607–11 (2010).

254. Y.-C. Wu, T.-H. Wu, D. L. Clemens, B.-Y. Lee, X. Wen, M. A. Horwitz, M. A. Teitell, and P.-Y. Chiou, "Massively parallel delivery of large cargo into mammalian cells with light pulses," Nat. Methods **12**, 439–444 (2015).

255. V. Mueller, C. Ringemann, A. Honigmann, G. Schwarzmann, R. Medda, M. Leutenegger, S. Polyakova, V. N. Belov, S. W. Hell, and C. Eggeling, "STED nanoscopy reveals molecular details of cholesterol- and cytoskeleton-modulated lipid interactions in living cells.," Biophys. J. **101**, 1651–60 (2011).

256. R. J. Arant and M. H. Ulbrich, "Deciphering the subunit composition of multimeric proteins by counting photobleaching steps.," Chemphyschem **15**, 600–5 (2014).

257. Z. Liu, W. R. Legant, B.-C. Chen, L. Li, J. B. Grimm, L. D. Lavis, E. Betzig, and R. Tjian, "3D imaging of Sox2 enhancer clusters in embryonic stem cells.," Elife **3**, e04236 (2014).

258. P. Kanchanawong, G. Shtengel, A. M. Pasapera, E. B. Ramko, M. W. Davidson, H. F. Hess, and C. M. Waterman, "Nanoscale architecture of integrin-based cell adhesions.," Nature **468**, 580–4 (2010).

259. S. H. Sternberg, S. Redding, M. Jinek, E. C. Greene, and J. A. Doudna, "DNA interrogation by the CRISPR RNA-guided endonuclease Cas9.," Nature **507**, 62–7 (2014).

260. K. Xu, G. Zhong, and X. Zhuang, "Actin, spectrin, and associated proteins form a periodic cytoskeletal structure in axons.," Science **339**, 452–6 (2013).

261. K. H. Chen, A. N. Boettiger, J. R. Moffitt, S. Wang, and X. Zhuang, "Spatially resolved, highly multiplexed RNA profiling in single cells.," Science **348**, aaa6090– (2015).

262. F. Tombola, M. H. Ulbrich, and E. Y. Isacoff, "The voltage-gated proton channel Hv1 has two pores, each controlled by one voltage sensor.," Neuron **58**, 546–56 (2008).

263. W. Ji, P. Xu, Z. Li, J. Lu, L. Liu, Y. Zhan, Y. Chen, B. Hille, T. Xu, and L.

Chen, "Functional stoichiometry of the unitary calcium-release-activated calcium channel.," Proc. Natl. Acad. Sci. U. S. A. **105**, 13668–73 (2008).

264. P. Sengupta, T. Jovanovic-Talisman, D. Skoko, M. Renz, S. L. Veatch, and J. Lippincott-Schwartz, "Probing protein heterogeneity in the plasma membrane using PALM and pair correlation analysis.," Nat. Methods **8**, 969–75 (2011).

265. S. A. Shelby, D. Holowka, B. Baird, and S. L. Veatch, "Distinct stages of stimulated FcεRI receptor clustering and immobilization are identified through superresolution imaging.," Biophys. J. **105**, 2343–54 (2013).

266. O. Rossier, V. Octeau, J.-B. Sibarita, C. Leduc, B. Tessier, D. Nair, V. Gatterdam, O. Destaing, C. Albigès-Rizo, R. Tampé, L. Cognet, D. Choquet, B. Lounis, and G. Giannone, "Integrins β1 and β3 exhibit distinct dynamic nanoscale organizations inside focal adhesions," Nat Cell Biol **14**, 1057–1067 (2012).

267. S. Letschert, A. Göhler, C. Franke, N. Bertleff-Zieschang, E. Memmel, S. Doose, J. Seibel, and M. Sauer, "Super-Resolution Imaging of Plasma Membrane Glycans," Angew. Chemie **126**, 11101–11104 (2014).

268. G. Zhong, J. He, R. Zhou, D. Lorenzo, H. P. Babcock, V. Bennett, and X. Zhuang, "Developmental mechanism of the periodic membrane skeleton in axons.," Elife **3**, e04581 (2014).

269. I. Izeddin, V. Récamier, L. Bosanac, I. I. Cissé, L. Boudarene, C. Dugast-Darzacq, F. Proux, O. Bénichou, R. Voituriez, O. Bensaude, M. Dahan, and X. Darzacq, "Single-molecule tracking in live cells reveals distinct target-search strategies of transcription factors in the nucleus.," Elife **3**, (2014).

270. J. Chen, Z. Zhang, L. Li, B.-C. Chen, A. Revyakin, B. Hajj, W. Legant, M. Dahan, T. Lionnet, E. Betzig, R. Tjian, and Z. Liu, "Single-molecule dynamics of enhanceosome assembly in embryonic stem cells.," Cell **156**, 1274–85 (2014).

271. Z. Liu, W. R. Legant, B.-C. Chen, L. Li, J. B. Grimm, L. D. Lavis, E. Betzig, and R. Tjian, "3D imaging of Sox2 enhancer clusters in embryonic stem cells.," Elife **3**, e04236 (2014).

272. Z. W. Zhao, R. Roy, J. C. M. Gebhardt, D. M. Suter, A. R. Chapman, and X. S. Xie, "Spatial organization of RNA polymerase II inside a mammalian cell nucleus revealed by reflected light-sheet superresolution microscopy.," Proc. Natl. Acad. Sci. U. S. A. **111**, 681–6 (2014).

273. I. I. Cisse, I. Izeddin, S. Z. Causse, L. Boudarene, A. Senecal, L. Muresan, C. Dugast-Darzacq, B. Hajj, M. Dahan, and X. Darzacq, "Real-time dynamics of RNA polymerase II clustering in live human cells.," Science **341**, 664–7 (2013).

274. B. Chen, L. A. Gilbert, B. A. Cimini, J. Schnitzbauer, W. Zhang, G.-W. Li, J. Park, E. H. Blackburn, J. S. Weissman, L. S. Qi, and B. Huang, "Dynamic imaging of genomic loci in living human cells by an optimized CRISPR/Cas system.," Cell **155**, 1479–91 (2013).

275. H. Ma, A. Naseri, P. Reyes-Gutierrez, S. A. Wolfe, S. Zhang, and T. Pederson, "Multicolor CRISPR labeling of chromosomal loci in human cells.," Proc. Natl. Acad. Sci. U. S. A. **112**, 3002–3007 (2015).

276. H. Ma, P. Reyes-Gutierrez, and T. Pederson, "Visualization of repetitive DNA sequences in human chromosomes with transcription activator-like effectors.," Proc. Natl. Acad. Sci. U. S. A. **110**, 21048–53 (2013).

277. Y. Wang, S. Maharana, M. D. Wang, and G. V Shivashankar, "Super-resolution microscopy reveals decondensed chromatin structure at transcription sites.," Sci. Rep. **4**, 4477 (2014).

278. M.-L. Visnapuu and E. C. Greene, "Single-molecule imaging of DNA curtains reveals intrinsic energy landscapes for nucleosome deposition.," Nat. Struct. Mol. Biol. **16**, 1056–62 (2009).

279. S. H. Sternberg, S. Redding, M. Jinek, E. C. Greene, and J. A. Doudna, "DNA interrogation by the CRISPR RNA-guided endonuclease Cas9.," Nature **507**, 62–7 (2014).

280. A. Raj, C. S. Peskin, D. Tranchina, D. Y. Vargas, and S. Tyagi, "Stochastic mRNA synthesis in mammalian cells.," PLoS Biol. **4**, e309 (2006).

281. S. Hocine, P. Raymond, D. Zenklusen, J. A. Chao, and R. H. Singer, "Single-molecule analysis of gene expression using two-color RNA labeling in live yeast.," Nat. Methods **10**, 119–21 (2013).

282. J. M. Halstead, T. Lionnet, J. H. Wilbertz, F. Wippich, A. Ephrussi, R. H. Singer, and J. A. Chao, "An RNA biosensor for imaging the first round of translation from single cells to living animals," Science (80-.). **347**, 1367–1671 (2015).

283. H. Y. Park, H. Lim, Y. J. Yoon, A. Follenzi, C. Nwokafor, M. Lopez-Jones, X.

Meng, and R. H. Singer, "Visualization of dynamics of single endogenous mRNA labeled in live mouse.," Science **343**, 422–4 (2014).

284. E. Lubeck and L. Cai, "Single-cell systems biology by super-resolution imaging and combinatorial labeling," **9**, (2012).

285. E. Lubeck, A. F. Coskun, T. Zhiyentayev, M. Ahmad, and L. Cai, "Single-cell in situ RNA profiling by sequential hybridization.," Nat. Methods **11**, 360–1 (2014).

286. N. Scherf and J. Huisken, "The smart and gentle microscope.," Nat. Biotechnol. **33**, 815–8 (2015).

CHAPTER 2

COMPARISON OF OBJECTIVE LENSES FOR MULTIPHOTON MICROSCOPY IN TURBID SAMPLES[1]

Even after two decades, nonlinear microscopies remain the preferred methods for deep-tissue fluorescence imaging in live animals. Despite their prominence, scattering of excitation and emission photons continue to limit the depth limit to <1 mm, even in mildly scattering tissue such as brain. Although neuroscience has benefited greatly from new tissue-clearing approaches that permit sample clearing and whole-brain connectomics imaging in fixed samples, microscopy in living samples remains an essential strategy for understanding the dynamics of behaviorial responses. This chapter investigates the effects of scattering on two-photon excitation and epifluorescence detection and models their dependence on fundamental objective lens parameters. I also provide guiding principles for lens choice and design of the fluorescence collection pathway.

ABSTRACT

Optimization of illumination and detection optics is pivotal for multiphoton imaging in highly scattering tissue and the objective lens is the central component in both of these pathways. To better understand how basic lens parameters (NA, magnification, field number) affect fluorescence collection and image quality, a two-detector setup was used with a specialized sample cell to separate measurement of

[1] This chapter was previously published as: Singh, A., McMullen, J. D., Doris, E. A., & Zipfel, W. R. (2015). Comparison of objective lenses for multiphoton microscopy in turbid samples. Biomedical optics express, 6(8), 3113-3127.

total excitation from epifluorescence collection. Our data corroborate earlier findings that low-mag lenses can be superior at collecting scattered photons, and we compare a set of commonly used multiphoton objective lenses in terms of their ability to collect scattered fluorescence, providing guidance for the design of multiphoton imaging systems. For example, our measurements of epi-fluorescence beam divergence in the presence of scattering reveal minimal beam broadening, indicating that often-advocated over-sized collection optics are not as advantageous as previously thought. These experiments also provide a framework for choosing objective lenses for multiphoton imaging by relating the results of our measurements to various design parameters of the objectives lenses used.

INTRODUCTION

Over the past 25 years, deep optical sectioning ability has made multiphoton microscopy the method-of-choice for fluorescence-based in vivo imaging [1,2]. Although confocal microscopy has long been able to achieve optical sectioning by using a pinhole to reject out-of-focus fluorescence, this method also rejects in-focus fluorescence that is scattered on its path to the detector. Nonlinear microscopies based on multiphoton absorption and harmonic generation achieve optical sectioning in a fundamentally different way. By employing the nonlinear intensity dependence of two-photon or higher order absorption to create a 3D localized observation volume, these methods are free to collect scattered fluorescence, resulting in increased signal at larger focal depths. For these reasons, multiphoton microscopies may image to depths of ~1mm while confocal microscopy is typically limited to a few hundred μm.

While two-photon excited fluorescence is usually confined to the objective lens focus when the laser power is sufficiently low, the loss of ballistic excitation photons by tissue scattering requires that the excitation intensity be increased to maintain constant signal as the focal plane is moved deeper into tissue. At higher laser powers, substantial out-of-focus background fluorescence may be generated, particularly near the sample surface. As the focal depth increases, the signal-to-background ratio (S/B) diminishes and image quality is degraded [3]. Several groups have used high rep-rate regenerative amplifier systems to redistribute energy into fewer, but much higher energy pulses. Using these systems, imaging depths of up to 1 mm in brain tissue have been achieved [4]. Analytical models indicate that shorter pulses produce a higher S/B ratio in scattering samples and that the effect is particularly strong for durations less than 50 fs [3]. However, since photobleaching and photodamage increase dramatically with excitation dose [5,6], higher energy approaches to increasing the imaging depth have significant drawbacks.

Excitation losses due to tissue scattering are greatly reduced at longer wavelengths. In addition, longer wavelengths allow for the use of redder fluorophores with emissions that are less scattered and absorbed by the sample. As new red dyes and fluorescent proteins become available, as well as ultrafast lasers that operate at wavelengths greater than 1000 nm, this strategy holds the most promise for deeper multiphoton imaging. Imaging depths beyond 1 mm in brain tissue have been demonstrated by moving to two-photon imaging at 1280 nm [7] and three-photon at 1700 nm [8].

While the strategies described above address ways of maintaining sufficient nonlinear excitation deep in tissue, optimizing signal collection is equally important. Two-photon microscopes typically employ whole-field non-descanned detection rather than a confocal pinhole approach since fluorescence photons originating from the focal volume are too precious to reject, regardless of whether they have been scattered. The collection efficiency of the microscope objective and the optical path to the detector is a key factor that determines the signal-to-noise ratio. Epifluorescence collection through the objective lens can be supplemented by a detector below the specimen to collect transmitted fluorescence, but this is not practical when dealing with thick specimens or live animals. While the fraction of ballistic photons detected is primarily determined by the objective numerical aperture (NA) and transmittance, scattered light collection is affected by additional parameters such as field-of-view (FOV) [9,10]. In highly scattering specimens, light collection depends on both the spatial and angular distribution of photons incident on the objective front aperture (OFA) [11].

Over the past decade microscope manufacturers have produced new dipping objectives optimized for MPM and in vivo imaging, the first being the Olympus XLUMPlanFl 20x/0.95 water immersion objective, which became a preferred MPM objective lens due to its high NA, large field-of-view (low magnification) and improved collection of scattered fluorescence. More recently, Olympus and other vendors have manufactured lenses that are even more promising for deep-tissue multiphoton microscopy. In this study, we compare some of these newer dipping objectives to the older generation and experimentally verify theoretical predictions

about multiphoton excitation and epifluorescence collection in turbid samples. Given the relatively high cost of the new optics, our comparisons are useful for assessing the value of currently available multiphoton objectives for use in scattering specimen.

THEORY

In a typical multiphoton microscope, scanning mirrors steer a collimated beam from a mode-locked laser to the objective back aperture (OBA) and the objective lens focuses this light down to a small diffraction-limited volume in its focal plane. If illumination enters the OBA parallel to the optic axis, the focus is located along the same axis at a distance *wd* (the working distance of the objective) from the objective front aperture (OFA) or front lens. When scanning, the beam enters the OBA at an angle (θ_f) and the focal spot is displaced laterally in the focal plane up to a distance r_f, which defines the objective's field-of-view radius for the given laser-scanning design. For beam delivery angles greater than the corresponding θ_f, illumination is not transmitted through the lens. Ideally, MPM objectives have high transmittance in both the visible and near-IR (with typical excitation wavelengths from Ti:Sapphire oscillators being in the 700-1000 nm range, and newer femtosecond lasers now tuning to 1300 nm or higher).

Two-photon fluorescence losses due to scattering of excitation.

As illumination photons propagate toward the objective focus, they can undergo scattering and absorption processes related to the optical properties and geometry of the sample. Since the precise distribution of refractive index

inhomogeneities is generally unknown, tissue scattering is often modeled using a few parameters that summarize the average behavior of the sample [9–11]. The scattering mean free path ℓ_s indicates the average distance traveled before a scattering event and increases with wavelength in accordance with Mie theory; for this reason, near-IR illumination photons undergo roughly half as much scattering as visible light photons. The degree of randomization of photon direction by scattering processes is embodied by the scattering anisotropy factor $g = \langle \cos\theta \rangle$. It is also conventional to define a transport mean free path $l_t = l_s /(1 - g)$ which characterizes the average length over which a photon maintains its direction of propagation. In addition to scattering, photons may be absorbed by either intrinsic molecules or exogenous labels. Typically, intrinsic one-photon absorption cross-sections are fairly small at NIR illumination wavelengths, but non-negligible for fluorescence emission. Although two-photon absorption is usually confined to the focal volume at low illumination levels, imaging in scattering media necessitates higher powers that yield out-of-focus excitation both at the specimen surface, where ballistic intensity is high, and in the space between the surface and perifocal region, where scattered photons can interact with ballistic ones [3]. The amount of background generated depends on the staining inhomogeneity and can be greatly reduced by using specific labels that localize only to structures of interest. Several reviews include comprehensive summaries of scattering and absorption parameters in various types of tissue [12,13]. Typical values for mouse cortex at a $\lambda = 500$ nm are $l_s = 100$ μm and $g = 0.9$, while skin, for example, can be considerably more turbid with values on the order of $l_s = 40$ μm and $g = 0.75$ [13].

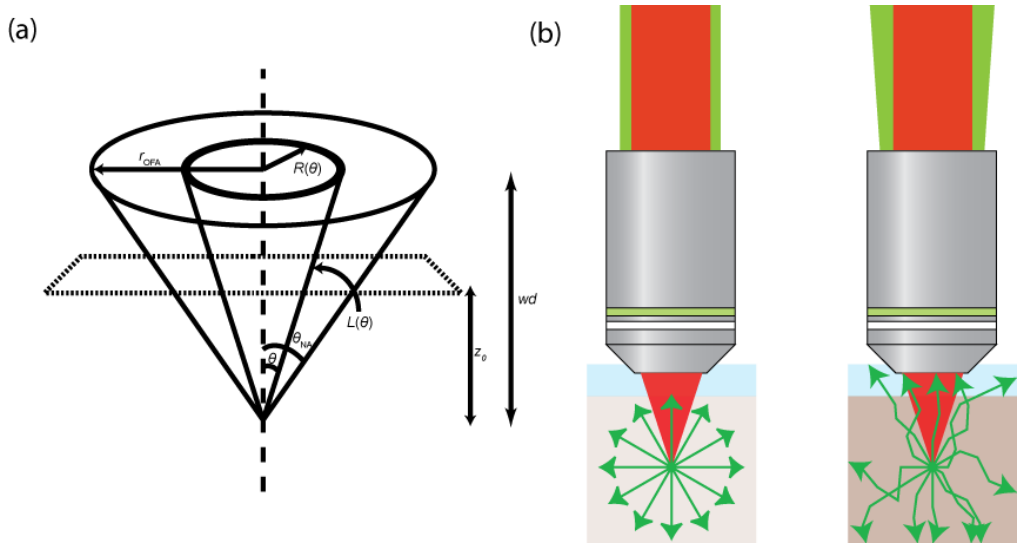

Figure 2.1. Scattered light collection in two-photon microscopy. (a) Diagram of illumination photons propagating from the Objective Front Aperture (OFA) to the objective focus. The flux through a ring of radius $R(\theta)$ at the OFA propagates a total distance of $wd / \cos\theta$, of which $L(\theta) = z_0 / \cos\theta$ is below the specimen surface, where θ ranges from 0 to θ_{NA}. (b) Schematic of the fluorescence beam exiting the Objective Back Aperture (OBA), showing a relatively collimated beam when imaging in a clear specimen and a more divergent beam when imaging in turbid samples.

When imaging at depths much less than one scattering length of the excitation wavelength, sufficient ballistic photons reach the objective focus that the illumination intensity can be kept relatively low. In these scenarios, out-of-focus two-photon absorption is negligible and excitation is confined to a small ~Gaussian ellipsoid volume with 1/e radii of $\omega_{x,y}$ and ω_z in the lateral and axial directions, respectively [2]. The rate of in-focus fluorescence emission is given by:

$$F = \tfrac{1}{2}\phi_F \sigma_{2P} \int C(\mathbf{r}) < I^2(\mathbf{r},t) > d\mathbf{r} \quad =$$

$$C_{avg} \frac{\sigma^*_{2P} g_p}{R\tau} \frac{\left(\frac{P\lambda}{hc}\right)^2}{\left(\iint_{area} PSF(x,y,0,NA,\lambda)dxdy\right)^2} \left(\iiint_{volume} PSF(x,y,z,NA,\lambda)^2 dxdydz\right) \quad \text{(eq. 1)}$$

In the generalized form for the generation of two photon fluorescence (first equation above), $C(\mathbf{r})$ is the position-dependent fluorophore concentration, σ_{2P} is the two-photon absorption cross-section, ϕ_F is the fluorescence quantum yield, and $\langle I^2(\mathbf{r},t)\rangle$ the time-averaged instantaneous intensity squared. The integral is over the bounds of the 3D focal volume, which converges due to the quadratic dependence on intensity, and is well-approximated as a 3D Gaussian volume. $\langle I^2(\mathbf{r},t)\rangle$ can be shown to be equal to $g_p\langle I\rangle^2/R\tau$ where $\langle I\rangle$ is the time-averaged intensity, R the laser repetition rate, τ is the pulse duration and g_P is a dimensionless factor that depends on the pulse shape (typically ~0.6). The second expression above is a working formulation that is more closely related to measurable system parameters. $P\lambda/hc$ is the average power passing through the z = 0 plane converted to photons per second, which is normalized by the area of the PSF at z = 0. $PSF(x,y,z)^2$ is the volume defined by the squared point spread function (i.e. the two photon PSF) and C_{ave} is the average concentration of fluorophore. A 3D Gaussian volume estimate of $PSF(x,y,z)^2$ is readily calculable based on NA and refractive index using the equations given in [2].

When imaging deeper into scattering specimen, scattered illumination photons may miss the objective focus and fail to be recorded as in-focus fluorescence. In order to maintain signal, the laser intensity must be increased to compensate for lost ballistic photons. An approximation of the fraction of ballistic photons lost as a function of NA and scattering length can be derived by assuming a uniform intensity distribution across the objective front aperture and calculating the ratio (γ) of the irradiance that reaches the focus in the scattering and non-scattering cases:

$$\gamma = \frac{2\pi \int_0^{r_{OFA}} R(\theta) I_0 e^{-\frac{L(\theta)}{l_s(\lambda_{exc})}} dR}{2\pi \int_0^{r_{OFA}} R(\theta) I_0 dR} \qquad \text{(eq. 2)}$$

Here, $2\pi R I_0 dR$ represents the photon flux through an infinitesimal ring located at a radius R on the OFA (Figure 2.1a). The exponential term in the numerator represents the fraction of these photons that remain ballistic during propagation to the focus. L is the path length for these ballistic photons within the scattering medium and $l_s(\lambda_{exc})$ is the mean free path between scattering events at the excitation wavelength. We can rewrite the above integral in terms of θ using $L(\theta) = z_0/(\cos\theta)$ and $R(\theta) = z_0 \tan\theta$, where z_0 is the depth of the focus below the specimen surface and θ is the angle between the optical axis and line segment connecting the ring at radius R with the focal point. Solving the ratio of the two integrals integrated from θ = 0 to θ_{NA} (i.e. arcsin (NA/n)) yields:

$$\gamma = \frac{\int_0^{\theta_{NA}} \tan\theta \sec^2\theta \, e^{-\frac{z_0}{l_s(\lambda_{exc})\cos\theta}} d\theta}{\int_0^{\theta_{NA}} \tan\theta \sec^2\theta \, d\theta} = \frac{2}{\tan^2(\theta_{NA})}\left[\left(1+\frac{z_0}{l_s(\lambda_{exc})\cos(\theta_{NA})}\right)e^{\frac{-z_0}{l_s(\lambda_{exc})\cos(\theta_{NA})}} - \left(1+\frac{z_0}{l_s(\lambda_{exc})}\right)e^{\frac{-z_0}{l_s(\lambda_{exc})}}\right] \quad \text{(eq.3)}$$

For a given z_0 and $l_s(\lambda_{exc})$, γ decreases with increasing NA because peripheral photons travel longer paths to the focus and thus have a higher probability of scattering. This equation quantifies the known reduction of effective NA in an absorbing-scattering sample [4], which increases significantly at higher NAs. Using the above derived parameter γ, we can modify our two-photon fluorescence relation to take the excitation scattering losses into account:

$$F = C_{avg} \frac{\sigma_{2P}^{*} g_p}{R\tau} \frac{\left(\frac{\gamma P \lambda}{hc}\right)^2}{\left(\iint_{area} PSF(x,y,0,NA,\lambda)dxdy\right)^2} \left(\iiint_{volume} PSF(x,y,z,NA,\lambda)^2 dxdydz\right) \quad \text{(eq.4)}$$

Two photon fluorescence losses due to emission collection.

Epifluorescence collection through the objective lens is also best understood by considering the non-scattering and scattering scenarios separately. In each case, a fraction of the light is captured by the OFA. If the sample is non-scattering, this fraction is equal to the fractional solid angle collected by the objective NA:

$$\Omega_f\left(NA,n\right) = \frac{1-\sqrt{1-\left(NA/n\right)^2}}{2} \qquad \text{(eq.5)}$$

The transmission of fluorescence photons back through the objective lens depends upon the transmittance of the lens, as well as the optical design (lens elements, positions of apertures and baffles, etc.). The emission beam exiting the OBA is typically picked off by a dichroic mirror and directed to collection optics that guide photons to a photodetector. If the specimen scatters fluorescence from a point emitter located at the objective focus, we have to consider the various photon trajectories to evaluate the fraction of light collected by the objective lens. Trajectories are generally grouped into three classes: ballistic, snake-like and diffuse. The ballistic fraction decays exponentially with focal depth and is negligible when the depth is much greater than $l_s(\lambda_{em})$. Snake-like trajectories undergo a few scattering events but still maintain some memory of their original direction. Meanwhile, diffuse photons have scattered so many times that their directions are essentially randomized. Snake-like trajectories

are dominant when the focal depth is small compared to the transport mean length $l_t(\lambda_{em})$, while the range $z_0 >> l_t(\lambda_{em})$ is referred to as the diffuse limit. Although analytical equations for the collected fraction are difficult to obtain, Monte Carlo simulations have been used to estimate the spatial and angular distributions of photons at the specimen surface for various sets of scattering parameters [3,9]. In the diffuse limit, photons at the specimen surface fall into a distribution that has a lateral FWHM of 1.53 z_0, irrespective of the scattering mean free path, and a Lambertian angular distribution [11]. In order to collect as many photons as possible, objective lenses with a large spatioangular acceptance range are preferred, i.e. lenses with a large field of view and numerical aperture. In addition, the increase in skew rays incident on the OFA is thought to result in a divergent beam exiting the OBA (Figure 2.1b), and many groups advocate large post-objective lens collection optics so that the emission beam does not suffer vignetting [9]. One goal of this work was to measure the emission beam divergence under realistic scattering conditions to determine how to best optimize the collection pathway.

METHODS AND RESULTS

Objective lenses for multiphoton microscopy.

As mentioned earlier, the Olympus XLUMPlanFl 20x/0.95W (now 20x/1.0W) ∞/0 objective is the lens-of-choice for many multiphoton imaging applications. Olympus also released the first lens specifically designed and optimized for multiphoton microscopy: the XLPlan N 25x/1.05 W MP ∞/0-0.23/FN18. This objective combines a high NA with high transmittance through the visible and IR to improve light collection. In addition, it has a correction collar that can be used to

minimize spherical aberration. Olympus also offers the XLUMPlanFl 10x/0.60 W, which provides a larger field-of-view. Zeiss and other vendors provide similar high-NA objectives with improved NIR coatings; for example, the Zeiss Plan-Apochromat 20x/1.0 Vis-IR ∞/0 objective is also an excellent choice for multiphoton use. For comparison, we also examined an older high-magnification objective that has been commonly used for multiphoton imaging, the Olympus LUMPlanFl 60x/0.90 W ∞/0. Key properties of these objectives are summarized in Table 1.

New optical coatings provide greater transmission in the IR than older lenses. Objective lens transmittance was measured using illumination from a white light source directed through a 150 μm diameter pinhole to create a light source much smaller than the OFA. The objective was mounted in the entrance port of an integrating sphere and output was connected to a spectrometer (Ocean Optics QE 65000) via an optical fiber to record spectra with and without the objective in place (Figure 2.2a). As expected, the newer objectives have substantially improved transmission through the visible and IR, particularly in comparison to the older Olympus 20x lens (Figure 2.2b). Our values matched manufacturer data within ~5-10%.

T**able 2.1: Summary of objective lens properties.**

Objective	***Abbrev.***	***NA*** θ_{NA}	***WD (mm)***	***FN (mm)***	***OBA (mm)***	***OFA (mm)***	***OBA / OFA***	***%T(800nm) %T(521nm)***
Olympus XLUMPlanFl 10x/0.60 W ∞/0	Oly. 10x	0.60 26.8°	3	28	21.6	3.0	7.1	75.4% 81.9%
Olympus LUMPlanFl 60x/0.90 W ∞/0 IR	Oly. 60x	0.90 42.6°	2	26.5	5.4	3.7	1.5	75.4% 83.4%
Olympus XLUMPlanFl 20x/0.95 W ∞/0	Oly. 20x	0.95 45.6°	2	22	17.1	4.0	4.2	62.5% 72.9%
Zeiss W Plan-Apochromat 20x/1.0 DIC Vis-IR ∞/0	Zeiss 20x	1.00 48.8°	2.4	20	16.5	5.5	3.0	81.3% 84.8%
Olympus XLPlan N 25x/1.05 W MP ∞/0-0.23/FN18	Oly. 25x	1.05 52.1°	2	18	15.1	5.1	2.9	86.1% 86.7%

Objective Back Aperture (OBA) and Objective Front Aperture (OFA) diameters were calculated as:

$$OBA = \frac{2NA\, f_{design\ tube\ length}}{Mag} \quad and \quad OFA = \frac{2wd\, NA}{n\sqrt{1-\left(NA/n\right)^2}}$$

Other abbreviations: *wd* = working distance; FN = field number; %T = transmittance

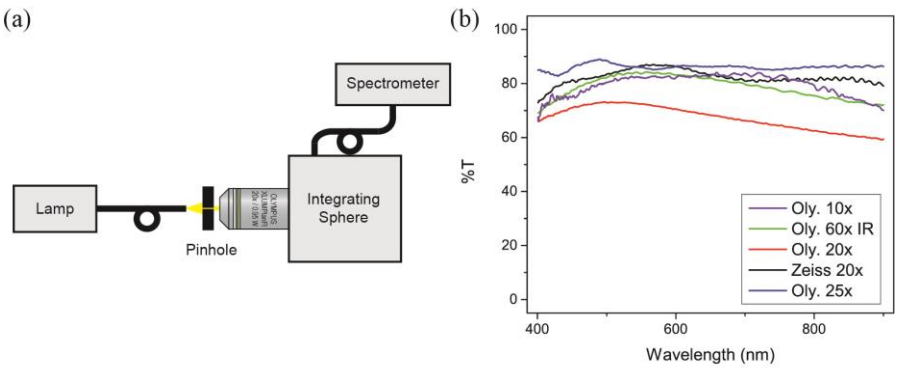

Figure 2.2. Measurement of objective lens transmittance using a broadband source. (a) Experimental apparatus used to measure lens transmittance. A small pinhole was used to create a thin "beam" of white light which was incident on the OFA of an objective lens. Light transmitted through the objective was collected by an integrating sphere and relayed to a spectrometer using an optical fiber. (b) Transmittance curves were generated by taking a ratio of the spectrometer counts at each wavelength when the objective was in place and removed from the apparatus. Newer lenses show substantially better transmission than the earliest version of the Olympus 20x/0.95W we used in these measurements.

MPE in turbid media

During *in vivo* multiphoton imaging, tissue scattering diminishes the number of ballistic excitation photons that reach the objective focus and creates a spread in the fluorescence distribution at the sample surface, reducing the objective's ability to collect emitted photons. To study these phenomena, we built a two-channel measurement chamber for photon-counting of both the transmitted and epi-detected fluorescence signals (Figure 2.3a). Mode-locked illumination at 800 nm (Spectra Physics Mai Tai) was intensity controlled using a Pockels cell and coupled through a beam expander to overfill the back aperture of each objective. Focused light was incident on a fluorophore-scatterer sample cell consisting of a layer of 100 μM

fluorescein (λ_{em} = 520 nm) below a layer of immersion medium. The layers were separated by a thin (~40 micron) plastic sheet of fluorinated ethylene propylene which has a refractive index similar to water (FEP, Welch Fluorocarbons, n = 1.338). Scattering properties of the immersion medium were set by controlling the concentration of 1 μm polystyrene microspheres (Polysciences). Scattering parameters were calculated using the online Mie scattering calculator (http://omlc.org/calc/mie_calc.html).

A measurement using two detection channels as described above provides a means to measure the epifluorescence collection efficiency of an objective lens under various scattering conditions. The ratio of the epi-signal to the transmitted signal is proportional to the fraction of fluorescence passing through the objective lens, since photons detected in the transmitted channel experience no scattering. A confocal pinhole was used in the transmission path to ensure that any fluorescence backscattered by the turbid layer was not collected by the transmission detector. The lower channel serves as a constant collection pathway that provides a measure of the total fluorescence generated at the focus. The fluorescence collected back through the objective lens was reflected by a 50 mm diameter dichroic mirror through a focusing lens onto a photomultiplier tube. The dichroic was 50 mm from the OBA for all objective lenses. A 50 mm adjustable iris was placed before a large area (30 mm photocathode) PMT, and was adjusted to controllably vignette the beam in order to measure the fluorescence beam divergence. The distance from the iris to the OBA was 100 mm. The output of the two PMTs were collected using a two-channel photon counter (SR400, Stanford Research Systems) and laser intensity was controlled to

keep the total counts in either channel less than ~8 x 10^5 s^{-1} to avoid pulse pileup. A micrometer stage was used to position our sample cell so that the objective focus was always at a depth of 50 μm within the fluorescein layer. By varying the laser power and recording counts in the lower (transmission) channel, P^2 curves were generated using water and various concentrations of polystyrene microspheres as the immersion media.

In these experiments we characterized the amount of scattering as a dimensionless parameter z_s, defined as the ratio of the imaging depth through the scattering solution (*wd* – 50 μm denoted as z_o) and l_s, the mean free path. Therefore z_s is the number of scattering mean free paths between the OFA and the focal plane. z_s' denotes the ratio in which the transport mean free path ($l_s /(1 - g)$) is used in place of l_s for certain calculations.

We note that there are some differences between our experimental geometry and an actual *in vivo* two-photon microscopy imaging scenario, in which the focus might be 0.8 mm into the sample with 1.2 mm of water between the OFA and sample surface. In our arrangement, there is no non-scattering, transparent layer of immersion medium directly after the OFA, but rather a continuous layer of non-fluorescent scattering beads. The separation of fluorophore and scattering microspheres into distinct layers was necessary so that the transmission channel could serve as a reference unaffected by the scattering properties of the sample, and in this way separate the measurement of multiphoton excitation from fluorescence detection. During a deep-tissue multiphoton imaging session in a typical sample, one also might expect some surface-level background [3], but our sample geometry precludes this

effect since no fluorophores are present within the scattering layer. The setup we employ allows us to understand specifically how scattering affects in-focus fluorescence and to study excitation in turbid samples without the complication of out-of-focus surface fluorescence. Finally, others have reported that fluorescence photons whose trajectories are initially directed away from the OFA (i.e. downward) have some finite probability of being back-scattered into the acceptance range of the objective [9]. Although a minor effect, the lack of scattering particles below the focal plane in our experimental setup means that we do not observe this phenomenon.

To measure the fractional loss of ballistic nonlinear excitation photons, the number of counts detected in the transmission channel was plotted against power delivered through the objective lens and fit to the equation $F_{trans} = \eta\gamma^2 P^2$ where η is the fraction of emission collected by the lower channel times the excitation related parameters (eq. 4), and P is the laser power out of the objective lens. η is independent of the sample scattering properties and a constant for each objective lens. η can be obtained from the P^2 curve collected in the absence of scattering (γ^2=1). The transmission path P^2 curves also showed that the Olympus 10x/0.6 NA lens generated fluorescence more efficiently than the other lenses (Figure 2.3b), demonstrating that the dogma that two-photon fluorescence is independent of NA (for example, ref [14]) is not quite true. Assuming a uniform fluorophore concentration, the two-photon excitation potential from the focal volume as a function of numerical aperture is proportional to (see equation 1):

$$\text{Focal volume 2P excitation potential} \propto \frac{\iiint_{volume} PSF(x,y,z,NA,\lambda)^2 dxdydz}{\left(\iint_{area} PSF(x,y,0,NA,\lambda)dxdy\right)^2} \qquad \text{(eq. 6)}$$

For a diffraction limited focus at high NA, the PSF is sufficiently complex and the conventional NA^{-1} and NA^{-2} formulas for radial and axial widths fail as approximations. The rate of two-photon excitation is not independent of NA and is less than one would expect based on paraxial approximations. In addition to the empirical measurements presented here, the NA dependence of nonlinear excitation is evident by applying more accurate approximations for intensity PSF dimensions at high NA [2,15], or by numerical integration of equation 6. The relatively large difference we found in the amount of 2P fluorescence generated between NA's of 0.6 and ~1.0 led us to detailed calculations in order to better understand our measured result. Using the method of Richards and Wolf [16], we calculated the two photon excitation potential (eq. 6) as a function of numerical aperture at different ratios of aperture diameter to 1/e beam diameter (a parameter we call β). As the paraxial limit is approached ($\beta \rightarrow \infty$), the rate of two photon excitation becomes independent of NA as expected (Figure 2.3c). However, for the diffraction limited case ($\beta = 0$), the non-linear excitation potential decreases with higher NA, reflecting our experimental observation that the focus of the 0.6 NA objective lens produced more fluorescence than the other four objectives used which have numerical apertures between 0.9 and 1.05. The inset graph in Figure 2.3c illustrates the net effect of decreasing 2P excitation as NA increases, coupled the expected NA-dependent increase in fluorescence collection (i.e. the product of the fractional solid angle (eq. 5) and the 2P

excitation potential (eq. 6)). In the diffraction-limited case, the net difference in collected two-photon generated epifluorescence as a function of NA is not as large as one might expect based on paraxial optical approximations.

The data shown in Figure 2.3b provides a means to extract γ^2 (defined in eq. 3) from P^2 curves measured at various levels of scattering. Since 1 μm beads mostly scatter in the forward direction (g = 0.93, similar to tissue), we expect that γ^2 would fall somewhere between calculations made using scattering mean free path (ℓ_s) and those made using the reduced or transport mean free path ($\ell_s /(1 - g)$), which represents the upper and lower limits expected for two-photon excitation loss due to scattering of the excitation beam. This allows us to estimate the degree to which slightly forward scattered photons can still generate two-photon fluorescence. We found that γ^2 lies much closer to calculations made using the non-reduced mean free path (ℓ_s, dotted line in Figure 2.3d), indicating that even small angular deviations in photon path have a significant effect on the nonlinear excitation potential. In actual samples, the reality is probably even closer to the non-reduced case, since a pool of dye gives scattered photons the highest opportunity to generate background fluorescence.

Epifluorescence collection from turbid media

In a non-scattering sample that is refractive index matched to the particular objective lens (1.33 for water, in our case), an objective lens collects a solid angle fraction (Ω_f) of the total fluorescence emitted at its focus (eq. 5). The collection efficiency is further influenced by the transmittance of the lens at the emission wavelength (Figure 2.2b), and the net collection is the product of fractional solid angle

times the lens transmission. Sample turbidity further influences the amount of light collected by the lens, as well as the divergence of the light delivered to the detector due to generation of skew rays from the scattering process. Using our objective lens testing setup, we measured the epi-collection efficiency and the divergence of the fluorescence beam exiting the objective lens as a function of sample scattering for five objective lenses commonly used in multiphoton microscopy. Figure 2.4a shows the ratio of epi-counts to transmitted (non-scattered) counts; Figure 2.4b normalizes these data for each lens by dividing by its collection efficiency in water. The reported quantity is a direct measure of the epi-collection efficiency of each objective under scattering conditions which is independent from scattering caused excitation losses. These values (uncorrected for differences in transmission) increase with NA more or less as expected based on their solid angle of collection. By fitting the decay of epi-signal as a function of the scattering parameter z_s, we obtained decay lengths that could be correlated with objective lens parameters such as the ratio of the objective back and front aperture diameters (OBA/OFA – Figure 2.4c) and the field number (Figure 2.4d). Although efficient epi-collection of scattered signal by objectives has been correlated with increasing field number (FN) of the objective [9], we found only a weak correlation. However, our data shows a much stronger correlation between the OBA/OFA ratio. This ratio can be expressed in terms of basic objective lens parameters (equation 7) to show the relationship between resolution (NA), field of view (Magnification) and working distance, with epi-collection efficiency in turbid samples. Depending on the particular multiphoton imaging scenario and objective

lenses available, these parameters can be selected based on the required resolution, imaging depth and field of view in order to achieve optimal performance.

$$\frac{OBA}{OFA} = \frac{2NA\, f_{obj}}{2\, wd \tan(\theta_{NA})} = \frac{f_{ref\ tube\ lens}\ n\sqrt{1-\left(\frac{NA}{n}\right)^2}}{Mag \times wd} \quad \text{(eq.7)}$$

Previous measurements with an infinite-plane diffuse light source indicated that there may be a substantial angular spread in the beam exiting the OBA [9] and based on this, many advocate the use of large (50 mm or larger) collection optics positioned close to the OBA. However, this can be difficult in implement within the confines of a microscope body, and further knowledge of the beam divergence in more realistic scenarios (below the diffuse limit) is useful to design optimal MPM systems. To this end, we used a calibrated iris to vignette the beam and calculate the emission beam divergence as a function of z_s. Assuming a Gaussian beam exiting the OBA, we expect the fraction of the emission beam clipped at iris radius r to be given by $1-\exp(-2r^2/\sigma^2)$, to which we fit our data to obtain the $1/e^2$ radius σ. Figure 2.4e shows these measurements for the five objective lenses we tested. In a non-scattering sample, σ measured at 100 mm from the OBA was slightly less than the radius of the OBA, in accordance with our expectation of a parallel emission beam. One exception was the Olympus 60x/0.9 objective which had a slight divergence in our setup even without scattering. The $1/e^2$ radius σ increases with z_s and approaches a limiting value for each objective. The amount of emission beam divergence in the presence of scattering decreased with increasing OBA/OFA (Figure 2.4f) and increasing field number (Figure 2.4g), further indicating that large OBA/OFA and field numbers are beneficial for imaging in scattering samples. We note however, that in our experimental

measurements based on a real 2P excitation volume located below a scattering layer, we never found divergence on the order of what has been previously reported (> 10 degrees) which was based on observation of white light from full-field uniformly diffusing surface [9] or from Monte Carlo simulations of scattered light passing through a 20x/0.95 Olympus objective lens model [17]. Even at $z_s = 5$, which would represent a highly scattering sample (equivalent, for example, to imaging ~500 μm deep into mouse brain), the change in divergence was typically less than two degrees. Based on these measurements, we believe need for extremely large optics in the post-objective lens collection path is unwarranted. As the schematic in Figure 2.4h illustrates, even at high scattering, 25 to 30 mm aperture optics are sufficient. Most high angle skew rays entering the objective are simply lost in the barrel of the lens and never pass through the OBA.

Finally, we examined the combined effects of scattering on illumination and fluorescence collection by measuring the power needed to achieve a given number of counts in solutions with increasing z_s (Figure 2.5a). At low scattering (z_s <3), the various objective lenses performed approximately the same, while at higher scattering (z_s >4), the Olympus 10x/0.6 lens showed a significant difference in this test, presumably due to its more efficient nonlinear excitation and larger field of view.

To assess the various objective lenses in an imaging scenario, a low concentration of fluorescent microspheres was embedded in an agarose gel. The objective was focused 50 μm below the agarose surface and data was recorded using water and calibrated concentrations of polystyrene microspheres in the immersion media. The laser intensity was kept constant for each objective and set so that the bead

Figure 2.3. Two-photon excitation in turbid media (a) Experimental setup for two-channel detection of epi-collected and transmitted fluorescence. Laser illumination was focused through a scattering medium into a solution of fluorescein. Emissions were collected in both epifluorescence and transmission channels. A confocal pinhole in the lower path was used to reject any back-scattered light from the bead layer. An iris in the upper channel was adjusted to controllably vignette the beam in order to measure the emission beam divergence. (b) Plot of fluorescence detected in the transmitted light channel as a function of power out of the objective lens without added scatterer. All data (with and without scatterer) fit well to $F = aP^2$, where $a = \eta\gamma^2$. η is the fraction of emission collected by the lower channel times excitation-related parameters (eq. 4) and γ is the fraction of ballistic photons lost (squared for two-photon excitation). For the data in 3b without added scatterer, $\gamma = 1$. (c) Calculated two-photon excitation potential within the focal volume as a function of NA for diffraction limited and under-filled back apertures demonstrating the NA-dependence of nonlinear excitation for a diffraction limited focal volume. The intensity PSF was calculated using the method of Richards and Wolf [16] modified to take OBA under-filling into account. The 3D intensity PSF was then squared, integrated and divided by the focal plane beam area (eq. 6). Data is normalized to the diffraction-limited ($\beta = 0$) case for lowest NA used in the calculation (0.25). $\beta = 3$ approaches the expected paraxial limit under which the two-photon excitation is independent of NA. Inset: Predicted relative net epifluorescence collection for the diffraction-limited (black line) and paraxial (blue line) cases, calculated as the fractional solid angle x two-photon excitation potential as a function of NA. (d) Comparison of experimental values for the ballistic fraction of illumination squared (γ^2) for two different values of z_s and z_s' to the theory presented in equation 3. Black lines and symbols (X's) are calculations and measurements, respectively, made with scattering conditions of $z_s = 1.6$ (dotted line) and $z_s' = 0.16$ ($g = 0.9$, solid line) at 800 nm. Blue lines and symbols are for scattering conditions of $z_s = 2.7$ (dotted line) and $z_s' = 0.27$ (solid line) at 800 nm.

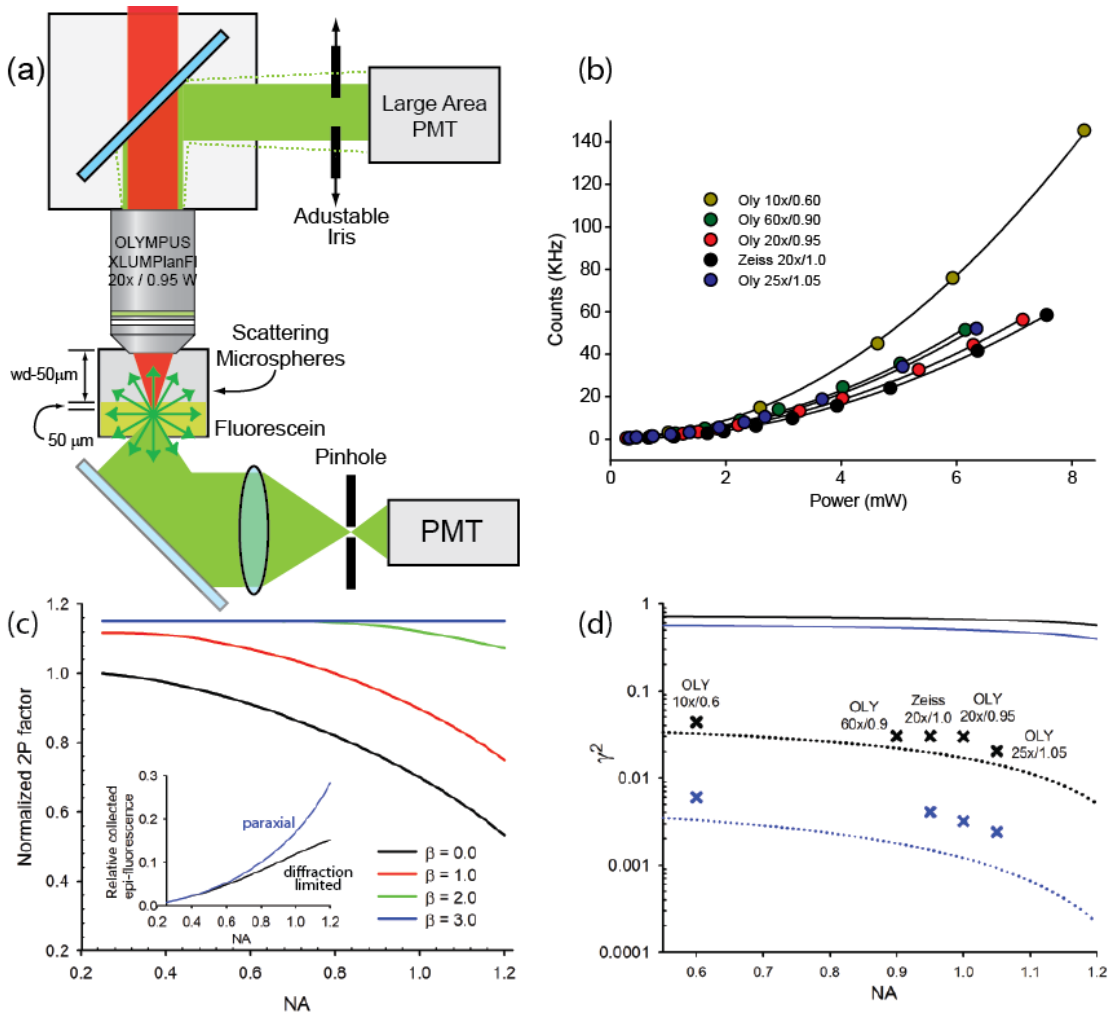
(a)
Large Area PMT
Adustable Iris
OLYMPUS XLUMPlanFI 20x / 0.95 W
Scattering Microspheres
wd-50µm
50 µm
Fluorescein
Pinhole
PMT
(b)
Counts (KHz)
Power (mW)
Oly 10x/0.60
Oly 60x/0.90
Oly 20x/0.95
Zeiss 20x/1.0
Oly 25x/1.05
(c)
Normalized 2P factor
NA
Relative collected epi-fluorescence
paraxial
diffraction limited
β = 0.0
β = 1.0
β = 2.0
β = 3.0
(d)
γ^2
NA
OLY 10x/0.6
OLY 60x/0.9
Zeiss 20x/1.0
OLY 20x/0.95
OLY 25x/1.05

Figure 2.4. Epifluorescence collection characteristics in scattering media. (a) Ratios of counts in the epifluorescence channel to counts in the transmission channel for each lens at $z_s = 0$ (water), 3 and 5, showing the decrease in epi-collection efficiencies as a function of sample scattering. (b) Normalized ratios (relative to $z_s = 0$ value for each lens) with data taken over a larger number of z_s values. Error bars are SEM (n=4). (c and d) Correlation between the scattering dependent epi-collected signal decay with objective lens OBA/OFA ratios (c) and objective field number (d). Signal decay lengths for each objective lens were obtained from fits of the data in (b) to a single exponential decay model: $y0 + \exp(-(z_s-z_{s,0})/\varepsilon)$ to parametrize the scattering loses through each lens. Each lens is colored coded as indicated by the key in (b). (e) Measured epi-collected fluorescence emission beam $1/e^2$ radius 100 mm from the OBA as a function of solution scattering ($z_s = 0$, 3, and 5) and objective lens. The corresponding angular divergence values are noted at top of each bar. (f and g) Correlation between the measured emission divergence angle and the OBA/OFA ratio (f) and field number (g). (h) Diagram illustrating the effect of the divergence for each lens measured at $z_s = 5$ (worst case scenario) 200 mm from the OBA (where a detector might typically be placed).

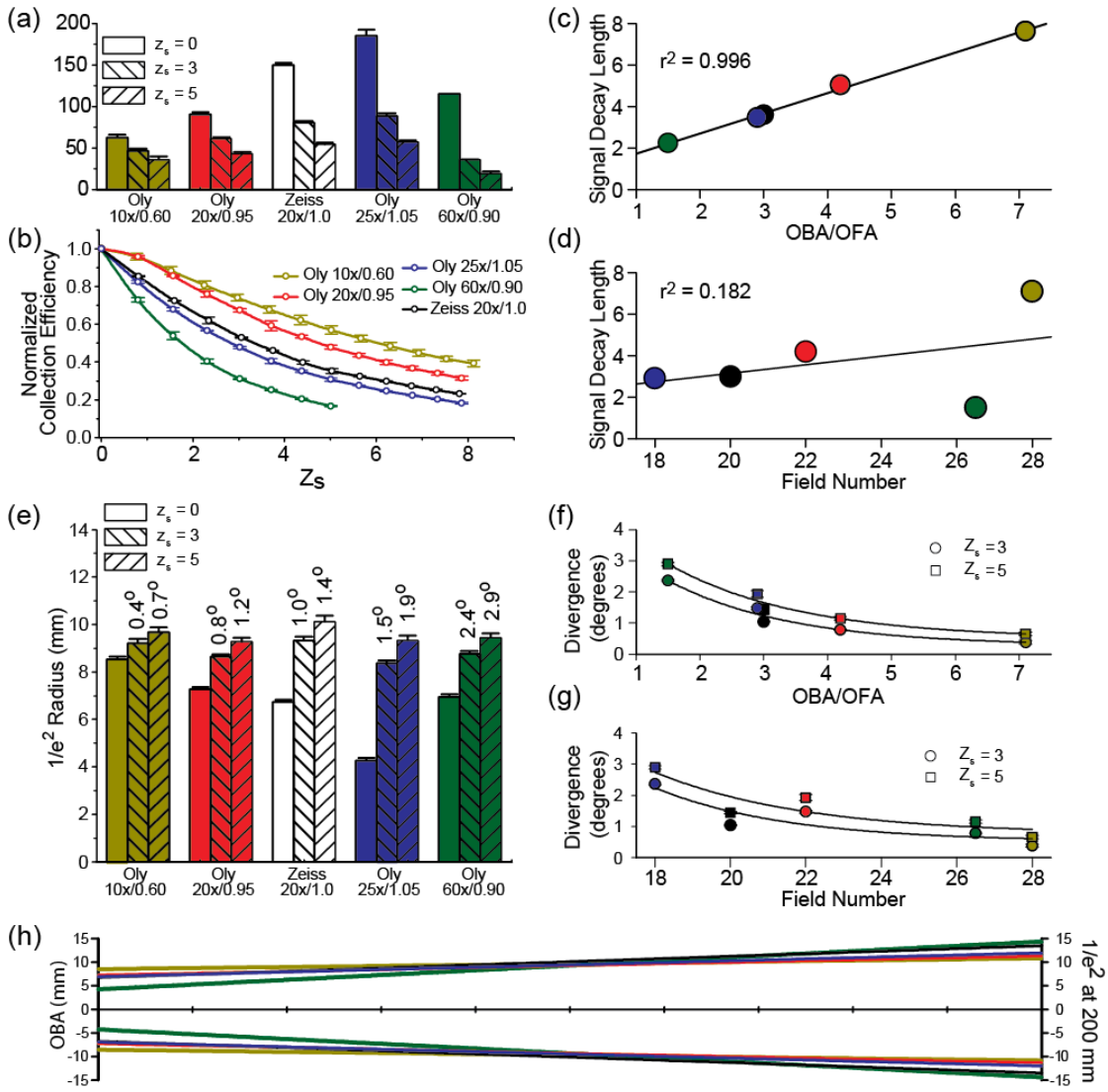
(a)
200
150
100
50
0
z_s = 0
z_s = 3
z_s = 5
Oly 10x/0.60
Oly 20x/0.95
Zeiss 20x/1.0
Oly 25x/1.05
Oly 60x/0.90
(b)
Normalized Collection Efficiency
1.0
0.8
0.6
0.4
0.2
0.0
0
2
4
6
8
Zs
Oly 10x/0.60
Oly 20x/0.95
Oly 25x/1.05
Oly 60x/0.90
Zeiss 20x/1.0
(c)
Signal Decay Length
r^2 = 0.996
OBA/OFA
(d)
Signal Decay Length
r^2 = 0.182
Field Number
(e)
z_s = 0
z_s = 3
z_s = 5
1/e^2 Radius (mm)
0.4°
0.7°
0.8°
1.2°
1.0°
1.4°
1.5°
1.9°
2.4°
2.9°
Oly 10x/0.60
Oly 20x/0.95
Zeiss 20x/1.0
Oly 25x/1.05
Oly 60x/0.90
(f)
Divergence (degrees)
Z_s = 3
Z_s = 5
OBA/OFA
(g)
Divergence (degrees)
Z_s = 3
Z_s = 5
Field Number
(h)
OBA (mm)
1/e^2 at 200 mm

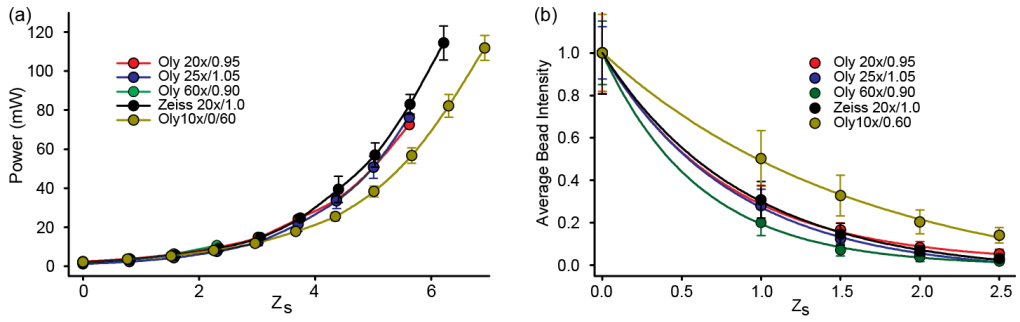

Figure 2.5 Objective lens performance in scattering media. (a) Excitation power needed to achieve 500,000 counts/second in the epifluorescence channel as a function of z_s. (b) Drop-off in integrated bead intensity (n = 3) when imaging fluorescent beads embedded in agarose with added polystyrene microspheres to vary z_s.

intensity was equal at $z_s = 0$ for each lens tested. In-focus emitters at 50 μm depth were selected and their average integrated density plotted vs z_s (Figure 2.5b). In agreement with our previous two-channel measurements, the Olympus 10x suffered the least degradation in pixel intensity while the Olympus 60x fared the worst. The other objectives (20x and 25x Olympus and Zeiss 20x) performed similarly.

CONCLUSION

Working with a new generation of high NA, water immersion dipping objective lenses now commonly used for multiphoton imaging in turbid media, we report that they are vastly superior to the older series of dipping objectives (e.g., 60x/0.9 LUMPlanFl). Within the set of newer objectives we examined, we found that the newest versions, such as the Olympus 25x/1.05 and Zeiss 20x/1.0 lenses also have improved collection characteristics compared to the earlier versions of the same types of objectives, such as the Olympus XLUMPlanFl 20x/0.95 due primarily to improved transmission. We note that the particular lens we tested was one of the first

XLUMPlanFl 20x/0.95 objectives made available, and Olympus now produces an upgraded version of their XLUMPlanFl workhorse lens, which has improved transmission characteristics and higher NA (1.0). If the lower resolution of a 0.6 NA lens can be tolerated, the Olympus 10x/0.6 objective further aids in the collection of scattered fluorescence. We also note that the diffraction-limited focus of the lower NA 10x/0.6 lens excites two-photon fluorescence more efficiently than the higher NA objectives used in our measurements, which may be particularly useful when imaging is power-limited. Others have also previously suggested that low-NA lenses may be advantageous for power-efficient two-photon imaging [18]. Related to epi-collection in a scattering medium, we noticed a strong correlation between the decay length of scattered light collection signal and the OBA/OFA ratio. This suggests that, for a given NA, one should seek a low-magnification objective to maximize collection. Furthermore, it helps to avoid using a lens with a working distance much longer than necessary, since this decreases the OBA/OFA ratio. We also find that the divergence of the fluorescence beam exiting the OBA is much less than previously reported. In general, 25 or 30 mm optics are sufficient for the detection pathway, provided they are situated relatively close to the objective. This finding is also conducive to the miniaturization of two-photon microscopes, which is a key consideration for commercial applications or custom multiphoton instruments designed for experiments with unusual spatial constraints.

The objective lens is a primary determinant of the epifluorescence collection efficiency and therefore plays a critical role in image quality (e.g. S/N) and in controlling photodamage and photobleaching. Although the mechanisms are still not

completely understood, photodamage during two-photon microscopy within the focal plane has been shown to be highly nonlinear, with multiple reports indicating that damage scales as P^{μ} where μ is typically greater than 2 [5,6]. Thermal damage due to one-photon absorption by water has been deemed largely inconsequential at wavelengths available from a typical Ti:S laser (700 – 1000 nm) [19], but as the use of longer wavelength lasers in the 1200 to 1700 nm range becomes more common, heating is once again becoming a concern due to strong water absorption in this wavelength range. For these reasons, efficient detection schemes are critical to minimize bleaching, phototoxicity and excess sample heating by reducing the excitation intensity required to collect a sufficient fluorescence signal for imaging.

Because two-photon excitation is largely confined to a diffraction-limited volume, all fluorescence may be collected as signal and, accordingly, several groups have published designs that decouple the illumination and detection pathways to improve collection. Vučinić et al. suggest constructing a reflective shroud around the refractive lens components and predict that collection efficiency may be improved two to four-fold [20]. Combs et al. take this idea one step further by implementing a parabolic reflector and second detector to achieve three times higher signal-to-noise than a standard 0.75 NA lens [21]. While these methods are promising, they rely on nonstandard components and restrict possible sample geometries. Others have proposed augmenting standard epifluorescence collection by surrounding the objective by a collar of waveguides [22] or light guides [23] and have profoundly increased detection efficiency. In particular, when the latter is used with a 4x 0.28 NA objective, the lens-light guide combination achieves an effective collection NA of 0.55 and 0.80-

0.90 in non-scattering and scattering specimens, respectively. These improvements have immediate implications for cell tracking, calcium imaging in neuronal networks, and other applications where large FOV is a priority and micron resolution is sufficient. Seeking to address these same niches for multiphoton microscopy, we have also designed a *de novo* multiphoton water-immersion objective with an incorporated dichroic beam splitter that achieves a collection NA of 0.98 while maintaining an excitation NA of 0.35 [24]. By placing an emphasis on photon-efficient collection for *in vivo* multiphoton microscopy, image quality (S/N) can be improved while specimen perturbation is minimized.

REFERENCES

1. W. Denk, J. Strickler, and W. Webb, "Two-photon laser scanning fluorescence microscopy," Science (80-.). **248**, 73–76 (1990).

2. W. R. Zipfel, R. M. Williams, and W. W. Webb, "Nonlinear magic: multiphoton microscopy in the biosciences.," Nat. Biotechnol. **21**, 1369–77 (2003).

3. P. Theer and W. Denk, "On the fundamental imaging-depth limit in two-photon microscopy.," J. Opt. Soc. Am. A. Opt. Image Sci. Vis. **23**, 3139–49 (2006).

4. P. Theer, M. T. Hasan, and W. Denk, "Two-photon imaging to a depth of 1000 microm in living brains by use of a Ti:Al2O3 regenerative amplifier.," Opt. Lett. **28**, 1022–4 (2003).

5. G. H. Patterson and D. W. Piston, "Photobleaching in two-photon excitation microscopy.," Biophys. J. **78**, 2159–62 (2000).

6. A. Hopt and E. Neher, "Highly nonlinear photodamage in two-photon fluorescence microscopy.," Biophys. J. **80**, 2029–36 (2001).

7. D. Kobat, N. G. Horton, and C. Xu, "In vivo two-photon microscopy to 1.6-mm depth in mouse cortex.," J. Biomed. Opt. **16**, 106014 (2011).

8. N. G. Horton, K. Wang, D. Kobat, C. G. Clark, F. W. Wise, C. B. Schaffer, and C. Xu, "In vivo three-photon microscopy of subcortical structures within an intact mouse brain.," Nat. Photonics **7**, 205–209 (2013).

9. M. Oheim, E. Beaurepaire, E. Chaigneau, J. Mertz, and S. Charpak, "Two-photon microscopy in brain tissue: parameters influencing the imaging depth.," J. Neurosci. Methods **111**, 29–37 (2001).

10. E. Beaurepaire, M. Oheim, and J. Mertz, "Ultra-deep two-photon fluorescence excitation in turbid media," Opt. Commun. **188**, 25–29 (2001).

11. E. Beaurepaire and J. Mertz, "Epifluorescence collection in two-photon microscopy.," Appl. Opt. **41**, 5376–82 (2002).

12. W. F. Cheong, S. A. Prahl, and A. J. Welch, "A review of the optical properties of biological tissues," IEEE J. Quantum Electron. **26**, 2166–2185 (1990).

13. S. L. Jacques, "Optical properties of biological tissues: a review.," Phys. Med. Biol. **58**, R37–61 (2013).

14. A. Diaspro, G. Chirico, and M. Collini, "Two-photon fluorescence excitation and related techniques in biological microscopy.," Q. Rev. Biophys. **38**, 97–166 (2005).

15. C. J. R. Sheppard and H. J. Matthews, "Imaging in high-aperture optical systems," J. Opt. Soc. Am. A **4**, 1354 (1987).

16. B. Richards and E. Wolf, "Electromagnetic Diffraction in Optical Systems. II. Structure of the Image Field in an Aplanatic System," Proc. R. Soc. A Math. Phys. Eng. Sci. **253**, 358–379 (1959).

17. J. P. Zinter and M. J. Levene, "Maximizing fluorescence collection efficiency in multiphoton microscopy.," Opt. Express **19**, 15348–62 (2011).

18. A. K. Dunn, V. P. Wallace, M. Coleno, M. W. Berns, and B. J. Tromberg, "Influence of optical properties on two-photon fluorescence imaging in turbid samples," Appl. Opt. **39**, 1194 (2000).

19. a Schönle and S. W. Hell, "Heating by absorption in the focus of an objective lens.," Opt. Lett. **23**, 325–7 (1998).

20. D. Vucinić, T. M. Bartol, and T. J. Sejnowski, "Hybrid reflecting objectives for functional multiphoton microscopy in turbid media.," Opt. Lett. **31**, 2447–9 (2006).

21. C. a Combs, A. V Smirnov, J. D. Riley, A. H. Gandjbakhche, J. R. Knutson, and R. S. Balaban, "Optimization of multiphoton excitation microscopy by total emission detection using a parabolic light reflector.," J. Microsc. **228**, 330–7 (2007).

22. C. J. Engelbrecht, W. Göbel, and F. Helmchen, "Enhanced fluorescence signal in nonlinear microscopy through supplementary fiber-optic light collection.," Opt. Express **17**, 6421–35 (2009).

23. J. D. McMullen, A. C. Kwan, R. M. Williams, and W. R. Zipfel, "Enhancing

collection efficiency in large field of view multiphoton microscopy.," J. Microsc. **241**, 119–24 (2011).

24. J. D. McMullen and W. R. Zipfel, "A multiphoton objective design with incorporated beam splitter for enhanced fluorescence collection.," Opt. Express **18**, 5390–8 (2010).

CHAPTER 3

A VERSATILE AZIMUTHAL SCANNING PLATFORM FOR TIRF AND SCANNING ANGLE INTERFERENCE MICROSCOPY

Homebuilt TIRF systems have become a staple instrument in labs conducting single-molecule or super-resolution fluorescence experiments. This chapter describes an azimuthal scanning platform that eliminates commonplace fringing artifacts while also providing push-button control of angle-of-incidence. Due to their simplicity and versatility, the CircleScan optoelectronics are expected to be of widespread interest to the microscopy community and have already been adopted by others at Cornell. The chapter also discusses a combination of CircleScan with Scanning Angle Interference Microscopy, demonstrating the robustness of the platform to improve other methods.

ABSTRACT

Recent developments in super-resolution microscopy have revolutionized our perspective of cellular architecture and nanoscale dynamics. Despite significant progress, tools for imaging in the axial dimension have consistently provided poorer localization precision than their lateral counterparts. For such applications, scanning angle localization microscopy (SAIM) has proven advantageous, offering molecular-scale axial precision in living cells with fairly simple data acquisition and image processing. Here, we present a new azimuthal scanning platform that boosts SAIM acquisition rates by an order of magnitude and also reduces fringing artifacts for TIRF. We demonstrate the utility of our CircleScan platform through various single-molecule and cellular applications and also develop a new TIRF-activation scheme

that improves SAIM contrast by minimizing contributions from freely diffusing fluorescent proteins. CircleScan is a versatile, inexpensive and simply-implemented routine that improves the performance of standard TIRF and SAIM microscopes.

INTRODUCTION

Nanoscale investigations of cellular architecture have been greatly bolstered by several recently developed imaging modalities that surpass the diffraction limit. Methods relying on fluorophore localization [1–3], stimulated emission [4,5] and patterned excitation [6] have revealed sub-resolution details about protein organization and movements that were previously obscured by diffraction, yielding new perspectives on organelle ultrastructure [7], supramolecular assemblies [8,9], cytoskeletal structures [10] and membrane topography [11]. Despite these advances, tools that provide sub-resolution optical precision in the axial dimension have lagged behind their lateral counterparts. New methods that are capable of resolving fine axial movements at second or better frames rates would notably benefit studies of cell motility, endocytosis and viral budding.

Because of their exceptional ability to measure small distances, interferometric approaches have been the primary direction for improvements in axial nanoscopy. Within this repertoire, scanning angle interference microscopy (SAIM) allows dynamic, multi-color imaging with sub-10 nm axial precision using standard, commercial TIRF instrumentation [12]. As currently implemented, cells are cultured onto a mirror substrate, which is then inverted above the microscope objective. Interference of the incident and reflected wavefronts generates axially-structured

excitation with the position of intensity minima and maxima (i.e. the anti-nodes) being determined by the angle of incidence (AOI) of illumination. A series of images is collected at different AOIs and individual pixels are then fit to a theoretical model to extract height information for axially thin samples. Dynamic mapping of topographic features with high precision using SAIM has proven useful for understanding focal adhesion dynamics during cell migration as well as glycocalyx dysregulation in cancer cells [11].

Although SAIM provides molecular-scale axial precision in live specimen, the initial implementation on a commercial TIRF microscope was somewhat limited in its frame rate. Improved temporal resolution would be advantageous for numerous applications, including mechanistic studies of receptor endocytosis, where axial positions of clathrin-coated pits can change on sub-second timescales [13], or the assembly and disassembly of actin waves, which transition between different states during their short lifetime (~7 minutes) [14]. Other super-resolution techniques, such as stimulated emission depletion (STED) microscopy and localization microscopy, permit sub-resolution imaging but fall short of SAIM's combination of axial precision and time resolution [5,8,15]. Recently, a new method for dynamic axial imaging based on variation in penetration depth at different wavelengths was shown to yield ~20 nm axial precision in real time [13]. However, Simultaneous Two-Wavelength Axial Ratiometry (STAR) requires dual-labeling of proteins-of-interest, complicating experimental design and reducing potential for multi-color imaging, while also being restricted to features near the glass-water interface. Conventional SAIM also suffers from fringing artifacts similar to those observed in TIRF microscopy. However, while

stray fringes largely affect only the signal intensity across the field of view in TIRF, reducing the quantitative nature of the data, fringes in SAIM interfere with the height reconstructions by introducing intensity fluctuations not predicted by the SAIM model.

Here, we present a second-generation scanning angle interference microscope platform that utilizes the fast azimuthal scanning of incident laser light described above to boost speed and eliminate fringing artifacts in SAIM. This concept has previously been used to improve illumination in TIRF and Highly Inclined Laminated Optical (HILO) sheet microscopy [16–18]. Our CircleScan platform with galvo-based angular deflection accelerates SAIM data acquisition by an order of magnitude while polarization complications from azimuthal rotation are not prohibitive to molecular-scale topographic imaging. Furthermore, the microscope hardware and firmware are incredibly versatile, allowing push-button control of AOI for widefield applications and facile interfacing with other optoelectronic components (Figure 3.1a, b). Two-color azimuthally-rotated SAIM was validated with focal adhesions (FAs), where it accurately resolves the stratification of distinct protein constituents. Furthermore, a TIRF activation scheme was developed to improve SAIM contrast for FAs situated in the cell interior, where background from freely diffusing labeled proteins has typically precluded SAIM imaging.

THEORY

Polarization effects on SAIM contrast

In SAIM, interference of incident and reflected beams produces an axial standing wave, with the positions of fringe extrema being determined by the wavelength of illumination, angle-of-incidence and indices of refraction of the silicon, oxide and water layers. A complete description of the electromagnetic fields is attained by Fresnel theory and has been detailed elsewhere [12,19]. Here, we reproduce only the main results. The intensity $I(H,\theta)$ of the electric field at a given height H is given by:

$$I_{TE/TM} = A\left|1 + r_{TE/TM}e^{i\varphi(H)}\right|^2 + B$$

Where A is an amplitude coefficient proportional to the laser intensity and B is a term that encapsulates various sources of background (out-of-focus fluorescence, stray light, detector noise, etc.). Intensity modulation results from the dependence of the phase term φ and the reflection coefficient on height and angle-of-incidence. The phase term is:

$$\varphi(H) = \frac{4\pi n_2}{\lambda} H\cos\theta_2$$

While the formulation of the reflection coefficient $r_{TE/TM}(H,\theta)$ depends on the polarization of the incident light. For TE and TM cases, these coefficients are given by:

$$r_{TE} = \frac{(m_{11}^{TE} + m_{12}^{TE}p_0)p_2 - (m_{21}^{TE} + m_{22}^{TE}p_0)}{(m_{11}^{TE} + m_{12}^{TE}p_0)p_2 + (m_{21}^{TE} + m_{22}^{TE}p_0)}$$

$$r_{TM} = \frac{(m_{11}^{TM} + m_{12}^{TM}q_0)q_2 - (m_{21}^{TM} + m_{22}^{TM}q_0)}{(m_{11}^{TM} + m_{12}^{TM}q_0)q_2 + (m_{21}^{TM} + m_{22}^{TM}q_0)}$$

Where the coefficients p_i, q, $m_{ij}^{TE/TM}$ are described as follows:

$$p_i = n_i \cos\theta_i \qquad q_i = \frac{n_i}{\cos\theta_i} \quad i = 0,\ 1,\ 2$$

$$M^{TE} = \begin{pmatrix} \cos\left(\frac{2\pi n_1}{\lambda} H\cos(\theta_1)\right) & -\frac{i}{p_1}\sin\left(\frac{2\pi n_1}{\lambda} H\cos(\theta_1)\right) \\ -ip_1\cos\left(\frac{2\pi n_1}{\lambda} H\cos(\theta_1)\right) & \cos\left(\frac{2\pi n_1}{\lambda} H\cos(\theta_1)\right) \end{pmatrix}$$

$$M^{TM} = \begin{pmatrix} \cos\left(\frac{2\pi n_1}{\lambda} H\cos(\theta_1)\right) & -\frac{i}{q_1}\sin\left(\frac{2\pi n_1}{\lambda} H\cos(\theta_1)\right) \\ -iq_1\cos\left(\frac{2\pi n_1}{\lambda} H\cos(\theta_1)\right) & \cos\left(\frac{2\pi n_1}{\lambda} H\cos(\theta_1)\right) \end{pmatrix}$$

Adaptation of the original for SAIM theory for azimuthal scanning is straightforward as a beam incident from any direction can be decomposed into TE and TM components. For cases where the incident light undergoes an integer number of complete rotations, the resultant intensity is given simply by:

$$I_{CScan} = \frac{1}{2}(I_{TE} + I_{TM})$$

Using the above relations, angle-intensity profiles can be explicitly calculated for any given set of parameters (object height, illumination wavelength and corresponding refractive indices). Figure 3.1c depicts such profiles for λ = 561 nm and H = 100 nm. It is immediately evident that interference contrast is optimal when light is TE-polarized, with TM light suffering from reduced modulation depth at higher angles of incidence. CircleScan illumination has substantial contrast at all angles (Figure 3.1c, d), being the average of the TE and TM states, and real performance is ultimately determined by the signal-to-noise of individual data points and the number of frames collected.

Figure 3.1 Azimuthally scanned modes of excitation. (a) Schematic of azimuthally scanned excitation at the objective back aperture (OBA). The laser spot is focused at discrete points at the OBA, tracing out a circle. The circle radius determines the angle-of-incidence, which can be varied to achieve widefield, HILO or TIRF imaging.(b) Cartoon depicting instantaneous laser propagation incident on a cellular sample. Widefield illumination traverses the full depth of each cell, while HILO and TIRF minimize background by limiting out-of-focus excitation. (c) Angle-intensity profiles showing the effects of polarization and feature distance from the reflective substrate. All curves are generated using a model of N-type silicon with a 1.9 μm silicon oxider spacer. For samples proximal to the mirror, SAIM contrast is lost at high angles when imaging with TM light. For features farther from the mirror, intensity profiles are squeezed in angular space, alleviating polarization effects. (d) Heatmaps depicting the effects of angle and feature height on SAIM intensity as well as contrast reduction at high angles for TM and CircleScan illumination. Heatmaps also demonstrate semi-periodicity in height, which can result in ambiguity when fitting to determine height in the presence of noise. (e) Angle vs. intensity profiles depicting the effects of feature size on SAIM data. For features smaller than 20 nm, the intensity distribution matches that of an infinitely thin feature while the positions of intensity minima/maxima are maintained even as features approach 200 nm in size. (f) Plot of extracted fluorophore height vs. actual height for various thicknesses of oxide. The SAIM model for height determination assumes 1.9 μm of SiO_2. Despite absolute errors when the true oxide thickness does not match the presumed thickness, relative heights are maintained in all cases.

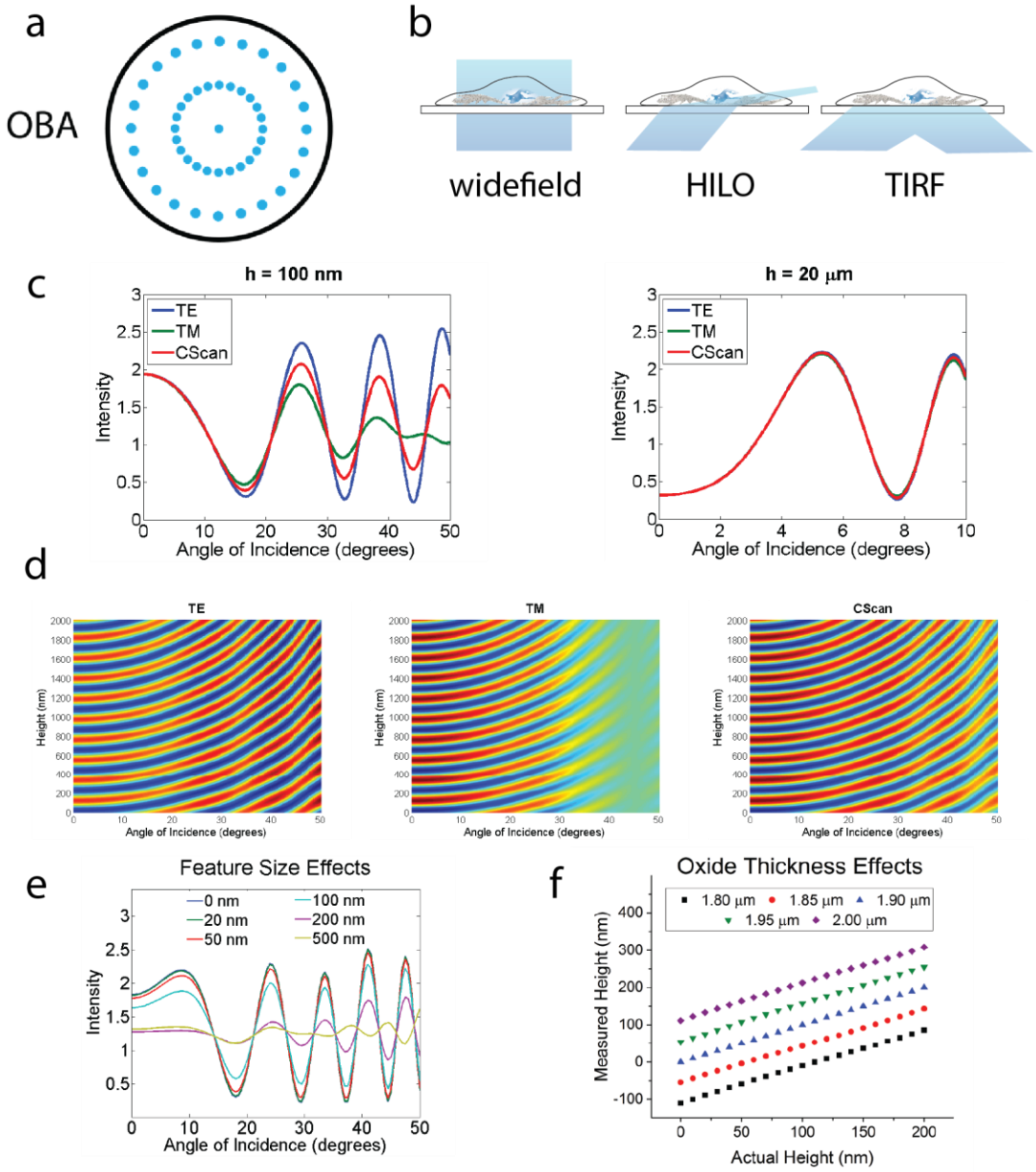
a
OBA
b
widefield
HILO
TIRF
c
h = 100 nm
h = 20 μm
TE
TM
CScan
Intensity
Angle of Incidence (degrees)
d
TE
TM
CScan
Height (nm)
Angle of Incidence (degrees)
e
Feature Size Effects
0 nm
20 nm
50 nm
100 nm
200 nm
500 nm
Intensity
Angle of Incidence (degrees)
f
Oxide Thickness Effects
1.80 μm
1.85 μm
1.90 μm
1.95 μm
2.00 μm
Measured Height (nm)
Actual Height (nm)

Relationship between object height and angular spacing of SAIM fringe extrema

So far, most SAIM applications have focused on mapping topographic features proximal to the SiO_2-water interface. However, there is no fundamental restriction that limits SAIM to working in this range. One slight complication is that angle-intensity profiles are semi-periodic, but other methods may be used to resolve height ambiguity at this coarser scale, with SAIM providing finer axial precision for topographic mapping. Another consideration when applying SAIM far from the oxide layer is that the angular spacing of fringes is much finer at larger heights. Typically, two inversions of this angular pattern are sufficient for SAIM reconstruction and thus, a smaller angular range needs to be scanned for more distal objects (Figure 3.1c). This has two primary benefits. First, azimuthal scanning at smaller angles can achieve higher angular frequencies than at larger angles since the galvanometers are displaced less per rotation. Second, the polarization effects described above are much less pronounced at shallower angles and interference contrast is close to optimal.

In addition to providing access to features buried within the cell, the application of SAIM far from the reflective substrate can have additional benefits. Routine cell culture methods developed for coverslips or glass-bottom dishes may be used rather to specialized techniques for silicon oxide. Furthermore, TIR-activation of features near the coverslip can be used to mitigate effects due to background fluorophores. Although these benefits highly encourage the use of SAIM in this non-traditional modality, there are limitations that must be considered. As the angular spacing of fringes becomes closer, the small divergence of laser light out of the objective becomes non-negligible and renders an upper limit on object heights that can

be measured. Moreover, methods for discerning between semi-periodic heights typically require additional instrumentation or sample complexity which must be weighed against the simplicity of a traditional SAIM experiment.

Structure thickness effects

Although SAIM ideally operates under the assumption of a thin sample, realistic cellular features will always have a finite thickness. SAIM contrast is clearly lost once labeled features exceed the axial distance between fringes, but many macromolecular complexes fall into 10-200 nm range—thicker than the single proteins but still below the inter-fringe spacing. To further investigate the upper size limit SAIM breaks down, we built a model of discretely spaced emitters and compared the resulting angle-intensity plots to the case for a thin sample (Figure 3.1e). For objects thinner than 20 nm, the resulting emission profile essentially matches the profile for a single emitter located at the center of fluorophore stack. As objects increase in size, contrast is continually lost, though the angular positions of fringe extrema remain unchanged for features as large as 200 nm.

Oxide thickness effects

The SAIM model assumes an accurate knowledge of the thickness of silicon dioxide deposited on the silicon wafer, but true oxide thickness can vary significantly over the chip (typically ~5%) and is impractical to characterize for each experiment. The effects of this mismatch between the true and putative oxide layers on SAIM reconstructions has not previously been studied. To address this, we simulated

intensity vs. angle profiles for fluorophores at various heights from a known thickness of oxide deposited on silicon. The true oxide thickness was allowed to vary by 5% from the desired value (1.9 μm), which was used in the model for fitting. In the case of oxide thickness mismatch (between the true and model values), extracted heights were found to vary from the actual distance between fluorophore and oxide but were merely offset by a constant value (Figure 3.1f). Thus, an inaccurate knowledge of oxide thickness prohibits absolute height measurements but does not preclude precise imaging of axial topography.

Future considerations

Although the basic SAIM theory has been put forward and corroborated with experimental data, further development of the model is necessary for a more complete understanding of the technique's performance. First, a detailed derivation of the fundamental equations from thin film electromagnetic theory would be instructive. Second, a comprehensive analysis of the effects of various noise sources (photon noise, out-of-focus fluorescence, etc.) on axial precision is essential and will help to understand where semi-periodicity becomes problematic. Third, the influence of other practical parameters such as angular spread of illumination and mirror tilt can be built into the model. Together, these future studies will improve our knowledge concerning SAIM feasibility under different scenarios and guide better quantification of SAIM data.

MATERIALS AND METHODS

CircleScan optics

An overview of the galvanometer-based TIRF/SAIM system is shown in Figure 3.2a. Laser lines were combined using a series of dichroic filters (Chroma Technology) and routed into a laser scanner consisting of two 6215H galvanometers mounted in a two-axis mount and driven by a MicroMax 678 dual-axis galvanometer driver (both from Cambridge Technology). The beam scanning is controlled by a lab-built scan controller which creates the circular scanning pattern. A 4f-system after the galvos serves as a beam expander (reducing the angular scan by the same factor) while a focusing lens prior to the objective back aperture cooperates with the objective lens to form a second 4f system. The galvo mirror center point is imaged to the sample plane to maintain a constant field-of-view over different scan angles. The relationship between angle-of-incidence and the scancard DAC values were measured using a screen and application of Snell's law (Figure 3.2c). The detection pathway consists of a tube lens and Andor TuCam system to chromatically separate emissions over two electron-multiplying CCDs (Andor Technology). The TuCam optical path is routinely aligned to achieve sub-pixel co-registration across channels.

Scan controller hardware

The scan controller card is a modified version of the raster-scan controller cards designed and built in the lab for confocal and multiphoton imaging (Figure 3.2b)**.** The heart of the controller consists of a 16 bit microcontroller (PIC24FJ256GB206, Microchip Inc) that communicates with the PC used for image acquisition via the HID

(Human Interface Device) USB protocol. The PC calculates the desired scan pattern and sends it to the PIC microcontroller on the scan controller card which is interfaced with a high speed 16-bit dual parallel interface multiplying DAC (DAC8822, Texas Instruments) to produce the two analog signals that position X and Y galvos. For circle scanned TIRF and SAIM we designed two different versions to better facilitate the two different types of cameras used in single molecule imaging. The first version is a designed to work with frame transfer EMCCD cameras that do not require any specialized synchronization – we drive the galvos circularly at ~1KHz and even the fastest frame rates (~10 ms) are averaged over many scans. The second board is for sCMOS cameras with a rolling shutter and it uses interrupt driven firmware to optimize the timing to provide uniform exposure during the stepwise readout. At the PC level, the scan controller card communications is through a 64 bit Windows program written in C/C++ (Microsoft Visual Studio 2015).

Substrate preparation

N-type silicon wafers coated with 1.9 μm of silicon oxide (Addison Engineering) was cut into square pieces approximately 1 cm in size and cleaned by sonication in 1 M KOH for 30 minutes and rinsed with water. Clean substrates were silanized by immersion in (3-mercaptopropyl)trimethoxy-silane (MPTS, 4% v/v in ethanol) for 30 minutes, rinsed with ethanol, and functionalized with N-γ-maleimidobutyryl-oxysuccinimide ester (GMBS, 4 mM in ethanol) for 30 minutes to facilitate protein attachment. GMBS-functionalized substrates were thoroughly rinsed with ethanol, rinsed with PBS and incubated with 5 μg/mL fibronectin for 2 hours at

room temperature. Fibronectin-coated reflective substrates were rinsed with PBS and stored at 4°C until use (up to several weeks).

Plasmid construction

Plasmids for mNeonGreen-tagged focal adhesion proteins (paxillin, VASP and zyxin) were obtained from Allele Biotechnology. The coding regions from each were excised and transferred into a lentiviral plasmid (pCDH puro, System Biosciences). A tetracycline-inducible mCherry-paxillin plasmid was a gift from Matt Paszek.

Cell culture and stable cell line generation

LLC-PK1 pig kidney epithelial cells were cultured in Media 199 with 3% FBS. A stable EGFP-tubulin cell line was generated by transient transfection with pIRESneo-EGFP-α-tubulin (Addgene #12298) and G418 selection (0.5 mg/mL).

U2OS human osteosarcoma cells were cultured in Dulbecco's Modified Eagle's Medium supplemented with 10% FBS. Cell lines stably expressing fluorescently-tagged focal adhesion constituents were produced using standard lentiviral protocols, using HEK293 cells to generate viral particles and polybrene to enhance infectivity. Stably infected cells were selected using the appropriate antibiotics (50 μg/mL hygromycin or 2 μg/mL puromycin).

Optical characterization and conventional imaging

A thorough mapping between arbitrary DAC units and angle-of-incidence was determined by placing a screen (black box) above the objective lens and noting the

beam position as a function of DAC value; AOIs were calculated using Snell's law and stored in a calibration file. The effects of azimuthal scanning on laser fringing artifacts were investigated by imaging a pool of fluorescein dye (15 μM in 0.1 NaOH). LLC-PK1 cells stably expressing EGFP-tubulin were used to demonstrate the ability to image in a HILO modality while RBL cells labeled with 3 μM cholera toxin-Alexa647 were used to validate TIRF imaging; free cholera toxin was retained in the imaging media to assess TIRF quality.

Tubulin polymerization assay

Single tubulin polymers were assembled using previously detailed protocols [20,21]. In short, microtubule seeds were generated by mixing tubulin (10 μM unlabeled, 5 μM biotin-tubulin and 5 μM rhodamine-tubulin) and GMP-CPP in BRB80 (80 mM PIPES, 1 mM EGTA, 1 mM $MgCl_2$, pH 6.8) and incubating at 37C for 30 minutes to allow polymerization. Unpolymerized tubulin was removed by ultracentrifugation at 55,000 rpm for 5 minutes at room temperature and removal of the supernatant. The pellet was resuspended in BRB80 (same concentration as above) and incubated on ice to depolymerize microtubules. For a second cycle of polymerization, GMP-CPP was added (10 mM) and the reaction was held at 37C for 30 minutes, followed by ultracentrifugation to remove unincorporated tubulin.

For imaging, standard polyethylene glycol-based single molecule flow chambers were assembled [22]. Flow chambers were washed with assay buffer (1x PIPES with 85 mM KCl, 85 mM KOAc, 0.2% Brij-35, 4 mM $MgCl_2$ and 1 mM EGTA, pH 6.8) and then passivated using a blocking mix (1% pluronic F-127, 50

μg/mL K-casein in assay buffer). Surfaces were activated with 50 μg/mL Neutravidin in assay buffer prior to incubation with seeds (diluted ~100-500x in assay buffer to achieve suitable concentration per imaging field). 10 μM tubulin (with 7.5% rhodamine-labeled tubulin, diluted in assay buffer supplemented with 1 mM GTP, 2 mM Trolox, 1% glucose, 0.5 mg/mL glucose oxidase and 40 μg/mL catalase, pH 8.5) was introduced into the imaging chamber and polymerization was observed at 37C.

Localization microscopy

For super-resolution imaging by dSTORM, LLC-PK1 pig kidney epithelial cells were cultured on glass-bottom dishes (Mat-Tek Corporation). Cells were fixed with 3% paraformaldehyde and 0.1% glutaraldehyde for 10 minutes, rinsed with PBS, permeabilized with 0.1% Triton X-100 for 10 minutes and rinsed with PBS. A blocking solution of 5% Normal Goat Serum (NGS) was then applied for 30 minutes to minimize nonspecific adsorption of antibodies, followed by incubation with ~5 ug/mL primary antibody (mouse anti-tubulin) in 5% NGS for one hour, rinsing with 0.1% Tween-20 and incubation with ~5 ug/mL secondary antibody (goat anti-mouse Alexa 647) for one hour. After labeling, cells were rinsed with 0.1% Tween-20 followed by PBS and stored in PBS at 4°C until imaging.

Immediately prior to imaging, PBS was exchanged for imaging buffer (0.5 mg/mL glucose oxidase, 40 μg/mL catalase, 5% glucose w/v and 1% β-mercaptoethanol in 200 mM Tris-HCl, pH 8.5). Candidate cells were located on the microscope using low 640 nm laser intensities (~30 W/cm^2). Laser power was increased to ~3-4 kW/cm^2 to drive molecules to the triplet and associated dark states

Scanning angle interference microscopy

U2OS cells expressing labeled focal adhesion proteins were sparsely plated onto fibronectin-coated reflective substrates and allowed to attach overnight. The next day, cells were washed with PBS, fixed with 4% paraformaldehyde for 10 minutes, rinsed with PBS, permeabilized with 0.1% Triton X-100 (to reduce background from soluble fluorescent protein fusions), washed with PBS and stored in PBS at 4°C. Substrates bearing fixed cells were inverted atop a glass-bottom dish (In Vitro Scientific) and immersed in PBS; a 10g weight was loaded onto the non-reflective side to minimize sample drift.

Samples were imaged using a 60x/1.2 NA water-immersion objective (Olympus). Custom SAIM software was used to automatically scan through 18 incidence angles spanning 0 to 40 degrees. For each angle-of-incidence, a focused spot was rapidly scanned around the periphery of the objective lens at a fixed radius to minimize laser fringing artifacts. For two-color imaging, data was collected sequentially with 561 nm excitation for mCherry-labeled proteins followed by 488 nm excitation for mNeonGreen fusions. Typically, the 18-angle scan was repeated ten times to increase signal-to-noise while mitigating the effects of photobleaching.

For TIRF-activated SAIM experiments, cells were cultured on glass-bottom dishes coated with a silicone elastomer gel (QGel 910, Quantum Silicones, n = 1.49). Silicones were cured at 60C overnight followed by activation by plasma cleaning, silane treatement and functionalization with fibronection for cell attachment. MCF10A cells stably expressing paxillin-PAmCherry or paxillin-mEos3.2 were plated on the dishes and allowed to adhere overnight before imaging with a 100x/1.49 NA oil-

immersion objective (Olympus). SAIM acquisition software was used to scan an angular range of 0 to 8 degrees after a brief 405 nm activation pulse in TIRF mode.

SAIM analysis routine

Custom MATLAB scripts were used to analyze SAIM data. Image series were imported and averaged vertically across frames corresponding to the same angle-of-incidence. Individual pixels were then subject to a user-defined contrast threshold (the difference between the maximum and minimum values across all angles) and groups of pixels were culled through a size threshold to identify focal adhesion structures. Pixels passing through both thresholds were fit to the theoretical model for azimuthally-scanned SAIM intensity variation, extracting amplitude, background and height parameters. Topographic reconstructions of feature height were generated and displayed as colormaps.

RESULTS

Conventional imaging with azimuthally scanned excitation

Previous methods for azimuthally scanning TIRF excitation have used wedges, galvanometers or AOMs to rapidly deflect the laser beam for stray fringe elimination [16,17,23]. Of these, the latter two permit flexible change of angle-of-incidence which is useful for varying between different illumination modes (widefield, HILO or TIRF) or adjusting the penetration depth for TIRF imaging. Our galvo-based CircleScan platform can scan a circle in 1-2 ms, resulting in frame rates that are camera- or sample brightness-limited. For brightly labeled samples, good signal-to-

noise is attainable with exposure times of 10-30 ms, meaning that full SAIM series can be readily acquired in sub-second intervals.

To characterize the effect on laser fringing artifacts, we examined a pool of fluorescein dye. Fringing was readily apparent in unidirectional HILO and TIRF images and was markedly reduced by azimuthal scanning (Figure 3.2d). Various other optical geometries produced similar fringe elimination without good TIRF quality—a design criterion that has not been prioritized or measured in prior azimuthal scanning work. Published designs also have not optimized the illumination field-of-view, which is important for gathering quantitative data across the camera (Figure 3.2e). Larger fields required a larger angle of rays to be focused into the objective back aperture, which also increases the probability of generating non-TIR rays that diminish TIRF quality. This quality was assessed by imaging fluorescent beads in a pool of dye. Beads were not discernable from background fluorescence until the incidence angle exceeded the critical angle, at which the signal-to-background ratio rose considerably (Figure 3.2f).

To validate the imaging setup and electronics with realistic samples, we performed HILO and TIRF imaging of mammalian cells (Figure 3.3a). HILO microscopy of LLC-PK1 cells expressing EGFP-labeled tubulin generated images similar to published results [24], with the large field-of-illumination allowing multiple cells to be captured per camera frame. RBL cells labeled with cholera toxin showed high background levels when imaged in widefield, but substantial contrast improvement in TIRF without any fringing artifacts. Live-cell imaging of antigen-

stimulated cells recorded membrane ruffling events with minimal photobleaching or phototoxicity over 5 minutes (Figure 3.3b).

Super-resolution and single-molecule imaging

Single molecule imaging is a powerful approach for learning about molecular heterogeneity in enzyme kinetics, conformational changes and oligomerization dynamics. Often, background suppression by TIRF or HILO is necessary to achieve sufficient sensitivity to detect single molecules labeled with as little as one dye. We tested the applicability of our azimuthal scanning system for these classes of experiments by performing a microtubule polymerization assay in which the rates of microtubule assembly and disassembly may be monitored on a single molecule basis (Figure 3.3c). This particularly application serves as a rigorous test because soluble tubulin must be available at substantial concentrations (10-20 μM) for assembly to occur. With our optimized optical geometry, polymerization dynamics were readily observed even in the presence of high levels of background tubulin. By comparison, other optical arrangements or widefield imaging were prohibitive to imaging.

As an extension of single-molecule imaging, localization microscopies such as STORM and PALM provide the ability to perform hundreds of thousands or millions of single molecule measurements in a single experiment. Most TIRF microscopes are capable of localization-based super resolution imaging without any instrument

Figure 3.2 CircleScan Optical Characterization. (a) Schematic of CircleScan optical path. The center point between the galvo mirrors is imaged to the specimen plane using a pair of beam telescopes. The first telescope (L1 and L2) magnifies the beam to overfill the focusing lens (L3), which forms a second telescope in conjunction with the objective lens. Typical values for f1, f2, f3 are 30 mm, 250 mm and 300 mm but the design may be varied to optimize for specific parameters (field uniformity, illumination intensity, TIRF quality). (b) Block diagram of CircleScan electronics. (c) Angle calibration between arbitrary DAC units and the angle-of-incidence for 100x TIRF objective and the optical arrangement described above. (d) Illumination profiles of a fluorescein pool, showing the advantages of azimuthal scanning for stray fringe reduction (e) Line profile of fluorescein intensity, showing the large field-of-view achieved under CircleScan illumination. (f) Assessment of TIRF quality by imaging small fluorescent beads in a pool of fluorescein (15 μM). Beads are barely visible in HILO (59°) with contrast significantly increased in TIRF (65°). At sub-HILO angles, beads are not discernable due to the strong background signal.

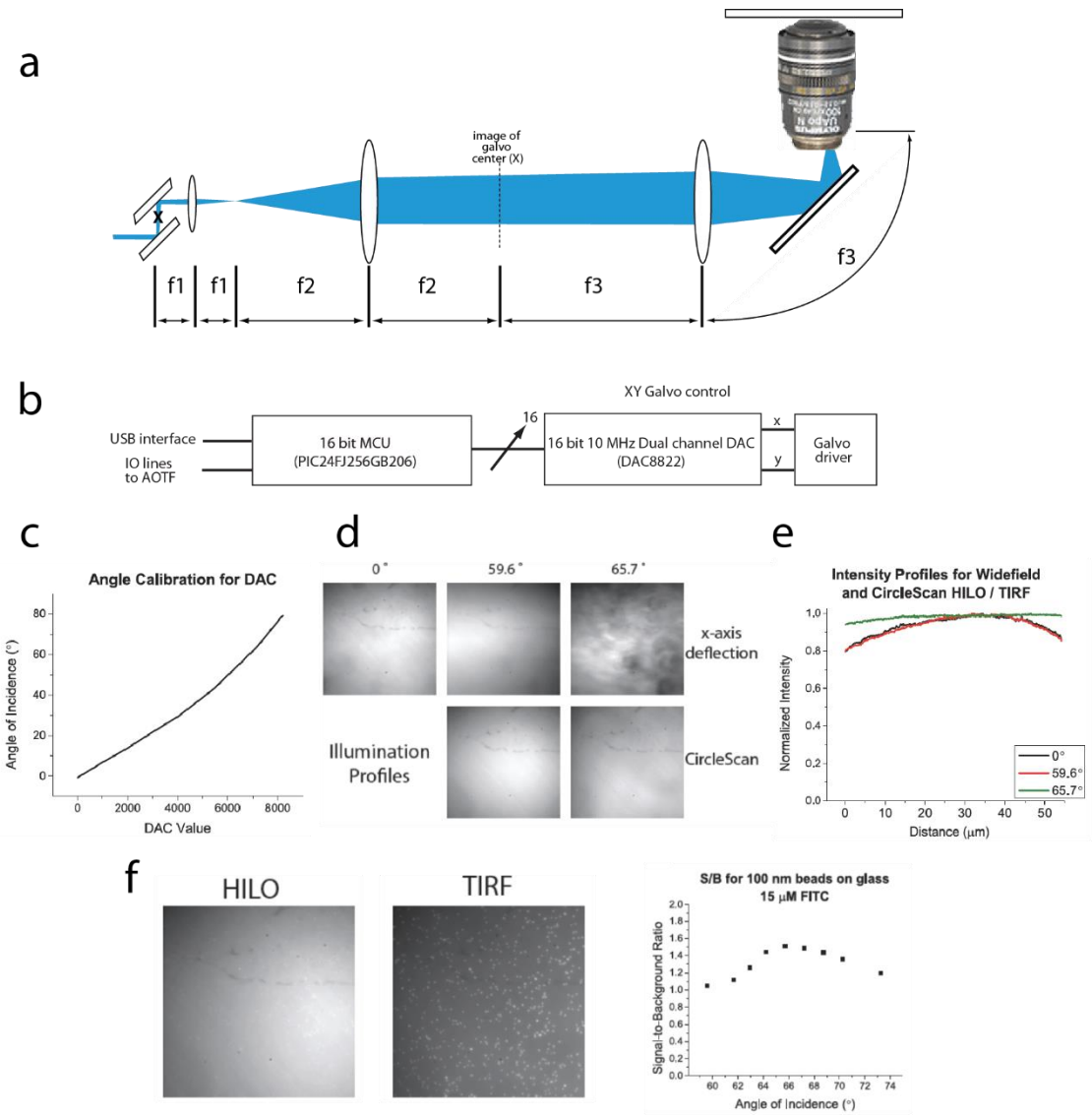
a
image of galvo center (X)
x
f1
f1
f2
f2
f3
f3
b
XY Galvo control
USB interface
IO lines to AOTF
16 bit MCU (PIC24FJ256GB206)
16
16 bit 10 MHz Dual channel DAC (DAC8822)
x
y
Galvo driver
c
Angle Calibration for DAC
Angle of Incidence (°)
DAC Value
d
0°
59.6°
65.7°
x-axis deflection
Illumination Profiles
CircleScan
e
Intensity Profiles for Widefield and CircleScan HILO / TIRF
Normalized Intensity
Distance (μm)
0°
59.6°
65.7°
f
HILO
TIRF
S/B for 100 nm beads on glass 15 μM FITC
Signal-to-Background Ratio
Angle of Incidence (°)

modification, besides the need for sufficiently powerful lasers. Instead, the burden is placed on the sample prep, where photoactivatable fluorophores must be used for labeling and special imaging buffers are used to bias molecular photophysics to favorable modes of operation. To demonstrate that azimuthal scanning doesn't diminish these capabilities, we performed direct STORM (dSTORM) [25] on

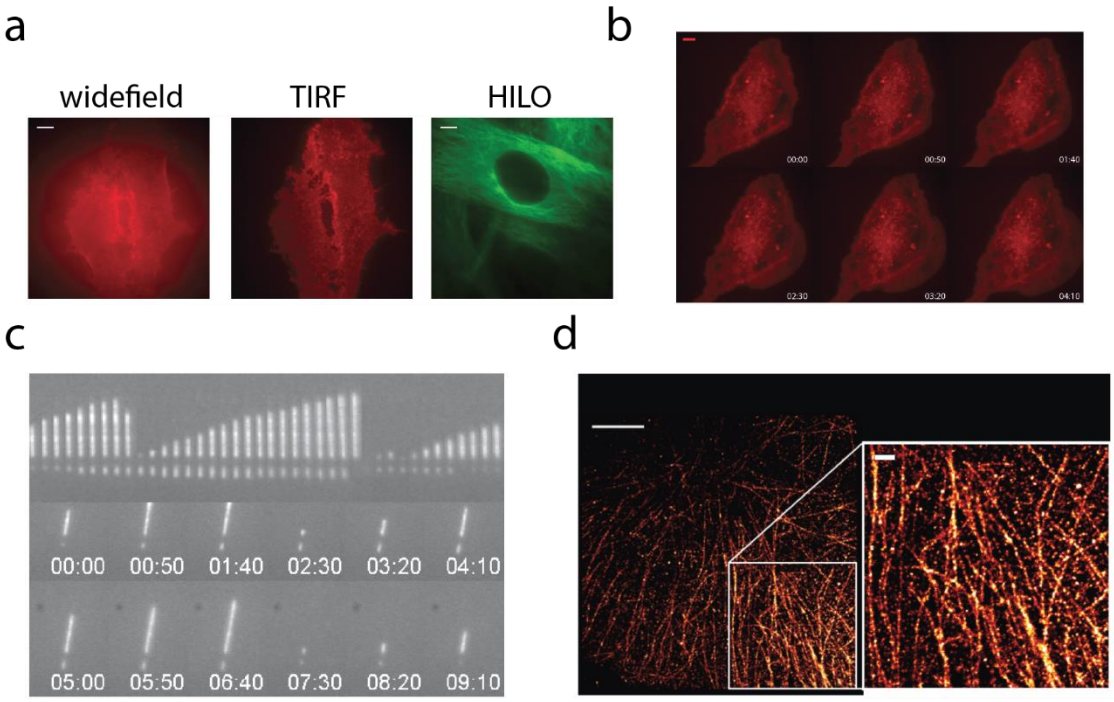

Figure 3.3 Conventional, Single Molecule and Super-Resolution Imaging with CircleScan. (a) Left two panels are widefield and TIRF images of RBL cells labeled with Alexa647-labeled cholera toxin, demonstrating advantages of TIRF to eliminate background from soluble dye. Right-most panel shows HILO image of LLC-PK1 cells expressing EGFP-tubulin with multiple cells visible due to the large field-of-view of CircleScan. (b) Live-cell imaging with CircleScan TIRF can be used to watch dynamic events, such as membrane ruffles after antigen stimulation of RBL cells. (c) CircleScan TIRF quality is sufficient for single-molecule microtubule polymerization assays, even in the presence of significant free labeled tubulin. (d) STORM reconstruction of microtubules labeled with Alexa647 by indirect immunofluorescence. Although individual frames show slight intensity variation due to fast frame rates (comparable to CircleScan period), STORM reconstructions seem to be unaffected.

antibody-labeled microtubules in LLC-PK1 cells (Figure 3.3d). Although asynchronous scanning combined with fast frame rates led to slight intensity variations across the camera frame, these did not seem to affect the final STORM reconstruction.

Scanning angle interference microscopy

The ability to scan complicated patterns with galvanometer-based deflection has advantages beyond fringe elimination. Here, we used azimuthal scanning to enhance scanning angle interference microscopy—a method of achieving molecular-scale axial resolution by collecting a series of images at various angles of incidence. Compared to its implementation with a commercial TIRF microscope, galvo-based deflection can greatly increase series acquisition speed since the time lag between collecting different angles is negligible compared to detector exposure time. In this case, time resolution is limited only by sample photophysical properties. CircleScan-SAIM was implemented by scanning a focused spot at the objective back aperture in a circular pattern. Individual camera frames in the series were acquired at different radii to vary the angle of incidence. We first validated the technique by imaging paxillin, a focal adhesion protein that has been previously studied using interferometric fluorescence microscopy [8,9]. Using CircleScan-SAIM, we recorded ten replicates of an 18-angle scan in 18 seconds (Figure 3.4a, b). Repetition of the scan pattern demonstrated that photobleaching of mNeonGreen-paxillin was not significant at the intensities required for SAIM. Frames corresponding to the same angle of incidence were averaged and thresholded to identify pixels corresponding to focal adhesions, which were then fit to a theoretical model for SAIM intensity variation under

CircleScan illumination (Figure 3.4c). Typically, good agreement was observed between raw data and fits.

Next, we used two-color CircleScan-SAIM to investigate the relative axial positions of different focal adhesion constituents. mCherry- and mNeonGreen- labeled proteins were imaged sequentially to minimize cross-talk between channels. Each channel was then analyzed in the same manner as above, rendering topographic maps of each protein (Figure 3.4d). Axial height distributions for each protein were tightly confined, generally showing a FWHM of < 10 nm, which is a convolution of the technique resolution with the physical variation of protein heights (Figure 3.4e). Different proteins also showed minimal overlap and their stratification agreed with previous measurements by interferometric PALM. [9]

Background from out-of-focus fluorophores is a key limitation for many SAIM experiments as it reduces the measured intensity contrast as interference fringes are swept across features-of-interest. Photoconversion is a proven method of increasing feature contrast in fluorescence microscopy and may be implemented in both point-scanning and widefield modes. In order to benefit from TIRF photoactivation of membrane-delimited structures-of-interest, we cultured cells on glass-bottom dishes and inverted a reflective substrate above for SAIM imaging. Although previous SAIM experiments have always used cells cultured directly on reflective substrates [11,12], it has largely been for analytical convenience rather than an experimental requirement. Photoconversion of mEos3.2-tagged paxillin followed by imaging in the red channel greatly enhances the signal-to-background ratio of focal adhesion structures compared to imaging in the green channel (Figure 3.4f), which also collects emissions from

Figure 3.4 Scanning Angle Interference Microscopy with Azimuthally Scanned Excitation. (a) Single frame from a SAIM acquisition, showing distinct focal adhesion structures labeled with mNeonGreen-VASP. (b) Intensity variation as angle-of-incidence is scanned over 18 distinct angles ranging from 0 to 40 degrees (repeated 10 times), showing negligible photobleaching for intensities used in SAIM. Top graph shows the intensity profile for a single focal adhesion, while the bottom graph shows single-pixel intensity profile, with additional noise due to Poisson photon statistics. (c) Nonlinear least squares fit of data from (b) shows good agreement with CircleScan SAIM model for mixed polarization states. (d) Two-color SAIM reconstruction of mNG-VASP and mCherry-paxillin in focal adhesions. Protein organization is color-coded by height on a pixel-by-pixel basis following SAIM analysis. (e) VASP and paxillin show organization into distinct strata with minimal overlap in the axial direction. (f) Comparison of conventional and TIRF-activated SAIM. Focal adhesions located in the interior of cells are buried in background due to soluble labeled paxillin, which is higher in thicker parts of the cell. TIRF activation improves contrast by restricting the photoconverted pool of paxillin to molecules located near the coverslip during the activation period, allowing topographic reconstruction throughout the cell.

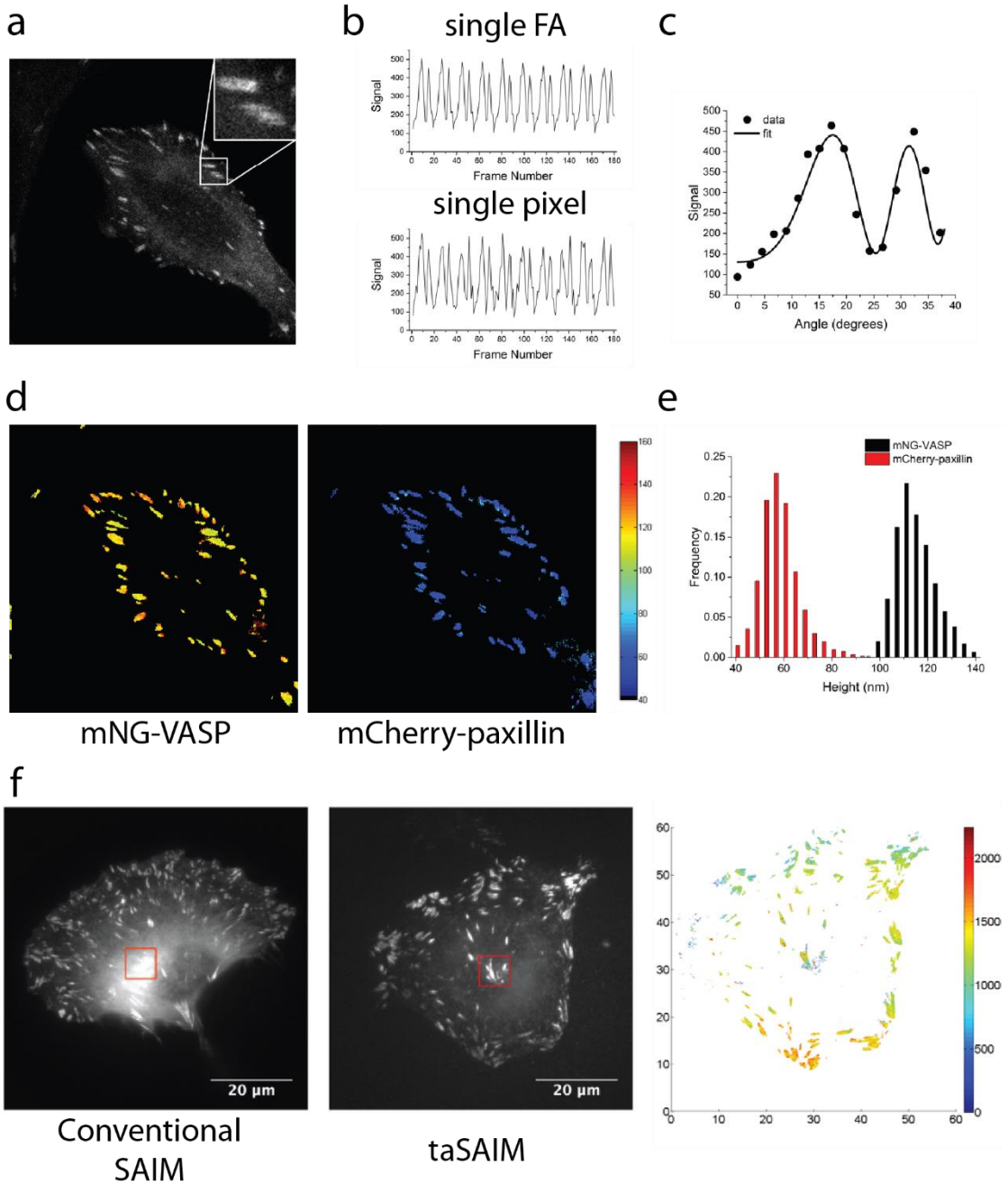
a
b
single FA
Signal
Frame Number
single pixel
Signal
Frame Number
c
data
fit
Signal
Angle (degrees)
d
mNG-VASP
mCherry-paxillin
e
mNG-VASP
mCherry-paxillin
Frequency
Height (nm)
f
20 μm
20 μm
Conventional
SAIM
taSAIM

soluble paxillin within the cytoplasm. Reconstruction of SAIM topography maps was largely successful, with many focal adhesion proteins falling within a tight distribution. However, some pixels displayed aberrant behavior owing to the semi-periodicity of the SAIM fit function. This could be resolved by increasing the number of images gathered, at the cost of speed, or by introducing complementary sources of information such as low-res measurements of z-position (e.g. by confocal microscopy z-scan).

DISCUSSION

Methods for tracking fast motions in live cells are necessary for understanding complex phenomena that underlie processes such as cell migration, viral infection and cell signaling. Although there has been a push to develop whole-cell techniques with high temporal resolution and minimal phototoxicity, precision in the axial dimension has always lagged the lateral dimensions. Scanning angle interference microscopy provides molecular-scale axial precision in living cells with low illumination intensities. Our CircleScan implementation boosts SAIM temporal resolution by an order of magnitude without adversely affecting precision. Furthermore, azimuthal scanning eliminates stray fringes that result from optical imperfections and is inexpensive to add onto existing TIRF instrumentation. Our well-documented hardware and software also make CircleScan simple to adopt.

Photoconversion is another modular addition that enhances SAIM performance. Because SAIM ideally localizes axially thin sample features, background fluorescence from out-of-focus fluorophores can diminish fit precision or

bias results. For cells cultured on glass coverslips, TIRF-based photoactivation may be used to isolate features near the plasma membrane; such a geometry remains compatible with scanning angle interference microscopy. Point-scanned photoconversion represents a more generalized approach to highlighting arbitrary cellular features, but requires an additional light path to be introduced.

Combinatorial applications of SAIM alongside other techniques are an exciting avenue of future developments. Extension of SAIM to the realm of single molecule measurements may provide a means of tracking single particles in three dimensions with higher precision than existing techniques. A confounding variable for these applications is variations in dark state occupancy across different camera frames. However, this may be alleviated by special redox buffers that minimize dark state transitions [26] or by use of novel "self-healing" dyes [27,28]. Clearing these hurdles may also open doors to combining SAIM with PSF localization techniques for 3D super-resolution microscopy (SRM) with unsurpassed axial resolution. A less challenging approach for coupling SAIM with SRM could be realized through combination with structured illumination microscopy [6,29,30].

Fast, sensitive fluorescence imaging modalities with minimal phototoxicity are critical to elucidating dynamics at the nanoscale. Azimuthally scanned SAIM provides the best combination of axial precision and temporal resolution amongst current localization techniques and is well-poised to help unravel mysteries in cell migration, viral infection and glycobiology.

REFERENCES

1. M. J. Rust, M. Bates, and X. Zhuang, "Sub-diffraction-limit imaging by stochastic optical reconstruction microscopy (STORM).," Nat. Methods **3**, 793–5 (2006).

2. E. Betzig, G. H. Patterson, R. Sougrat, O. W. Lindwasser, S. Olenych, J. S. Bonifacino, M. W. Davidson, J. Lippincott-Schwartz, and H. F. Hess, "Imaging intracellular fluorescent proteins at nanometer resolution.," Science **313**, 1642–5 (2006).

3. S. T. Hess, T. P. K. Girirajan, and M. D. Mason, "Ultra-high resolution imaging by fluorescence photoactivation localization microscopy.," Biophys. J. **91**, 4258–72 (2006).

4. S. W. Hell and J. Wichmann, "Breaking the diffraction resolution limit by stimulated emission: stimulated-emission-depletion fluorescence microscopy," Opt. Lett. **19**, 780 (1994).

5. T. A. Klar, S. Jakobs, M. Dyba, A. Egner, and S. W. Hell, "Fluorescence microscopy with diffraction resolution barrier broken by stimulated emission," Proc. Natl. Acad. Sci. **97**, 8206–8210 (2000).

6. M. G. L. Gustafsson, "Surpassing the lateral resolution limit by a factor of two using structured illumination microscopy.," J. Microsc. **198**, 82–7 (2000).

7. L. Schermelleh, P. M. Carlton, S. Haase, L. Shao, L. Winoto, P. Kner, B. Burke, M. C. Cardoso, D. a Agard, M. G. L. Gustafsson, H. Leonhardt, and J. W. Sedat, "Subdiffraction multicolor imaging of the nuclear periphery with 3D structured illumination microscopy.," Science **320**, 1332–6 (2008).

8. G. Shtengel, J. a Galbraith, C. G. Galbraith, J. Lippincott-Schwartz, J. M. Gillette, S. Manley, R. Sougrat, C. M. Waterman, P. Kanchanawong, M. W. Davidson, R. D. Fetter, and H. F. Hess, "Interferometric fluorescent super-resolution microscopy resolves 3D cellular ultrastructure.," Proc. Natl. Acad. Sci. U. S. A. **106**, 3125–30 (2009).

9. P. Kanchanawong, G. Shtengel, A. M. Pasapera, E. B. Ramko, M. W. Davidson, H. F. Hess, and C. M. Waterman, "Nanoscale architecture of integrin-based cell adhesions.," Nature **468**, 580–4 (2010).

10. K. Xu, G. Zhong, and X. Zhuang, "Actin, spectrin, and associated proteins form a periodic cytoskeletal structure in axons.," Science **339**, 452–6 (2013).

11. M. J. Paszek, C. C. DuFort, O. Rossier, R. Bainer, J. K. Mouw, K. Godula, J. E. Hudak, J. N. Lakins, A. C. Wijekoon, L. Cassereau, M. G. Rubashkin, M. J. Magbanua, K. S. Thorn, M. W. Davidson, H. S. Rugo, J. W. Park, D. A. Hammer, G. Giannone, C. R. Bertozzi, and V. M. Weaver, "The cancer glycocalyx mechanically primes integrin-mediated growth and survival," Nature **advance on**, (2014).

12. M. J. Paszek, C. C. DuFort, M. G. Rubashkin, M. W. Davidson, K. S. Thorn, J. T. Liphardt, and V. M. Weaver, "Scanning angle interference microscopy reveals cell dynamics at the nanoscale.," Nat. Methods **9**, 825–7 (2012).

13. D. R. Stabley, T. Oh, S. M. Simon, A. L. Mattheyses, and K. Salaita, "Real-time fluorescence imaging with 20 nm axial resolution," Nat. Commun. **6**, 8307 (2015).

14. L. B. Case and C. M. Waterman, "Adhesive F-actin waves: a novel integrin-mediated adhesion complex coupled to ventral actin polymerization.," PLoS One **6**, e26631 (2011).

15. B. Huang, W. Wang, M. Bates, and X. Zhuang, "Three-dimensional super-resolution imaging by stochastic optical reconstruction microscopy.," Science **319**, 810–3 (2008).

16. A. L. Mattheyses, K. Shaw, and D. Axelrod, "Effective Elimination of Laser Interference Fringing in Fluorescence Microscopy by Spinning Azimuthal Incidence Angle," **647**, 642–647 (2006).

17. M. van ’t Hoff, V. de Sars, and M. Oheim, "A programmable light engine for quantitative single molecule TIRF and HILO imaging.," Opt. Express **16**, 18495–504 (2008).

18. D. S. Johnson, R. Toledo-Crow, A. L. Mattheyses, and S. M. Simon, "Polarization-controlled TIRFM with focal drift and spatial field intensity correction.," Biophys. J. **106**, 1008–19 (2014).

19. A. Lambacher and P. Fromherz, "Fluorescence interference-contrast microscopy on oxidized silicon using a monomolecular dye layer," Appl. Phys. A Mater. Sci. Process. **63**, 207–216 (1996).

20. C. Gell, V. Bormuth, G. J. Brouhard, D. N. Cohen, S. Diez, C. T. Friel, J. Helenius, B. Nitzsche, H. Petzold, J. Ribbe, E. Schäffer, J. H. Stear, A. Trushko, V. Varga, P. O. Widlund, M. Zanic, and J. Howard, "Microtubule dynamics reconstituted in vitro and imaged by single-molecule fluorescence microscopy.," Methods Cell Biol. **95**, 221–45 (2010).

21. I. A. Telley, P. Bieling, and T. Surrey, "Reconstitution and quantification of dynamic microtubule end tracking in vitro using TIRF microscopy.," Methods Mol. Biol. **777**, 127–45 (2011).

22. R. Roy, S. Hohng, and T. Ha, "A practical guide to single-molecule FRET.," Nat. Methods **5**, 507–16 (2008).

23. D. S. Johnson, R. Toledo-Crow, A. L. Mattheyses, and S. M. Simon, "Polarization-controlled TIRFM with focal drift and spatial field intensity correction.," Biophys. J. **106**, 1008–19 (2014).

24. N. M. Rusan, C. J. Fagerstrom, A.-M. C. Yvon, and P. Wadsworth, "Cell Cycle-Dependent Changes in Microtubule Dynamics in Living Cells Expressing Green Fluorescent Protein- Tubulin," Mol. Biol. Cell **12**, 971–980 (2001).

25. S. van de Linde, A. Löschberger, T. Klein, M. Heidbreder, S. Wolter, M. Heilemann, and M. Sauer, "Direct stochastic optical reconstruction microscopy with standard fluorescent probes.," Nat. Protoc. **6**, 991–1009 (2011).

26. I. Rasnik, S. A. McKinney, and T. Ha, "Nonblinking and long-lasting single-molecule fluorescence imaging.," Nat. Methods **3**, 891–3 (2006).

27. R. B. Altman, D. S. Terry, Z. Zhou, Q. Zheng, P. Geggier, R. A. Kolster, Y. Zhao, J. A. Javitch, J. D. Warren, and S. C. Blanchard, "Cyanine fluorophore derivatives with enhanced photostability.," Nat. Methods **9**, 68–71 (2012).

28. R. B. Altman, Q. Zheng, Z. Zhou, D. S. Terry, J. D. Warren, and S. C. Blanchard, "Enhanced photostability of cyanine fluorophores across the visible spectrum.," Nat. Methods **9**, 428–9 (2012).

29. M. G. L. Gustafsson, "Nonlinear structured-illumination microscopy: wide-field fluorescence imaging with theoretically unlimited resolution.," Proc. Natl. Acad. Sci. U. S. A. **102**, 13081–6 (2005).

30. D. Li, L. Shao, B.-C. Chen, X. Zhang, M. Zhang, B. Moses, D. E. Milkie, J. R.

Beach, J. A. Hammer, M. Pasham, T. Kirchhausen, M. A. Baird, M. W. Davidson, P. Xu, and E. Betzig, "Extended-resolution structured illumination imaging of endocytic and cytoskeletal dynamics," Science (80-.). **349**, aab3500–aab3500 (2015).

CHAPTER 4

STOICHIOMETRIC ANALYSIS OF PROTEIN COMPLEXES BY CELL FUSION AND SINGLE MOLECULE IMAGING

One of the key problems when trying to perform single molecule experiments inside cells is reconciling the high native concentrations of proteins with the low concentrations needed for single molecule experiments. For this reason, most single molecule imaging has been performed in dilute aqueous suspensions or with molecules immobilized on glass substrates, missing out on physiological details of the cellular environment out of experimental necessity. This chapter describes a new means of diluting proteins for single molecule observation after physiological expression. Although much of the work presented is aimed toward studying the subunit stoichiometry of cellular protein complexes, the method is generalizable for extending a number of single molecule methods to the cellular milieu.

ABSTRACT

The composition and stoichiometry of supramolecular protein complexes are critically intertwined with their biological functions and are of the utmost interest when aiming to understand their molecular mechanisms. Unfortunately, existing techniques to probe subunit stoichiometry at the single molecule level significantly bias expression levels or perturb the cellular state in order to attain suitable concentrations for single molecule imaging. Here, we present an alternative approach wherein protein complexes may be assembled at physiological concentrations and subsequently diluted for single-molecule observation while preserving them in a semi-native environment. Coupling this dilution strategy with fluorescence correlation

spectroscopy permits quantitative assessment of cytoplasmic oligomerization while stepwise photobleaching during total internal reflection microscopy may be used to study the subunit stoichiometry of membrane receptors. Single Protein Recovery After Dilution (SPReAD) is a simple and versatile means of extending the concentration range of single molecule measurements into the cellular regime.

INTRODUCTION

Dynamic networks of protein interactions underlie most of cell biology. A key goal of biomedical science is to understand the nature of these interactions and how they change in response to various extracellular cues. Screening methods such as yeast-two hybrid analysis or phage display are useful for identifying potential binding partners in a high-throughput manner, but generally ignore the biological context of these interactions [1]. Targeted approaches relying on co-immunoprecipitation or fluorescence spectroscopy more accurately capture interactions within the cellular environment and may be used to examine changes that occur in response to external stimuli [1,2]. However, bulk measurements yield little information about the stoichiometry of subunits within complexes and suffer from ensemble averaging. In contrast, single molecule methods have the sensitivity to probe single protein complexes and quantitatively report on their individual architectures.

Early uses of single-molecule fluorescence for subunit counting relied on artificially low expression to resolve individual protein complexes [3]. While effective, non-physiological concentrations can shift binding equilibria and alter the composition of assemblies in a biologically irrelevant manner. More recently, a single-

molecule pulldown (SiMPull) approach has been developed so that complexes can be assembled at native expression levels, extracted into a cell lysate and then captured on an antibody-coated slide for single-molecule imaging [4]. Antibody concentrations and lysate dilutions can be tuned to maintain single-molecule resolution without compromising on cellular conditions. Although SiMPull has successfully measured the subunit stoichiometry of membrane receptors, mitochondrial proteins and signaling complexes, the use of detergents and wash steps may affect the integrity of assemblies [5].

Here, we introduce a simple wash-free method to examine single protein complexes in semi-native environments. Two cell populations—one containing a protein complex of interest and the other lacking it—are plated on a coverslip and fused into large syncytia. Diffusion within these syncytia results in a net dilution of labelled complexes, permitting their examination at reduced concentrations. Dilution factors are controllable by varying the plating ratio and can be made sufficiently high to resolve single protein complexes in TIRF or to aid in fluorescence fluctuation spectroscopy. Stepwise photobleaching and brightness analysis may then be used to study stoichiometry of a single component while colocalization analysis or cross-correlation spectroscopy can probe heteromeric interactions. We call our approach Single Protein Recovery After Dilution (SPReAD) as it yields concentrations suitable for single molecule imaging after physiological oligomer assembly.

METHODS

Cloning of inducible VSVG and labeled proteins

To avoid the deleterious effects of long-term VSVG expression, the coding sequence for VSVG (Addgene #8454) was cloned into the BamHI and EcoRI sites of the lentiviral pLV Puro Tet vector for doxycycline-inducible expression. A constitutively expressed mNeonGreen lentiviral plasmid was also produced by excising mNeonGreen from mNeonGreen-N1 (Allele Biotech) using NheI and NotI and subcloning into pCDH-puro (System Biosciences).

Synthetic dimers of fluorescent proteins were produced by placing a helical linker $A(EAAAK)_5A$ after the mNG sequence in mNG-C1 (between the BspEI and BglII sites). mNG or mCh2 were then PCR amplified and placed after this linker (between NotI and SpeI sites) to generate mNG-mNG or mNG-mCh2, respectively. pCDH-puro and mNG-C1 were both digested with NheI and BamHI to excise the fluorescent protein and place it into the pCDH lentiviral plasmid to generate pCDH-puro-mNG, which was used to produce a stable mNG cell line.

mNG-tagged ADRβ2 and EGFR were generating by cloning into the pSNAPf-ADRβ2 backbone (New England Biolabs). mNG was PCRed from mNG-C1 and placed between the EcoRI and SbfI sites of pSNAPf-ADRβ2 (replacing the SNAP tag) to yield mNG-ADRβ2. Site-directed mutagenesis was used to remove a ClaI site from wildtype EGFR. This mutated EGFR was then PCR amplified and placed between the SbfI and XhoI sites of the pSNAPf-ADRβ2 plasmid, replacing ADRβ2. The EGFR signal sequence was purchased as a gBlock (Integrated DNA Technologies) and placed between the ClaI and BmtI sites to generate mNG-EGFR. Lentiviral versions of

mNG-ADRβ2 and mNG-EGFR were produced by cutting each plasmid with XbaI and NotI to place the fusion protein after the promoter in pCDH-puro. To make Orai1-mNG, Orai1-YFP (Addgene #19756) and mNG-N1 were both digested with AgeI and NotI to remove YFP and replace it with mNG.

Cell culture and generation of stable cell lines

U2OS human osteosarcoma cells were cultured in DMEM without phenol red, supplemented with 10% FBS, sodium pyruvate, 1x Glutamax and 1x antibiotic-antimycotic; all cell culture media and supplements were purchased from Life Technologies. For stable expression of VSVG under tetracycline control, U2OS cells were first stably transduced with the rtTA NeoR plasmid for the reverse tetracycline-controlled transactivator (rtTA) protein. Lentiviral particles were generated in HEK293 cells and used to transduce U2OS cells as previously described [6]. Stably transduced cells were selected using 700 μg/mL G418. U2OS rtTA cells were then transduced with pLV puro Tet-VSVG and selected using 2 μg/mL puromycin. Doxycycline was withheld from cell culture media until 24 hours prior to cell fusion. Stable mNeonGreen cell lines was produced by transducing U2OS Tet-VSVG cells with pCDH-puro-mNG-C1, pCDH-puro-mNG-ADRβ2 and pCDH-puro-mNG-EGFR and selecting with 2 μg/mL puromycin.

Fusion assay

U2OS Tet-VSVG cells were plated onto collagen coated glass-bottom dishes. After reaching confluence, fresh media with 2 μg/mL doxycyline was added and cells

were returned to a CO_2 incubator for 24 hours. Cells were then fused by removing culture media, washing with PBS and incubating in fusion buffer (PBS with 25 mM MES, pH 5.5) for 5 minutes. Cells were washed with PBS and culture media was restored before returning cells to the CO_2 incubator. Cell membranes and nuclei were labelled at various timepoints by incubating with 5 μg/mL Wheat Germ Agglutinin Alexa 647 (Life Technologies) and 5 μg/mL Hoechst in Hank's balanced salt solution for 10 minutes prior to fixation with 4% paraformaldehyde. Fixed cells were imaged on a spinning disk confocal microscope (Olympus) with air objectives (40x/0.9, 20x/0.7 and 10x/0.4) and examined for syncytia formation.

Long-term time-lapse imaging

A home-built brightfield microscope housed in a CO_2 incubator was used to examine the time-course of cell fusion. The microscope consists of an x-y stage (Applied Scientific Instrumentation), ring illuminator and camera (Chameleon, Point Grey Research). Custom software allows for autofocus and tiling of the culture dish.

U2OS Tet-VSVG cells were plated and induced with doxycycline for 24h as described earlier. Cells were fused by a brief 30 second incubation in fusion buffer, washed with PBS and restored to normal culture media. Immediately, the dish was loaded into the incubator microscope and imaged for ~30 hours.

Confocal microscopy and fluorescence correlation spectroscopy

U2OS Tet-VSVG cells were transfected with FP control plasmids or FP-tagged PKA-subunits using Lipofectamine 3000; for cytoplasmic mNG measurements, stable

U2OS mNG cells were used to accurately control the number of expressing cells. Serum-free Fluorobrite DMEM (Life Technologies) was used to minimize cellular autofluoresence, which was particularly important for FCS measurements. Cells were harvested 8h after transfection and counted, as were nontransfected Tet-VSVG cells. The two were mixed at a various ratios and $5x10^5$ cells were plated in the well of a 14mm diameter glass-bottom dish (collagen/fibronectin-coated) using doxycyline-supplemented media (2 ug/mL); additional media was added 2-12 hours after plating, after cells were visibly attached and spread.

Cells were imaged on a confocal microscope (Zeiss LSM 880). Fluorescence correlation spectroscopy was performed on the same instrument using a 32-channel GaAsP detector in photon counting mode. Data was fit to a one-component diffusion with triplet model:

$$G(\tau) = G(0) \cdot \left(1\text{-}F_T + F_T\, e^{-\frac{\tau}{\tau_T}}\right) \cdot \left[\left(\frac{1}{1+\frac{\tau}{\tau_d}}\right) \cdot \sqrt{\frac{1}{1+\frac{\tau}{S \cdot \tau_d}}}\right]$$

where τ_T and F_T are the triplet time and fraction, respectively, τ_d is the diffusion time, S is the structure factor for the focal volume and G(0) is the correlation at $\tau = 0$. The structure factor was set to 10 for all fits. For Protein Kinase A experiments, PKA-transfected U2OS cells were mixed 1:10 with non-expressing VSVG cells and incubated in doxycycline-supplemented Fluorobrite DMEM for 24h. Cells were then fused by a 5 minute incubation in fusion buffer and FCS was performed in syncytia one hour later. In order to maintain the same syncytial position for post-stimulation measurements, 2x cAMP-stim buffer (50 μM forskolin, 200 μM IBMX in Fluorobrite

DMEM) was added directly to the imaging dish in equal volume to the residual media and a second FCS recording was initiated 5 minutes later.

Timecourse imaging of cell fusion dynamics

The kinetics of cell fusion and subsequent protein diffusion were thoroughly investigated to guide the timing of single molecule experiments. These dynamics will vary for each protein of interest and thus, similar experiments ought to be conducted prior to FCS or stepwise photobleaching measurements. As an example of cytoplasmic proteins, U2OS cells expressing mNG were co-plated with non-expressing VSVG cells at a ratio of 1:10 or 1:100. Cells were fused using a quick 30 second incubation in fusion buffer and then returned to imaging media (Fluorobrite DMEM). The imaging dish was loaded onto a confocal microscope (Zeiss LSM 880) and a time-series was started 2 minutes after fusion was initiated. Both the 1:10 and 1:100 co-plating ratios were imaged at room temperature (23C), while the former was also imaged at 37C to examine the effects of temperature on protein diffusion.

Diffusion of mNG-ADRβ2 was investigated by fixing syncytia at various timepoints after cell fusion. Fusion was accomplished by a 30 second incubation in fusion buffer and cells were then returned to imaging media (Fluorobrite DMEM) at 37C. Cells were fixed with 4% PFA for 3 hours and then washed with PBS and imaged in PBS on a commercial TIRF microscope (Zeiss Elyra).

Single-molecule imaging after cell fusion

U2OS Tet-VSVG cells were transfected with FP-tagged receptor constructs and plated onto glass-bottom dishes with non-transfected cells at a ratio of 100:1 (non-transfected:transfected), as described above. After 24h of doxycycline induction, cells were fused and imaged live (1-2 hours after fusion) or fixed for stoichiometry/colocalization analysis. Cells were fixed with 4% paraformaldehyde for 3 hours in the dark at room temperature to eliminate residual mobility of membrane proteins after short fixation [7]. For mNG-EGFR experiments, the syncytia was stimulated with 200 ng/mL EGF 75 minutes after cell fusion was initiated and fixed 5 minutes later or fixed without EGF treatment.

TIRF microscopy

A home-built azimuthal-scanning objective-TIRF microscope was used for single molecule imaging (See Supp Fig). 488 nm and 561 nm illumination were used to excite mNeonGreen and mCherry, respectively, and were directed to the sample using a quad polychroic (ZT405/488/561/640rpc, Chroma Technology) housed in the filter wheel. A 100x/1.49 NA lens was used. A TuCam unit with band pass filters (ET525/50 for mNeonGreen and ET605/52m for tdTomato) was used to split emissions onto two EMCCDs (Andor iXon). Image coregistration was accomplished by acquiring brightfield images of a calibration objective (Zeiss) prior to each imaging experiment and ensuring that the images were coregistered to better than 1 pixel over the camera field-of-view through alignment of the detection pathway. Live-cell data

was acquired at 37C using an objective heater (Bioptechs), while fixed cell experiments were performed at room temperature.

Coverslips were scanning for regions with a suitable density of molecules for single molecule analysis; regions with unfused fluorescent cells or too few/too many molecules were avoided. For bleach step analysis, 2000 frames were recorded at 10-30 Hz; laser intensity was kept low to mitigate blinking artifacts. For colocalization analysis, 20 frames were acquired and averaged during postprocessing.

Single molecule data analysis

Photobleaching movies were recorded and analyzed using custom software written in C (available upon request). Spots were automatically found by thresholding a summed projection of the stack. For each molecule, the data in each frame was fit to a Gaussian and an ROI was centered around the molecular coordinates. The ROI center was allowed to move at most 1 pixel per frame to avoid blinking-induced artifacts. Fluorescence traces were generated by plotting ROI summed intensity against time. The number of steps in each trace was manually determined (example traces in Supplementary figures); traces without discernable bleach steps were discarded. At least 300 molecules were analyzed for each sample.

For colocalization analysis, data from two EMCCDs were analyzed to find spots in both the green and red channels using a custom MATLAB script. PSFs were fit to a Gaussian model to determine center locations and a colocalization fraction was calculated to be the fraction of mNeonGreen spots with an mCherry spot less than 1 pixel away.

Substrate preparation

To minimize glass autofluorescence and maximize cell attachment, plain glass-bottom dishes were cleaned and coated with fibronectin. Dishes were etched with 1 M KOH for 20 minutes, followed by a water rinse. For fibronectin coating, dishes were incubated in 4% (3-Mercaptopropyl)trimethoxysilane (Sigma-Aldrich) in ethanol for 30 minutes, rinsed with ethanol, incubated with (N-γ-maleimidobutyryl-oxysuccinimide ester) crosslinker (4 mM in ethanol, Thermo Scientific), rinsed with ethanol and dried thoroughly in a sterile biosafety cabinet. Dishes were then incubated with 5 μg/mL fibronectin for 2 hours at room temperature, followed by overnight at 4C, then rinsed with PBS and stored in PBS at 4C until use (up to several weeks).

RESULTS

Formation of large syncytia using an inducible VSVG

Controlled cell fusion was achieved by stably infecting human osteosarcoma cells with vesicular stomatitis virus G protein (VSVG), a well-characterized fusogen which can be reversibly activated by a pH drop [8]. In order to dilute protein complexes for stoichiometry analysis, a sufficient ratio of non-expressing to expressing cells must be fused to bridge the gap between physiological expression levels and concentrations viable for single molecule experiments (Figure 4.1a). After activating VSVG in a confluent monolayer of cells, we observed rapid formation (<1 h) formation of massive syncytia whereas cells expressing an inactive VSVG displayed a normal phenotype (data not shown). Qualitatively, all cells in contact were fused into a single syncytium, estimated to contain hundreds of thousands of cells

(Figure 4.1b). At longer timeframes, nuclei migrated away from the syncytium periphery and formed a clustered arrangement, as previously reported [9,10]. Together, these results suggest that substantial dilution factors may be attained in a time interval comparable to handling times for cell lysate preparation, implying that the two approaches have similar bounds on detecting transient oligomerization.

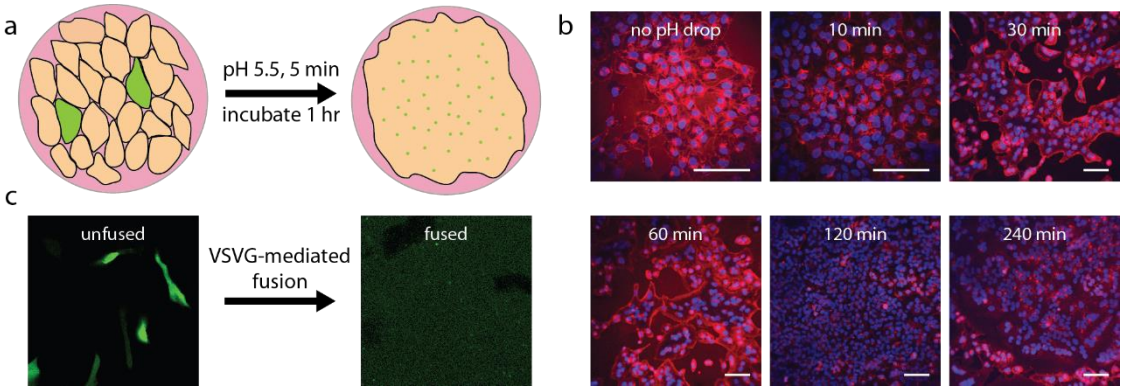

Figure 4.1 Single Protein Recovery After Dilution. (a) Cartoon depicting the SPReAD concept. Cells expressing a labeled protein-of-interest (green) are co-plated with unlabeled cells (pink) which express VSVG on their cell membrane. A brief incubation in low-pH (5.5-6.0) buffer is sufficient to initiate massive fusion, upon which mobile protein complexes may diffuse out of their parent cells into the larger syncytium; with appropriate co-plating ratios, final concentrations suitable for single molecule observation are attainable irrespective of the initial labeled protein concentration.c(b) Cell fusion assayed by nuclear (blue) and membrane (red) staining after pH drop. Unfused cells display a normal phenotype, with each nucleus bounded by a contiguous cell membrane. After pH drop, cells form massive syncytia that seem to only be limited by the number of cells in the imaging dish (typically hundreds of thousands). (c) Dilution of a cytoplasmic fluorescent protein by VSVG-mediated cell fusion. Initially, cells display heterogeneous fluorescence levels with the brightest cells surpassing micromolar fluorophore concentrations. After fusion, fluorescence is homogeneous and greatly reduced compared to the levels in unfused transfected cells.

Continuous darkfield imaging was used to better visualize the dynamics of cell fusion and long term viability of syncytia (Figure 4.2). Fusion was accompanied by a loss of cell boundaries approximately 40 minutes after pH drop. For the next ~4-5 hours, the syncytium remained bound to the coverslip and displayed few morphological changes. Thereafter, adhesion was slowly lost over the course of 12 hours and, at 20 hours, concerted cell death was observed. All in all, this suggests that we have a 4-5 hour window during which cells are fused, but otherwise minimally perturbed. Cells may be imaged live during this window or fixed for later observation. Large scale fusion was also possible in other mammalian cell lines due to the broad tropism of VSVG, signifying another means of experimental control by which cofactors can be included or excluded by choice of cell type. The formation of syncytia is a key step in the development of various mammalian tissues, including bone, muscle and placenta [11]. In these cases, cell fusion is well-regulated and part of the normal developmental program. Cell fusion can also play a role in the progression of disease. Many enveloped viruses are able to trigger fusion between an infected cell and its neighbors, resulting in new and abnormal hybrids. Accidental cell fusion, both due to viral infection and otherwise, has also been implicated in cancer, where polyploid cells display high levels of chromosomal instability and may acquire tumorogenic phenotypes [12]. These natural examples of cell fusion suggest that large syncytia represent a minimally perturbative system in which to study protein oligomerization wherein the biophysical environments of membrane and cytosolic protein complexes are largely preserved, albeit under the umbrella of large-scale phenotypic changes.

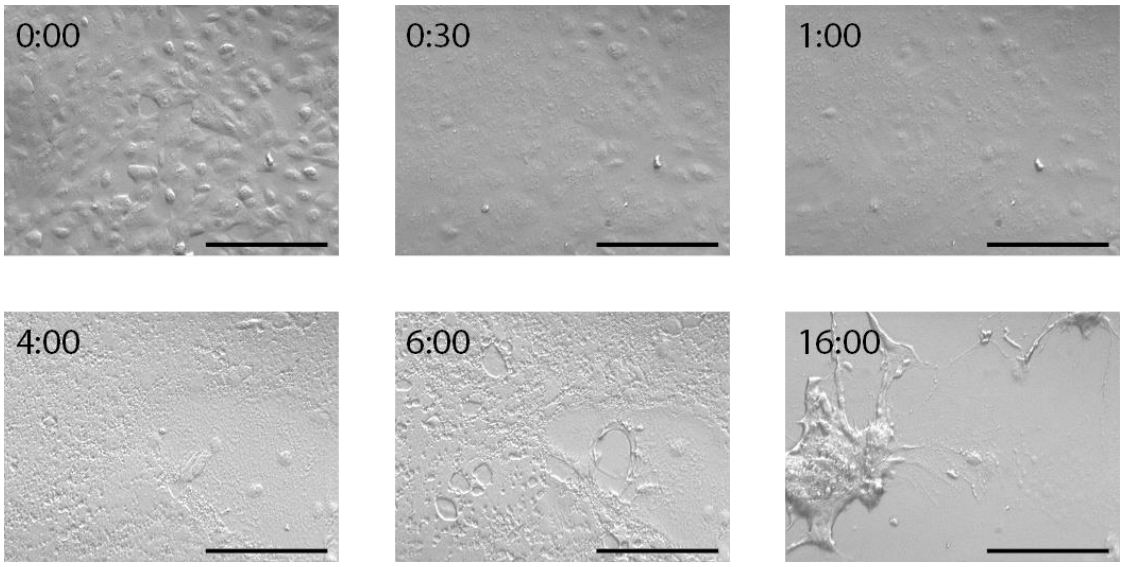

Figure 4.2 Dark-field imaging of cell fusion dynamics. Images of cell fusion process acquired using a custom microscope housed in an incubator. Prior to fusion, each cell's bounding membranes are clearly discernable but this normal morphology disappears within 30 minutes. Cells remain in this state for 4-6 hours, at which point they begin to detach from the substrate. By 16 hours, cells are largely detached and begin to undergo massive cell death.

Dilution of labeled cytosolic proteins by cell fusion

For cell fusion to function as a dilution strategy, protein complexes must be sufficiently mobile to diffuse out of their parent cells into the larger syncytium. Proteins confined to specific organelles or stably tethered to cytoskeletal components will generally fail to satisfy this criterion. However, many transcription factors and signaling complexes have mobile cytoplasmic fractions and are candidates for dilution. Furthermore, most membrane proteins are freely mobile in two dimensions, unless tethered to intracellular actin, and are of significant interest to biomedical research, representing 20-30% of all ORFs in the human genome and being the target of 50% of pharmaceutical drugs. As a proof-of-principle of dilution, VSVG-expressing cells were transfected with a cytoplasmic fluorescent protein,

mNeonGreen, and fused (Figure 4.3c). Unfused cells exhibited great heterogeneity in fluorescence levels, owing to transfection efficiency and varying plasmid copy numbers. Upon fusion, signal was homogenized across the glass-bottom dish with the only exceptions being due to unfused cells showing up as bright (transfected) or dark (non-transfected) blemishes in a sea of uniform fluorescence.

In order to test the range of dilutions possible, non-fluorescent VSVG-expressing cells were mixed with cells stably expressing mNeonGreen at various ratios and plated onto a glass-bottom dish (Figure 4.3a,b). After fusion, fluorescence signal was seen to drop in accordance with the plating ratio. Absolute numbers for syncytial concentrations were obtained by correlation spectroscopy and followed a similar trend, deviating only at the higher concentrations where FCS-based quantification is unreliable. Fusion-based dilution proved capable of adjusting cytoplasmic levels of mNeonGreen over two orders of magnitude and is likely extensible to larger dilutions, limited only by the number of cells that will fit onto the cell culture vessel. Importantly, larger dilutions brought cytosolic levels down from the low-micromolar range to sub-50 nM, where correlation spectroscopy functions best.

The kinetics of syncytium formation and protein mobility determine the ideal timeframes for imaging and fixation after fusion is initiated. Time-lapse imaging revealed that membrane fusion was immediate and synchronized across the imaging vessel, with cytosolic proteins beginning to escape their parent cells within 2 minutes of pH drop (Figure 4.4a-d). The initially heterogeneous fluorescence distribution was

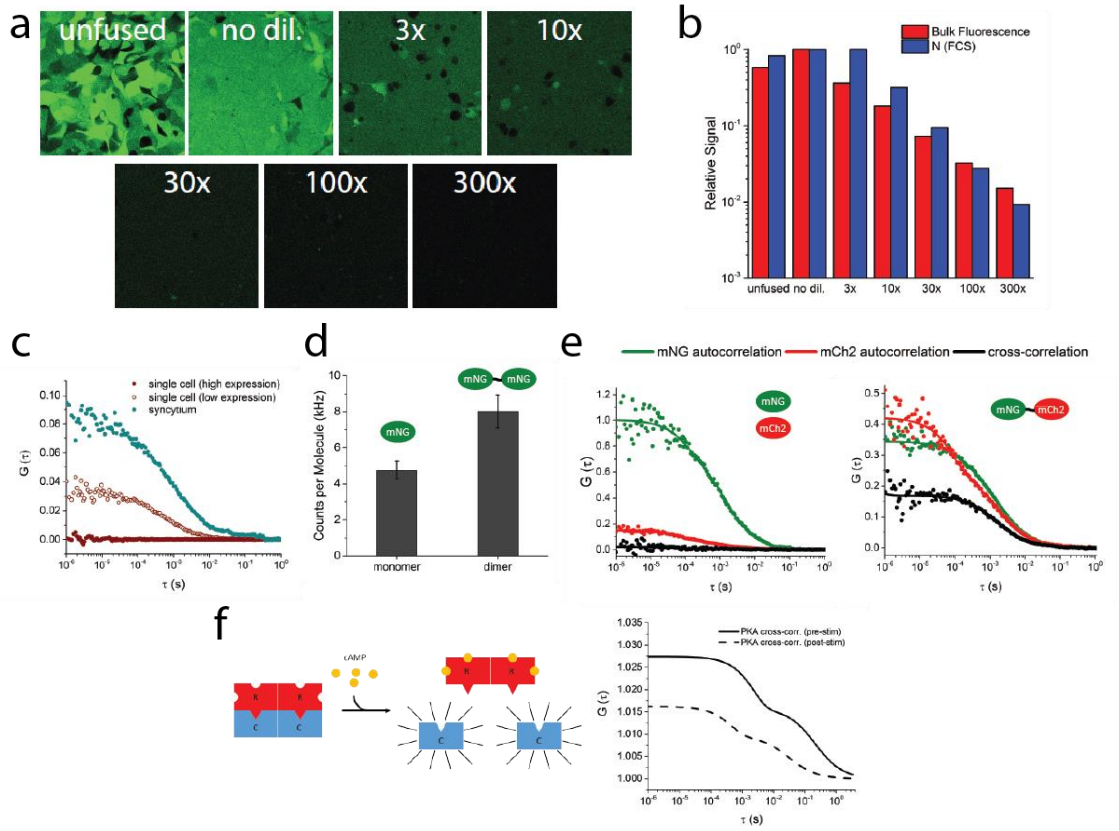

Figure 4.3 SPReAD-FCS observations of cytosolic protein complexes. The equilibrium concentration of labeled proteins in syncytia is controllable by adjusting the co-plating ratio. Here, we show that it may be varied over two orders of magnitude but the upper limit is constrained only by the number of cells in the culture vessel and the diffusion time of labeled protein complexes compared to syncytium lifetime.(b) Quantification of the data shown in (a), using confocal pixel values (red) and fluorescence correlation spectroscopy (blue). Absolute concentrations, calculated from the FCS data, are given above. (c) High intracellular concentrations of labeled proteins prohibit fluorescence correlation spectroscopy due the comparably low fluorescence fluctuations relative to the average signal (solid red circles). SPReAD removes concentration limits on FCS and diffusive properties in syncytia (solid blue circles) mirror those in unfused cells (hollow red circles). (d) Brightness analysis may be used to discriminate between monomeric and dimeric species in the cytoplasm of large syncytia and is useful for studying the stoichiometry of a single oligomer component. (e) Cross-correlation spectroscopy is useful for studying heteromeric interactions. Here, mNeonGreen and mCherry produce an appreciable cross-correlation (black line) when covalently joined (right) but not when co-transfected (left). In both cases, auto-correlations for each protein are clearly discernable (green and red lines). (f) FCS in massive syncytia may be used to study functional differences in protein oligomerization. Protein Kinase A regulatory and catalytic subunits form complexes in the baseline state, indicating repressed activity. Stimulation of adenylyl cyclase generated cAMP, causing complex dissociation and increased activity.

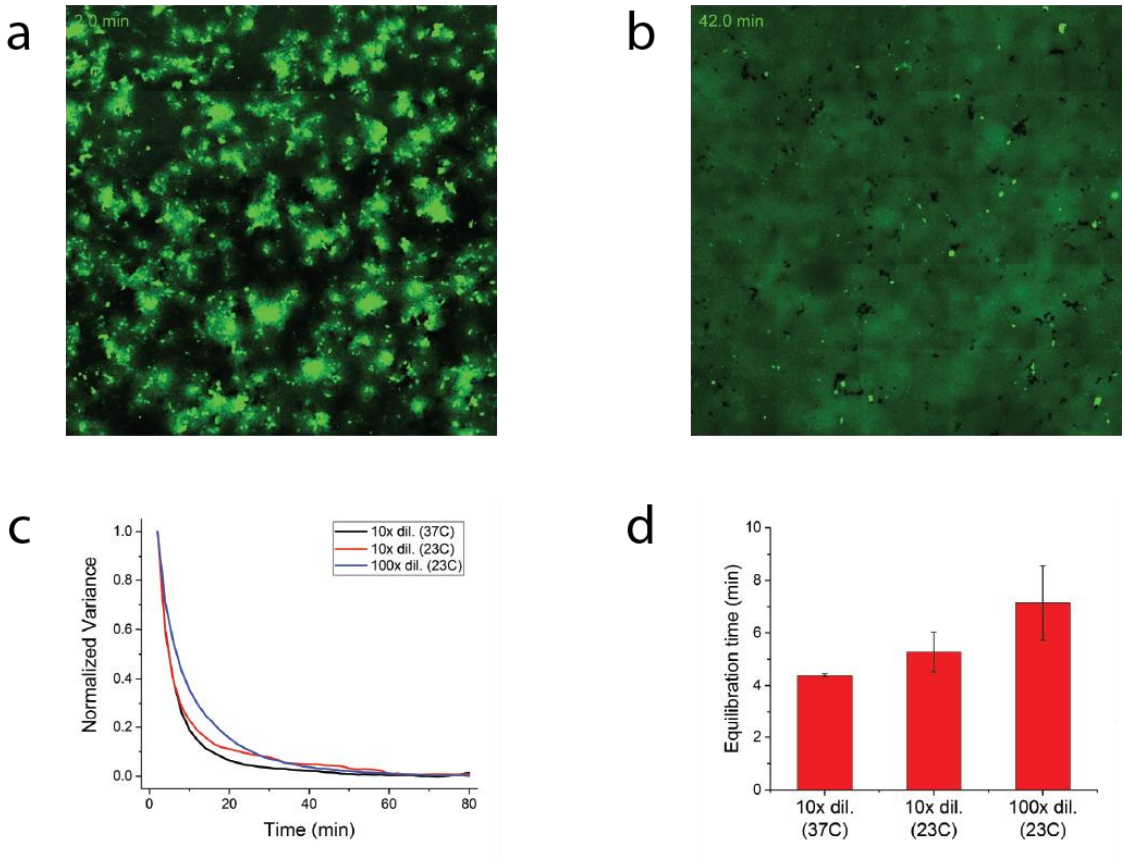

Figure 4.4 Dynamics of cell fusion and protein complex diffusion. (a) Image of U2OS VSVG-expressing cells (mixture of mNG and unlabeled cells) immediately after pH drop. mNeonGreen has already begun to diffuse out of its parent cells into the larger syncytium, but is still very heterogeneous across the imaging dish. (b) Image of the same cells as (a) at 42 minutes after pH drop. Fluorescence is now homogenously distributed throughout the syncytium. (c) Kinetics of mNeonGreen diffusion in the VSVG-induced syncytium, as measured by the signal variance across the image. Equilibrium is reached within 30-60 minutes for all conditions (different co-plating ratios and temperatures). (d) Exponential decay times for image variance in syncytia. Equilibration takes longer for higher co-plating ratios and lower temperatures, as expected for 3D diffusion of macromolecules.

continually reshaped by diffusion until reaching a uniform steady-state level after ~30 minutes. Due to its diffusive underpinnings, this equilibration time will depend on the size of protein complexes being studied, their interactions with static cellular components, experimental conditions (e.g. temperature) and the ratio of expressing and non-expressing cells. Overall, the kinetics of cell fusion and protein redistribution suggest two possible modes of measurement. Measurements made in the non-equilibrium stage will most accurately report on stoichiometry of complexes because assemblies are given minimal time to disassemble before recording. However, concentration measurements during this stage are unreliable due to the heterogeneity across the imaging dish. In contrast, equilibrium stage measurements can be used to estimate cellular concentrations, with a known plating ratio, but may perturb complexes with fast dissociation rates. This flexibility renders SPReAD a versatile method for quantification of oligomeric state and cellular expression levels.

Fluorescence correlation spectroscopy in mega-syncytia

Since its inception in the 1970s, fluorescence correlation spectroscopy has become a valuable tool for investigation of molecular transport and interactions [13–15]. Autocorrelation analysis readily provides information about per-particle brightness and local concentrations while two-color cross-correlation can probe molecular associations. While both FCS and FCCS are regularly used inside cells, a number of complications present themselves in these cases. Many cellular proteins fall outside the ideal concentration range of FCS studies, limiting the accuracy of these measurements or rendering them inaccessible. Furthermore, most fitting models assume an infinite pool of diffusive species such that molecular motions are

unconstrained and photobleaching is inconsequential. However, this is hardly the case within the cellular environment and is known to lead to artifacts. Cell fusion is a promising means to address both of these limitations as concentrations can be arbitrarily adjusted to fall inside the FCS range and the relatively large size of the syncytium, compared to a single cell, can serve to alleviate the effects of constrained motion or bleaching.

To demonstrate these benefits, we compared FCS curves obtained in unfused cells with those in syncytia (Figure 4.4c). In cells, transient mNeonGreen expression from a CMV promoter often failed to produce satisfactory autocorrelation curves, owing to the high cytosolic concentration of labeled protein following transient transfection. FCS tended to fail when the fluorophore levels exceeded ~1 μM, which is within the range of normal protein abundance [16]. Cells with lower mNeonGreen concentrations produced correlations with an average residence time of 2.2 ± 1.3 ms and corresponding diffusion coefficient of 10 ± 5.8 $\mu m^2/s$, which is comparable to reported values for GFP in mammalian cells. Syncytial FCS curves yielded similar times and diffusion coefficients (1.2 ± 0.1 ms; 13 ± 1.1 $\mu m^2/s$), implying that cell fusion does not significantly perturb the intracellular environment. Furthermore, cellular measurements suffered from bleaching, manifested as a change in G(0) over time, and higher variation in measured diffusing times, likely due to the poorer data quality (lower correlation values) and altered mobility near bounding membranes. By comparison, syncytial data was far more stable due to the larger pool of diffusing fluorophores and increased homogeneity.

Brightness analysis and cross-correlation spectroscopy are two valuable modes of investigation of protein-protein interactions within the cellular environment [17,18]. In order to evaluate these modes in conjunction with cell fusion, we compared measurements made with covalent dimers of fluorescent proteins to the corresponding monomeric proteins. mNG dimers were 1.7 times brighter than monomers; assuming negligible quenching, this suggests a maturation efficiency of 85% for mNG, which is on par with that of other green/yellow fluorescent proteins (Figure 4.4d). FCCS of an mNeonGreen-mCherry2 covalent dimer yielded a 58% dimer population while a cotransfection of the monomeric proteins showed negligible cross-correlation amplitude (Figure 4.4e). In addition to brightness and cross-correlation analyses, photon counting histograms, dwell time distributions, photon anti-bunching and single-molecule FRET have been used to examine oligomerization states could be used in conjunction with SPReAD sample preparation.

Next, we used syncytial FCS to study the oligomerization of protein kinase A (PKA), a Ser/Thr kinase that functions in the cAMP-dependent pathway of GPCR signaling (Figure 4.3e). Upon GPCR activation, adenylyl cyclase catalyzes the conversion of ATP into cAMP, causing PKA regulatory subunits to dissociate from catalytic subunits, which are then free to phosphorylate downstream targets. Syncytial FCS of YFP-tagged catalytic subunits and mCherry-tagged regulatory subunits revealed a significant cross-correlation, indicating functional repression in the baseline state. Upon stimulation with the adenylyl cyclase activator forskolin and the phosphodiesterase inhibitor IBMX, cross-correlation amplitude decreased, reflecting cAMP-induced dissociation of subunits and mirroring previous results obtained by

FCS [19]. By extending the concentration range of FCS and mitigating unwanted effects due to confined cellular volumes, SPReAD holds promise for understanding functional differences in oligomerization.

Single molecule imaging of membrane protein complexes

The biomedical significance of membrane receptors has motivated comprehensive investigation of their basic structures and mechanisms of action. Oligomerization is known to play a role in the function of all major receptor types (metabotropic, ionotropic and tyrosine kinases) and thus, considerable effort has been made to elucidate their interaction profiles. From a single-molecule perspective, subunit counting in oocytes has been the widely used approach, with many receptors being studied after controlled mRNA injection to control receptor levels [20]. However, the concentration-dependence of oligomerization has always been at odds with the sub-physiological expression employed in this technique. We aimed to explore whether cell fusion combined with single molecule imaging could lift this restriction to allow single molecule imaging after physiological assembly of receptor complexes.

To test whether cell fusion could dilute membrane receptors from their initial levels, we expressed an mNG-tagged derivative of the beta-2 adrenergic receptor in a subpopulation of cells, which were co-plated with VSVG-expressing neighbors. ADRβ2 is a prototypical G protein coupled receptor and is known to form both homodimers as well as heterodimers with other members of the GPCR family. Unfused mNG-ADRβ2 cells generally showed diffuse fluorescence due to overlap of receptor point spread functions on the detector. After cell fusion and incubation at 37C

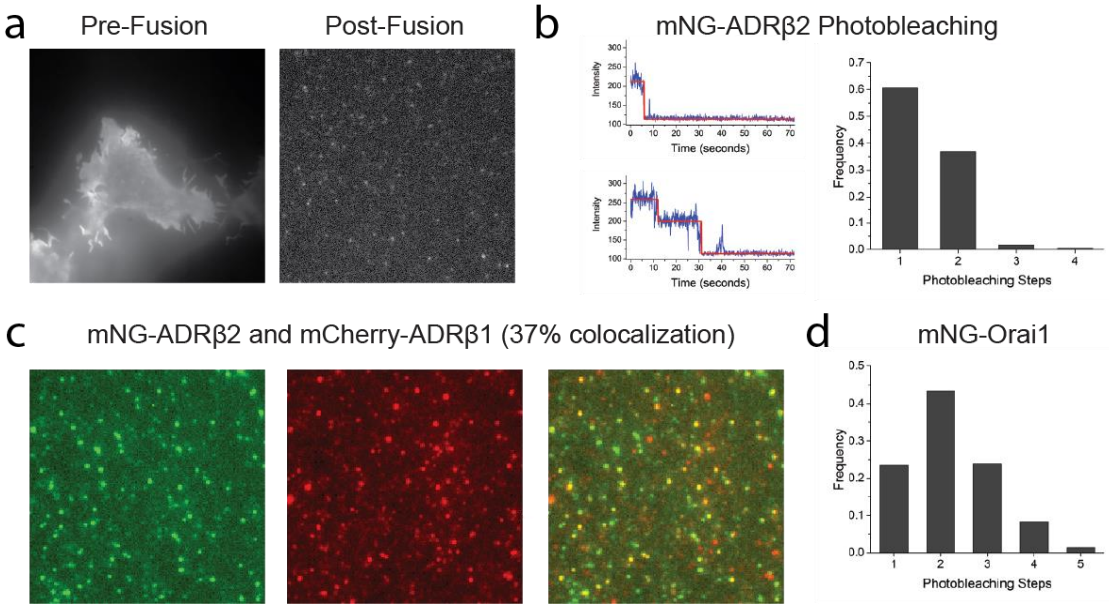

Figure 4.5 SPReAD Imaging of Membrane Protein Oligomers. (a) Total internal reflection fluorescence image of a cell expressing mNG-ADRβ2 (left) and single mNG-ADRβ2 puncta after cell fusion (right). Unfused cells show fluorescence haze characteristic of membrane proteins in TIRF, due to overlap of emitter point spread functions on the camera. Meanwhile, single receptor complexes are clearly discernable in syncytia. (b) Fluorescence time traces for single mNG-ADRβ2 puncta showing one-step and two-step photobleaching and the corresponding histogram of bleach steps. (c) Green, red and overlay images of mNG-ADRβ2 and mCherry-ADRβ1 revealing substantial colocalization of adrenergic receptors after cell fusion. (d) Stepwise photobleaching for the calcium-release activated channel Orai1 showing character ranging from monomer to tetramer.

for 1 hour, individual receptor complexes were clearly discernible and mobile within the plasma membrane (Figure 4.5a). Immobile receptors were occasionally observed, with the disparity in receptor mobility perhaps mirroring the heterogeneity in actin structures observed within the syncytium. Receptor concentration across the imaging dish was also fairly uneven, even 2-3 hours after fusion, likely due to the much slower diffusion rate for proteins in the membrane compared to the cytoplasm. Although this

precludes equilibrium stage measurements for concentration estimation, stoichiometry measurements remain accessible by cell fusion and single molecule imaging.

Syncytia were fixed with paraformaldehyde to immobilize receptor complexes and facilitate stoichiometry determination by stepwise photobleaching. ADRβ2 puncta showed distinct bleach steps, with mNeonGreen proving to be an excellent fluorophore for single molecule imaging (Figure 4.5b). Analysis of the receptor population revealed that ADRβ2 was fairly evenly distributed between monomeric and dimeric and dimeric states, with 37% of photobleaching traces showing two bleach steps, signifying a 47% dimer population after accounting for mNG's maturation efficiency. We also examined the subunit stoichiometry of Orai1, a calcium-selective ion channel which forms the central pore of the calcium release-activated channel. Most Orai1 puncta bleached in 1-4 steps, as expected for the putative tetramer (Figure 4.5d). However, the distribution was significantly sub-tetrameric compared to previous measurements in oocytes, perhaps due to the presence of endogenous unlabeled Orai1 in mammalian cells or interactions with other cellular proteins [21,22]. Targeted knockdown of endogenous proteins or careful choice of cell lines may be used to refine understanding of physiologically-relevant oligomerization in specific tissue types.

To demonstrate the ability the probe heteromeric association with cell fusion and single molecule imaging, we expressed mNG-ADRβ2 with mCherry-ADRβ1 in a subset of cells. After fusion, the respective color channels showed a high degree of colocalization with 37% of green spots overlapping with red spots, agreeing well with published SiMPull results (Figure 4.5c). Unfortunately the poor photophysics and

relatively low maturation efficiency of mCherry prohibit accurate stepwise photobleaching in the red channel. However, thorough investigation of the stoichiometric character of multi-component complexes has been achieved by multiple complementary experiments [23]. Alternatively, enzymatic labeling methods may be used for high-efficiency orthogonal labeling with bright organic dyes in multiple spectral channels, but nonspecific binding of excess label remains problematic. Future developments in fluorescent protein technology, specifically targeted toward improving single-molecule photophysics, will facilitate stoichiometry measurements.

Ligand-dependent oligomerization of epidermal growth factor receptor

One of the primary evolutionary advantages conferred by oligomerization is new modes of regulatory control over protein activity. Allosteric oligomerization is known to play a role in the mechanisms of both metabotropic receptors and receptor tyrosine kinases, with extracellular ligands modulating the formation of dimers or higher order structures. Monomer-oligomer transitions can prime receptors for downstream signaling events, such as posttranslational modifications or the recruitment of adapter proteins. As an example of ligand-dependent multimerization, we looked at epidermal growth factor receptor—a member of the receptor tyrosine kinase family whose abnormal regulation has been implicated in a number of human cancers [24]. The canonical model for receptor activation asserts that EGFR is monomeric in the plasma membrane prior to stimulation, whereupon it is driven to dimerize upon binding of its cognate ligands, resulting in autophosphorylation of

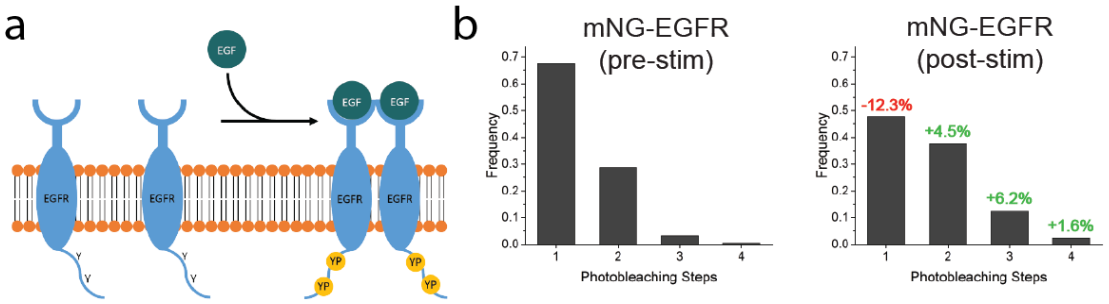

Figure 4.6 Ligand-induced oligomerization of EGFR (a) Cartoon of the canonical model for epidermal growth factor receptor activation. Growth factor binding stimulates EGFR dimerization and autophosphorylation of tyrosine residues on EGFR's cytoplasmic tail, leading to recruitment of downstream signaling proteins. (b) Histograms of EGFR oligomerization before (left) and after (right) EGF stimulation. Although EGFR is largely monomeric prior to growth factor addition, there is a substantial dimer fraction as well. After stimulation, this dimer component increases in abundance and higher-order oligomers are also formed.

tyrosine residues on its cytoplasmic tail and recruitment of specific effector proteins (Figure 4.6a).

Although the EGFR pathway has been extensively studied using both bulk and single molecule approaches, there are still open questions about receptor oligomerization. There is increasing evidence that pre-formed dimers of EGFR exist on the cell surface prior to ligand stimulation and that EGFR is capable of forming higher-order oligomers that may function in receptor activation. To examine each of these possibilities, we expressed an mNeonGreen-tagged EGFR on the cell surface and performed stepwise photobleaching measurements in large syncytia. Even in its baseline state, EGFR was found to be significantly dimeric, with 29% of traces bleaching in two steps. Upon stimulation with EGF, this dimer fraction increased substantially and higher-order oligomers (trimers and tetramers) were also observed (Figure 4.5b). Together, these results support a model where at least some EGFR

signaling is accomplished by conformational changes in pre-formed dimers and trans-activation by higher-order oligomers. The use of SPReAD to study ligand-dependent oligomerization of EGFR validates its potential for studying transient interactions. Future studies may aim to visualize the recruitment of specific factors such as GRB2 or PLCγ1, which relay extracellular signals to downstream effectors, or the impact of pharmacological agents or EGFR mutations on oligomerization propensity.

DISCUSSION

By achieving detergent-free dilution of protein complexes after physiological assembly, SPReAD facilitates minimally perturbative measurements of subunit stoichiometry for both cytosolic and membrane-bound oligomers. Furthermore, the use of VSVG as a means of accomplishing cell fusion is highly efficient, nontoxic and requires only a simple buffer exchange. In contrast, existing methods for probing oligomerization are significantly more complex or disruptive. Use of stimulated emission depletion to reduce excitation volumes by >100-fold can extend the upper limit on FCS measurements but requires complicated optics and enhances photobleaching. As mentioned earlier, single molecule pulldown approaches can probe molecular heterogeneity in oligomerization but extract protein complexes from their native environment [4,25]. Meanwhile, efforts to apply conventional imaging or localization microscopy to stoichiometry analysis rely on *a priori* assumptions about protein distribution or fluorophore blinking [26,27]. Considered amongst these other methods, SPReAD holds a unique place, affording single molecule sensitivity for oligomerization studies while maintaining a more physiologically relevant setting.

Although the use of cell fusion for dilution is both simple and rapid, the dynamics of various intracellular processes need to be considered when interpreting results. Syncytia form almost instantly after pH drop, but protein redistribution is diffusion-limited and thus, much slower for membrane-bound proteins undergoing 2D diffusion compared to cytosolic proteins moving much more rapidly in 3D. This yields two possible modes of analysis: an equilibrium mode, where the final concentration of labeled protein complexes is uniform and proportional to the initial concentration (divided by the co-plating ratio), and a non-equilibrium mode, where concentrations across the imaging dish are non-uniform. The latter mode is most conducive to measuring subunit stoichiometry as it minimizes time during which protein complexes can dissociate and was typically in the range of 10-45 minutes for all proteins studied here. Beyond diffusion times, syncytia appeared to be morphologically stable for 5-6 hours but it is still largely unclear how the intracellular environment is reshaped during the fusion process. Future work will aim to understand how the syncytium transition affects major signaling pathways.

A number of strategies may be used to augment the SPReAD technique and build upon its versatility. The non-equilibrium mode of measurement lends itself to single-cell analysis and is readily accomplished by using large co-plating ratios and limiting the time from fusion to measurement/fixation such that proteins from neighboring labeled cells do not mix. For true measurement of physiologically relevant interactions, endogenous proteins can be labeled using prevalent genome editing techniques [28] or, ideally, primary cells can be extracted from genetically-modified organisms to understand tissue-specific phenotypic variation. Future work

may also extend SPReAD applications beyond the cytoplasm and plasma membrane by making using of membrane contact sites between organelles, examining proteins which exchange between the cytoplasm and other compartments or by retargeting of proteins through signal sequence engineering.

By removing limits on expression levels compatible with single molecule experiments without requiring chemical agents for dilution, SPReAD permits minimally perturbative measurements in a variety of cell lines. Aside from the FCS- and stepwise photobleaching-based analyses of subunit stoichiometry highlighted here, we expect SPReAD to enhance other methods traditionally limited to working at low concentrations such as smFRET, single-particle tracking and single molecule spectroscopy, thus providing a powerful addition to the single molecule toolkit.

REFERENCES

1. T. Berggård, S. Linse, and P. James, "Methods for the detection and analysis of protein-protein interactions.," Proteomics **7**, 2833–42 (2007).

2. B. N. G. Giepmans, S. R. Adams, M. H. Ellisman, and R. Y. Tsien, "The fluorescent toolbox for assessing protein location and function.," Science **312**, 217–24 (2006).

3. M. H. Ulbrich and E. Y. Isacoff, "Subunit counting in membrane-bound proteins.," Nat. Methods **4**, 319–21 (2007).

4. A. Jain, R. Liu, B. Ramani, E. Arauz, Y. Ishitsuka, K. Ragunathan, J. Park, J. Chen, Y. K. Xiang, and T. Ha, "Probing cellular protein complexes using single-molecule pull-down.," Nature **473**, 484–8 (2011).

5. S. Kalipatnapu and A. Chattopadhyay, "Membrane protein solubilization: recent advances and challenges in solubilization of serotonin1A receptors.," IUBMB Life **57**, 505–12 (2005).

6. I. Barde, P. Salmon, and D. Trono, "Production and titration of lentiviral vectors.," Curr. Protoc. Neurosci. **Chapter 4**, Unit 4.21 (2010).

7. K. A. K. Tanaka, K. G. N. Suzuki, Y. M. Shirai, S. T. Shibutani, M. S. H. Miyahara, H. Tsuboi, M. Yahara, A. Yoshimura, S. Mayor, T. K. Fujiwara, and A. Kusumi, "Membrane molecules mobile even after chemical fixation.," Nat. Methods **7**, 865–6 (2010).

8. A. Gottesman, J. Milazzo, and Y. Lazebnik, "V-fusion: a convenient, nontoxic method for cell fusion.," Biotechniques **49**, 747–50 (2010).

9. E. Wang, R. K. Cross, and P. W. Choppin, "Involvement of microtubules and 10-nm filaments in the movement and positioning of nuclei in syncytia.," J. Cell Biol. **83**, 320–37 (1979).

10. F. Steinberg, S. D. Gerber, T. Rieckmann, and B. Trueb, "Rapid fusion and syncytium formation of heterologous cells upon expression of the FGFRL1 receptor.," J. Biol. Chem. **285**, 37704–15 (2010).

11. B. M. Ogle, M. Cascalho, and J. L. Platt, "Biological implications of cell

fusion.," Nat. Rev. Mol. Cell Biol. **6**, 567–75 (2005).

12. D. Duelli and Y. Lazebnik, "Cell-to-cell fusion as a link between viruses and cancer.," Nat. Rev. Cancer **7**, 968–76 (2007).

13. D. Magde, E. Elson, and W. W. Webb, "Thermodynamic Fluctuations in a Reacting System—Measurement by Fluorescence Correlation Spectroscopy," Phys. Rev. Lett. **29**, 705–708 (1972).

14. K. Bacia, S. A. Kim, and P. Schwille, "Fluorescence cross-correlation spectroscopy in living cells.," Nat. Methods **3**, 83–9 (2006).

15. S. T. Hess, S. Huang, A. A. Heikal, and W. W. Webb, "Biological and chemical applications of fluorescence correlation spectroscopy: a review.," Biochemistry **41**, 697–705 (2002).

16. M. Beck, A. Schmidt, J. Malmstroem, M. Claassen, A. Ori, A. Szymborska, F. Herzog, O. Rinner, J. Ellenberg, and R. Aebersold, "The quantitative proteome of a human cell line.," Mol. Syst. Biol. **7**, 549 (2011).

17. Y. Chen, J. D. Müller, Q. Ruan, and E. Gratton, "Molecular brightness characterization of EGFP in vivo by fluorescence fluctuation spectroscopy.," Biophys. J. **82**, 133–44 (2002).

18. P. Schwille, F. J. Meyer-Almes, and R. Rigler, "Dual-color fluorescence cross-correlation spectroscopy for multicomponent diffusional analysis in solution.," Biophys. J. **72**, 1878–86 (1997).

19. H. Park, C. Pack, M. Kinjo, and B.-K. Kaang, "In vivo quantitative analysis of PKA subunit interaction and cAMP level by dual color fluorescence cross correlation spectroscopy.," Mol. Cells **26**, 87–92 (2008).

20. R. J. Arant and M. H. Ulbrich, "Deciphering the subunit composition of multimeric proteins by counting photobleaching steps.," Chemphyschem **15**, 600–5 (2014).

21. A. Penna, A. Demuro, A. V Yeromin, S. L. Zhang, O. Safrina, I. Parker, and M. D. Cahalan, "The CRAC channel consists of a tetramer formed by Stim-induced dimerization of Orai dimers.," Nature **456**, 116–20 (2008).

22. W. Ji, P. Xu, Z. Li, J. Lu, L. Liu, Y. Zhan, Y. Chen, B. Hille, T. Xu, and L.

Chen, "Functional stoichiometry of the unitary calcium-release-activated calcium channel.," Proc. Natl. Acad. Sci. U. S. A. **105**, 13668–73 (2008).

23. A. Jain, E. Arauz, V. Aggarwal, N. Ikon, J. Chen, and T. Ha, "Stoichiometry and assembly of mTOR complexes revealed by single-molecule pulldown.," Proc. Natl. Acad. Sci. U. S. A. **111**, 17833–8 (2014).

24. A. Gschwind, O. M. Fischer, and A. Ullrich, "The discovery of receptor tyrosine kinases: targets for cancer therapy.," Nat. Rev. Cancer **4**, 361–70 (2004).

25. H.-W. Lee, T. Kyung, J. Yoo, T. Kim, C. Chung, J. Y. Ryu, H. Lee, K. Park, S. Lee, W. D. Jones, D.-S. Lim, C. Hyeon, W. Do Heo, and T.-Y. Yoon, "Real-time single-molecule co-immunoprecipitation analyses reveal cancer-specific Ras signalling dynamics.," Nat. Commun. **4**, 1505 (2013).

26. A. G. Godin, S. Costantino, L.-E. Lorenzo, J. L. Swift, M. Sergeev, A. Ribeiro-da-Silva, Y. De Koninck, and P. W. Wiseman, "Revealing protein oligomerization and densities in situ using spatial intensity distribution analysis.," Proc. Natl. Acad. Sci. U. S. A. **108**, 7010–5 (2011).

27. F. Fricke, J. Beaudouin, R. Eils, and M. Heilemann, "One, two or three? Probing the stoichiometry of membrane proteins by single-molecule localization microscopy.," Sci. Rep. **5**, 14072 (2015).

28. J. Stewart-Ornstein and G. Lahav, "Dynamics of CDKN1A in Single Cells Defined by an Endogenous Fluorescent Tagging Toolkit.," Cell Rep. **14**, 1800–1811 (2016).

CHAPTER 5

CONCLUSIONS AND FUTURE DIRECTIONS

SUMMARY

Fluorescence microscopy and spectroscopy have long held a unique place amongst modes of analysis for biological systems. The ability to highlight specific biomolecules and report on a wide variety of quantifiable parameters—such as expression levels, molecular organization and dynamics—both *in vitro* or *in situ* has been invaluable to understanding complexity at scales ranging from single molecules to whole tissues and has served a complementary role to information derived from bulk biochemistry, electron microscopy and structural biology. The work described in this thesis encompasses a broad set of efforts to extend the capabilities of fluorescence approaches and to apply cutting-edge methods to relevant problems in molecular biology.

The breadth of technological development comprised in this dissertation reflects the tremendous progress in fluorescence microscopy over the past decade. Nonlinear microscopies and new tissue clearing approaches have laid the groundwork for dynamic functional imaging of the brain and mapping of neuronal connectomes in an unprecedented manner. Single molecule and super resolution imaging have enjoyed an especially prosperous period, with a surge in new techniques to surpass the diffraction limit and to image single molecules in three dimensions with high speed and sensitivity. Furthermore, there has been a push to develop methods that more accurately measure the physiological state and to minimize perturbations introduced

by sample preparation or imaging. These underlying themes have motivated much of the work here and have enabled new imaging-based modes of inquiry throughout biology.

DEEP-TISSUE NONLINEAR IMAGING

Nonlinear microscopies based on multiphoton excitation or harmonic generation have gained a foothold in deep-tissue imaging because of their ability to collect all emissions without a need to spatially filter background and their use of longer wavelengths for excitation [1,2]. Although these modalities have been around for over two decades, fundamental processes governing excitation and emission in turbid media are still not completely understood due to the complexity of interactions between light and the sample. Chapter 2 presents a simplified system to decouple excitation and emission losses in two-photon microscopy, permitting a thorough analysis of how these effects depend on fundamental parameters in the optical pathway [3]. Application of this system to studying two-photon excitation uncovered an NA-dependence that was previously unknown and yielded data on effective excitation NAs for each lens as a function of sample scattering length. The latter phenomena was modeled as a γ^2 factor that modifies the traditional $F \propto P^2$ relation for two-photon microscopy. Measurements of epifluorescence collection reinforced previous notions about the superiority of low-magnification objective lenses for detecting scattered photons while also revealing a crucial OBA/OFA parameter that scales with both the decay length of detection as well as beam divergence.

Furthermore, our data comparing the performance of a new class of multiphoton-optimized objective lenses serves as a valuable resource for the microscopy community. As more and more labs seek to image deeper into brain and other types of tissue using a combination of higher-order nonlinear processes, new laser sources and optical clearing methods, a fundamental understanding of the tissue scattering and its effects on multiphoton excitation and fluorescence detection are essential.

HIGH-SPEED IMAGING OF FINE AXIAL TOPOGRAPHY

The breaking of the diffraction limit on optical fluorescence imaging was one of the largest scientific developments over the past decade. Although there remains skepticism about the genuine utility of these approaches for understanding biology, given the added experimental complexity they introduce and potential for artifacts, it is easy to forget that they overcame a fundamental limit in microscopy that had stood for over a century. That reason alone may have been enough to warrant their recognition by the Nobel Committee in 2014 and, as the techniques have become more engrained in the biophysical toolbox, we have witnessed a number of applications that have benefited from their combination of nanoscale resolution with molecular specificity. Because these breakthroughs required novel perspectives on image formation and some outside-the-box thinking [4–7], today's microscopes are significantly different from their predecessors and typically require a certain level of expertise to understand the workflow spanning sample preparation to image analysis. Furthermore, while the earliest iterations strove to push the spatial resolution limit as far as possible—often ignoring the thresholds for light doses that healthy cells can

tolerate—there is an increasing emphasis on developing whole-cell or whole-organism volumetric imaging methods that faithfully capture physiologically relevant biological processes [8,9]. In pursuit of these goals, the field of microscopy has expanded the boundaries of the metaphorical pyramid of tradeoffs (spatial resolution, temporal resolution, signal-to-noise and sample health) and created a new Swiss army knife of instruments for the coming years.

Amongst the broader set of challenges facing the super-resolution community, precise imaging in the axial dimension has been particularly difficult. The asymmetric nature of the point spread function for most widefield and point-scanning microscopies has disproportionately smeared features in the longitudinal direction and prohibited molecular-scale resolution, even with many advanced imaging techniques. To address these limitations, interferometric approaches have proven advantageous [10,11]. In particular, scanning angle interferometric microscopy (SAIM) permits axial topographic mapping with sub-10 nm precision in living cells. Chapter 3 describes a new galvo-based azimuthal scanning platform (CircleScan) that accelerates SAIM acquisitions by an order of magnitude and also improves data quality in traditional TIRF or widefield microscopy. CircleScan SAIM performs similarly to conventional SAIM with regard to providing molecular-scale precision, despite polarization complications. Furthermore, TIRF-activation of features prior to SAIM improves contrast and enables SAIM even in the presence of substantial background fluorescence. These advances have yielded a new imaging modality with the best combination of axial precision and temporal resolution in the super-resolution toolbox.

Although SAIM is already a quite powerful approach for topographic imaging, the technique is still in its infancy. A thorough characterization of various noise sources (Poisson noise, out-of-focus fluorescence, etc.) and their effects on axial precision is critically needed for data assessment. The contributions of practical experimental factors such as beam divergence, mirror tilt and substrate roughness is also important. Furthermore, current SAIM fitting routines are fairly computationally intensive, requiring tens of minutes for a single reconstruction. Faster approaches based on simpler fits or calculations and GPU implementations may enable SAIM with real-time data processing for on-the-fly topographic rendering. Photoactivation has proven itself to be a useful addition to SAIM imaging by greatly enhancing feature contrast. Non-TIR activation modes based on point-scanning are essential to extend SAIM imaging beyond membrane-associated features into the rest of the cell. For applications where cells are cultured on coverslips, particularly for TIR-activation SAIM, methods are still needed to resolve height ambiguity between semi-periodic intensity profiles. Finally, one of the most exciting areas of future development for SAIM relies on combinatorial applications with other super-resolution and single-molecule imaging methods. Methods for lateral resolution enhancement based on structured illumination or localization microscopy will enable precise imaging in all three dimensions while improvements in sensitivity will enable direct measurement of single molecule axial movements. As SAIM technology progresses, it promises new modes to analyze cell motility, membrane topography in disease states, mechanisms of endocytosis and fine 3D localization of intracellular features.

IN SITU SINGLE MOLECULE IMAGING

As fluorescence microscopy and spectroscopy move forward, there is an increasing emphasis on accurate quantification and measurements that reflect physiological states. One regime where this has been especially challenging is in the assessment of protein complex stoichiometry. Previous approaches relying on sub-physiological expression or detergent-based dilution come with a host of potential complications that can misrepresent the biologically relevant oligomerization state [12,13]. Chapter 4 presents a new method for single-molecule stoichiometry determination that relies on virus-mediated cell fusion to achieve protein complex dilution after physiological assembly. We demonstrate the fusion is rapid and that mobile protein complexes remain in a semi-native environment where they are diluted by spreading into adjacent spaces devoid of fluorescently labeled oligomers. After dilution, subunit stoichiometry may be probed by correlation spectroscopy or stepwise photobleaching for cytosolic or membrane protein complexes, respectively. From a broader perspective, our method represents a general strategy to extend single molecule imaging into the cellular milieu without relying on inefficient labeling or subphysiological expression.

There are already many applications where accurate subunit stoichiometry determination would provide important mechanistic details about cell signaling. Having looked at the oligomerization dynamics of epidermal growth factor receptor, it would be interesting to examine how assembly is perturbed in the presence of known oncogenic mutations or in the presence of other HER2 partners. Furthermore, the recruitment of downstream effectors remains an intriguing area of inquiry, particularly

for understanding the temporal dynamics of EGFR signaling. Besides EGFR, there are countless other membrane receptors where the SPReAD technique would be useful for analyzing oligomerization. There are also opportunities to expand upon the basic technology to facilitate a broader set of applications. New CRISPR-based tools for fluorescent tagging of endogenous proteins will enable true physiological expression levels in native tissue rather than the heterologous expression systems used in the initial SPReAD proof-of-principle. Currently, SPReAD imaging is limited to studying cytosolic and membrane protein complexes but this may be extended to other organelles by exploiting membrane-ER contacts or by isolating organelles and fusing with supported lipid bilayers. Extension of the SPReAD technique to other eukaryotic cell lines such as plant cells or yeast would also be an exciting area of development, but would require new protocols to deal with their bounding cell walls. Finally, although our method has been validated with a number of known oligomers, thorough assessment of fusion effects on various cell signaling pathways remains an important control for understanding biologically relevant oligomerization states.

OUTLOOK

From its infancy nearly three decades ago, single molecule imaging has come a long way. The last decade has been especially fruitful, with the boom in super-resolution imaging recruiting an army of researchers to drive technology development and biological applications. The scanning angle interference microscopy and single molecule stoichiometry work described in this dissertation fall in line with broader goals to extract meaningful information from previously inaccessible regimes using

minimally perturbative methods. Other approaches to achieve dynamic high-resolution imaging with low phototoxicity or to probe single-molecule heterogeneity inside live cells promise new perspectives on oligomerization, cytoskeletal dynamics, neural development, gene expression, transcription factor binding and a wide variety of other important phenomena. These and other functional applications of exotic microscopy tools signify a giant leap forward in the longstanding dream to watch biology unfold at the nanoscale and herald a new age where imaging can begin to shed light on phenomena typically relegated to biochemical investigation.

REFERENCES

1. W. Denk, J. Strickler, and W. Webb, "Two-photon laser scanning fluorescence microscopy," Science (80-.). **248**, 73–76 (1990).

2. W. R. Zipfel, R. M. Williams, and W. W. Webb, "Nonlinear magic: multiphoton microscopy in the biosciences.," Nat. Biotechnol. **21**, 1369–77 (2003).

3. A. Singh, J. D. McMullen, E. A. Doris, and W. R. Zipfel, "Comparison of objective lenses for multiphoton microscopy in turbid samples," Biomed. Opt. Express **6**, 3113–3127 (2015).

4. T. A. Klar, S. Jakobs, M. Dyba, A. Egner, and S. W. Hell, "Fluorescence microscopy with diffraction resolution barrier broken by stimulated emission," Proc. Natl. Acad. Sci. **97**, 8206–8210 (2000).

5. M. J. Rust, M. Bates, and X. Zhuang, "Sub-diffraction-limit imaging by stochastic optical reconstruction microscopy (STORM).," Nat. Methods **3**, 793–5 (2006).

6. E. Betzig, G. H. Patterson, R. Sougrat, O. W. Lindwasser, S. Olenych, J. S. Bonifacino, M. W. Davidson, J. Lippincott-Schwartz, and H. F. Hess, "Imaging intracellular fluorescent proteins at nanometer resolution.," Science **313**, 1642–5 (2006).

7. M. G. L. Gustafsson, "Surpassing the lateral resolution limit by a factor of two using structured illumination microscopy.," J. Microsc. **198**, 82–7 (2000).

8. B.-C. Chen, W. R. Legant, K. Wang, L. Shao, D. E. Milkie, M. W. Davidson, C. Janetopoulos, X. S. Wu, J. A. Hammer, Z. Liu, B. P. English, Y. Mimori-Kiyosue, D. P. Romero, A. T. Ritter, J. Lippincott-Schwartz, L. Fritz-Laylin, R. D. Mullins, D. M. Mitchell, J. N. Bembenek, A.-C. Reymann, R. Bohme, S. W. Grill, J. T. Wang, G. Seydoux, U. S. Tulu, D. P. Kiehart, and E. Betzig, "Lattice light-sheet microscopy: Imaging molecules to embryos at high spatiotemporal resolution," Science (80-.). **346**, 1257998–1257998 (2014).

9. A. G. York, P. Chandris, D. D. Nogare, J. Head, P. Wawrzusin, R. S. Fischer, A. Chitnis, and H. Shroff, "Instant super-resolution imaging in live cells and embryos via analog image processing.," Nat. Methods **10**, 1122–6 (2013).

10. G. Shtengel, J. a Galbraith, C. G. Galbraith, J. Lippincott-Schwartz, J. M. Gillette, S. Manley, R. Sougrat, C. M. Waterman, P. Kanchanawong, M. W. Davidson, R. D. Fetter, and H. F. Hess, "Interferometric fluorescent super-resolution microscopy resolves 3D cellular ultrastructure.," Proc. Natl. Acad. Sci. U. S. A. **106**, 3125–30 (2009).

11. M. J. Paszek, C. C. DuFort, M. G. Rubashkin, M. W. Davidson, K. S. Thorn, J. T. Liphardt, and V. M. Weaver, "Scanning angle interference microscopy reveals cell dynamics at the nanoscale.," Nat. Methods **9**, 825–7 (2012).

12. M. H. Ulbrich and E. Y. Isacoff, "Subunit counting in membrane-bound proteins.," Nat. Methods **4**, 319–21 (2007).

13. A. Jain, R. Liu, B. Ramani, E. Arauz, Y. Ishitsuka, K. Ragunathan, J. Park, J. Chen, Y. K. Xiang, and T. Ha, "Probing cellular protein complexes using single-molecule pull-down.," Nature **473**, 484–8 (2011).

APPENDIX A

FRET STUDIES OF THE LARGE G-PROTEIN ATLASTIN-1[1]

INTRODUCTION

Hereditary Spastic Paraplegia (HSP) is progressive neurodegenerative disease whose main symptoms are stiffness and spasticity in the lower extremities due to deterioration of axons in corticospinal motor neurons at their distal ends [1,2]. Although HSP cases are rare, affecting 2-7.4 in 100,000 people [1,3–5], most are caused by mutations in just three loci: spastin-1, REEP-1 and atlastin-1 [5,6]. These proteins are often found as part of co-complexes in neurons at the cis-Golgi, endoplasmic reticulum (ER) and in axon growth cones [7–10]. Atlastins, in particular, are involved in maintaining the tubular ER network, promoting homotypic fusion of membranes and the formation of three-way junctions [9–13].

Evolutionarily, atlastins are part of the dynamin superfamily, which also includes dynamin, MxA, Guanylate-Binding Protein (GBP) and mitofusin [14]. All members of this family have an N-terminal globular G domain followed by an α-helical middle-domain and are involved in membrane fusion or fission. Most dynamin superfamily members also contain a GTPase effector domain (GED) that forms a three-helix bundle called a bundle signaling element (BSE) in conjunction with the C-terminus of the G domain. Atlastin, however, lacks a GED but has two transmembrane

[1] This appendix is adapted from: Byrnes, L. J., Singh, A., Szeto, K., Benvin, N. M., O'Donnell, J. P., Zipfel, W. R., & Sondermann, H. (2013). Structural basis for conformational switching and GTP loading of the large G protein atlastin. *The EMBO journal*,*32*(3), 369-384.

helices and a C-terminal domain in addition to its G and middle domains. The prototypical family member, dynamin, catalyzes membrane fission via a mechanism in which GTP hydrolysis is coupled to conformational changes that alter the position of dynamin's BSE relative to the G domain dimer [15–17]. Higher-order oligomerization can further stimulate dynamin activity [18,19]. Such oligomerization-dependent activation of GTPase activity is a trait shared by several dynamin family members [13,20–22].

Previously, the Sondermann lab produced the first crystal structures of atlastin-1's N-terminal cytoplasmic module with bound GDP, discovering two dimeric assemblies with variable positioning of the middle domain relative to the G domain [23]. In the form 1 structure, the middle domain is disengaged from the G domain in a "relaxed-parallel" arrangement. In contrast, atlastin displays an "extended" conformation in the form 2 structure, with middle domains engaging their respective G domains. These states are hypothesized to represent pre- and post-fusion forms of atlastin, respectively. Although this earlier study proposed a mechanism by which GTP binding and hydrolysis triggered conformational changes that tethered two opposing membranes via G domain dimerization, the crystals structures depicted only GDP-bound state; the form of atlastin in the presence of GTP and the exact catalytic mechanism was still unknown.

More recently, the Sondermann lab crystallized atlastin's cytoplasmic module in the presence of GTP analogs (GppNHp and GDP•AlF_4^-), discovering a "tight-parallel" arrangement which resembles the form 1 structure aside from a 18 degree rotation of the middle domain with respect to the G domain [24] (Figure A.1a-d). This

change also yielded a more extensive dimerization interface, with interfacial area increasing from 2797 $Å^2$ in the form 1 structure to 3852 $Å^2$ in the new form 3 structure. Furthermore, switch regions in the G domain which had previously adopted an open conformation with respect to the nucleotide binding pocket in the GDP-bound structures now folded over the phosphate and AlF_4^- moieties. This conformational change also positioned an arginine residue (R^{77}) such that it could interact with the α and γ phosphates of the bound nucleotide. In the GDP-bound structures, R^{77} was surface exposed and formed a salt bridge with an adjacent G domain. The Sondermann lab used R^{77} mutants to probe the role of this key arginine in dimerization and catalysis. A charge reversal mutant $R^{77}E$ was found to destabilize atlastin dimerization in the presence of GppNHp and GDP•AlF_4^-. Furthermore, this mutant bound nucleotide poorly and lacked enzymatic activity. A less severe mutation where the side chain was simply removed ($R^{77}A$) had little effect on dimerization but eliminated GTPase activity, suggesting a critical role for R^{77} in GTP hydrolysis.

Work presented in this appendix is part of a published collaboration with the Sondermann lab to study the catalytic mechanism of atlastin-1. Fluorescence methods were used to ascertain whether the aforementioned crystal structures represent viable states in solution. Furthermore, the crystals guided the interpretation of fluorescence results to build an understanding of atlastin's catalytic cycle. Equilibrium FRET measurements were used to measure the conformational state of atlastin in the presence of various nucleotides and non-hydrolyzable analogs. In order to study atlastin-1 kinetics, we used a stopped flow fluorimeter with sub-millisecond mixing dead time to measure FRET changes.

Figure A.1 Crystal structures of atlastin-1 cytoplasmic module. (a) Schematic of atlastin-1 domain structure. The N-terminal cytoplasmic domain consists of a globular G domain (orange) and stalk-like middle domain (blue), connected by a short linker (green). Following the middle domain, atlastin-1 has two transmembrane helices (black) and a C-terminal amphipathic helix which interacts with the membrane. (b) Protomer structure of crystal forms 1 and 2, with G domains aligned. Variable positioning of middle domains is apparent. (c) Protomer structure of crystal form 3 superimposed on crystal form 1 (grey), showing an 18 degree rotation of middle domain. (d) Dimeric structures of forms 1 ("extended" geometry), 2 ("relaxed-parallel") and 3 ("tight-parallel") (e) Crystal form 3 dimer interface with interfacial residues colors according to their position in the G domain, middle domain or linker

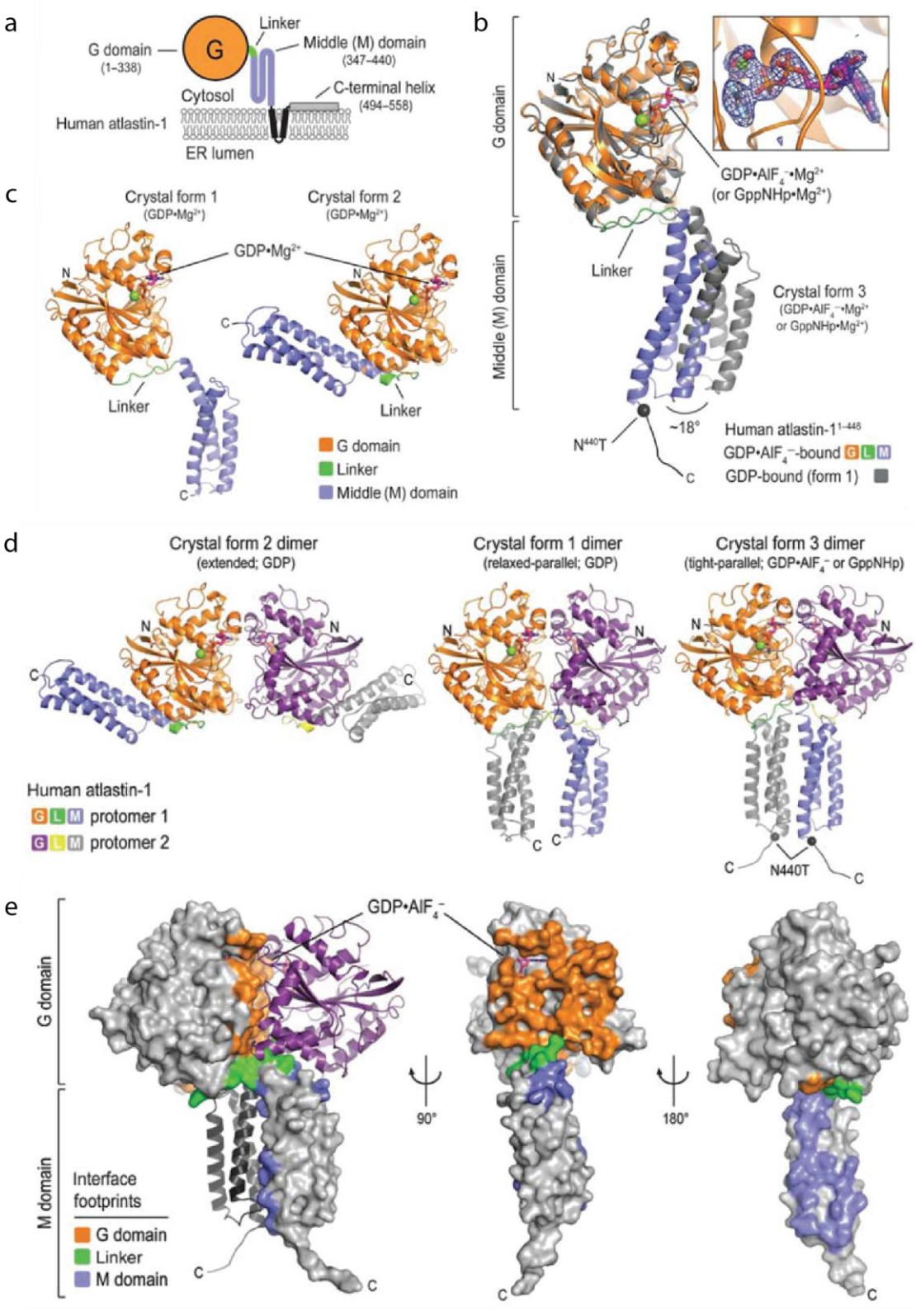
a
G domain
(1–338)
G
Linker
Middle (M) domain
(347–440)
C-terminal helix
(494–558)
Cytosol
Human atlastin-1
ER lumen
b
G domain
Middle (M) domain
N
GDP•AlF4−•Mg2+
(or GppNHp•Mg2+)
Linker
Crystal form 3
(GDP•AlF4−•Mg2+
or GppNHp•Mg2+)
~18°
N440T
C
Human atlastin-1 1–446
GDP•AlF4−-bound G L M
GDP-bound (form 1)
c
Crystal form 1
(GDP•Mg2+)
Crystal form 2
(GDP•Mg2+)
GDP•Mg2+
N
C
Linker
Linker
C
G domain
Linker
Middle (M) domain
d
Crystal form 2 dimer
(extended; GDP)
Crystal form 1 dimer
(relaxed-parallel; GDP)
Crystal form 3 dimer
(tight-parallel; GDP•AlF4− or GppNHp)
N
C
Human atlastin-1
G L M protomer 1
G L M protomer 2
N440T
e
G domain
M domain
GDP•AlF4−
90°
180°
Interface
footprints
G domain
Linker
M domain
C

MATERIALS AND METHODS

Protein purification

ECFP- and EYFP-fusion proteins (atlastin-1 residues 1-446 followed by GSTSTG and ECFP/EYFP) were cloned into a modified pET28a bacterial expression plasmid (Novagen) with an N-terminal 6xHis-SUMO tag. Proteins were expressed in BL21 (DE3) *E. coli* (Novagen) and purified by standard NiNTA chromatography and size-exclusion chromatography. SUMO and 6xHis tags were removed using the yeast protease Ulp-1 at 4°C overnight.

Dye-labeling of atlastin-1 G domain

For dye labeling of atlastin G domains, atlastin-1 $^{1\text{-}446}$ was mutated to remove the sole cysteine residue in its middle domain ($C^{375}A$) and a new cysteine was introduced in the G domain at a solvent-exposed residue ($K^{295}C$). Based on the crystal structures, labeling at this position would support FRET in all three forms of atlastin. Cysteine mutants were labeled with maleimide-modified Alexa dyes (Alexa 488 C_5 maleimide and Alexa647 C_2 maleimide) according to manufacturer protocols. Unconjugated dye was removed using dialysis-based spin concentrators (Millipore 30 kDa MWCO). All reactions used for these measurements achieved a degree-of-labelling of 0.9-1.1, as measured by UV-Vis spectrophotometry.

Equilibrium FRET

FRET measurements were made with either ECFP/EYFP-labelled atlastin to study middle domain conformations or Alexa488/Alexa647-labelled proteins to study

atlastin G domains. 1 μM of donor-labeled and 20 μM of acceptor-labeled protein were mixed in assay buffer (25 mM Tris-HCl pH 7.4, 100 mM NaCl and 4 mM MgCl2) with or without 2 mM GDP, GTP or GppNHp. Measurements with GDP•AlF_4^-were made in GDP•AlF_4^- buffer (25 mM Tris-HCl pH 7.4, 100 mM NaCl, 4 mM MgCl2, 2 mM EGTA, 2 mM AlCl2 and 2 mM NaF) with or without 2 mM GDP. Data was acquired using a spectrofluorometer (PTI Quantamaster 40) with the excitation monochromator set to 445 nm (ECFP) or 493 nm (Alexa488) and scanning emission spectra from 455 to 650 nm (ECFP/EYFP) or 505 to 850 nm (Alexa488/647). FRET efficiencies were calculated by comparing the donor intensity (F_{DA}) at the emission peak (λ_{em}= 473 nm for ECFP and λ_{em} = 516 nm for Alexa488) in the presence of nucleotide to the donor intensity in the absence of any nucleotide (F_D); the latter was used as a no-FRET control since atlastin has been shown to be monomeric in its apo state. FRET efficiency E was calculated using the standard formula:

Interfluorophore distances were calculated using:

$$E = \frac{R_0^6}{R_0^6 + r^6}$$

where r is the distance to be calculated and R_0 is the Forster distance for each dye pair (47 Å for ECFP/EYFP and 56 Å for Alexa 488/647).

Stopped-Flow FRET of atlastin-1 conformational changes

Kinetics of atlastin conformational changes were measured using a stopped-flow fluorometer with submillisecond mixing dead time (Kintek SF-2004). A mixture

of donor- and acceptor-labelled atlastin were mixed in assay buffer at 1 μM each and loaded into one of the drive syringes of the stopped-flow instrument. The other syringe was loaded with either assay buffer alone or buffer supplemented with 2 mM GDP, GTP, GppNHp or GTPγS. Measurements with GDP•AlF4- used proteins diluted in GDP•AlF_4^- buffer and the drive syringe was loaded with 2 mM GDP in GDP•AlF_4^- buffer. Solutions were mixed 1:1 at 8 mL/s in a 30 uL sample cell. A monochromator was used to select a narrow excitation band (centered around 445 nm for ECFP/YFP and 493 nm for Alexa 488/647) from a xenon arc lamp. Time-dependent fluorescence signal was collected from two photomultiplier tubes using appropriate filters (B460-490 and D535/25 for ECFP/EYFP; D525/50 and HQ645/75 for Alexa488/647).

N-Methylanthraniloyl (Mant)-nucleotide binding assay

Mant-labelled nucleotides were used to measure nucleotide binding and dissociation rates to various atlastin constructs. Mant fluorescence is sensitive to the fluorophore environment and changes upon nucleotide binding. 2.5 μM of Mant-nucleotide (-GDP, -GTP, -GppNHp) were loaded into one of the syringes of the stopped-flow instrument and 10-50 μM of atlastin-1 was loaded into the other drive syringe. Mant was excited at λ = 366 nm and fluorescence was collected using a bandpass filter (HQ460/40m, Chroma). The first 500 ms of data was fit to a single exponential and used to extract a rate constant for nucleotide association at each protein concentration. Observed rate constants were plotted against atlastin concentration and fit to a linear model to determine k_{on} (slope) and k_{off} (y-intercept). K_{off} was also independently measured by loading atlastin pre-mixed with mant-

labelled nucleotide into one syringe and a high concentration of unlabeled GDP into the other syringe. The first 500 ms of the resulting data was fit to a single exponential to directly measure k_{off}.

RESULTS

Nucleotide-binding kinetics

Since nucleotide binding is a prerequisite for dimerization, association and dissociation rates were measured using mant-modified versions of GDP, GTP and GppNHp. All nucleotides showed similar on-rates for the full-length wildtype atlastin and, surprisingly, similar rates for the $R^{77}A$ mutant form.

Based on the atlastin crystal structures, the Sondermann lab also identified a central helix (residues 184-204) in the linker region and docking site of the middle domain on the G domain which differs in the form 2 and form 3 structures. In particular, the helix is bent in form 2, cradling the middle domain, but straight in form 3 and occluding the middle domain docking site. They hypothesized that this could signify a regulatory role and perhaps influence nucleotide binding. Measurements with mant-nucleotides showed that the isolated G domain (atlastin-1 $^{1-339}$) binds GDP at a similar rate to wildtype atlastin, but fails to bind GTP, suggesting that the middle domain may be necessary for GTP loading. As a follow-up, the isolated middle domains (atlastin-1 $^{340-446}$) were added *in trans* and found to rescue mant-GTP binding, albeit with a lower affinity than the intact cytoplasmic unit (atlastin-1 $^{1-446}$). Another mutant with a truncated middle domain (atlastin-1 $^{1-366}$) achieved similar results. Additional data from the Sondermann lab showed that co-incubation with the middle

domain could also rescue GTPase activity which is absent for the isolated G domain and that a similar result is observed with the middle domain truncation (atlastin-1^{1-366}).

Equilibrium FRET of atlastin-1 middle domain

In order to determine the role of the new form 3 structure and to investigate the role of GTP hydrolysis in atlastin's catalytic cycle, we developed a FRET assay to measure conformational changes (Figure A.2a). Assuming that atlastin can occupy one of the three proposed dimeric arrangements, we expected no FRET from fluorophores fused to atlastins middle domains when they adopted the form 2 configuration. In contrast, forms 1 and 3 would bring the fluorophores into close proximity and be FRET-permissive. Middle domain conformations were probed by fusing ECFP/EYFP to atlastin-1^{1-446} using a short linker and the fusion proteins showed similar dimerization propensity and GTPase rates to wildtype atlastin.

In the presence of GDP, no FRET was observed relative to the apo state—as expected, since atlastin-1 is known to monomeric in both cases. In the presence of GppNHp or GDP•AlF_4^-, donor and acceptor fluorescence changes indicated strong FRET (E = 30% for GppNHp and 22% for GDP•AlF_4^-) (Figure A.2d,e). These FRET efficiencies were used to calculate interfluorophore separations of 54 Å and 57 Å for GppNHp and GDP•AlF_4^-, respectively.

Figure A.2 Equilibrium FRET of atlastin middle domains. (a) Cartoon depicting fluorescent-protein (FP) labelled atlastin-1 and its geometry in form 2 (non-FRET) and form 1/3 (FRET-competent) dimeric assemblies. Distance estimates are based on crystallographic data. (b) Nucleotide-dependent dimerization of unlabeled atlastin and atlastin-FP fusions in the presence of nucleotide analogs measured by size exclusion chromatography multi-angle light scattering (SEC-MALS). (c) GTPase activity of atlastin variants measured by production of inorganic phosphate. (d) Raw fluorescence data for equilibrium FRET assay, with 1 μM ECFP-labelled atlastin-1 and 20 μM EYFP-labelled atlastin-1 in the apo state or in the presence of nucleotide. (e) Calculated FRET efficiencies for wildtype atlastin-1 and the R77A mutant in the presence of nucleotide. (f) FRET efficiency change over time in the presence of GTP. Wildtype atlastin-1 FRET decreases gradually over time due the GTP hydrolysis, but can be recovered by spiking in additional GTP (t = 30 min). The catalytically-inactive $R^{77}A$ mutant shows no such decrease.

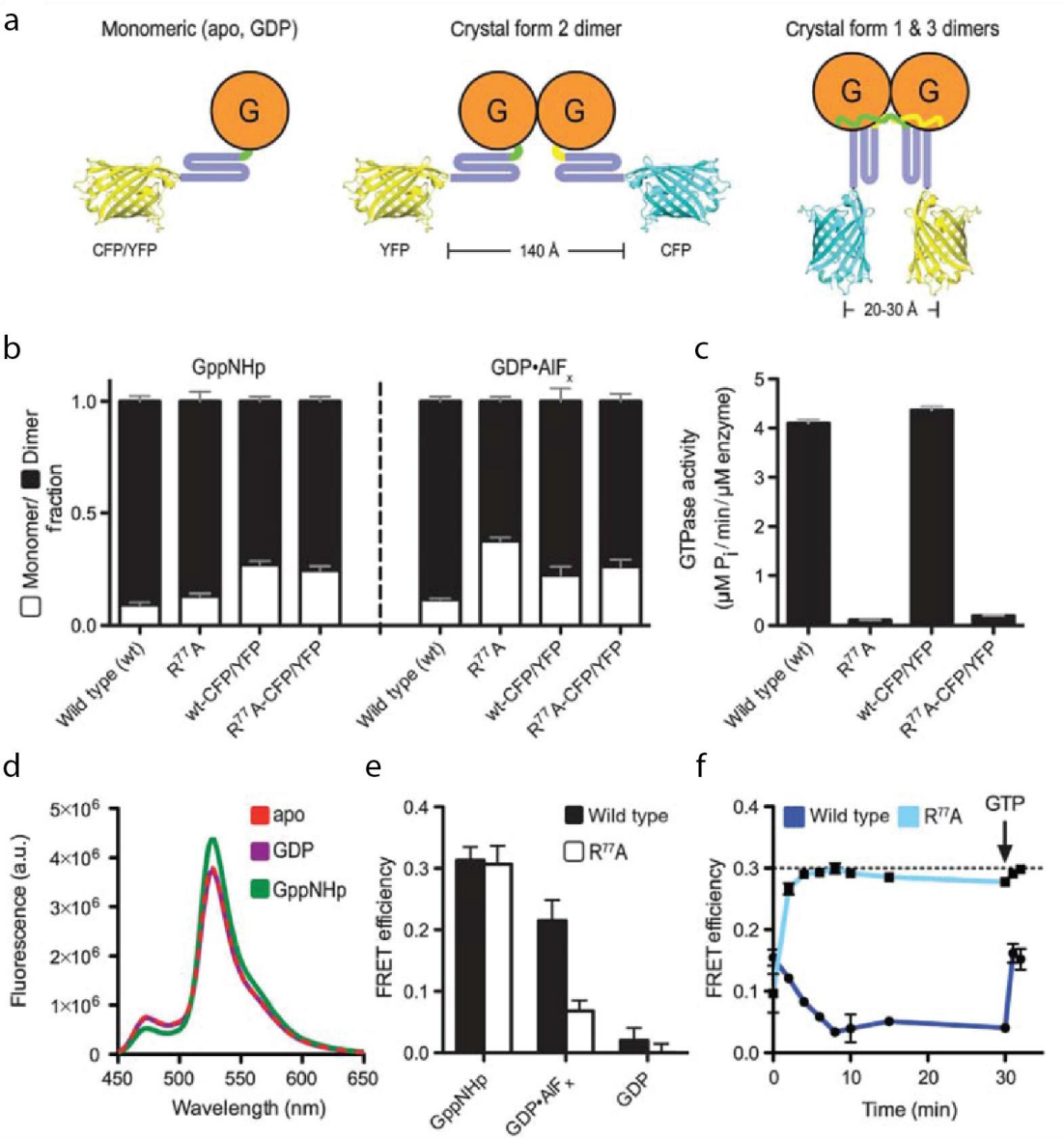
a
Monomeric (apo, GDP)
Crystal form 2 dimer
Crystal form 1 & 3 dimers
G
CFP/YFP
YFP
140 Å
CFP
20-30 Å
b
GppNHp
GDP•AlF$_x$
Monomer/ Dimer fraction
1.0
0.5
0.0
Wild type (wt)
R^{77}A
wt-CFP/YFP
R^{77}A-CFP/YFP
c
GTPase activity
(μM P$_i$/ min/ μM enzyme)
5
4
3
2
1
0
d
Fluorescence (a.u.)
5×10^6
4×10^6
3×10^6
2×10^6
1×10^6
0
apo
GDP
GppNHp
450
500
550
600
650
Wavelength (nm)
e
FRET efficiency
0.4
0.3
0.2
0.1
0.0
Wild type
R^{77}A
GppNHp
GDP•AlF$_x$
GDP
f
FRET efficiency
Wild type
R^{77}A
GTP
0
10
20
30
Time (min)

When GTP was added, a much lower FRET efficiency was observed. This is explained by the fact that atlastin-1 efficiently hydrolyzes and depletes the GTP pool, resulting in a build-up of GDP which does not support dimerization and thus FRET (Figure A.2f). This was further supported by noticing that the FRET efficiency continually decreased as GTP was hydrolyzed, but could be recovered by spiking in additional GTP at a later time point. Still, the maximum value never approached that of the non-hydrolyzable GTP analogs, suggesting that perhaps atlastin-1 occupies multiple or different conformations in the presence of GTP. Notably, the GTP-bound catalytically inactive $R^{77}A$ mutant form of atlastin achieved similar FRET efficiencies to wildtype atlastin in the presence of GTP analogs. Overall, these results suggest that the FRET-competent state may be transient due to atlastin's fast rate of GTP hydrolysis.

Middle domain kinetics

The equilibrium FRET data in the presence of GTP indicate that atlastin-1 may occupy several different conformations during its catalytic cycle. In order to probe the kinetics of this conformational switching, stopped-flow fluorometry was used to synchronize the reaction events upon mixing with nucleotide. Equimolar concentrations of ECFP and EYFP-labeled atlastin were loaded into one drive syringe of a stopped-flow instrument while another syringe was loaded with excess nucleotide. Submillisecond mixing dead time ensured that we could observe FRET changes with minimal lag time.

Figure A.3 Stopped-flow kinetics of atlastin middle domain conformational changes. (a) FRET donor (ECFP) and acceptor (EYFP) traces for atlastin-1 middle domain conformational changes in the apo state or in the presence of nucleotide. No FRET is observed in the case of GDP, while GTP analogs (GppNHp and GDP•AlF_4^-) cause a steady increase in FRET over 10 minutes. When GTP is present, wildtype atlastin-1 middle domains quickly achieve a maximal FRET state (2 seconds after mixing), which soon decays to an intermediate value before slowly decaying. The catalytically-inactive $R^{77}A$ mutant shows a slow-but-steady increase in FRET, much like in the case of non-hydrolyzable analogs with wildtype atlastin. (b) Simulations of three-state kinetics and two-state kinetics used to model nucleotide-dependent conformational changes resemble the observed FRET data.

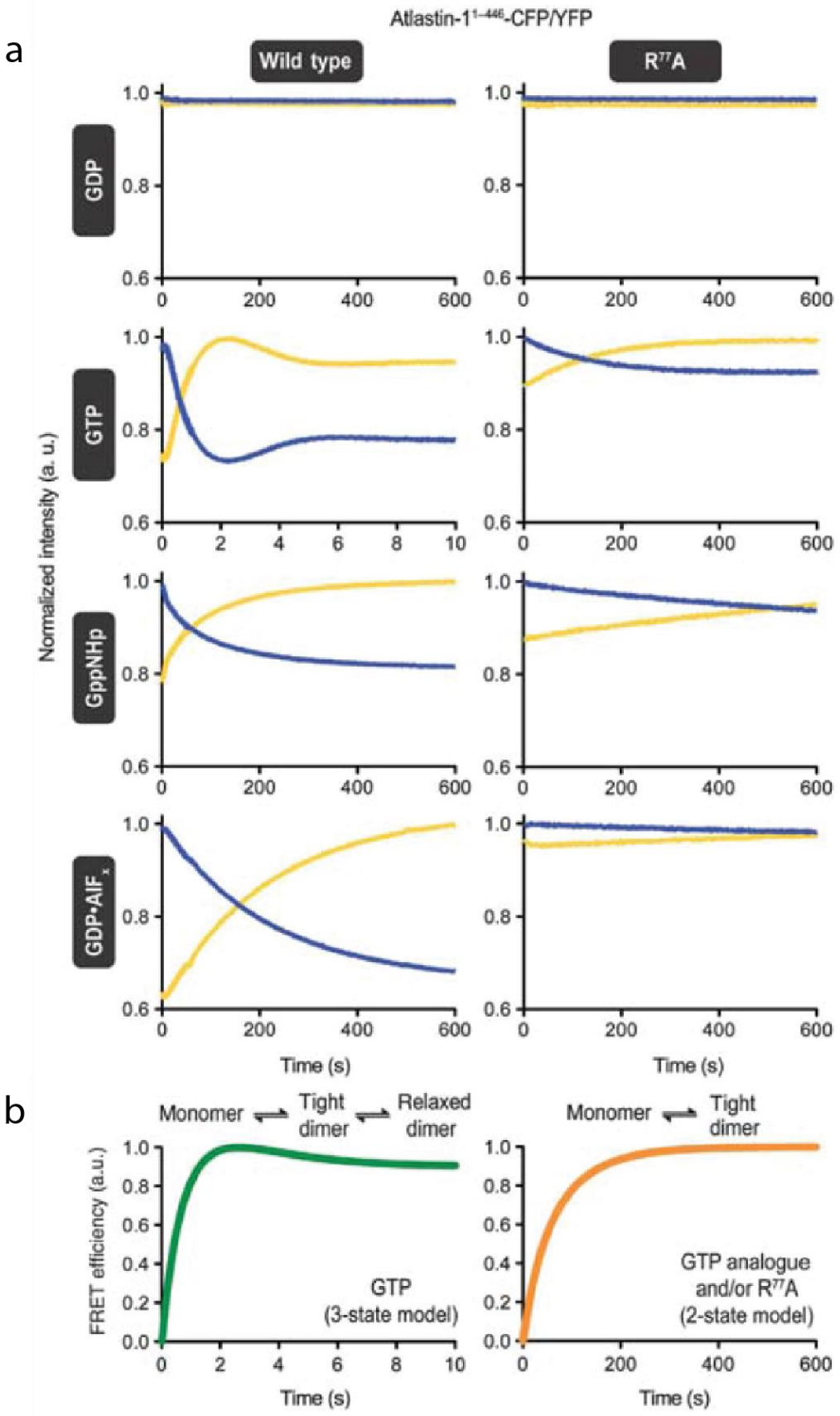
a
Atlastin-1$^{1-446}$-CFP/YFP
Wild type
R^{77}A
GDP
GTP
GppNHp
GDP•AlF$_x$
Normalized intensity (a. u.)
Time (s)
b
Monomer
Tight dimer
Relaxed dimer
FRET efficiency (a.u.)
GTP
(3-state model)
GTP analogue
and/or R^{77}A
(2-state model)

As with equilibrium FRET, mixing with GDP yielded no FRET changes for either wildtype atlastin or the catalytically inactive mutant (Figure A.3a). Meanwhile, in the presence of GppNHp, GDP•AlF_4^- or GTPγS, donor fluorescence decayed gradually with a concomitant increase in acceptor signal over the course of 10 minutes. When GTP was added to wildtype atlastin, FRET peaked after only 2 seconds followed by an intermediate FRET state and an eventual decay after several minutes as the GTP pool was depleted. By comparison, when GTP was mixed with the catalytically inactive $R^{77}A$ mutant, FRET efficiency increased slowly over 10 minutes, much like for wildtype atlastin in the presence of GTP analogs. Together, these results suggest a model where the GTP hydrolysis reaction is initially synchronized, leading the dimer to adopt a very close conformation (possibly the form 3 "tight parallel" structure) followed by relaxation to an intermediate value (perhaps the "relaxed parallel" form 1) (Figure A.3b). Furthermore, the significant difference in timescale between FRET in the case of GTP versus GTP analogs warrants attention. Although all nucleotides have similar on-rates, the faster conformational change for GTP signifies that hydrolysis may drive dimerization and adoption of a FRET-competent state (e.g. form 3).

G and middle domain kinetics

While the first set of kinetic data showed that nucleotide hydrolysis may drive middle domain dimerization, it remained unknown whether G domain dimerization occurred previously or at a similar timescale. Further measurements were made using cysteine-mutant forms of atlastin labelled with Alexa 488/Alexa 647 at a solvent-

Figure A.4 Equilibrium FRET of atlastin G domains. (a) Cartoon depicting Alexa488 (green) / Alexa647 (red)-labelled atlastin G domains. All crystal forms (1-3) support FRET in their respective dimeric assemblies. Distance estimates are based on crystallography data. (b)SDS-PAGE gel of labelled atlastin cysteine mutants. Coomassie absorbance shows presence of protein bands and a fluorescence gel scanner was used to detect Alexa488 labeling. (c) Nucleotide-dependent dimerization of Alexa-labeled atlastin mixtures measured by SEC-MALS. (d) GTPase activity of Alexa-labeled atlastin measured by production of inorganic phosphate (e) Raw fluorescence data for G domain equilibrium FRET assay, using 1 μM donor (Alexa488)-labeled atlastin and 20 μM donor (Alexa647)-labeled atlastin. Decrease in donor fluorescence in the presence of GTP analogs (e.g. GppNHP) was accompanied by a concomitant rise in acceptor fluorescence. (f) Calculated FRET efficiencies for atlastin cysteine mutant without and with the additional $R^{77}A$ mutation which renders atlastin catalytically-inactive. (g) Middle domain FRET for the catalytically active variant decreases gradually over time as GTP is hydrolyzed, but can be recovered by spiking in additional nucleotide at a later time point. The catalytically-inactive variant achieves a stable FRET value

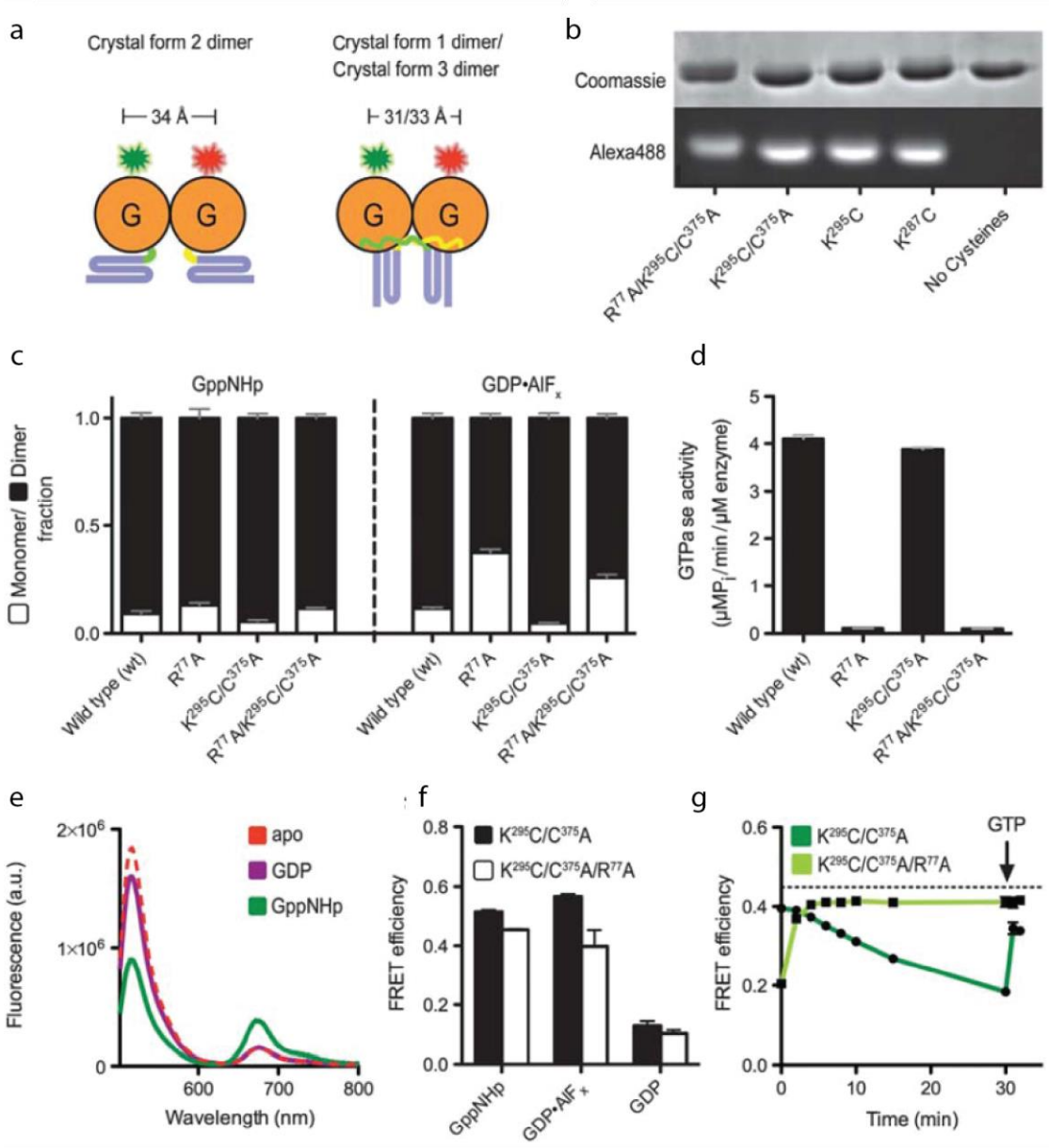
a
Crystal form 2 dimer
Crystal form 1 dimer/
Crystal form 3 dimer
34 Å
31/33 Å
G
G
b
Coomassie
Alexa488
R77A/K295C/C375A
K295C/C375A
K295C
K287C
No Cysteines
c
GppNHp
GDP•AlFx
Monomer/ Dimer fraction
1.0
0.5
0.0
Wild type (wt)
R77A
K295C/C375A
R77A/K295C/C375A
d
GTPase activity
(μMPi/min/μM enzyme)
5
4
3
2
1
0
e
Fluorescence (a.u.)
2×10^6
1×10^6
0
apo
GDP
GppNHp
600
700
800
Wavelength (nm)
f
K295C/C375A
K295C/C375A/R77A
FRET efficiency
0.8
0.6
0.4
0.2
0.0
GppNHp
GDP•AlFx
GDP
g
K295C/C375A
K295C/C375A/R77A
GTP
FRET efficiency
0.6
0.4
0.2
0.0
0
10
20
30
Time (min)

Figure A.5 Stopped-flow kinetics of atlastin G domain conformational changes. Donor (Alexa 488) and acceptor (Alexa 647)-labeled G domains were pre-mixed 1:1 and mixed with buffer (apo) or various nucleotides. Fluorescence traces were recorded over time using appropriate filters. No FRET was observed in the presence of GDP or the apo state, while GTP analogs showed a steady increase in FRET. In the case of GTP, the catalytically active cysteine mutant reached a maximal FRET value after 2 seconds before decaying to an intermediate value. In contrast, the catalytically inactive $R^{77}A$ mutant showed a steady rise in FRET over time, much like the data for non-hydrolyzable analogs.

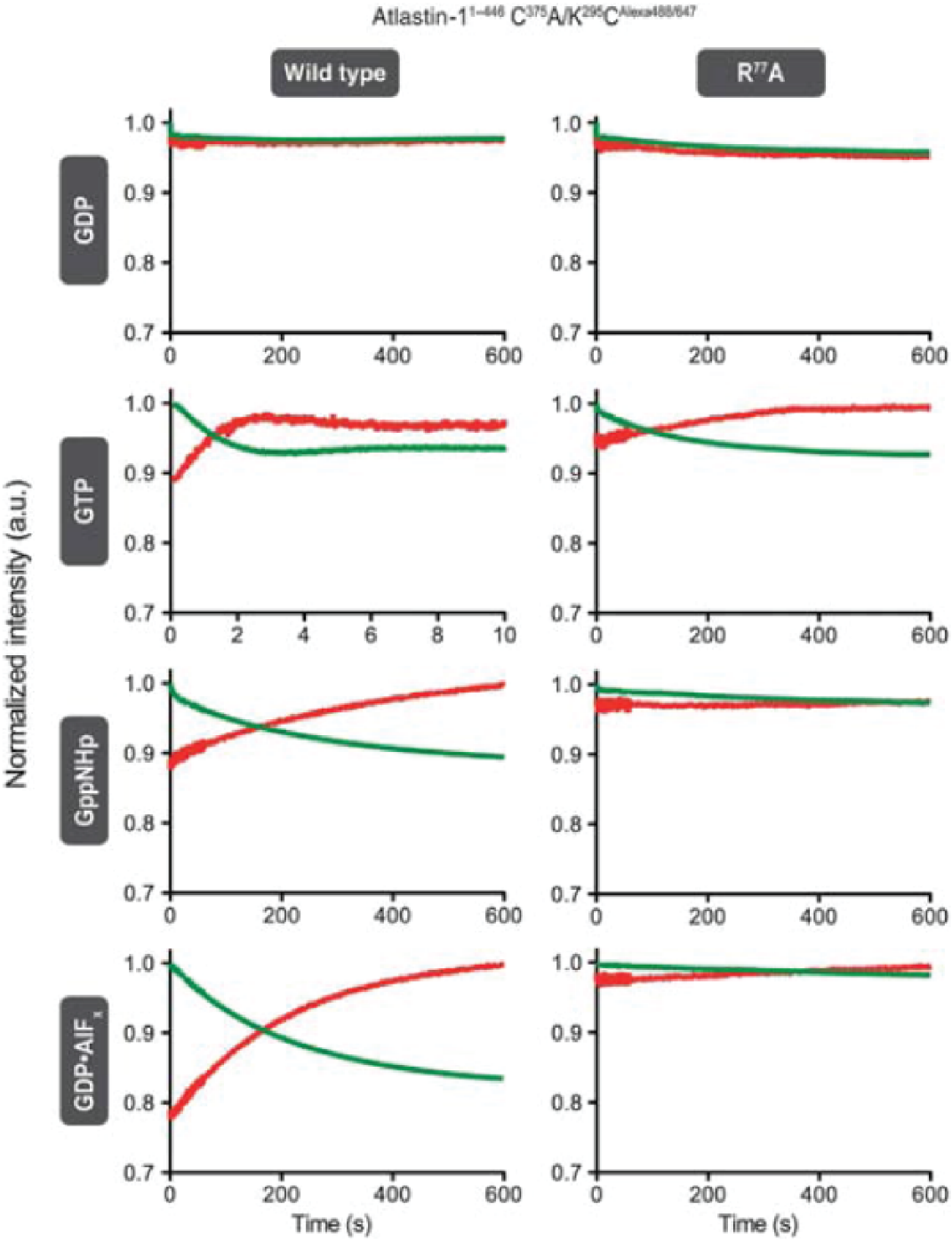
Atlastin-1 1–446 C375A/K295C Alexa488/647
Wild type
R77A
GDP
GTP
GppNHp
GDP•AlFx
Normalized intensity (a.u.)
Time (s)
Time (s)

exposed position on the G domains ($K^{295}C$) (Figure A.4a,b). Mutants showed similar dimerization characteristics and GTPase activity as wildtype atlastin (Figure A.4d). As before, GDP-bound atlastin showed no equilibrium FRET while GTP analogs showed considerable FRET efficiency (51% for GppNHp and 56% for GDP•AlF_4^-) (Figure A.4e,f). As with middle domain FRET, GTP caused a fast increase in FRET efficiency followed by a steady decay, presumably due to nucleotide hydrolysis (Figure A.4g). However, unlike for the middle domains, FRET for wildltype atlastin G domains in the presence of GTP achieved a similar efficiency as for GTP analogs and the catalytically inactive $R^{77}A$ mutant. This suggests that perhaps the middle domains populate a mixture of states upon GTP hydrolysis (with differing FRET efficiencies) while the G domains adopt a single stable state. G domain dimerization rates were measured using stopped-flow FRET and found to follow similar kinetics as middle domain dimerization (Figure A.5). Together, these data suggest that G and middle domain dimerization occurs concomitantly following GTP hydrolysis. With regard to atlastin's role in membrane fusion, this means that the entire cytoplasmic module acts as a tethering unit to bring together opposing membranes in a single step.

DISCUSSION

Based on our results, we were able to build a model for atlastin's role in membrane fusion (Figure A.6):

1. Initially, atlastin-1 resides as monomers on opposing membranes. G domains are engaged with their respective middle domains and ready to bind GTP.

2. Upon GTP binding, G domains begin to slowly disengage from their respective middle domains. Simultaneously, atlastin-1 protomers from each membrane begin to slowly dimerize with each other.
3. GTP hydrolysis drives this disengagement, leading to fast dimerization.
4. Dimerization induces curvature in the two opposing membranes, due to stress caused by atlastin's transmembrane domains and C-terminal amphipathic helix.
5. Membrane fusion occurs to minimize stress from curvature.
6. Phosphate release and dimer disassembly follow.

FUTURE DIRECTIONS

As all of the data gathered so far used the cytoplasmic module of atlastin-1 in solution, it remains a goal to study the catalytic cycle in membranes, ideally with full-length atlastin. Furthermore, there have been recent studies showing links between a different atlastin isoform, atlastin-3, and oncogenesis. Preliminary studies by the Sondermann show that this form of atlastin is localized to ER 3-way junctions and has diminished GTPase activity relative to atlastin-1, whose distribution in the ER is also more ubiquitous. FRET-based Studies of atlastin-3's catalytic cycle should provide insight into the reasons for its diminished activity. Furthermore, the Sondermann lab hypothesizes that atlastin-3's reduced activity is responsible for its distinct localization. This may be tested by studying the distribution of mutant forms of atlastin-1 and atlastin-3 with slower and faster activity, respectively. A few potential

Figure A.6 Proposed model for atlastin-1 catalytic cycle. Atlastin initially resides it its monomeric state, with middle and G domains engaged (much like the form 2 structure). GTP binding triggers a slow release of the G domain from the middle domain and concomitant dimerization, which is accelerated upon GTP hydrolysis. Fast dimerization upon GTP hydrolysis tethers the two membranes to each other and the resulting high-curvature state is energetically unfavorable, causing spontaneous membrane fusion. Inorganic phosphate release and dimer disassembly complete atlastin's catalytic cycle.

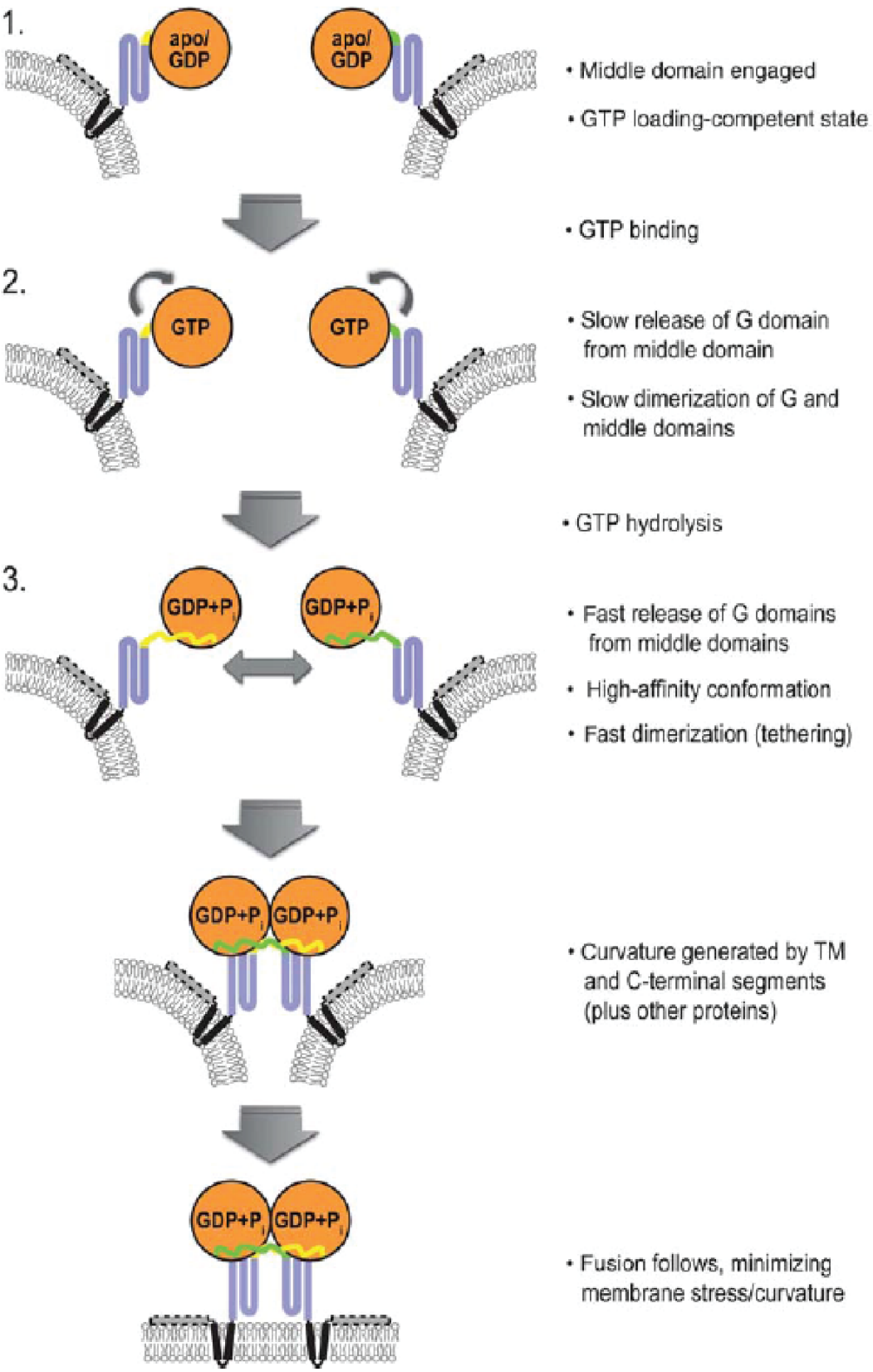
1.
apo/ GDP
apo/ GDP
• Middle domain engaged
• GTP loading-competent state
• GTP binding
2.
GTP
GTP
• Slow release of G domain from middle domain
• Slow dimerization of G and middle domains
• GTP hydrolysis
3.
GDP+P$_i$
GDP+P$_i$
• Fast release of G domains from middle domains
• High-affinity conformation
• Fast dimerization (tethering)
GDP+P$_i$
GDP+P$_i$
• Curvature generated by TM and C-terminal segments (plus other proteins)
GDP+P$_i$
GDP+P$_i$
• Fusion follows, minimizing membrane stress/curvature

experiments are outlined below:

1. Comparison of ATL1 and ATL3 kinetics by stopped flow fluorometry

   As a straightforward extension of the work in our EMBO paper, stopped-flow FRET of atlastin-3 dimerization and conformational changes would provide insight into its molecular mechanism. These studies may be supplemented by incorporating atlastin isoforms into into proteoliposomes to restrict molecular geometries. In this case, a subset of proteoliposomes may contain donor-labelled atlastin while another subset has acceptor-labelled atlastin to isolate *trans*-interacting molecules (molecules on different membranes). Alternatively, both donor- and acceptor-labelled molecules may be incorporated into the same vesicle to observe *cis*-interactions (molecules on the same membrane). While previous experiments examined only intermolecular FRET between atlastin G and middle domains, we can also use site-specific labeling strategies(maleimide-dye conjugates, unnatural amino acids, small tags such as ybbR or S6) for dual-labeling to probe intramolecular conformational changes. Furthermore, it would be interesting to see if atlastin partners (e.g. REEP-1) affect the kinetic cycle.

2. Bulk FRET on supported lipid bilayers

   A recent study by the Rapaport lab used a supported lipid bilayer system to examine competition between *cis* and *trans* atlastin interactions [25]. In this case, *cis* interactions were between atlastin molecules in the bilayer while *trans* interactions were with atlastin molecules in solution. They conclude that atlastin undergoes multiple GTP hydrolysis cycles to break associations with

cis-molecules before successfully achieving *trans*-membrane fusion. It would be interesting to compare the behavior for atlastin-1 and atlastin-3 to see if the less active isoform 3 behaves similarly.

3. smFRET of soluble atlastin in porous encapsulated vesicles

   While bulk FRET has given us much insight into atlastin's catalytic cycle, the data may be obfuscated by ensemble averaging of multiple populations. Single molecule FRET (smFRET) experiments provide a means to probe this heterogeneity, but atlastin protomers fail to dimerize at the low concentrations needed for single molecule observation. To overcome this limitation, we can use small nanocontainers to maintain high local concentrations but low overall concentrations, permitting simultaneous dimer assembly and single-molecule data acquisition. For vesicles of ~50 nm diameter, even a single molecule constitutes a concentration of ~10 μM. Protein pores or leaky membranes may be used to facilitate exchange of GTP and analogs. As alternative strategies, zero-mode waveguides may be used to create attoliter volumes for single-molecule observation. In all of these cases, single-molecule time trajectories should provide information about the entire atlastin catalytic cycle and provide insight and better resolve some of the features expected from the bulk data.

4. smFRET of atlastin in membranes

   smFRET may also be used to examine intramolecular conformational changes by incorporating a dual-labeled atlastin catalytic core into a lipid bilayer at a low concentration with excess unlabeled atlastin in the solution phase for

dimerization. The cytoplasmic core may be properly oriented in the membrane by using Ni-NTA lipids and a 6xHis tag on the atlastin molecule.

5. Dimerization state of atlastin measured by Spatial Intensity Distribution Analysis (SpIDA)

   The distinct cellular localizations of atlastin-1 and atlastin-3 raise questions as to whether regional subpopulations of atlastins are in discrete catalytic and oligomeric states. Spatial Intensity Distribution Analysis provides a means of measuring these oligomeric states through well-calibrated fluorescent protein oligomer controls. We can try applying this method to compare atlastin oligomerization at three-way junctions to other locations in the ER. The AiryScan module on the Zeiss 880 may be used to boost spatial resolution.

REFERENCES

1. J. K. Fink, "Hereditary spastic paraplegia.," Curr. Neurol. Neurosci. Rep. **6**, 65–76 (2006).

2. S. Salinas, C. Proukakis, A. Crosby, and T. T. Warner, "Hereditary spastic paraplegia: clinical features and pathogenetic mechanisms.," Lancet. Neurol. **7**, 1127–38 (2008).

3. J. M. Polo, J. Calleja, O. Combarros, and J. Berciano, "Hereditary ataxias and paraplegias in Cantabria, Spain. An epidemiological and clinical study.," Brain **114 (Pt 2**, 855–66 (1991).

4. A. Filla, G. De Michele, R. Marconi, L. Bucci, C. Carillo, A. E. Castellano, L. Iorio, C. Kniahynicki, F. Rossi, and G. Campanella, "Prevalence of hereditary ataxias and spastic paraplegias in Molise, a region of Italy.," J. Neurol. **239**, 351–3 (1992).

5. C. Depienne, G. Stevanin, A. Brice, and A. Durr, "Hereditary spastic paraplegias: an update.," Curr. Opin. Neurol. **20**, 674–80 (2007).

6. X. Zhao, D. Alvarado, S. Rainier, R. Lemons, P. Hedera, C. H. Weber, T. Tukel, M. Apak, T. Heiman-Patterson, L. Ming, M. Bui, and J. K. Fink, "Mutations in a newly identified GTPase gene cause autosomal dominant hereditary spastic paraplegia.," Nat. Genet. **29**, 326–31 (2001).

7. K. Evans, C. Keller, K. Pavur, K. Glasgow, B. Conn, and B. Lauring, "Interaction of two hereditary spastic paraplegia gene products, spastin and atlastin, suggests a common pathway for axonal maintenance.," Proc. Natl. Acad. Sci. U. S. A. **103**, 10666–71 (2006).

8. C. M. Sanderson, J. W. Connell, T. L. Edwards, N. A. Bright, S. Duley, A. Thompson, J. P. Luzio, and E. Reid, "Spastin and atlastin, two proteins mutated in autosomal-dominant hereditary spastic paraplegia, are binding partners.," Hum. Mol. Genet. **15**, 307–18 (2006).

9. J. Hu, Y. Shibata, P.-P. Zhu, C. Voss, N. Rismanchi, W. A. Prinz, T. A. Rapoport, and C. Blackstone, "A class of dynamin-like GTPases involved in the generation of the tubular ER network.," Cell **138**, 549–61 (2009).

10. S. H. Park, P.-P. Zhu, R. L. Parker, and C. Blackstone, "Hereditary spastic

paraplegia proteins REEP1, spastin, and atlastin-1 coordinate microtubule interactions with the tubular ER network," J. Clin. Invest. **120**, 1097–1110 (2010).

11. M. Namekawa, M.-P. Muriel, A. Janer, M. Latouche, A. Dauphin, T. Debeir, E. Martin, C. Duyckaerts, A. Prigent, C. Depienne, A. Sittler, A. Brice, and M. Ruberg, "Mutations in the SPG3A gene encoding the GTPase atlastin interfere with vesicle trafficking in the ER/Golgi interface and Golgi morphogenesis.," Mol. Cell. Neurosci. **35**, 1–13 (2007).

12. N. Rismanchi, C. Soderblom, J. Stadler, P.-P. Zhu, and C. Blackstone, "Atlastin GTPases are required for Golgi apparatus and ER morphogenesis.," Hum. Mol. Genet. **17**, 1591–604 (2008).

13. G. Orso, D. Pendin, S. Liu, J. Tosetto, T. J. Moss, J. E. Faust, M. Micaroni, A. Egorova, A. Martinuzzi, J. A. McNew, and A. Daga, "Homotypic fusion of ER membranes requires the dynamin-like GTPase atlastin.," Nature **460**, 978–83 (2009).

14. G. J. K. Praefcke, S. Kloep, U. Benscheid, H. Lilie, B. Prakash, and C. Herrmann, "Identification of Residues in the Human Guanylate-binding Protein 1 Critical for Nucleotide Binding and Cooperative GTP Hydrolysis," J. Mol. Biol. **344**, 257–269 (2004).

15. J. S. Chappie, J. A. Mears, S. Fang, M. Leonard, S. L. Schmid, R. A. Milligan, J. E. Hinshaw, and F. Dyda, "A pseudoatomic model of the dynamin polymer identifies a hydrolysis-dependent powerstroke.," Cell **147**, 209–22 (2011).

16. K. Faelber, Y. Posor, S. Gao, M. Held, Y. Roske, D. Schulze, V. Haucke, F. Noé, and O. Daumke, "Crystal structure of nucleotide-free dynamin.," Nature **477**, 556–60 (2011).

17. M. G. J. Ford, S. Jenni, and J. Nunnari, "The crystal structure of dynamin.," Nature **477**, 561–6 (2011).

18. P. L. Tuma and C. A. Collins, "Activation of dynamin GTPase is a result of positive cooperativity.," J. Biol. Chem. **269**, 30842–7 (1994).

19. D. E. Warnock, J. E. Hinshaw, and S. L. Schmid, "Dynamin self-assembly stimulates its GTPase activity.," J. Biol. Chem. **271**, 22310–4 (1996).

20. B. D. Song, M. Leonard, and S. L. Schmid, "Dynamin GTPase domain mutants

that differentially affect GTP binding, GTP hydrolysis, and clathrin-mediated endocytosis.," J. Biol. Chem. **279**, 40431–6 (2004).

21. H. H. Low and J. Löwe, "A bacterial dynamin-like protein.," Nature **444**, 766–9 (2006).

22. R. Gasper, S. Meyer, K. Gotthardt, M. Sirajuddin, and A. Wittinghofer, "It takes two to tango: regulation of G proteins by dimerization.," Nat. Rev. Mol. Cell Biol. **10**, 423–9 (2009).

23. L. J. Byrnes and H. Sondermann, "Structural basis for the nucleotide-dependent dimerization of the large G protein atlastin-1/SPG3A.," Proc. Natl. Acad. Sci. U. S. A. **108**, 2216–21 (2011).

24. L. J. Byrnes, A. Singh, K. Szeto, N. M. Benvin, J. P. O'Donnell, W. R. Zipfel, and H. Sondermann, "Structural basis for conformational switching and GTP loading of the large G protein atlastin.," EMBO J. **32**, 369–84 (2013).

25. T. Y. Liu, X. Bian, F. B. Romano, T. Shemesh, T. A. Rapoport, and J. Hu, "Cis and trans interactions between atlastin molecules during membrane fusion.," Proc. Natl. Acad. Sci. U. S. A. **112**, E1851–60 (2015).

APPENDIX B

ACCURATE EMCCD PHOTOELECTRON CALIBRATION USING PHOTON TRANSFER TECHNIQUES

INTRODUCTION

Super-resolution and single molecule imaging approaches have yielded a new perspective on cell biology, extracting information about molecular localization, dynamics and conformational distributions which were previously inaccessible to ensemble methods. These measurements have been enabled by sensitive detectors that permit high signal-to-noise imaging in low light scenarios. In particular, electron-multiplying charge coupled devices (EMCCDs) and scientific complementary metal oxide semiconductor (sCMOS) have become the cameras-of-choice due to their low (effective) read noises and high quantum efficiencies in the visible and near-infrared. Furthermore, the respective technologies have advanced rapidly, with larger format sensors and higher frame rates expanding the possibilities for single molecule science.

Quantitative comparisons of fluorescence microscopy data are often challenging due to the range of instrumentation, acquisition parameters and image processing used by researchers. This often confounds attempts to reproduce or understand datasets produced by other labs, especially when judging new tools such as fluorescent proteins or image processing methods. Scientific cameras introduce their own source of variability as data is often reported in arbitrary units ("counts") which depend on the gain settings and analog-to-digital conversion on the chip. While photoelectrons are the natural unit for fluorescence data, a variety of methods [1–3]

have been used for photoelectron calibration with little quantitative evaluation of their performance. Furthermore, camera manufacturers have provided formulas for conversion that many researchers have used without scrutiny. Many of these theoretical expressions rely on factory-measured camera parameters which change over time as the camera ages.

Here, we present a simple application of a photon transfer method for EMCCD photoelectron calibration. Photon transfer methods isolate the different noise sources present in camera data and present relevant detector parameters (e.g. gain, read noise, dark noise, full-well capacity, linearity and offset) in absolute terms. Although the method here is applied to EMCCDs, it is generalizable to sCMOS cameras or any other detector system. Photon transfer methods have also been used to evaluate both of these detectors for localization microscopy [4–6]. This appendix provides a theoretical description of the method and corroboration with a photon-counting approach. A simple protocol for data acquisition and analysis is also presented, along with guidelines for optimal camera usage.

THEORY

A typical frame-transfer EMCCD chip consists of a charge collection or imaging region along with a storage region and readout registers (Figure B.1a). The charge collection area is an array of silicon photodiodes, or pixels, which are sensitive to incident photons. The EMCCD spectral response is determined by the chip quantum efficiency, which can often surpass 90% in the visible for back-thinned EMCCDs. Each imaging pixel has a corresponding pixel in the storage array, which is masked to

protect it from incident light. Between imaging cycles, charge is rapidly transferred from the imaging array to the storage array to reset the imaging sensor for the next round of incident photons. The storage sensor is then read out row-by-row while new photoelectrons are accumulated on the imaging sensor. Pixel readout requires a series of charge transfer steps where clocking voltages are used to move electrons through gates connecting vertical pixels. Once pixels reach the edge of the storage array, they are shifted into the readout register which precedes an electron multiplication register and an output amplifier. Here, clocking voltages shift charges serially through the registers and into the amplifier. Electron multiplication is achieved by using particularly high voltages for clocking in the EM register, giving rise to secondary electrons by a process called impact ionization. After undergoing multiple rounds of amplification, typically 536 for the most common chip (manufactured by e2v Technologies), charge is converted to a voltage by the camera output amplifier and then digitized for data storage.

The aforementioned processes rescale the photoelectron data into new units ("counts") while also introducing new noise sources, in addition to the Poisson noise inherent to the signal [7] (Figure B.1b). Thermal energy in the silicon creates spontaneous electron-hole pairs during each acquisition cycle. Statistical variation in this dark current yields dark noise, which may be mitigated by cooling the sensor. Often, dark current is negligible at the frame rates used for single molecule imaging (with a cooled EMCCD) but must be considered for very long exposures (many seconds). Non-uniformity in the response of individual pixels to photons can yield fixed pattern noise which is evident when illuminating the sensor uniformly. As

electrons are shifted through the array for eventual readout, even the fairly low clocking voltages can create secondary electrons termed clock-induced charge (CIC) via impact ionization, much like the deliberate process in the electron-multiplication register. This is also a fairly small effect, noticeable only when signals are low, and fast vertical shift speeds may be used to further minimize CIC. A more significant noise is introduced during the readout process, as electrons are converted into voltages by the output amplifier. This read noise can easily exceed 50 e-/pixel for an EMCCD. However, the key feature of EMCCDs, electron multiplication, amplifies the electron signal relative to this noise so that the effective read noise is sub-electron. This electron multiplication does not come without a cost as the probabilistic nature of impact ionization introduces an additional multiplication noise factor to the signal. The net effect of electron multiplication is to practically eliminate the read noise, while effectively reducing the sensor quantum efficiency by this noise factor (~2). Finally, in addition to electron multiplication and newly introduced noise, electron values are scaled by a pre-amplifier gain and a constant offset is often added to keep count values positive.

Overall, the signal to noise of the EMCCD is summarized by the simple formula:

$$\mathrm{SNR}_{\mathrm{EMCCD}} = \frac{\mathrm{N}_{\mathrm{signal}}}{\sqrt{\mathrm{F}^2\left(\mathrm{N}_{\mathrm{signal}} + \mathrm{N}_{\mathrm{dark}} + \mathrm{N}_{\mathrm{CIC}}\right) + \left(\frac{\mathrm{N}_{\mathrm{read}}}{\mathrm{G}}\right)^2}}$$

Where N_{signal} is the number of signal photoelectrons, N_{dark} is the average number of thermally generated electrons, N_{CIC} is the average number of clock-induced electrons, N_{read} is the average number of read noise electrons, G is the overall gain (product of

EM gain and pre-amplifier gain) and F^2 is the noise factor from electron multiplication. Photon transfer methods isolate each of these noise sources to determine their relative contributions. Once the relevant parameters are measured, signals may be converted to electron units using:

$$\#\ \text{electrons} = \frac{(\text{counts-offset})}{\text{gain}}$$

In order to isolate the different noise components, a series of images is acquired under uniform illumination at varying light intensities. Next, these images are processed to generate a series of difference-frame images which has the net effect of removing fixed-pattern noise from the image, but doubling all other noise. Thus

$$\sigma^2_{\text{diff}} = 2(\sigma^2_{\text{shot}} + \sigma^2_{\text{read}} + \sigma^2_{\text{dark}} + \sigma^2_{\text{CIC}})$$

Since dark current and CIC are negligible, we simplify this to:

$$\sigma^2_{\text{diff}} = 2\left(\sigma^2_{\text{shot}} + \sigma^2_{\text{read}}\right)$$

The noise in the raw images may be expressed:

$$\sigma^2_{\text{total}} = \sigma^2_{\text{shot}} + \sigma^2_{\text{read}} + \sigma^2_{\text{FPN}}$$

With zero incident light, the read noise may be measured directly.

$$\sigma^2_{\text{total}}(\text{signal} = 0) = \sigma^2_{\text{read}}$$

Once the read noise is known, it can be subtracted from the difference noise (σ^2_{diff}) to isolate the shot noise term. Since the shot noise term may be rewritten as:

$$\sigma^2_{\text{shot}} = F^2 G^2 N$$

And the signal may be rewritten as:

$$\text{Counts} = GN + \text{offset}$$

The slope of the shot-noise line equals GF^2. The gain may be further analyzed by measuring the slope of the var_diff curve at zero EM gain, for which $F^2 = 1$ and

$$\sigma^2_{\text{shot}}(\text{no EM gain}) = \text{G}^2\text{N} = \text{A}^2\text{N}$$

Where A is defined as the preamp gain (total gain at zero EM gain) and the total gain $G = MA$ where M is the EM gain. The EM gain may be isolated by measuring the camera counts at a given light intensity under different gain settings

$$\text{M}_\text{i} = \frac{\text{counts } (\text{M} = \text{M}_\text{i})^2}{\text{counts } (\text{M} = 1)}$$

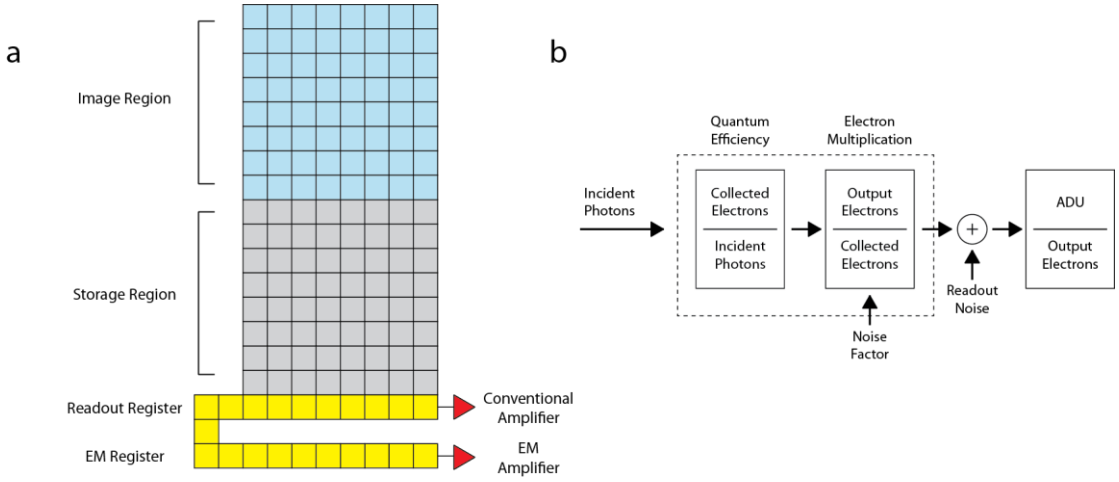

Figure B.1 EMCCD Architecture and Noise Characteristics. (a) Schematic of EMCCD architecture, depicting image sensor pixels (blue), storage pixels of frame transfer array (grey) and readout registers (yellow). (b) Block diagram of EMCCD function. Incident photons generate photoelectrons at a rate determined by the photon flux and quantum efficiency of the sensor. In frame transfer mode, charge is rapidly transferred to the storage array in the brief interval between camera frames, from where it is read out simultaneously as new charge is accumulated on the imaging array. Readout involves a series of vertical charge transfers to move rows of data to the readout register, where charges are then moved horizontally. Impact ionization due to high clocking voltages in the EM register serves to amplify the signal but not the readout noise from the output amplifier. With sufficiently high EM gain, EMCCDs can boost single photon signals above the read noise.

Using this method, the noise factor can be empirically measured

$$F^2(M \neq 1) = \frac{1}{G^2}\frac{\Delta\sigma^2_{shot}}{\Delta counts}$$

METHODS

Photoelectron calibration by digital photon counting

As a straightforward method for camera calibration, light from an LED array was spectrally filtered (541/5 bandpass filter) and projected onto a 1 μm pinhole (Figure B.2a). The LED was connected to a tunable current supply to control illumination power and a reference photodiode was incorporated into the illumination pathway to measure relative light intensities. The pinhole was imaged onto different detectors using an objective (Olympus UPlanSApo 4x/0.16) and tube lens, mounted in an Olympus IX-81 inverted microscope. To obtain a "ground truth" measurement, a photomultiplier tube was used in the detection path in conjunction with a photon counter (SR400, Stanford Research Systems). Photon counts and reference photodiode measurements were acquired simultaneously for a range of illumination intensities. Next, the PMT was replaced with an EMCCD and image series were recorded at different LED intensities while photodiode measurements were taken as a reference. Both the EMCCD and PMT responses were found to be linear with photodiode intensity (Figure B.1c). Furthermore, EMCCD response was fairly uniform over different pixels (<2% variation). Using these two datasets, the total gain could be

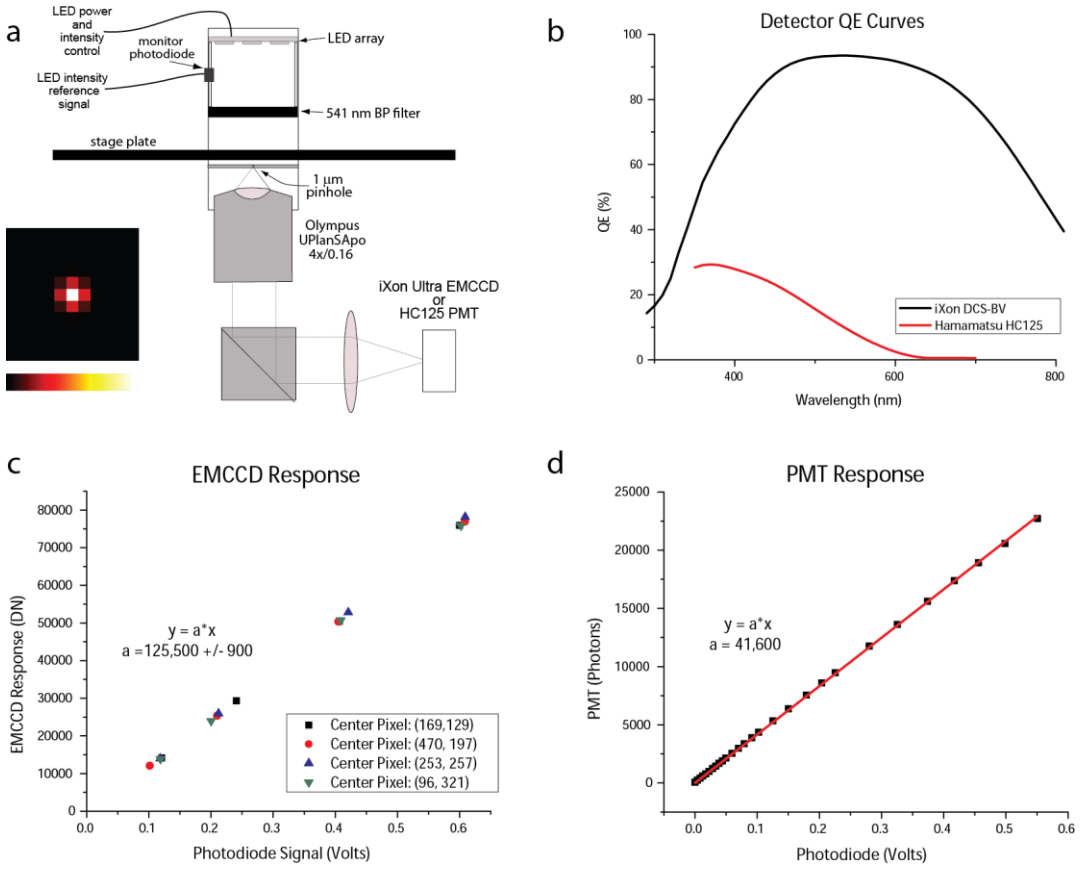

Figure B.2 Photon Counting Based EMCCD Calibration. (a) Schematic of the apparatus used for EMCCD calibration by photon counting. An LED array was projected through a narrow-band filter (541/5 bandpass) and onto a 1 micron pinhole. The pinhole was imaged onto a detector (PMT or EMCCD) using a low-magnification (4x) objective and tube lens. LED intensity was controlled using a tunable power supply and monitored using a reference photodiode built into the LED housing. (b) Detector Quantum Efficiency curves for the EMCCD (iXon DCS-BV) and bialkali PMT (HC125). QE values at 541 nm were used in the final CCF calculation. (c) EMCCD response was linear with LED intensity and very linear (<2% difference) over different pixels on the chip. (d) Photomultipler tube response was also very linear in this range (well below rates where pulse pile-up occurs during photon counting).

calculated via the simple formula (Figure B.1d):

$$\text{Total Gain} = \frac{\Delta\text{Counts}_{\text{EMCCD}}}{\Delta\text{Volts}_{\text{diode}}} \frac{\Delta\text{Volts}_{\text{diode}}}{\Delta\text{Photons}_{\text{PMT}}} \frac{\text{T}_{\text{PMT}}}{\text{T}_{\text{EMCCD}}} \frac{\text{QE}_{\text{PMT}}}{\text{QE}_{\text{EMCCD}}}$$

Photoelectron calibration by photon transfer curves

Uniform illumination was generated by projecting light from an LED through two pieces of opal glass (Figure 3). Image series (500 frames each) were recorded at different light intensities for a 64x64 sensor subregion over which the light was sufficiently uniform (<1% non-uniformity). Difference frames were calculated and noise was analyzed according to methods detailed in the "Theory" section. Frame differencing dramatically removed fixed pattern noise present at higher light levels (most apparent at low gains and high illumination intensities) (Figure B.3a-c). FPN renders traditional mean-variance methods of gain measurement ineffective for CCDs and EMCCDs due to its N^2 dependence on the number photons. We also recovered a measurement of the noise factor F^2 which resembles published results [8] (Figure B.3d).

DISCUSSION

Both the photon counting and photon transfer methods agreed fairly well on two different EMCCDs that we tested, with measured gains differing by less than ~10%. A newer camera feature, called Andor Count Convert achieved remarkable similarity to the photon transfer-based calibration and is easily enabled in Andor's camera software. In contrast, an Andor-supplied formula for calibration disagreed

Figure B.3 Photon Transfer Curves for Photoelectron Calibration. (a) Pixels of EMCCD data under uniform illumination at no EM gain, showing significant fixed pattern noise which is removed by subtraction of consecutive frames. Blue and red plots show intensity profiles across the same row in the raw and processed data. (b) Photon transfer curves acquired at Gain 25 with the iXon 897 Ultra. PTC Analysis separates different noise components and permits measurement of fundamental camera quantities. DN = digital numbers (counts). (c) Black and red points show mean-variance data before and after difference-frame processing. Although it has been used in the literature, mean-variance analysis is not strictly applicable for raw EMCCD data due to the presence of non-Poissonian noise sources. However, this effect is mitigated at higher gains (and lower light intensities). (d) Excess noise factor due to multiplicative noise as a function of EM gain, as measured from mean-variance plots of difference-frame data (in conjunction with extracted gain values from constant-light measurements). The overall shape of the noise factor curve resembles that in previous publications and plateaus near the widely-accepted approximation of 2. (e) Comparison of camera calibration results using the PTC method (uniform illumination), Andor Count Convert and photon counting approaches using an Andor 897 Ultra EMCCD. All methods agree reasonably well (within 10-20%). (f) Comparison of camera calibration results for an Andor iXon 860. Note that the measured gain is highly nonlinear with respect to the software gain setting. Both photon counting and photon transfer recover similar gain values, but an Andor-provided formula disagrees significantly with the measured gains (overshooting at low software values and undershooting at higher values).

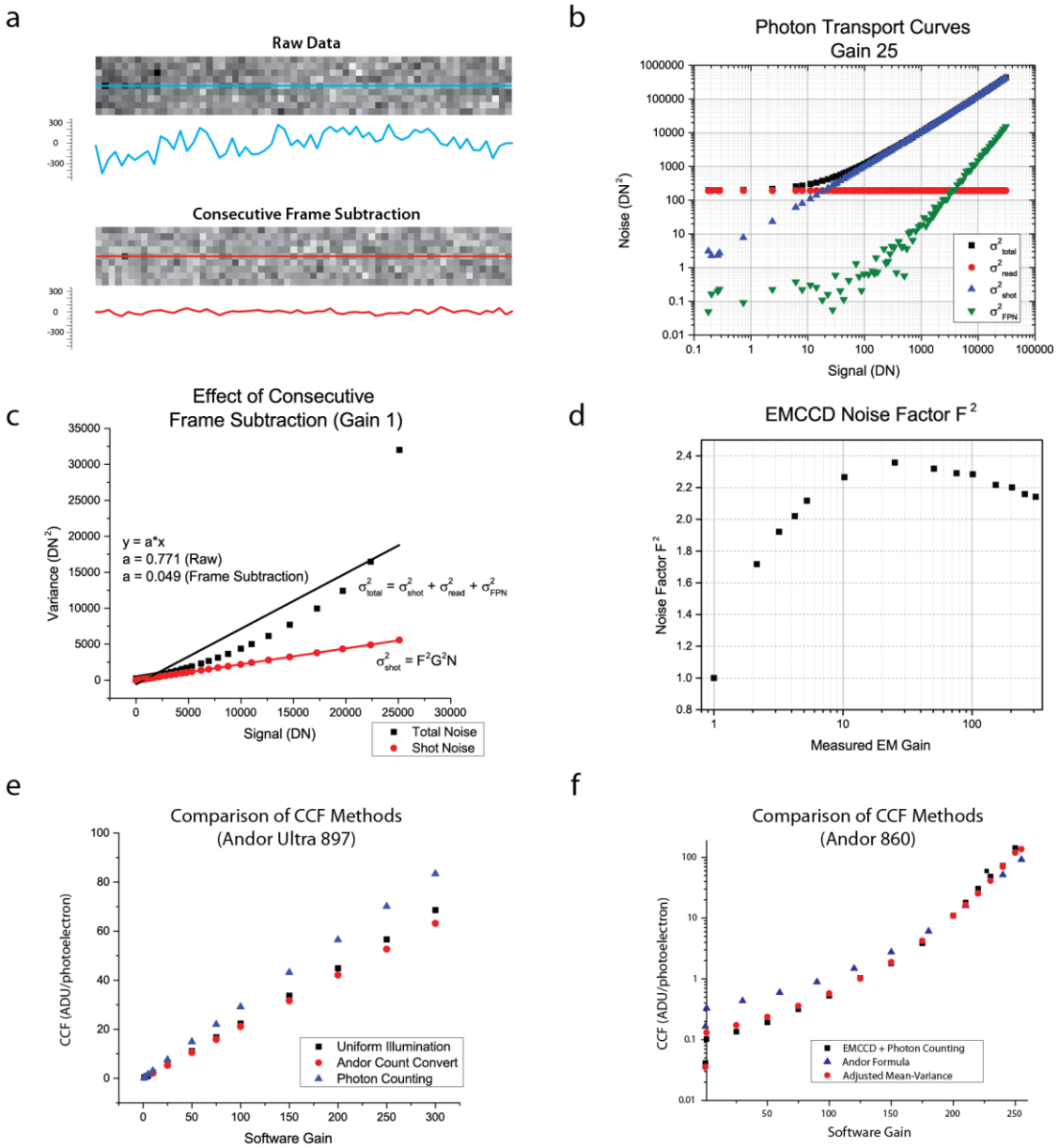
a
Raw Data
300
0
-300
Consecutive Frame Subtraction
300
0
-300
b
Photon Transport Curves
Gain 25
Noise (DN²)
Signal (DN)
σ²total
σ²read
σ²shot
σ²FPN
c
Effect of Consecutive
Frame Subtraction (Gain 1)
Variance (DN²)
y = a*x
a = 0.771 (Raw)
a = 0.049 (Frame Subtraction)
σ²total = σ²shot + σ²read + σ²FPN
σ²shot = F²G²N
Signal (DN)
Total Noise
Shot Noise
d
EMCCD Noise Factor F²
Noise Factor F²
Measured EM Gain
e
Comparison of CCF Methods
(Andor Ultra 897)
CCF (ADU/photoelectron)
Uniform Illumination
Andor Count Convert
Photon Counting
Software Gain
f
Comparison of CCF Methods
(Andor 860)
CCF (ADU/photoelectron)
EMCCD + Photon Counting
Andor Formula
Adjusted Mean-Variance
Software Gain

significantly with the measured calibrations, likely due to misapplied semiconductor theory (Supplementary Note) and significant gain ageing for the older iXon 860 EMCCD (Figure B.3e,f). Unfortunately, numerous labs have cited this formula in their quantification of single molecule data. While it is promising that newer cameras can achieve a more accurate photoelectron conversion, through features such as Count Convert, it is important to remember that such features still rely on factory-measured camera properties which may change over the timecourse of user operation. Andor offers a user-initiated gain recalibration (EM Cal) on some of its models which can compensate for gain ageing, but users must remain vigilant for accurate quantification. The described photon transfer method is a simple operation which can measure camera properties with inexpensive optics and a few hours of measurement and analysis.

We conclude with a few tips about EMCCD use:

1. **EM Gain**: EMCCD gain is useful for elimination of read noise (typically 50-60 e- per pixel at the highest readout rates used). However, too much gain will also accelerate gain ageing and negatively impact the lifetime of the camera. We recommend using as low a gain as possible to overcome read noise and achieve high signal-to-noise imaging. Typically, a gain of 100 is more than sufficient because it will drop the read noise below 1 e- rms while gains above 200 only age the camera without improving image quality.
2. **Vertical Shift Speed**: Using faster vertical shift speeds can help minimize clock-induced charge.

3. **Readout Rate**: Using the slowest acceptable readout rate for a given frame rate will minimize the readout noise and improve SNR. For an Andor 897 EMCCD, the camera is capable of 17 MHz readout which permits 19 ms frames at full frame (512x512). However, if you aim to image at a much slower speed, operating at a lower readout rate will improve image quality or permit the use of lower gains. The 17, 10, 5 and 1 MHz settings on the Ultra achieve frame transfer rates of 19, 31, 59 and 287 ms with read noise of 91, 67, 37 and 15 electrons rms, respectively (at pre-amp setting 3).
4. **Frame rates and binning/cropping**: Sensor frame rates can be improved considerably by cropping. While the 897 Ultra operates at a max speed of 47 Hz in full-frame mode, this can be increased to 197 Hz for a 64x64 subregion. Further boosts are possible by moving the imaging area to the region adjacent to the readout register.

SUPPLEMENTARY NOTE ON ANDOR FORMULA

Andor provided us with the following formula for count conversion:

$$\mathrm{eV} = 3.65 \frac{\text{counts}}{\text{EM gain}} \frac{\text{electrons per A/D count}}{\text{QE}}$$

where 3.65 is a constant for photoelectron production in silicon. This is intended to aid back-calculation of the number of photons incident on the silicon. However, it misuses a principle which applies in the X-ray regime, where a single photon can generate multiple photoelectrons. Instead, we used the simpler formula

$$\#\text{electrons} = \frac{\text{counts}}{\text{EM gain}} \text{electrons per A/D count}$$

which still failed to match the measured camera properties, likely due to camera gain ageing, which was particularly bad for the older 860 model.

.

REFERENCES

1. S. T. Hess, T. P. K. Girirajan, and M. D. Mason, "Ultra-high resolution imaging by fluorescence photoactivation localization microscopy.," Biophys. J. **91**, 4258–72 (2006).

2. T. Plakhotnik, A. Chennu, and A. V. Zvyagin, "Statistics of single-electron signals in electron-multiplying charge-coupled devices," IEEE Trans. Electron Devices **53**, 618–622 (2006).

3. M. H. Ulbrich and E. Y. Isacoff, "Subunit counting in membrane-bound proteins.," Nat. Methods **4**, 319–21 (2007).

4. J. R. Janesick, *Scientific Charge-Coupled Devices*, Press Monographs (Society of Photo Optical, 2001).

5. Z.-L. Huang, H. Zhu, F. Long, H. Ma, L. Qin, Y. Liu, J. Ding, Z. Zhang, Q. Luo, and S. Zeng, "Localization-based super-resolution microscopy with an sCMOS camera.," Opt. Express **19**, 19156–68 (2011).

6. F. Long, S. Zeng, and Z.-L. Huang, "Localization-based super-resolution microscopy with an sCMOS camera part II: experimental methodology for comparing sCMOS with EMCCD cameras.," Opt. Express **20**, 17741–59 (2012).

7. J. Hynecek and T. Nishiwaki, "Excess noise and other important characteristics of low light level imaging using charge multiplying CCDs," IEEE Trans. Electron Devices **50**, 239–245 (2003).

8. M. S. Robbins and B. J. Hadwen, "The noise performance of electron multiplying charge-coupled devices," IEEE Trans. Electron Devices **50**, 1227–1232 (2003).